

Bayesian Modelling of Nuclear Fusion Experiments

vorgelegt von

B.Sc.

Sehyun Kwak

ORCID: 0000-0001-7874-7575

an der Fakultät II – Mathematik und Naturwissenschaften

der Technischen Universität Berlin

zur Erlangung des akademischen Grades

Doktor der Naturwissenschaften

– Dr. rer. nat. –

genehmigte Dissertation

Promotionsausschuss:

Vorsitzender: Prof. Dr. Holger Stark

Gutachter: Prof. Dr. Dieter Breitschwerdt

Gutachter: Prof. Dr. Robert Wolf

Gutachter: Prof. Young-chul Ghim

Tag der wissenschaftlichen Aussprache: 04.11.2020

Berlin 2020

*As far as the laws of mathematics refer to reality,
they are not certain, as far as they are certain, they
do not refer to reality.*

Albert Einstein, 1921

Abstract

Bayesian probability theory as a general framework for scientific modelling and inference is introduced and applied to nuclear fusion experiments in order to provide consistent inference solutions given multiple heterogeneous data sets. Fusion plasmas are complex physical systems, in which charged particles are confined by the electromagnetic force. The physics parameters of the plasmas involve various independent measurements from sophisticated scientific instruments. Owing to the complexity of the experiments and the fusion plasmas, so far, no physics model can predict major physical phenomena, like transport, sufficiently well. Hence, generic, non-parametric Gaussian processes are used to model physics parameters such as plasma current density and pressure. Multiple predictive models of scientific instruments have been developed individually, and they have been combined into a joint model with Gaussian process priors in order to perform robust and consistent inference. The joint model provides the joint posterior probability distribution of the physics parameters, hyperparameters and other unknown parameters, such as calibration factors. This thesis theoretically and experimentally shows that *the joint posterior distribution intrinsically embodies Bayesian Occam's razor*. Therefore, *by exploring the joint posterior distribution, inference solutions can be found with optimal values of all the model parameters, based on the principle of Occam's razor*. In other words, we can apply Bayesian Occam's razor to real-world problems without calculation of the model evidence, typically requiring marginalisation over a high-dimensional parameter space, which is one of the major obstacles to Bayesian model selection. Based on this foundation, several applications have been developed for consistent inference of the physics parameters of the fusion plasmas at two major fusion experiments, the Joint European Torus (JET) and Wendelstein 7-X (W7-X). The first application has been developed by modelling emission spectra and relevant atomic physics for the lithium beam emission spectroscopy system at JET to provide the edge plasma electron density profiles and their posterior uncertainties. Additionally, interferometers, Thomson

scattering and spectroscopy systems have been combined, improving the consistency of the inference solutions. These joint inference applications have been developed for JET and W7-X to provide the marginal posterior distribution of the plasma density and temperature profiles. Furthermore, the full joint posterior distribution of axisymmetric plasma equilibria, given magnetic field and plasma pressure measurements, has been explored for the first time at JET. These equilibrium solutions suggest two different possible plasma equilibrium current distributions for high-confinement mode fusion plasmas: either a strong toroidal current density or a poloidal current flux hole in the edge region. The principles and methods developed in this thesis are general and applicable to all kinds of scientific problems. This new approach to model selection by exploring the joint posterior distribution contributes to the general automatisisation of scientific discovery.

Zusammenfassung

Die Bayes'sche Wahrscheinlichkeitstheorie wird als allgemeines Framework für wissenschaftliche Modellierung und Inferenz eingeführt und auf Kernfusionsexperimente angewandt, um konsistente Inferenzlösungen bei mehreren heterogenen Datensätzen zu ermöglichen. Fusionsplasmen sind komplexe physikalische Systeme, in denen geladene Teilchen durch die elektromagnetische Kraft eingeschlossen sind. Die physikalischen Parameter der Plasmen umfassen verschiedene unabhängige Messungen mit hochentwickelten wissenschaftlichen Instrumenten. Aufgrund der Komplexität der Experimente und der Fusionsplasmen kann bisher kein physikalisches Modell wichtige physikalische Phänomene, wie den Transport, ausreichend gut vorhersagen. Daher werden generische, nichtparametrische Gauß'sche Prozesse verwendet, um physikalische Parameter wie die Plasmastromdichte und den Druck zu modellieren. Mehrere prädiktive Modelle wissenschaftlicher Instrumente wurden einzeln entwickelt und in einem gemeinsamen Modell mit Gauß'schen Prozess-Prioren kombiniert, um robuste und konsistente Schlussfolgerungen zu ermöglichen. Das kombinierte Modell liefert die gemeinsame posteriore Wahrscheinlichkeitsverteilung der physikalischen Parameter, Hyperparameter und anderer unbekannter Parameter, wie zum Beispiel Kalibrierfaktoren. Diese Arbeit zeigt theoretisch und experimentell, dass *die gemeinsame Posteriorverteilung inhärent Ockhams Rasiermesser verkörpert*. Daher können *durch die Untersuchung der gemeinsamen Posteriorverteilung Inferenzlösungen mit optimalen Werten aller Modellparameter gefunden werden, die auf dem Prinzip von Ockhams Rasiermesser basieren*. Mit anderen Worten: Wir können Ockhams Rasiermesser mittels Bayes'scher Wahrscheinlichkeitstheorie auf Probleme der realen Welt anwenden, ohne die Evidenz des Modells zu berechnen, was typischerweise eine Marginalisierung über einen hochdimensionalen Parameterraum erfordert, was eines der Haupthindernisse für die Bayes'sche Modellauswahl darstellt. Auf dieser Grundlage wurden mehrere Anwendungen zur konsistenten Inferenz der physikalischen Parameter der Fusionsplasmen bei zwei großen Fusionsexperimenten, dem

Joint European Torus (JET) und Wendelstein 7-X (W7-X), entwickelt. Die erste Anwendung wurde durch die Modellierung von Emissionsspektren und relevanter Atomphysik für das Lithiumstrahl-Emissionsspektroskopiesystem bei JET entwickelt, um die Randplasma-Elektronendichteprofile und ihre Posteriorunsicherheiten zu ermitteln. Zusätzlich wurden Interferometer, Thomson-Streuung und Spektroskopiesysteme kombiniert, um die Konsistenz der Inferenzlösungen zu verbessern. Diese gemeinsamen Inferenzanwendungen wurden für JET und W7-X entwickelt, um die marginale Posteriorverteilung der Plasmadichte- und Temperaturprofile zu liefern. Darüber hinaus wurde bei JET zum ersten Mal die volle gemeinsame Posteriorverteilung der achsensymmetrischen Plasmagleichgewichte bei gegebenen Magnetfeld- und Plasmadruckmessungen untersucht. Diese Gleichgewichtslösungen schlagen zwei verschiedene mögliche Plasmagleichgewichtsstromverteilungen für High-Confinement-Mode-Fusionsplasmen vor: Entweder eine starke toroidale Stromdichte oder ein poloidales Stromflussloch im Randbereich. Die in dieser Arbeit entwickelten Prinzipien und Methoden sind universell nutzbar und auf alle Arten von wissenschaftlichen Problemen anwendbar. Dieser neue Ansatz zur automatischen Modellauswahl durch Untersuchung der gemeinsamen Posteriorverteilung trägt zur allgemeinen Automatisierung der wissenschaftlichen Entdeckung bei.

Preface

When I conducted a free fall experiment in a physics lab course in science high school similar to what Galileo did from the Leaning Tower of Pisa, I did wonder, why should we select a second order polynomial equation as a model to explain the law of free fall? Or, more precisely, how could we *know a priori* a second order polynomial equation is the law of free fall? It was very obscure for me, but, on the other hand, it looked like it was very obvious for everyone in the class, that we should use the second order polynomial function as if it was given by God. Nevertheless, I did not raise this question to my physics teacher there at that time, because I could expect the answer that the law of free fall can be derived from Newton's laws of motion, $F = ma$. However, what if we would have been born before Newton, like Galileo was? Even though we know Newton's laws of motion, why should we not try other models instead of *believing* this model since we have some experimental data? Since then, this enigmatic question had stayed in my mind for over seven years until I finally got to know Bayesian Occam's razor, which is one of the deepest and most profound principles that I have ever seen in my entire life.

Many people often regard the principle of Occam's razor, complexity should not be posited without necessity, as a philosophical or an ad hoc principle, not a scientific one. However, in probability theory, this principle is one of the most fundamental logical nature of probability. In short, since a complex model can generate a greater variety of output than a simple model does, the probability that we would observe a specific value of the output from the complex model is intrinsically lower than the one of the simple model. Based on the lecture notes [1] where these probabilities were calculated for Galileo's free fall experiment, I made the calculations by myself and confirmed that the probability of the second order polynomial equation was the highest. That was one of the most enlightening moments; the answer to the enigmatic question was brought to light in the light of the data. I did completely understand that this is one of the most important keys to achieve the automation of science that is one of my

dreams and at the same time, one of mankind's most ambitious missions. The principle of Occam's razor should be now rewritten like this: *complexity is not probable without evidence*.

This is just the beginning of our journey to the automation of science, and we do still have many unsolved problems and unanswered questions. Nevertheless, my story starts here. Before we move onto the first page, I would very much like to express my deepest gratitude to a number of people: Prof Dr Thomas Klinger for accepting me into his division and for continuous support. Dr Young-Mu Jeon, Dr Mathias Brix, Dr Joanne Flanagan, Dr Alexandru Boboc, Dr Gabor Szepesi, Dr Jon Hillesheim, Dr Elena de la Luna, Dr Humberto Trimiño Mora, Dr Sergey Bozchenkov, Dr Daihong Zhang and Dr Maciej Krychowiak for critical discussions in different experimental topics relating to my work. Dr Henri Weisen, Dr Marco Sertoli and Dr David Terranova for organising scientific collaborations at JET. Udo Höfel, Andrea Pavone, Jonathan Schilling, Robert Hofstetter, Jaewook Kim, Semin Jeong, Tae-suk Oh and Bin Ahn for insightful, thought-provoking and interesting conversations. Hyeonyeong Kim, Yeona Jin, Sehoon An, Marco Krause, Sandra Corinna Hauck, Dave Rose, Olga Siddons, Andreas Werner, Per Helander and his family and other PhD students at the IPP and KAIST for delightful company with their kind minds. Dr Hyun-tae Kim for sharing his enthusiasm and inspiration for fusion energy. Dr Lynton Appel and Dr Oliver Ford for deepening my understanding of this subject. Prof Dr Robert Wolf and Prof Dr Dieter Breitschwerdt for giving me the very opportunity to complete my work at TU Berlin. Special thanks to my supervisor Professor Young-chul Ghim, one of the most high-minded classical physicists, for continuous support, mentorship and concern in good and bad times. Many thanks to Dr Jakob Svensson, my right honourable supervisor, without whose imagination, intuition and the deepest intelligence, this work would have never been possible. Finally, I genuinely appreciate my dear families and friends.

Sehyun Kwak
Greifswald, March 2020

Contents

Abstract	v
Zusammenfassung	vii
Preface	ix
1 Introduction: Do α-machines dream of artificial scientists?	1
2 Scientific Modelling	7
2.1 Hypothesis and probability	8
2.2 Model, prediction and inference	9
2.3 Model complexity and Occam's razor	14
2.4 Prior knowledge	20
2.5 Outlook	25
2.6 Minerva framework	26
3 Nuclear Fusion	27
3.1 Plasma equilibrium	30
3.2 Fusion experiments	32
3.3 Plasma diagnostics	35
3.4 Bayesian inference in nuclear fusion research	38
4 Thesis Articles	41
4.1 Article I	52
4.2 Article II	67
4.3 Article III	87
4.4 Article IV	113
4.5 Article V	133
5 A look ahead	169

Contents

Statutory declaration	171
List of Figures	173
Publications as first author	175
Publications as coauthor	179
Acronyms	183
Bibliography	185

1

Introduction: Do *a*-machines dream of artificial scientists?

When I had finished most of my university studies in chemistry and chemical/biomolecular engineering, and after I had executed chemical experiments for five years, I ended up having one of my dreams. In a lab course, typically all students were supposed to execute a series of recipes as precisely as possible, for example, to stir a solution while keeping its temperature of 50 °C for three hours. Please keep in mind that there are plenty of recipes, requiring much more sophisticated and complicated techniques in chemical experiments. Nevertheless, the point is that what scientists have been doing in a laboratory is a series of operations which in principle a machine would be able to execute. One might ask, as many people are fond of saying, ‘No one will ever make a machine to replace the human mind that does many things that no machine could ever do.’ An insightful answer to this question given by John von Neumann in his lecture on computers given in Princeton in 1948, ‘You insist that there is something a machine cannot do. If you will tell me precisely what it is that a machine cannot do, then I can always make a machine which will do just that!’ [2] In principle, the only operations that a machine cannot execute for us are those which cannot be precisely described in detail or which cannot be definitely completed in a finite number of operations [3, 4]. Fortunately, every science, by definition, that has thrived has thrived upon its own experiments that can be precisely described in detail and at the same time definitely completed in a finite number of operations. In other words, science is one of the very fields in which *a*-machines [4] are eager to be employed. Unlike other fields of study such as language or music, every piece of work in science has been done by mankind so

far is repeatable by a reasonable mind of either a man or a machine.¹ Here, one might argue that a machine can only do what it does, but not *think*. In recent years, we have been seeing that, in many fields, machines started to recognise patterns and, in some context, even better than humans. If this is the case, why can they not recognise such patterns throughout the history of science or in the context of thinking? I imagine that, given a chronological pattern of scientific discovery, we train a machine to autonomously derive physics formulas, which consist of a combination of mathematical symbols. I would claim that we are capable of creating a machine that understands such a pattern like a scientist. Moreover, I believe that *a*-machines will be able to think in a way like or even better than another *one*, which exists inside everyone's head, *does*.

The reason why I introduced my dream of artificial scientists here is that the work presented in this thesis does primarily intend to contribute a step towards the quest of the automation of science. In order to create a machine, who can reason things out like a scientist, will make scientific discoveries autonomously in the future, we have to explain two important concepts to the machine as precisely as possible: knowledge and causality. Fortunately, we have a number of great minds who have been developing the language of knowledge and causality over the last few centuries in probability theory. The key abstraction in this context is that, in probability theory, knowledge can be represented by a probability, and causality can be seen as a unidirectional, counterfactual conditional dependency.² Obviously, this abstraction has been founded throughout all the philosophical discussions that might go deep down to the meaning of probability as well as knowledge and causality [1, 2, 9–20], but I will not dwell here on this but rather make a point that we have a formal framework for scientific inference in which knowledge can be represented in a quantitative way, as described in the following chapter. This formal framework has been elegantly realised in the form of a software framework, Minerva [21, 22], for general

¹The modern artificial intelligence systems become more and more capable of working in such fields of study, for example language [5] and music [6], and at the same time achieving a certain goal in a specific environment [7, 8]. Surprisingly, they figure out, by themselves, what to do, by learning patterns based on observations given to them or made by them.

²David Hume made the first explicit definition of causation in terms of counterfactuals, as he wrote in this book [9], 'We may define a cause to be *an object followed by another, and where all the objects, similar to the first, are followed by objects similar to the second*. Or, in other words, *where, if the first object had not been, the second never had existed*.' This counterfactual interpretation of causation has been formalised in the language of probability theory, which a machine in principle would be able to understand [10].

scientific modelling and inference in which all the applications in this thesis have been developed. When I started this work, I did immediately understand that one of the missions that Minerva was designed to eventually undertake is the automation of science. It might not be apparent in the thesis articles that describe applications because they tend to focus on practical and technical issues. Nevertheless, one of the main missions in this thesis is to show that this framework for scientific inference is applicable to a complex system in order to provide consistent inference solutions based on quantitative knowledge in a systematic way, in which *a*-machines will make scientific discoveries autonomously in the future. A nuclear fusion experiment is an excellent example since it is itself, undoubtedly, one of the greatest challenges of our time to provide safe, clean and unlimited sources of energy, and it is at the same time an extraordinarily complex system where we could explore the feasibility of this framework. In a nuclear fusion experiment, the fuel is in a state of hot, ionised, collectively behaving gas, also known as a plasma, which is a very complex physical system. The fusion plasma can be quantified by a number of physics parameters, which involve multiple heterogeneous data sets from sophisticated and complicated scientific instruments. Owing to the high complexity of the experiment and the fusion plasma, so far, no physics model can predict major physical phenomena, like transport, sufficiently well. Hence, generic, non-parametric Gaussian processes are used to model physics parameters such as plasma current density and pressure. Moreover, the system parameters of these scientific instruments, for example, their calibration factors, are often unknown. For these reasons as well as for the mission that I mentioned, I did intentionally let a machine (an optimisation algorithm on a number of computers) decide the complexity of physics models and calibrate the scientific instruments based on the principle of Bayesian Occam's razor [14, 19, 20], which is one of the key solutions to the automation of science. The principle of Occam's razor allows any human or machine mind to find an optimal model of a system with an appropriate complexity in the light of the data.

This thesis suggests a novel approach of applying Bayesian Occam's razor to real-world problems: *representing the inference solution as the joint posterior probability distribution of the parameters and models which intrinsically embodies the principle of Occam's razor. Every sample drawn from the joint posterior distribution is a possible solution for the model and its parameters which is automatically found with an appropriate complexity based on the principle of Occam's razor. In other words, By exploring the joint posterior distribution, we can find*

an optimal solution not only for the model of a system but also for its parameters given observations. This approach can be more practical and effective than the conventional one based on exploring the marginal probability distribution of observations, also known as the *model evidence*. I view this as a contribution to the automation of science. We only let a machine have the observations but nothing else, and as we see in an example of Galileo's free fall experiment [13] shown in Figure 1.1, the machine autonomously reveals that the law of free fall is a second order polynomial equation $h = \frac{1}{2}gt^2$ and at the same time its parameter, the gravitational acceleration, $g = 9.810 \text{ m/s}^2$. This inference solution is close to 9.807 m/s^2 , the underlying value of the gravitational acceleration used to generate the observations by physics model. Here, the model space is a set of different polynomial models, but in principle, we can explore an arbitrary model space which includes any parametric/non-parametric model.

This theoretical foundation is applied to all the applications, which have been developed to obtain consistent inference of the physics parameters of the fusion plasmas given multiple heterogeneous data sets at two major fusion experiments, the Joint European Torus (JET) and Wendelstein 7-X (W7-X). The first application described in Article I and Article II has been developed by modelling emission spectra and relevant atomic physics for the lithium beam emission spectroscopy system at JET to provide the edge plasma electron density profiles and their posterior uncertainties. Article III and Article IV describe that consistent inference of the plasma density and temperature profiles based on joint models of various scientific instruments such as interferometers, Thomson scattering and spectroscopy systems at JET and W7-X. Furthermore, the full joint posterior distribution of axisymmetric plasma equilibria given magnetic field and electron pressure measurements has been explored for the first time at the JET experiments as described in Article V. By exploring the joint posterior distribution, these applications obtain optimal inference solutions for the physics parameters as well as hyperparameters and other unknown parameters, such as calibration factor, based on the principle of Occam's razor. Further explanation of the theoretical foundation and the applications will be provided in the following chapters.

Although we have made some efforts towards the automation of science, we undoubtedly have many unsolved problems and unanswered questions. Nevertheless, I believe that we will achieve the automation of science, and that the solution will be built on probability theory. Finally, if someone would ask me

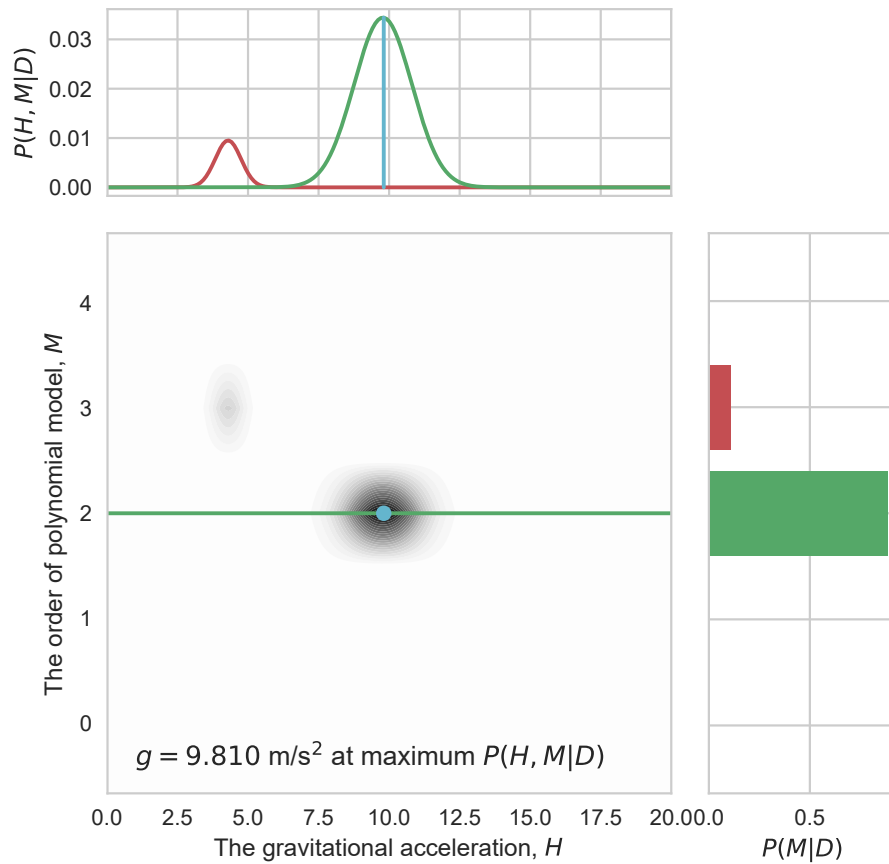


Figure 1.1: An optimal solution (in cyan) for the model M for the law of free fall (the second order polynomial model, $M = 2$) and its parameter, the gravitational acceleration H ($H = 9.810 \text{ m/s}^2$) can be found given the observations from Galileo’s free fall experiment by exploring the joint posterior probability distribution $P(H, M|D)$. The green and red lines shown in the top plot are the joint posterior probability densities $P(H, M = 2|D)$ and $P(H, M = 3|D)$. The green and red bars shown in the right plot are the marginal posterior probabilities $P(M = 2|D)$ and $P(M = 3|D)$. The underlying value of the gravitational acceleration used to generate the observations by simulating Galileo’s free fall experiment was 9.807 m/s^2 .

Chapter 1 Introduction: Do a-machines dream of artificial scientists?

a question, 'Do *a*-machines dream of artificial scientists?' My answer to this will be, 'Yes, *I* do dream of artificial scientists, who have mind over data, like human scientists.'

2

Scientific Modelling

The actual science of logic is conversant at present only with things either certain, impossible, or entirely doubtful, none of which (fortunately) we have to reason on. Therefore the true logic for this world is the calculus of probabilities, which takes account of the magnitude of the probability which is, or ought to be, in a reasonable man's mind.

(James C. Maxwell)

Throughout history, mankind has been facing more and more complex problems in science and technology which require solutions based on scientific methods. Scientific methods involve making conjectures, modelling systems, deriving predictions, conducting experiments and updating knowledge based on observations as logical consequences [9, 11–13, 15]. Bayesian methods for scientific inference have been developed over the last few centuries by Reverend Thomas Bayes [23], Pierre-Simon Laplace [24], John Maynard Keynes [25], Sir Harold Jeffreys [14, 17], Richard Threlkeld Cox [16], Edwin Thompson Jaynes [2] and few others. Since then, the usage of Bayesian methods has been steadily growing in many fields of study, especially physics [26–28], machine learning [20, 29, 30], artificial intelligence [18, 31], causality [10] and nuclear fusion [21, 32–39]. Nevertheless, Bayesian methods have often been used as one of many statistical tools, not as a framework for scientific inference, even to most of the scientists who use the Bayesian methods. We will therefore briefly introduce the framework for scientific inference and its constituents which this thesis is based on, especially for the readers who are not familiar with this perspective. These constituents are: (i) to assign a probability to a hypothesis, (ii) to model

a system as a joint probability, (iii) to compare alternative models of differing complexities by Bayesian Occam's razor and (iv) to impose physics/empirical knowledge in a prior probability.

2.1 Hypothesis and probability

When we try to solve complex problems in science, we always have a limited data set and an incomplete understanding of a system, thus it is virtually impossible to give an exact answer without uncertainties. We can propose a number of possible hypotheses which can explain how the system works in the real world, but most of the times, we can not know whether these hypotheses are true or false with absolute certainty, like logic. For example, when we start out for a walk, we can not know that our hypothesis that it is going to be raining in ten minutes is either certainly true or false (perhaps our expectation of rain might be less likely than not) [25]. Even a weather forecast model, which has been developed by thousands of scientists and simulated on supercomputers, would not be able to tell you, at least on some occasions, whether it is going to be raining in ten minutes or not with absolute certainty. Instead, we would assign a probability to our hypothesis, for example, our probability of raining in ten minutes is 0.7. Intuitively, it would be very reasonable to assign not only true or false but also a probability to propositions. We have been already doing this intuitively in daily life, but in science, we need to have a quantitative rule so that even a machine can reason things out like a thinker.

Since Reverend Thomas Bayes made the first attempt to assign a probability to his hypothesis for a non-trivial problem of data analysis in his work [23], Pierre-Simon Laplace pioneered classical probability theory [24] and used it to solve problems in celestial mechanics. Edwin Thompson Jaynes developed a formal system, known as probability theory as the logic of science [2], which influences the framework for scientific inference in this thesis to a large extent.¹ In this interpretation of probability theory, the probability is defined based on Cox's desiderata [16]: (i) Representation of degrees of plausibility by real numbers, (ii) Qualitative correspondence with common sense and (iii) consistency.

¹I would like to remark that this logic of science [2] is influenced by the work of Sir Harold Jeffreys [17].

Jaynes proved that this epistemic interpretation of probability does not contradict modern probability theory, which is based on the Kolmogorov axioms [40].² Unlike logic, in which every proposition is either true or false, in probability theory, a probability is assigned to every proposition. A certainty is represented by a probability 0.0 or 1.0 (for being false or true) whereas uncertainties are represented by a probability in a range from 0.0 to 1.0. When the probability of proposition A is higher than the one of proposition B , then A is more probable than B , and vice versa.

Based on the epistemic interpretation of probability, we will now assign a probability or a probability function $P(H)$ to a hypothesis or a set of hypotheses H , for example our expectation of rain. Any human or machine whose probability of rain is small might start out for a walk. Unlike the conventional theory of probability, also known as Frequentism, in which a probability is associated with a physical system, in Bayesianism, a probability is epistemic knowledge of hypothetical propositions in a system such as a human or a machine mind. As one might imagine, these probabilities can be different in different observers for the same hypothesis, depending on the observations and models that they rely on. For example, your expectation of rain can be different from those of other people or weather forecast machines. However, this does not mean that these probabilities are inconsistent. Everyone would have exactly the same probability of rain if they had the same observations and models.

We have now a quantitative formal system to reflect our knowledge to any hypothesis. We can now compare more than two hypotheses quantitatively in probability theory. However, probability theory is not ready yet to be used to solve problems in the real world. Before we make full use of it, we have to define all the necessary *apparatus*: hypothesis space, prior probability, predictive distribution and model.

²Kolmogorov developed the mathematical foundation of probability theory in the language of set theory and measure theory which modern probability theory is based on. Jaynes claimed that the Kolmogorov axioms are, for all practical purposes, derivable from Cox desiderata of rationality and consistency, therefore his perspective on probability does not contradict the Kolmogorov axioms [2].

2.2 Model, prediction and inference

The foundation of scientific methods is that we acquire our knowledge of reality through refinement or elimination of hypotheses and models based on observations in the real world [9, 11–13, 15]. Hypotheses are conjectures which derive predictions through models of a system, and the purpose of experiments is to make observations in the real world from which we carry out inference via a logical connection between the observations and hypotheses. In other words, we update our epistemic knowledge of hypotheses based on these observations and models as logical consequences.

Let us suppose that we have a set of hypotheses, known as a *hypothesis space* H . For example, it is going to be raining in ten minutes which can be true or false $H = \{\text{true}, \text{false}\}$, or the mass of Saturn [24] which can be any positive real number $H = \{h \in \mathbb{R} | h > 0\}$. We can assign either a discrete or a continuous probability function to these hypothesis spaces. For example, a discrete probability function can be assigned to the former hypothesis space (weather forecast), and a continuous probability function can be assigned to the latter hypothesis space (the mass of Saturn). We start with our *prior knowledge and assumptions* over these hypothesis spaces before we make observations by an experiment which can be quantitatively represented by an initial probability, also known as a *prior probability* $P(H)$. For example, we can assign 50-50 to a prior probability of our expectation of rain (it is going to be raining in ten minutes) or a uniform distribution to the mass of Saturn greater than zero to some maximum, for instance, the total mass of the universe. These example prior distributions express that our prior knowledge is not in favour of any particular hypothesis.

From a hypothesis, we derive a prediction as a conditional probability of the observations $P(D|H)$. This conditional probability can be seen as a model which associates each hypothesis with a *predictive distribution* over the observations to which the model reflect predictive uncertainties, thus we call $P(D|H)$ a *predictive model*. This probability distribution function and its parameters form one part of the model specification. A typical way to construct this part is to define the mean of $P(D|H)$ by a function, which encapsulates the physical processes happening during an experiment, to derive underlying quantities directly related to the observations from a hypothesis, known as a *forward model*:

$$f = f(H). \quad (2.1)$$

For example, we can formulate a predictive model of an experiment, in which we obtain the observation with Gaussian noise, as a Gaussian distribution whose mean is given by a forward model of the experiment, which can be written as:

$$P(D|H) = \mathcal{N}(\mu = f(H), \sigma^2). \quad (2.2)$$

This predictive model makes a prediction as the Gaussian distribution given a hypothetical value of H over the observation from the experiment. The standard deviation σ here specifies a *predictive uncertainty* of the model [1]. This epistemic interpretation of an *error bar* as a model predictive uncertainty rather than as a given observational error, is a deviation from the view exposed above by Jaynes [2] and others, but is the interpretation used in this framework.

As one might notice, this predictive model does not encapsulate our prior knowledge and assumptions which are the other important part of the model specification. The prior distribution together with the predictive model, therefore, constitutes a scientific model as a joint probability of the hypotheses and observations $P(D, H)$, also known as a *generative model* [41], which is:

$$P(D, H) = P(D|H) P(H). \quad (2.3)$$

This model is a mathematical representation of a system which embodies the full relationship between the hypotheses and observations and can give a probability of an arbitrary combination of the hypotheses and observations in the joint space (Figure 2.1). Therefore, in this regard, the model is indeed the landscape of a system.

Now given a certain hypothesis, we can make a prediction as a predictive distribution over the observations $P(D|H)$ from the joint distribution (Figure 2.1). On the other hand, we can also calculate our inference solution as a conditional distribution of the hypotheses if we make actual observations D in the real world, also known as the posterior distribution $P(H|D)$, given by Bayes formula:

$$P(H|D) = \frac{P(D, H)}{P(D)} = \frac{P(D|H) P(H)}{P(D)}, \quad (2.4)$$

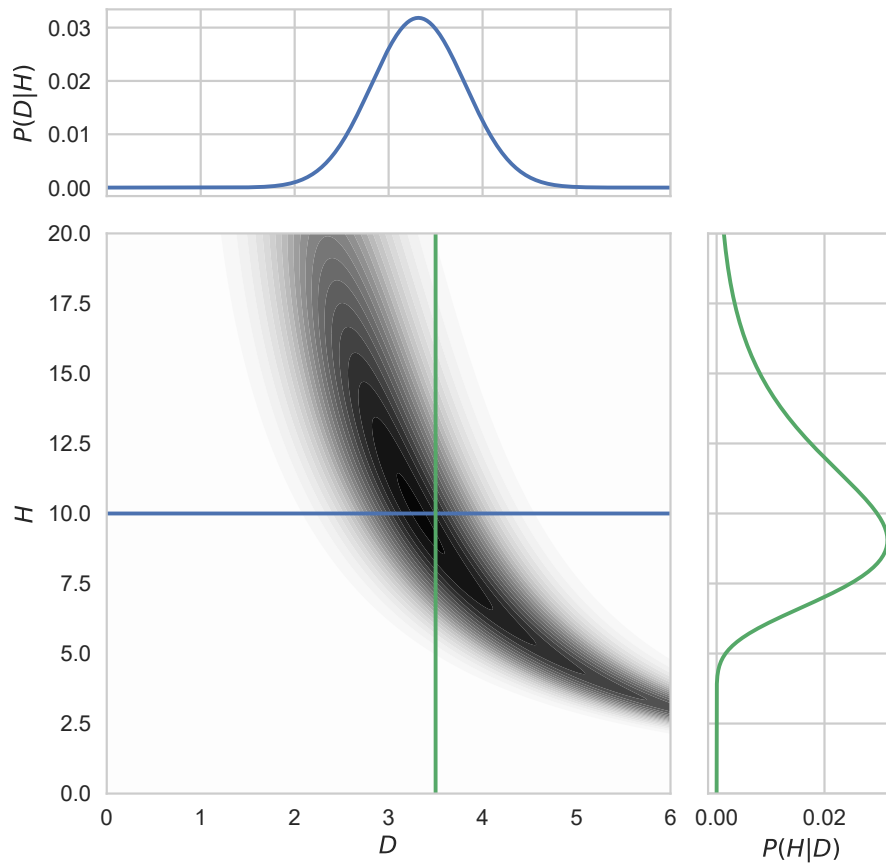


Figure 2.1: An example of a model of a system. The contour plot shows the joint probability distribution $P(D, H)$ (darker regions mean higher probability density). The model prediction can be made, for instance, at $H = 10.0$ as a predictive distribution $P(D|H)$, as shown in the top plot with the blue line. On the other hand, the inference solution can also be calculated, for example, at $D = 3.5$ as a posterior distribution $P(H|D)$, as shown in the right plot with the green line.

where the denominator is a marginal probability of the observations $P(D)$, also known as the *model evidence*, which is a normalisation constant in this context. We remark that the posterior distribution is the inference solution. In other words, in Bayesian probability theory, the solution is not a single value such as an estimation at the maximum of the likelihood function in the conventional theory of probability, but the posterior distribution. All possible hypotheses can be drawn from this posterior distribution as a set of posterior samples which can explain the observations in the real world, and this means that we can assign preferences to alternative hypotheses. If we need a single value solution, we can find the most probable hypothesis at the maximum of the posterior probability, known as a maximum a posteriori (MAP) solution. For example, if our posterior probability of rain is 0.3, we might start for a walk (perhaps we might take an umbrella when we leave the house). If we draw posterior samples of the mass of Saturn given the observations, we can calculate all possible trajectories of a spaceship with respect to all possible values of the mass of Saturn and check them out to ensure secure travel for our astronauts in the space ship. Our epistemic knowledge of the hypothesis given the observations is quantitatively expressed by the posterior distribution, which is calculated through the inference process.

Moreover, the posterior distribution is very important to determine whether a hypothesis space is meaningful or not in scientific methods. If the posterior distribution given observations is (substantially) different from the prior distribution, epistemic knowledge over the hypothesis space can be *updated a posteriori* given the observations. We can measure this difference between the two pieces of knowledge before and after any experiment (the posterior and prior distributions) with the relative entropy, also known as the Kullback-Leibler divergence [42]. If we can find a notable difference between the posterior and prior distributions over a hypothesis space, implying that it is *updatable a posteriori*, then the hypothesis space is meaningful in this framework.

The hypothesis space can be seen as a parameter space of a model in which we can fit the parameters to the observations. For example, let us suppose that our problem is to infer the gravitational acceleration near Earth's surface from Galileo's free fall experiment [13]. In this case, we can define a hypothesis space by a set of possible values of the coefficients of a second order polynomial equation, and the coefficient of the quadratic term would be the gravitational acceleration. Given a set of observations of the time of free fall from the experiment, we can calculate the posterior distribution of the gravitational acceleration. To find a

MAP solution for the gravitational acceleration by an optimisation algorithm is equivalent to fit the parameter of the model to the data.

We have reviewed the basic apparatus (hypothesis space, prior probability, predictive distribution and model) to quantitatively express our epistemic knowledge over a hypothesis space after we make observations in the real world by an experiment. Based on our inference solutions, we can decide our actions, for example, whether we go out for a walk or not, or organise a safe space journey. However, all we have done so far can be done when we have a single model of a system. What if we have many alternative models? How can we compare these models and find a model with an *appropriate complexity* which is capable of generalising the underlying principles of a system in an optimal way? As one might notice, to compare the models is not as straightforward as to compare their parameters, since a complex model can always predict the observations better than a simple model does. Nevertheless, we would expect that a complex model can be too specialised to specific observations and poorly generalise the underlying principles of a system. Intuitively, it would be very reasonable to follow the principle of Occam's razor: complexity should not be posited without necessity [43]. Remarkably, in this framework, model complexity is represented by the posterior probability of the models $P(M|D)$ which intrinsically embodies Occam's razor [14, 19, 20]. In the following section, we will briefly introduce the principle of Bayesian Occam's razor and review how to compare alternative models of differing complexities given the observations.

2.3 Model complexity and Occam's razor

The central task in science is to generalise the relationship between hypotheses and observations by developing and comparing the models of differing complexities which are capable of generalising the underlying principles of a system in an optimal way. As soon as we find the optimal model of a system, we have the full relationship between the hypotheses and observations so that we can extrapolate our epistemic knowledge of the hypotheses beyond our boundaries of previous observations. With the model, we can predict and even trigger unforeseen physical phenomena in the real world by manipulating the parameters of a system.

Let us suppose that we would like to compare alternative candidates to the model of a system given observations. As we discussed in the previous section,

to compare these models is not as straightforward as to compare their parameters. When we compare alternative values of the parameters of the model, we calculate the posterior distribution over the parameter space and find a MAP solution or posterior samples which can explain the observations better than the other parameters. However, when we compare alternative models of differing complexities, we can not compare these models with their optimal parameters which can explain the observations better than the other models, since a complex model can always predict the observations better than a simple model does. A complex model can adapt its parameters to explain not only major phenomena of a system, which we want the model to generalise but also minor phenomena specific to an experiment such as electronics noise which we do not want the model to learn. For example, a hundredth or thousandth order polynomial model can always adapt to the observations better than a first or second order polynomial model does. The principle of Occam's razor, therefore, is not optional but essential to compare these models in science. Surprisingly, the principle of Occam's razor is intrinsically implemented in a predictive distribution over observations given models, also known as the model evidence $P(D|M)$, and we will discuss how this is possible.

Let us suppose that we have a set of alternative models which might be able to generalise the underlying principles of a system appropriately. Such cases, a hypothesis space would not be a set of their parameters but a set of these models, thus we call it a *model space* M . In a model space, we have all the alternative models. Each of them is a joint probability $P(D, H)$ with a different model specification which can be defined over an entirely different parameter space or have a different value of its model parameters, which does not belong to the parameters of the model, for example, the parameters of prior distributions, also known as *hyperparameters*. A discrete probability function can be assigned to a model space, which contains a finite number of alternative models, for example, a set of ten polynomial models with different orders, and a continuous probability function can be assigned to a model space, which contains an infinite number of alternative models, for example, a set of non-parametric models with different values of hyperparameters. We can start with a prior probability of the models $P(M)$, in which we can quantitatively reflect prior knowledge and assumptions to every alternative model with a different model specification. In general, we can assign a uniform distribution to this prior probability in order to express an equal preference to every alternative model.

Given a model, we can derive a prediction as a predictive distribution over the

observations $P(D|M)$ by marginalising out the parameter space of the model, which can be written:

$$P(D|M) = \int P(D, H|M) dH. \quad (2.5)$$

This predictive distribution can be seen as a predictive function which associates each model with a predictive distribution over the observations by taking into account all possible values of the parameters, also known as the *model evidence*. The model evidence is the denominator in Bayes formula, given by Equation (2.4), for the inference process in the previous section.

As mentioned previously, the model evidence embodies the principle of Occam's razor. Let us imagine that we try to explain a set of observations in the output space with respect to a set of input parameters in the input space. A simple model can generate a small variety of observations, while a complex model can generate a great variety of observations. For example, a first order polynomial model can only generate a set of observations which can be represented by a linear function. In contrast, a second order polynomial model can generate a set of observations which can be represented by a parabolic function and at the same time by a linear function. Thus, a second order polynomial model can generate a greater variety of observations than a first order polynomial model. In the same way, a higher order polynomial model, which is a more complex model, can generate a greater variety of observations than a lower order polynomial model, which is a simpler model. In other words, a predictive distribution over the observations given a complex model is broader than one given a simple model, but the sum of these predictive distributions must be equal to one. Hence, *a probability of a particular set of observations given a complex model is generally lower than one given a simple model*. Nevertheless, if a model does not have an appropriate complexity which is capable of explaining the observations to which the underlying principles of a system are reflected, a predictive probability of the observations given that model would be small. For example, a first order polynomial model cannot explain a set of observations which have been generated from a parabolic function or a cubic function.

Here an example of the model evidence given a first, second and third order polynomial model denoted as $P(D|M_1)$, $P(D|M_2)$ and $P(D|M_3)$ with respect to a set of observations generated by a first, second, third and fourth order polynomial function denoted as D_1 , D_2 , D_3 and D_4 is shown in Figure 2.2. Each of these polynomial functions generates a thousand sets of observations with

a randomly chosen set of their parameters and with a predictive uncertainty $\sigma = 1.0$ which are shown in a different region shaded in a different colour. The predictive distribution given a first order polynomial model $P(M_1|D)$ (the blue line) is narrowly distributed over the sets of observations generated by a first order polynomial equation D_1 (the blue region) but with a high probability. On the other hand, the predictive distributions given second or third polynomial models $P(M_2|D)$ (the green line) and $P(M_3|D)$ (the red line) are broadly distributed over the sets of observations generated not only by the first order polynomial function but also by the second and their order polynomial functions D_2 (the green region) and D_3 (the red region). For example, we observed a set of data generated by the underlying principles of a system which follow a second order polynomial function (the green region) by an experiment, the model evidence given a second order polynomial model will be the highest. An overly simple model which is not capable of generalising the underlying principle, for instance, a first order polynomial model, would not be able to explain the data set. On the other hand, an over-complex model which poorly generalise the underlying principle and can be too specialised to the data set, for example, a third order polynomial model, would be penalised by the principle of Occam's razor. Therefore, the model evidence quantitatively represents a model complexity, which intrinsically embodies the principle of Occam's razor [14, 19, 20].

The model evidence together with the prior distribution of the models constitutes the posterior distribution $P(M|D)$, given by Bayes formula:

$$P(M|D) = \frac{P(D, M)}{P(D)} = \frac{P(D|M) P(M)}{P(D)}, \quad (2.6)$$

where the denominator is the marginal model evidence $P(D)$, which is a normalisation constant in this context. Here, again the inference solution for model comparison is the posterior distribution. If necessary, we can draw all possible models from this posterior distribution which can explain the underlying principles with an appropriate complexity. We can also find the most probable model at the maximum of the posterior probability (a MAP solution) which does have an optimal complexity to generalise a system. For example, if we have a set of observations from Galileo's free fall experiment which is somewhere in the green region in Figure 2.2, we will infer that a second order polynomial model is the optimal model for the law of free fall.

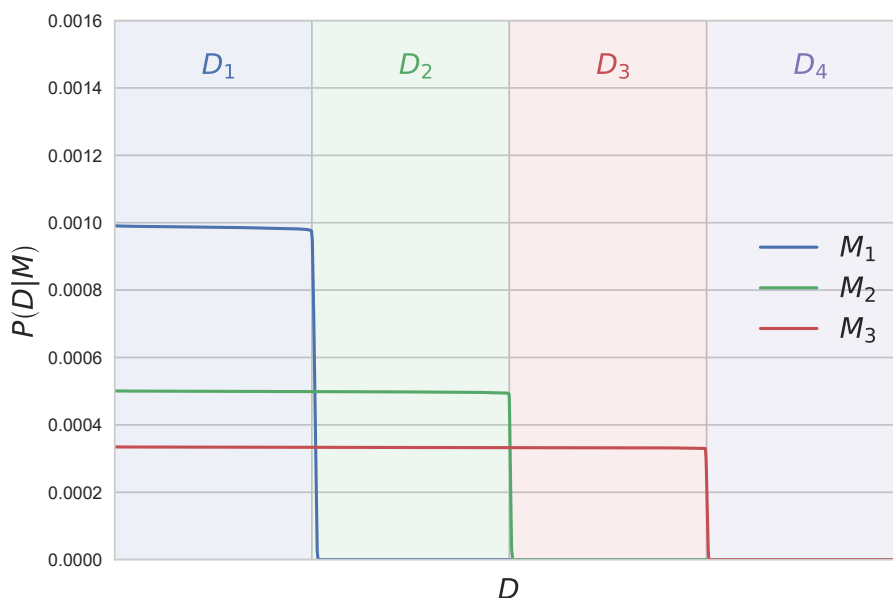


Figure 2.2: An example of the model evidence given a first, second and third order polynomial model M_1 , M_2 and M_3 with respect to a set of observations generated by a first, second, third and fourth order polynomial function D_1 , D_2 , D_3 and D_4 . The blue, green and red lines are $P(D|M_1)$, $P(D|M_2)$ and $P(D|M_3)$ over the observation sets generated by a first, second, third and fourth order polynomial function D_1 , D_2 , D_3 and D_4 in the blue, green, red and purple regions.

As one might already notice, calculation of the model evidence is unfortunately often computationally challenging, since we have to integrate over the parameter space, which can be high-dimensional. If the dimension of the parameter space is more than twenty or thirty, which is often the case in real-world problems, it is virtually impossible to calculate the model evidence unless we have an analytic formula. This is the major obstacle to applying Bayesian Occam's razor to real-world problems.

Remarkably, this obstacle can be completely avoided by taking into account the joint posterior distribution of the parameters and models $P(H, M|D)$, which as well intrinsically embodies the principle of Occam's razor, which can be

written as:

$$P(H, M|D) = P(H|M, D) P(M|D), \quad (2.7)$$

where $P(H|M, D)$ is the posterior distribution of the parameters of a specific model and $P(M|D)$ is the posterior distribution of the models, which, as we discussed previously, embodies Occam's razor. In other words, the principle of Occam's razor is as well intrinsically implemented in the joint posterior distribution. This is indeed very important, because the calculation of the joint posterior probability is often much easier than the one of the model evidence, especially if the models have a high-dimensional parameter space. This means that we can apply Bayesian Occam's razor to any problem in the real world without worrying about the major obstacle, integration over a high-dimensional space. One might argue that the posterior distribution of the models is different from the joint posterior distribution of the parameters and models. However, we have to pay attention to the meaning of the joint posterior distribution. *The joint posterior distribution of the parameters and models is, by definition, the inference solution for the parameters and models at the same time.* For example, if we calculate the joint posterior distribution given the observations from Galileo's free fall experiment, a MAP solution will be an optimal solution not only for the model for the law of free fall but also for the gravitational acceleration simultaneously, as shown in Figure 1.1. This means that we can find an optimal model and at the same time its optimal parameters by exploring the joint posterior distribution, which intrinsically embodies Bayesian Occam's razor, without any heavy calculation such as marginalisation over a high-dimensional space. This is one of the important contributions to the automation of science, made in this thesis. If we let a machine (an optimisation algorithm) explore the joint posterior distribution, the machine will autonomously find an optimal solution for the model and its parameters given the observations. Furthermore, we can draw a set of posterior samples from the joint posterior distribution which are all possible solutions for the parameters and models which can explain the observations. Therefore, we have explored the joint posterior distribution of the parameters and models in most of the applications in this thesis.

We have reviewed the model complexity and the principle of Occam's razor to quantitatively express our epistemic knowledge over a model space after we make observations in the real world. Since we have a quantitative rule for model comparison, any human or machine can compare alternative models of

differing complexities and find an optimal model of a system with an appropriate complexity like a scientist. At this moment, we might already be able to automatise science in principle. However, before we have a further discussion on the automation of science, we have one more thing which still remains in the veil: prior knowledge.

2.4 Prior knowledge

As we have already discussed in the previous sections, we encode prior knowledge and assumptions to the prior probability. We can formulate a prior distribution of hypotheses or models as a uniform distribution, in which we express an equal preference to every hypothesis or model. We can also take the posterior distribution given previous observations and use it as a prior distribution for the next observations. In any case, all our knowledge of reality starts from our prior knowledge and assumptions, and it is indeed very important to assign an appropriate prior distribution according to them. Therefore here we are back to the prior probability. There is a number of methods to formulate prior distributions in order to encode different types of prior knowledge and assumptions. In this thesis, we mainly make use of three different priors: (i) uninformative priors (maximum entropy priors, mostly uniform and Gaussian priors), (ii) Gaussian process priors and (iii) physics/empirical priors based on virtual observations.

2.4.1 Uninformative prior

When we have very little knowledge of parameters and models, for example, if we only know that temperature is a positive real number to some maximum, then we can reflect our ignorance in a prior probability. In such cases, one of the most reasonable priors is an *uninformative* prior [2, 14, 19]. The uninformative prior can be derived from the principle of maximum entropy [2], stating that the probability distribution with the largest information entropy [44] encodes maximum *uninformativeness*.³ The maximum entropy priors would be one of

³In most practical cases, prior distributions might be able to be derived by a set of conserved quantities which associate to the distributions in inference problems, for example, first and second moments (mean and variance). These quantities are often assumed to be *invariants* in a physical system, thus we might be able to justify the maximum entropy principle, in

the best choices for our prior distribution when we have very little knowledge. We typically use two uninformative priors in this thesis: one is a uniform prior and the other one is a Gaussian prior. A uniform prior is the maximum entropy distribution when we only know that the parameters are real numbers in a certain range, for example, temperature is a real number from zero to some maximum. A Gaussian prior is the maximum entropy distribution when we only know that the variance of the parameters, for example, we often measure the variance of electronics signals for which the maximum entropy distribution would be a Gaussian distribution.

2.4.2 Gaussian process prior

One of the common problems with expressing physical quantities such as temperature or density over space and time is that the parametric model (analytic formula) of physical quantities is often unknown. If we already know the parametric model, we can use it to express these physical quantities and formulate an uninformative prior of parameters of the formula. Otherwise, any choice of a parametric model would exclude a great variety of possible behaviours of physical quantities over space and time thus severely limit the inference solutions for these physical quantities. Therefore, if the parametric model is not known, it would be good to use a *non-parametric* model such as Gaussian processes to avoid such limitations.

A Gaussian process [29, 45, 46] is a probabilistic function that associates each element of a domain with a single element of a multivariate random variable following a Gaussian distribution. The Gaussian process defines the function space by a multivariate Gaussian distribution whose mean and covariance are given by a mean function $\mu(x)$ and a covariance function $\Sigma(x, x')$:

$$f(x) \sim \mathcal{N}(\mu(x), \Sigma(x, x')), \quad (2.8)$$

where x contains every point of the domain and $f(x)$ is the output of the Gaussian process. The Gaussian process represents the relationship between the input and output of the function through the mean and covariance function of the Gaussian distribution. Thus, the function is not constrained by any specific

which we maximise the entropy given these invariants to formulate uninformative priors for some inference problems, for instance, some problems in statistical thermodynamics. Nevertheless, the maximum entropy principle might not be valid for some other problems.

parameterisation. Rather, the mean and covariance functions determine the properties of the Gaussian process. For example, the correlation between any two points will be given by the covariance function. The parameters of the mean and covariance function are also known as *hyperparameters* of the Gaussian process.

One of the most common specifications of Gaussian processes is zero mean and squared exponential covariance function, which can be written as:

$$\mu(x) = 0 \tag{2.9}$$

$$\Sigma(x_i, x_j) = \sigma_f^2 \exp\left(-\frac{(x_i - x_j)^2}{2\sigma_x^2}\right) + \sigma_y^2 \delta_{ij}, \tag{2.10}$$

where x is a point in the domain and the superscripts i and j mean i^{th} point and j^{th} point. The hyperparameters of the covariance function are overall scale σ_f , length scale σ_x and noise scale σ_y . The smoothness of the Gaussian process is determined by σ_f and σ_x . Typically, we set σ_y as a relatively small number with respect to σ_f , for instance, $\sigma_y/\sigma_f = 10^{-3}$, to avoid any numerical instability.⁴ δ_{ij} is the Kronecker delta function. We show two examples of the Gaussian processes in Figure 2.3. The Gaussian process with a large length scale ($\sigma_x = 1.0$) is smoother (higher correlation values between two arbitrary points) than one with a small length scale ($\sigma_x = 0.2$).

As soon as observations are available, we can adapt these two Gaussian processes to the observations as much as possible within their smoothness. Figure 2.4 shows examples of the two Gaussian processes which learn the features of the underlying function. Since the Gaussian process with a smaller length scale ($\sigma_x = 0.2$) has a lower correlation between two points, it is capable of adapting to the observations better than the one with a larger length scale ($\sigma_x = 1.0$). We remark that these hyperparameters, here in this example the length scale, determine the model complexity of Gaussian processes which is corresponding to the order of polynomial models. As we can see in Figure 2.3, the Gaussian process with a smaller length scale would be able to be adapted to a greater variety of the data sets, which means that it has higher complexity.

⁴By definition, the covariance matrix Σ is positive semi-definite ($x^T \Sigma x \geq 0, \forall x \in \mathbb{R}^n$), which allows us to perform Cholesky decomposition [47]. In practice, due to a possible numerical instability, for example floating-point error [48], on some occasions, Σ may not be positive semi-definite. To ensure positive semi-definiteness of the covariance matrix, we can add ϵI (ϵ is a small positive number) to Σ .

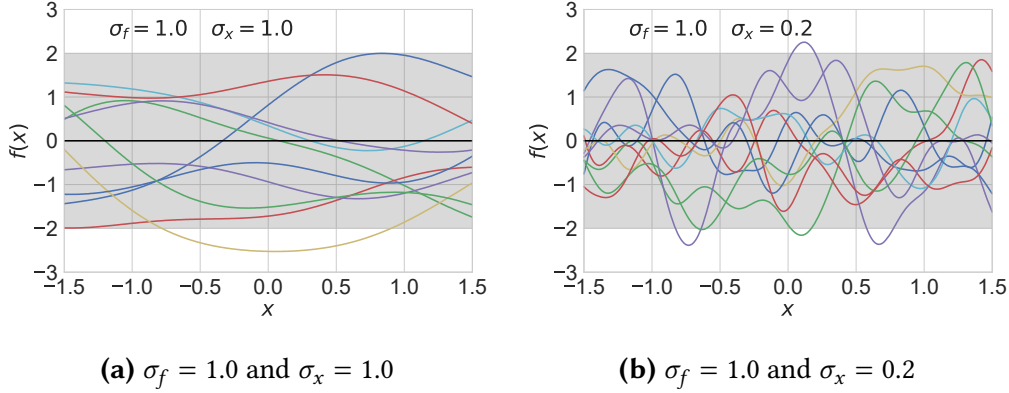


Figure 2.3: Examples of Gaussian processes with zero mean and squared exponential covariance function. The black lines and shaded regions are the mean and two standard deviation uncertainty of the Gaussian processes, respectively. The coloured lines are ten samples of the Gaussian processes. The Gaussian process with a large length scale ($\sigma_x = 1.0$) is smoother (higher correlation between two arbitrary points) than one with a small length scale ($\sigma_x = 0.2$).

These hyperparameters of Gaussian processes can be optimised by Bayesian Occam’s razor. In nuclear fusion research, no parametric model can describe spatial distributions or profiles of physical parameters of fusion plasmas sufficiently well. Therefore, Gaussian processes are used to model these physics parameters, such as plasma current density and pressure, in all the applications developed in this thesis. Gaussian processes were first used in nuclear fusion research in [38], followed by a number of applications [39, 49–51].

2.4.3 Physics and empirical prior

When we perform experiments, we sometimes have prior physics or empirical knowledge that we would like to impose in order to exclude physically or empirically improbable solutions. We do often have some physics laws such as the Grad-Shafranov equation [52, 53] which our model can prescribe at a certain point in space and time without explicit observations on the relevant physical quantities. For example, let us suppose that we have a metal plate, which can move upwards and downwards freely (in z direction), inside a vertical supporting tube and induce a current in x direction through the plate perpendicular

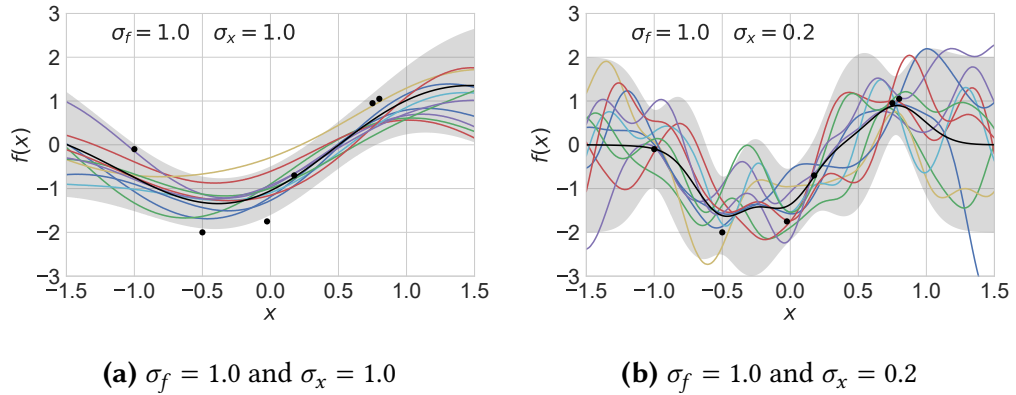


Figure 2.4: Examples of Gaussian processes with zero mean function and squared exponential covariance function which adapt to the observations (black dots).

to a magnetic field in y direction from magnets inside the tube. This metal plate can ascend or descend by the Lorentz force (the $\mathbf{J} \times \mathbf{B}$ force) depending on the current and magnetic field (a Lorentz elevator). When the plate does move neither upwards nor downwards and stays in a certain level, it is physically reasonable to introduce the force balance between the Lorentz force and the gravitational force on the metal plate to our model. On the other hand, we do also often have some empirical laws which our model can implement. For example, let us suppose that we have empirical knowledge that the flames on a gas stove have never made any iron pot meltdown. In such cases, when we measure flame temperatures, it would be empirically reasonable to assume that the flame temperatures should not be much higher than the melting temperature of iron.

These physics/empirical knowledge can be imposed by *virtual observations* at any point in space and time as if we make such observations [35, 37]. For example, when we perform the Lorentz elevator experiment, we would like to introduce the force balance to our model. The force balance between the Lorentz force and the gravitational force can be written as:

$$\mathbf{J} \times \mathbf{B} = m\mathbf{g}, \tag{2.11}$$

where \mathbf{J} is the current through the plate, \mathbf{B} the perpendicular magnetic field, m the mass of the plate and \mathbf{g} the gravitational acceleration. Now we can make a virtual observation on the force balance at a spatial location of the centre of

mass of the plate when it does not move either upwards or downwards (in z direction) as a Gaussian distribution, which is:

$$P(D_v|H) = \mathcal{N}((\mathbf{J} \times \mathbf{B} - m\mathbf{g}) \cdot \mathbf{k}, \sigma_v^2), \quad (2.12)$$

where \mathbf{k} is the standard unit vector in z direction. Here, if we set $D_v = 0.0$, then we prescribe the force balance. We can also prescribe the force balance at multiple positions in space and time by making multiple virtual observations, for example, we can make virtual observations at several spatial locations over the entire plate. The standard deviation σ_v is the virtual observation uncertainty to which we reflect our epistemic uncertainty of the force balance to our model. For example, we can set σ_v as a large number to express our epistemic uncertainty that the force balance between the Lorentz force and the gravitational force might not be fulfilled since we have substantial friction between the plate and supporting tube. On the other hand, we can set σ_v as a small number since the plate and tube are almost frictionless. In the same way, we can implement constraints on physical quantities at any point in space and time. For example, we can introduce the temperature constraints (the temperature should not be much higher than the melting temperature of iron) at spatial locations over the surface of the iron pot, when we measure the flame temperatures on a gas stove. These virtual observations $P(D_v|H)$ can be seen as a part of a prior probability in Bayes formula:

$$P(H|D, D_v) = \frac{P(D|H) P(D_v|H) P(H)}{P(D) P(D_v)} = \frac{P(D|H) P(H|D_v)}{P(D)} \quad (2.13)$$

where $P(H|D_v)$ is the physics/empirical prior that prescribes our physics/empirical knowledge by using the virtual observations. Article IV and Article V make use of virtual observations to impose empirical prior knowledge that the plasma density and temperature should be low at plasma facing components (PFCs). In addition, Article V prescribes the Grad-Shafranov force balance by using the equilibrium prior based on virtual observations.

2.5 Outlook

We have reviewed every constituent of the framework for scientific inference in this thesis. We define our hypothesis space and start with our prior knowledge

before experiments. After the experiments, we update our knowledge given observations. We define our model as a joint probability which represents the full relationship between the hypotheses and observations. We compare alternative models of differing complexities by Bayesian Occam's razor. We impose our physics/empirical constraints by introducing virtual observations. We have established the framework for scientific inference in which we have defined our epistemic knowledge (probability) as the cost function of scientific problems. In this framework, any human or machine can carry out scientific inference like a scientist, and perhaps we will be able to create *a*-machine capable of making scientific discoveries autonomously.

2.6 Minerva framework

All the apparatus and constituents of the framework for scientific inference described in this chapter have been elegantly implemented in a software framework, Minerva [21, 22]. Minerva provides a standardised format for model components, for example, prior probabilities and forward models, and a standardised interface for component dependencies, a set of input parameters, which can be connected from output of other components. These connections are mathematically represented by conditional dependencies, and all these model components and connections together constitute a scientific model as a joint probability $P(D, H)$, which can be represented by a Bayesian graphical model [18]. Minerva automatically manages all the components and connections in the model. The modular structure, graphical representation and automatic model administration allow us to handle a complex model and keep track of a large number of parameters, prior knowledge, predictive models and observations in a systematic way. Once we declare the model, Minerva can provide MAP solutions and posterior samples automatically by different inversion methods, for example, the linear Gaussian inversion [37, 54], pattern search [55], and Markov chain Monte Carlo (MCMC) algorithms [56–58].

Minerva is designed to work for all kinds of scientific problems with arbitrary complexity. Minerva has been used for a number of scientific applications [37, 38, 49, 51, 54, 59–62] in nuclear fusion research, and it is the main inference framework at one of the world's largest advanced fusion experiments, Wendelstein 7-X (W7-X). All the applications in this thesis have been developed in

Minerva. These scientific models in Minerva can be accelerated by a field-programmable gate array (FPGA) [63] and an artificial neural network [64, 65] for real-time applications.

3

Nuclear Fusion

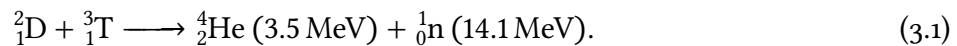
I sought the fount of fire in hollow reed
Hid privily, a measureless resource
For man, and mighty teacher of all arts.

(Aeschylus, Prometheus Bound)

One of the greatest challenges of our time is to earn safe, clean and inexhaustible sources of energy. Fusion energy, mankind's ambitious mission of stealing the fire of the Sun and giving it to humanity, might be a solution to the quest for a form of energy production that is capable of meeting the steadily growing global energy demand and possibly opening up virtually limitless energy supplies for generations. Fusion energy is generated as the manifestation of mass-energy equivalence [66] by a fusion reaction in which two lighter atomic nuclei (lighter than iron-56) fuse into heavier nuclei. Unlike fission power, fusion can avoid producing a considerable amount of long term radioactivity and nuclear waste. In addition, fusion is safe and has ample fuel supplies [67]. For this reason, fusion energy would be one of the best alternatives to fossil fuel and fission.

The Sun, which is a natural fusion reactor, like other stars, fuses hydrogen into helium. In spite of a very small probability of the fusion reaction, the Sun creates an environment with sufficiently high density by its gravity, in which it produces enough fusion energy to light up the entire solar system [68]. On Earth, we have been trying to build fusion reactors capable of sustaining an environment for fusion reactions in which they produce enough energy to light up our civilisation. To undergo the fusion reaction, two reactant nuclei have to be given enough kinetic energy to overcome the repulsive electrostatic force by their positive charge and get close enough to each other so that the nuclear

force becomes active. This can be achieved by heating up the fuel (increasing the kinetic energy of the reactants) to the astounding temperature of the order of 10^8 °C, hotter than the core of the Sun.¹ The fusion reaction rates at these temperatures are high enough to be considered for fusion energy. Since the deuterium-tritium (D-T) fusion reaction rate is substantially higher than other reaction rates (Figure 3.1), we mainly consider D-T fusion, which is:



At such temperatures, the fuel is fully ionised becoming a *plasma*, in which electrons and ions move independently and behave collectively by the electromagnetic force. Once the fuel is heated up, we must have a method to hold the plasma together despite its large thermal energy, which makes the plasma confinement extremely difficult. Ideally, a fusion reactor should allow the plasma to have sufficient thermal energy (density and temperature) for long enough, so that it produces enough fusion energy that can maintain the plasma confinement and at the same time can be harnessed. One of the two major approaches is to make use of (superconducting) magnets to create a magnetic cage capable of confining the charged particles of the plasma by the electromagnetic force, also known as magnetic confinement fusion [67].²

In order to build such a fusion reactor, we have to investigate the conditions in which it produces enough fusion energy that can sustain the plasma confinement and generate electricity simultaneously. The energy of plasma particles can be lost through radiation, conduction and convection and replenished by fusion energy. In magnetic confinement fusion, when the fusion reactions produce charged particles, for example alpha particles from D-T fusion, they can be confined by the electromagnetic force and heat up the plasma through collisions. On the other hand, neutral particles, for example neutrons, will escape from the magnetic cage, and their kinetic energy can be used to generate electricity. If the plasma can have sufficient thermal energy for long enough, it can produce sufficient fusion energy to sustain itself. Plasma density, temperature and confinement time are the critical quantities to set up the conditions to *ignite* a self-sustaining plasma. The *ignition* conditions for D-T fusion can be derived by assuming that the fusion alpha particle heating is sufficiently large to balance

¹The temperature at the core of the Sun is approximately 2.0×10^7 °C [68].

²The other approach is inertial confinement fusion which attempts to compress the fuel by using high energy lasers to produce fusion energy [69].

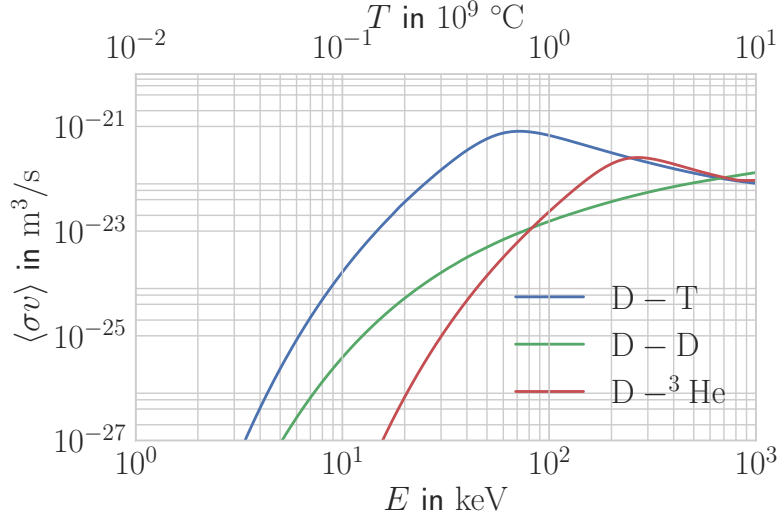


Figure 3.1: Fusion reaction rates of deuterium and tritium (D-T), deuterium and deuterium (D-D) and deuterium and helium-3 (D- ^3He) fusion. At the temperature of the order of $10^8 \text{ }^\circ\text{C}$ or 10 keV, the D-T fusion reaction rate is substantially higher than other reaction rates so that commonly considered for fusion energy [70].

out the power loss, also known as the *triple product* [71]:

$$nT\tau_E \geq 3 \times 10^{21} \text{ keV s/m}^3, \quad (3.2)$$

where n is the plasma density, T is the plasma temperature and τ_E is the energy confinement time, which can be written as:

$$\tau_E = \frac{W}{P_{\text{loss}}}, \quad (3.3)$$

where W is the plasma energy and P_{loss} is the power loss, which can be balanced by externally supplied heating power in steady state. In short, we have been trying to maximise this triple product to ignite the self-sustaining plasma and harness the fusion energy. This thesis is concerned with the inference of these parameters.

The triple product $nT\tau_E$ can be separated into two important parts. The first part is the energy confinement time τ_E that is determined by energy *transport*

induced by a microscopic behaviour of the plasma: collisions and microinstabilities. This energy transport distinguishes classical [72–74] and anomalous [73–78] processes. The classical transport is caused by the Coulomb collision between the plasma particles orbiting around the magnetic field. The anomalous transport, on the other hand, might be driven by microinstabilities and *turbulence*, for example, temperature gradient instabilities. This anomalous transport often exceeds the classical transport prediction by an order of magnitude or more. Since these phenomena involve individual particle motions on the short length and fast time scales, we make use of kinetic models [79, 80] to predict the transport. However, because of the complexity of the problem, transport has not been fully understood so far in fusion research.

The second part is the plasma pressure $p = nT$ that is a part of the force balance between the pressure gradient and the magnetic force, also known as plasma *equilibrium* [52, 53, 81–85]. Since the force balance involves particle behaviours on the relatively large spatial length and long time scales compared to kinetic behaviours, we make use of fluid models to describe these phenomena. The most basic and well-developed fluid model is the ideal magnetohydrodynamic (MHD) model [85], which describes how the plasma pressure gradient and magnetic forces interact within an ideal plasma (a perfect conductor) in an arbitrary magnetic field geometry. The MHD model describes the macroscopic equilibrium and magnetic field geometry of the plasma which are crucial for understanding macroscopic instabilities and for plasma control. Moreover, the plasma equilibrium provides a magnetic coordinate system through which we can map the physics parameters to the magnetic field geometry of the plasma. Thus, the plasma equilibrium is fundamental to all the other physics studies in fusion research. This thesis develops a novel approach to plasma equilibrium inference based on previous work.

3.1 Plasma equilibrium

The foundation of magnetic confinement fusion is to confine the plasma having large thermal energy by the magnetic force. This magnetic force is the Lorentz force of the plasma current \mathbf{J} and the magnetic field \mathbf{B} that balances out the plasma pressure gradient ∇p . The Lorentz force can hold the plasma in a stable, macroscopic equilibrium thereby allowing fusion reactions to take place. This macroscopic plasma *equilibrium* can be well predicted by a single fluid

model capable of describing macroscopic behaviours of the plasma particles, also known as the magnetohydrodynamic (MHD) model [85].

In order to derive the force balance of the plasma equilibrium, we can start with the MHD momentum equation, which is given by:

$$mn \left[\frac{\partial \mathbf{v}}{\partial t} + (\mathbf{v} \cdot \nabla) \mathbf{v} \right] = \mathbf{J} \times \mathbf{B} - \nabla p, \quad (3.4)$$

where m is the total mass of the plasma particles, \mathbf{v} is the fluid velocity of the plasma and p is the isotropic pressure. If the plasma is in steady state the convective derivative is assumed to be zero. Under these assumptions, the MHD momentum equation reduces to implying the force balance between the pressure gradient and the Lorentz force, which is:

$$\nabla p = \mathbf{J} \times \mathbf{B}. \quad (3.5)$$

From this force balance, we can deduce two important general properties of the plasma equilibrium. The first property can be derived by forming the dot product of the force balance equation with the magnetic field \mathbf{B} :

$$\mathbf{B} \cdot \nabla p = 0. \quad (3.6)$$

This equation implies that the magnetic field is perpendicular to the pressure gradient. Similarly, the other property can be derived by forming the dot product of the force balance equation with the current \mathbf{J} :

$$\mathbf{J} \cdot \nabla p = 0. \quad (3.7)$$

This equation implies that there is no current parallel to the pressure gradient.

In macroscopic plasma equilibria, physics parameters can be given as a function of the *poloidal magnetic flux* $\psi(R, Z)$, which can be defined as the integral of the poloidal magnetic field through a lateral surface of a truncated cone determined by an arbitrary fixed reference point to the point (R, Z) in the poloidal plane. Equation (3.6) and Equation (3.7) imply that the magnetic field \mathbf{B} and the current \mathbf{J} lie on poloidal magnetic flux surfaces on which the pressure p is constant. Therefore, we use the magnetic flux surfaces as a coordinate system to map these physics parameters, for example, the plasma pressure as a function of ψ , like $p(\psi)$. These magnetic flux surfaces are often normalised to 0.0 at the plasma centre, also known as the magnetic axis, and to 1.0 at the plasma edge

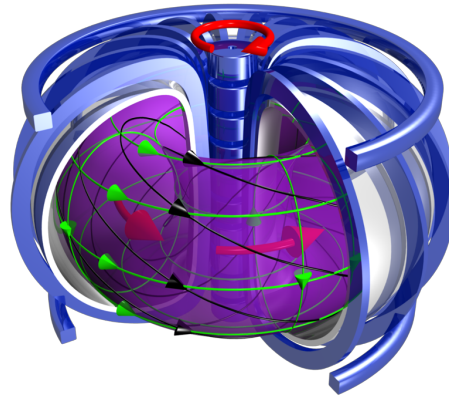
boundary, which is the outermost closed surface, also known as the last closed flux surface (LCFS). The magnetic axis and the LCFS determine the spatial location and shape of the confined plasma, thus they are crucial to plasma control. In the ideal MHD model, no magnetic reconnection can occur, therefore the magnetic flux surface topology has to be preserved during any macroscopic motion which constraints macroscopic instabilities. For this reason, the magnetic field geometry of the plasma is essential to the macroscopic instabilities, plasma control and inference of physics parameters.

We have reviewed the macroscopic plasma equilibrium and its general properties based on the MHD model. Now we will briefly review two major concepts of magnetic confinement fusion: the tokamak and the stellarator.

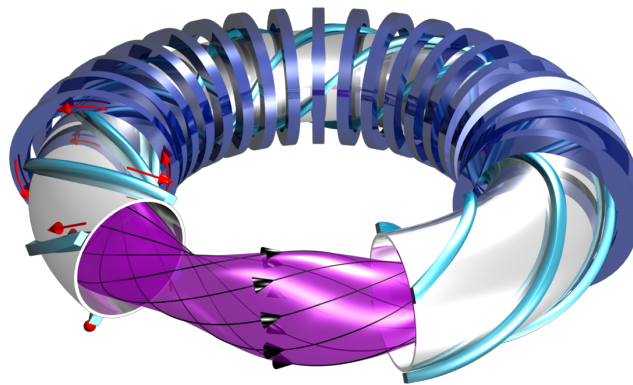
3.2 Fusion experiments

There are various concepts of magnetic confinement fusion under consideration, and each of these concepts is designed primarily to confine the plasma in order to generate fusion energy. The tokamak (Figure 3.2a) and the stellarator (Figure 3.2b) are the two major concepts, which have achieved the best overall performance so far [86–93]. Both have toroidal magnetic field geometry but differing from each other in the way that they generate the Lorentz force and produce the rotational transform to compensate the drift motions [67, 94, 95]. In the tokamak [95], the external coils drive the toroidal plasma current, which generates the poloidal magnetic field, along the toroidal magnetic field. The Lorentz force of the plasma current and the magnetic field confines the plasma, and the superposition of the toroidal and poloidal field produces the rotational transform which compensates the drift motions and keeps the plasma stable. On the other hand, in the stellarator [94], the external coils generate the helically twisted magnetic field, which intrinsically produces the required rotational transform.

Applications in this thesis have been developed for the largest fusion experiments for these two major concepts: one is the Joint European Torus (JET) which is the world’s largest operational tokamak experiment located at Culham Centre for Fusion Energy in Oxfordshire, the United Kingdom, and the other one is Wendelstein 7-X (W7-X), the world’s largest advanced stellarator experiment located at the Max-Planck-Institut für Plasmaphysik in Greifswald, Germany. We will now briefly introduce these two fusion experiments.



(a) Tokamak



(b) Stellarator

Figure 3.2: Schematic structures of the tokamak and the stellarator. The tokamak drives the toroidal plasma current along the toroidal magnetic field by the external coils and confines the plasma by the Lorentz force of the plasma current and the magnetic field. The superposition of the toroidal and poloidal field (black arrows) produces the rotational transform, which compensates the drift motions and keeps the plasma stable. On the other hand, the stellarator creates the helically twisted external magnetic field, which intrinsically produces the required rotational transform. © IPP

3.2.1 Joint European Torus (JET)

The Joint European Torus (JET) [87, 96, 97] is the world's largest tokamak in operation and designed for D-T fusion. JET has the current world record for the highest fusion power of 15.8 MW produced by an input heating power of 25.6 MW, which means that the ratio of output fusion power to input heating power Q is approximately 0.64 [88, 98]. JET has a major radius of 2.96 m and a minor radius of 0.9 m. JET currently makes use of the poloidal field coils to create a diverted plasma with the total plasma volume of approximately 90 m³. The divertor configuration reduces the impurities, which otherwise could dramatically increase the radiation power loss, entering the plasma and aids high performance mode (H-mode) operations [99]. JET is one of the major references to the International Thermonuclear Experimental Reactor (ITER), which will be the world's largest international fusion experiment. The goal of ITER is to produce a fusion power of 500 MW produced by an input heating power of 50 MW ($Q = 10$) [100]. The typical ranges of the major parameters of JET are shown in Table 3.1. The applications in this thesis provide the consistent inference of important physics parameters from a number of JET plasma diagnostic data which have been thoroughly modelled in Article I, Article II and Article III. Furthermore, the plasma equilibrium inference has been achieved based on the consistent inference of physics parameters and the force balance prescribed by the virtual observations in Article V.

3.2.2 Wendelstein 7-X (W7-X)

The Wendelstein 7-X (W7-X) [90–93] is the world's largest advanced stellarator for accomplishing a steady state operation under reactor-like conditions in order to demonstrate the suitability of stellarator as a fusion reactor. It is based on five-fold symmetry of the magnetic field, which was optimised to overcome the disadvantages of classical stellarators [101]. It has a major radius of 5.5 m and a minor radius of 0.53 m, and the total plasma volume is approximately 30 m³. So far the first limiter [90, 91] and island divertor [92, 93] operation phases have been successfully completed and achieved the highest triple product in stellarators or other helical devices in relevant collisionality regimes. W7-X is currently preparing the actively cooled divertor operation phase in order to achieve higher performance with a heating power of up to 10 MW and a plasma duration of 1800 s. Table 3.1 gives the typical ranges of major parameters of

Table 3.1: Typical ranges of major parameters of Joint European Torus and Wendelstein 7-X.

Symbol	Parameter	JET	W7-X
R_0	Major radius	2.96 m	5.5 m
a	Minor radius	0.9 m	0.53 m
V_{plasma}	Plasma volume	90 m ³	30 m ³
B_0	Vacuum magnetic field	3.5 T	2.5 T
I_{plasma}	Plasma current	5 MA	-
P_{total}	Total heating power	38 MW	10 MW
n_e	Electron density	$\leq 2.0 \times 10^{20}/\text{m}^3$	$\leq 2.0 \times 10^{20}/\text{m}^3$
T_e	Electron temperature	≤ 20 keV	≤ 20 keV
T_i	Ion temperature	< 50 keV	< 5 keV

W7-X during the latest operation phases. The application in this thesis for W7-X provides the consistent inference of important physics parameters from a number of W7-X plasma diagnostic data, as described in Article IV.

3.3 Plasma diagnostics

A large-scale fusion experiment has a number of plasma diagnostics to measure physics parameters of the plasma: magnetic field, pressure (density and temperature), radiation and other quantities. Magnetic field and pressure measurements are essential to infer the plasma equilibrium and energy transport in fusion research. The density and temperature can be different for each species, and we usually have two different temperatures for electrons and ions of the plasma. Each of the plasma diagnostics is sophisticated and complex, therefore we have to model each of them thoroughly. Now we will briefly introduce the diagnostics relevant to this thesis.

3.3.1 Active beam diagnostics

Active beam diagnostics typically measure the density and temperature of the electrons and ions. These diagnostics inject particle beams into the plasma and

collect spectral emission as a result of interactions of the beam atoms and plasma particles, for example excitation, de-excitation, charge exchange, spontaneous emission, etc. The spectral emission depends on the density and temperature of electrons and ions, and typically the intensity and width of spectra are determined by the density and temperature, respectively. In this thesis, the JET lithium beam and W7-X helium beam diagnostic systems have been modelled. The JET lithium beam system [102, 103] provides 26 local measurements of the electron density n_e in edge regions from lithium line emission along the vertically injected beam from the top of the machine with a spatial resolution of approximately 1.0 cm and a temporal resolution of 10 ms to 20 ms. Article I and Article II provide inference solutions of edge electron density profiles from the raw data of the JET lithium beam system, and the edge density profiles are used in Article V. The W7-X helium beam system [104, 105] provides eight local measurements of the electron density n_e and temperature T_e in edge regions from helium line ratios near the divertor with a spatial resolution of 1.0 cm and a temporal resolution of 25 ms. The edge electron density and temperature measurements from the W7-X helium beam system is combined with other diagnostic data in Article IV, whose application provides consistent inference solutions of overall density and temperature profiles.

3.3.2 Thomson scattering diagnostics

Thomson scattering diagnostics, which is one of the main methods to obtain local electron density n_e and temperature T_e measurements, inject laser pulses into the plasma and collect photons scattered by the electrons via Thomson scattering processes [106]. The intensity and width of Thomson scattered spectra are determined by the electron density and temperature, respectively. In this thesis, the JET high-resolution Thomson scattering (HRTS) and W7-X Thomson scattering systems have been modelled. The JET HRTS system [107] provides 63 local measurements of the electron density and temperature along the vertical laser path with a spatial resolution of 0.8 cm to 1.6 cm and a temporal resolution of 20 Hz. Article III combines the HRTS data with the interferometer data to provide consistent inference solutions of overall electron density and temperature profiles. The W7-X Thomson scattering system [60] provides 16 local measurements of the electron density and temperature along the laser path with a spatial resolution of 1.5 cm and a temporal resolution of 10 Hz. The

electron density and temperature information from the W7-X Thomson scattering system is combined with other diagnostic data for overall density and temperature profiles in Article IV.

3.3.3 Interferometer

Interferometers, which provide line integrated measurements of the electron density $\int n_e d\ell$ along the lines of sight, launch electromagnetic waves into the plasma and detect interference patterns with reference waves due to optical path differences between the two waves. The optical path differences are related to the electron density of the plasma through its refractive index. In this thesis, the JET far infrared (FIR) interferometer and W7-X dispersion interferometer data have been used. The JET FIR interferometer system [108–110] provides eight line integrated measurements of the electron density along four vertical and four lateral lines of sight. The JET interferometer data can be used to infer electron density profiles through tomographic inversion [38] as well as to calibrate the HRTS system automatically as described in Article III. The W7-X dispersion interferometer system [111] provides a single line integrated measurement of the electron density along a line of sight which is approximately the same path of the laser of the Thomson scattering system. Again, the W7-X interferometer data is used to calibrate the Thomson scattering system automatically as described in Article IV.

3.3.4 X-ray imaging crystal spectroscopy (XICS)

The X-ray imaging crystal spectroscopy (XICS) is designed to measure the density and temperature of the electrons and impurity ions, for example, argon or iron ions, by collecting their X-ray emission, which is spatially and spectrally resolved by the crystal. The measurements of the X-ray emission are line integrated spectra along the lines of sight. Since the local X-ray emission depends on the density and temperature for the electrons and impurities, they can be inferred through tomography from the line integrated spectra. In this thesis, the W7-X XICS data has been used. The XICS system [51] provides 20 line integrated X-ray spectra covering more than half of the poloidal cross section. The XICS data is combined with the interferometer, Thomson scattering, and helium beam data in Article IV. This joint inference solutions of the four diagnostics

provide the most probable profiles of the electron density and temperature in addition to the ion temperature consistent with all the measurements.

3.3.5 Magnetic diagnostics

Magnetic diagnostics measure the magnetic field \mathbf{B} by quantifying voltage induced in coils by the magnetic flux through the surfaces spanning the coils outside the plasma. These magnetic diagnostics can have different configurations of the coils, for example, pickup coils (local magnetic field measurements) or Rogowski coils (plasma current measurements), depending on the measurement surface geometry. In this thesis, the JET magnetic data have been used. The magnetic data consists of 230 local measurements of the magnetic field by pickup coils, 88 local magnetic flux measurements by saddle coils, and six total magnetic flux measurements by flux loops [54]. Article V makes use of the magnetic field measurements from these JET magnetic diagnostics and polarimeters as well as the density and temperature (pressure) measurements provided by other applications, described in Article I, Article II and Article III, to carry out consistent inference solutions of plasma equilibria.

3.3.6 Polarimeter

Polarimeters provides line integrated measurements of the electron density n_e and magnetic field \mathbf{B} by measuring the polarisation angle rotations of electromagnetic waves injected into the plasma. These polarisation angle rotations can be represented by two quantities: the Faraday rotation $\Delta\phi$ and ellipticity angle χ , which are proportional to $\int n_e B_{\parallel} d\ell$ and $\int n_e B_{\perp}^2 d\ell$, respectively. Typically, polarimeters share the electromagnetic waves launched by interferometers. In this thesis, the JET polarimeter model [59] has been used. Article V combines the JET polarimeter data with the magnetic and profile diagnostic data to provide consistent inference solutions of plasma equilibria.

3.4 Bayesian inference in nuclear fusion research

All the applications based on the framework for scientific inference described in the previous chapter have been developed in the context of nuclear fusion

research in the Minerva framework. I would like to remark that this framework can be used for all kinds of scientific problems with arbitrary complexity. Nevertheless, a large-scale nuclear fusion experiment is an excellent example for its applications based on the following observations: (i) each of the scientific instruments, which are often very sophisticated and complex in fusion research, involves a large number of physics parameters and model assumptions, (ii) a large-scale fusion experiment employs several tens of such scientific instruments which makes consistent inference extremely difficult and (iii) the fusion plasma in such an experiment is extraordinarily complex, so far, no physics model can predict major physical phenomena, like transport, sufficiently well.

Of the five articles in this thesis, Article I and Article II present how to deal with such sophisticated scientific instruments in a systematic way concerning the observation (i), and Article III, Article IV and Article V provide consistent inference solutions for all the physics parameters given multiple heterogeneous data sets with respect to the observations (ii) and (iii). All these applications make use of Bayesian Occam's razor to compare the models of physics parameters of the fusion plasma which is one of the key strength of this framework regarding the observation (iii). Article V demonstrates the usage of the physics prior knowledge introduced by virtual observations and provides all possible inference solutions for the fusion plasma in a stable, macroscopic equilibrium state given all the measurements from the major plasma diagnostics in such a complex system.

4

Thesis Articles

In this chapter, I will introduce the articles which constitute the main outcome of this thesis. I, together with the other authors and contributors, have developed applications based on the principles and methods in order to improve scientific modelling and inference in nuclear fusion research. These articles are mostly concerned with solutions to practical and technical issues that arise in inference problems in a complex nuclear fusion experiment. I would like to emphasise that the principles and methods are generally applicable to any scientific problem, and the reader, who is interested in the principles and methods, is recommended to read the previous chapters.

The main articles

Authors contributions to the main articles:

I am the original author of all the text and content in all the main articles in this chapter as well as the person who specifically developed and implemented all the scientific models and applications.

Bayesian modelling of atomic physics and spectroscopy systems

Article I

‘Bayesian modelling of the emission spectrum of the Joint European Torus Lithium Beam Emission Spectroscopy system’

S. KWAK, J. SVENSSON, M. BRIX and Y.-C. GHIM

Review of Scientific Instruments, Vol. 87.2 (2nd Feb. 2016), DOI: 10.1063/1.4940925

This article describes a Bayesian approach to model arbitrary instrument functions and emission spectra by using Gaussian processes. This approach has been applied to the lithium beam emission spectroscopy system at Joint European Torus (JET). The instrument functions of the JET lithium beam system which consists of interference filters and spectral response functions are modelled by non-parametric Gaussian processes, which is capable of representing an arbitrary shape of these functions. The posterior distributions of these instrument functions are calculated given a set of spectral observations separately collected during calibration procedures with the optimal smoothness (hyperparameters) of the Gaussian processes which are found by exploring the model evidence through linear Gaussian inversion. Given these inferred instrument functions all the lithium line and plasma background emissions in the emission spectra are inferred given each of measurements during a plasma discharge. This approach provides all possible inference solutions for the lithium line and plasma background emissions with their associated uncertainties which can be used to infer the electron density and the effective ion charge in the edge region of the plasma. Furthermore, this approach does not require separate measurements of the plasma background emissions by a beam modulation. During the beam-off frame measurements, the lithium line emissions cannot be collected due to lack of the lithium beam

atoms, which means that during the beam modulation, the electron density cannot be measured. This approach, therefore, improved the quality and quantity of the inference at the same time. Article II employs this application in order to infer the electron density in the edge region of the plasma.

Article II

‘Bayesian electron density inference from JET lithium beam emission spectra using Gaussian processes’

S. KWAK, J. SVENSSON, M. BRIX and Y.-C. GHIM

Nuclear Fusion, Vol. 57.3 (11th Jan. 2017), DOI: 10.1088/1741-4326/aa5072

This article describes Bayesian modelling of a spectroscopy system based on a general atomic physics model which takes into account interactions between different atomic species such as excitation, de-excitation, charge exchange, ionisation, spontaneous emission, etc. This physics model, also known as the collisional-radiative model, which has been implemented in the Minerva framework in a generic way, can simulate populations of all the relevant excited states of any atomic species. The application to the lithium beam emission spectroscopy system at the Joint European Torus (JET) has been developed for inference of the electron density in the edge region of the plasma given the intensity of lithium line emission, which is obtained by the spectral model developed in Article I. The Bayesian model of the lithium beam emission spectroscopy system provides the posterior distribution of the edge electron density profiles by fully taking into account atomic physics, lithium line emissions, instrument functions and their associated uncertainties. Unlike the conventional approach, this approach provides the full uncertainties of the edge electron density profiles. The edge electron density profiles are modelled by non-parametric Gaussian processes, and due to the usage of them, the quality and quantity of inference solutions have been improved. Furthermore, this approach does not require an unreasonable assumption such as a monotonicity condition which has been used in the conventional Bayesian approach. In other words, the inference solutions for the edge electron density profiles are physically more reasonable and at the same time available with their uncertainties in a wider range. Moreover, this Bayesian approach can automatically infer the calibration factor of the lithium beam system

without additional preconditions which are essential to the conventional approach. In addition, the beam modulation, which is necessary for the conventional approach, is not any more needed in this application since the results of Article I has been used here.

Bayesian joint modelling of multiple scientific instruments

Article III

‘Bayesian modelling of Thomson scattering and multichannel interferometer diagnostics using Gaussian processes’

S. KWAK, J. SVENSSON, S. BOZHENKOV, J. FLANAGAN, M. KEMPENAARS, A. BOBOC and Y.-C. GHIM

Nuclear Fusion, Vol. 60.4 (26th Feb. 2020), DOI: 10.1088/1741-4326/ab686e

This article describes Bayesian joint modelling of the high-resolution Thomson scattering (HRTS) and multichannel far infrared (FIR) interferometer systems at Joint European Torus (JET). Each of the predictive models of both systems has been individually developed and combined into a single joint model through Bayes formula. The full electron density and temperature profiles are modelled by Gaussian processes with a non-stationary covariance function which can reproduce different gradient in the core and edge regions of the plasma. The calibration factor of the HRTS system is regarded as an additional unknown parameter since it has not been fully identified so far. The full joint posterior distribution of the electron density and temperature profiles as well as the hyperparameters of the Gaussian processes and the calibration factor is explored by an adaptive Metropolis-Hastings algorithm. The marginal posterior solutions for the electron density and temperature profiles are obtained by taking into account all possible values of the hyperparameters and the calibration factor. For this reason, the inference solutions do not depend on specific values of the hyperparameters and the calibration factor due to marginalisation. Furthermore, this application automatically calibrates the HRTS system and propagate the calibration uncertainties to the inference solutions in a consistent way. This means that these marginal

posterior solutions for all the unknown parameters are optimal given the observations.

Article VI

‘Bayesian modelling of multiple diagnostics at Wendelstein 7-X’

S. KWAK, J. SVENSSON, S. BOZHENKOV, H. T. MORA, U. HOEFEL, A. PAVONE, M. KRYCHOWIAK, A. LANGENBERG and Y.-C. GHIM

Plasma Physics and Controlled Fusion, (2020), in preparation

This article describes Bayesian joint modelling of multiple scientific instruments at Wendelstein 7-X (W7-X). The application makes use of the various measurements from the Thomson scattering, dispersion interferometer, helium beam emission spectroscopy and X-ray imaging crystal spectroscopy (XICS) systems in order to provide consistent inference solutions for the electron density and temperature and ion temperature profiles. The predictive models of the beam emission spectroscopy and Thomson scattering systems implemented in Article II and Article III have been used in this application. The electron density and temperature and ion temperature profiles are modelled by Gaussian processes with a non-stationary covariance function which can reproduce different gradient in the core and edge regions of the plasma. These profiles are inferred given different combinations of heterogeneous data as well as the prior knowledge introduced by *virtual observations* which exclude physically and empirically improbable solutions. Furthermore, this article theoretically and experimentally shows that the full joint posterior distributions of the unknown parameters and hyperparameters intrinsically embody Bayesian Occam’s razor. By exploring the full joint posterior distributions inference solutions for the unknown parameters with the optimal hyperparameters can be found without calculation of the model evidence that requires integration over the high-dimensional parameter space, which is one of the major obstacles to Bayesian model selection.

Bayesian inference of plasma equilibria

Article V

‘Bayesian equilibria of axisymmetric plasmas’

S. KWAK, J. SVENSSON, O. FORD, L. APPEL and Y.-C. GHIM

Nuclear Fusion, (2020), in preparation

This article describes Bayesian equilibria of axisymmetric plasmas in a magnetic confinement fusion experiment by making full use of all the principles and methods which have been developed through the thesis. This approach has been applied to the Joint European Torus (JET). The Bayesian equilibrium models employ a large number of different heterogeneous data sets from the magnetic sensors (pickup coils, saddle coils and flux loops), interferometers, polarimeters, high-resolution Thomson scattering (HRTS), lithium beam emission spectroscopy systems. Since inference of plasma equilibria is a complex tomographic problem, the two different prior distributions have been introduced in order to exclude physically unreasonable solutions: a Gaussian process prior and an equilibrium prior. The Gaussian process prior constrains the plasma current distributions by their covariance (smoothness) function whose hyperparameters are optimally found by Bayesian Occam’s razor. The equilibrium prior, on the other hand, imposes MHD force balance, given by the Grad-Shafranov equation, by introducing *virtual observations* as if this force balance has been observed over the plasma current distributions. These Bayesian equilibrium models with the two priors provide *consistent solutions* for all the physics parameters relevant to plasma equilibria for the first time at JET. The full joint posterior distributions of plasma equilibria are extraordinarily complex and high-dimensional, therefore exploring them is computationally challenging. For this reason, a new method based on the Gibbs sampling scheme has been developed to explore these full joint posterior distributions of the plasma current distributions and pressure profiles, the MAP solutions and posterior samples are presented. Interestingly, these inference solutions propose two different possible plasma equilibrium current distributions for an H-mode plasma: either strong toroidal current densities or poloidal current flux holes in the edge region.

Main coauthor articles

Authors contributions to coauthor articles:

In this chapter, I have listed some of the coauthor articles to which I have made critical contributions, which will be explicitly described below.

Artificial Neural network

Coauthor Article III

‘Neural network approximated Bayesian inference of edge electron density profiles at JET’

A. PAVONE, J. SVENSSON, S. KWAK, M. BRIX and R. C. WOLF

Plasma Physics and Controlled Fusion, Vol. 62.4 (Mar. 2020), DOI: 10 . 1088/1361-6587/ab7732

This article describes a real-time application to providing approximated Bayesian inference of electron density from the lithium beam emission spectroscopy system at Joint European Torus (JET) by an artificial neural network. The neural network maps the lithium beam emission spectra, measurement positions and calibration factor of the lithium beam system to the electron density profiles in the edge region of the plasma. The training data set is automatically generated from the joint probability distribution, which has been developed in Article II. The posterior distribution of the neural network parameters is approximated with Bernoulli distributions via variational inference. These approximated posterior distributions are calculated through Monte Carlo (MC) dropout method during the training process. The posterior predictive mean and uncertainties of the electron density profiles are provided as real-time inference solutions. I am the original author of the Bayesian model of the lithium beam system at JET which is approximated by the neural network in this article. I also engaged in theoretical and technical discussions about the neural network model and approximated uncertainties.

Coauthor Article IV

‘Deep neural network Grad-Shafranov solver constrained with measured magnetic signals’

S. JOUNG et al.

Nuclear Fusion, Vol. 60.1 (Jan. 2020), DOI: 10 . 1088 / 1741 - 4326 /

ab555f

This article describes a real-time application to providing a plasma equilibrium solution consistent with magnetic field measurements by an artificial neural network. The neural network maps the magnetic field measurements to the plasma current distributions as well as the poloidal magnetic flux surfaces. The training data, which contains the magnetic field measurements and results of the equilibrium fitting (EFIT) code as input and output, respectively, have been collected over a thousand of plasma discharges at the Korea Superconducting Tokamak Advanced Research (KSTAR) fusion experiment. This application can provide a plasma equilibrium reconstruction in approximately 1 ms and can be used for real-time plasma control in principle. I am the original author of the first version of the artificial neural network model which maps the magnetic field measurements to the poloidal magnetic flux surfaces in R, Z coordinates [119, 120] and have been engaged in the further development described in this article.

Bayesian modelling of microwave radiometer calibration

Coauthor Article XII

‘Bayesian modeling of microwave radiometer calibration on the example of the Wendelstein 7-X electron cyclotron emission diagnostic’

U. HOEFEL et al.

Review of Scientific Instruments, Vol. 90.4 (Apr. 2019), DOI: 10.1063/1.5082542

This article describes Bayesian modelling of calibration experiments of microwave radiometers and its application to the electron cyclotron emission (ECE) system developed at the W7-X experiment. This Bayesian calibration model has been thoroughly developed, and this application performs the first model-based calibration of a microwave radiometer system. I have contributed to the concept and model of this model-based calibration.

Bayesian modelling of Thomson scattering system

Coauthor Article XV

'Feasibility study of direct spectra measurements for Thomson scattered signals for KSTAR fusion-grade plasmas'

K.-R. PARK, K.-H. KIM, S. KWAK, J. SVENSSON, J. LEE and Y.-C. GHIM
Journal of Instrumentation, Vol. 12.11 (Nov. 2017), DOI: 10.1088/1748-0221/12/11/C11022

This article describes a feasibility study of direct measurements of Thomson scattering signals for the fusion plasma in the Korea Superconducting Tokamak Advanced Research (KSTAR) experiment. The posterior distribution of the electron density and temperature has been calculated given different sets of the experimental setup of a spectrometer-based Thomson scattering system. The bias errors, posteriors uncertainties and entropy for the spectrometer-based system are quantified in order to investigate its feasibility. I am the main author of the forward model for a Thomson scattering system which is used in this article and extensively engaged in theoretical and technical discussions.

Coauthor Article XVI

'FPGA acceleration of Bayesian model based analysis for time-independent problems'

H. T. MORA et al.
(Nov. 2017), DOI: 10.1109/GlobaSIP.2017.8309065

This article describes an acceleration of Bayesian inference by a field-programmable gate array (FPGA) and its application to the Thomson scattering and dispersion interferometer systems developed at Wendelstein 7-X (W7-X). This application dramatically accelerates the inference process in order to obtain the posterior samples of the electron density and temperature profiles in a second from the Bayesian joint model of the Thomson scattering and interferometer systems. This means that the full posterior uncertainties are available in a second, which is indeed close to a real-time frame. I am the main author of the forward model for a Thomson scattering system which is used in this article and extensively engaged in theoretical and technical discussions.

Bayesian inference of effective ion charge

Coauthor Article VIII

‘Measurements of visible bremsstrahlung and automatic Bayesian inference of the effective plasma charge Z_{eff} at W7-X’

A. PAVONE et al.

Journal of Instrumentation, Vol. 14.10 (Oct. 2019), DOI: 10.1088/1748-0221/14/10/C10003

This article describes Bayesian inference of effective ion charge from a visible Bremsstrahlung measurement at Wendelstein 7-X (W7-X). This application provides inference solutions for effective ion charge automatically and robustly given the visible Bremsstrahlung measurement from a compact USB-spectrometer. The electron density and temperature profiles, which are necessary for the inference, are provided by the Thomson scattering model with Gaussian processes. I am the main author of the forward model for a Thomson scattering system and the Thomson scattering model with Gaussian processes which are used in this article and extensively engaged in theoretical and technical discussions.

Bayesian tomography of radiation power

Coauthor Article IX

‘First Observation of a Stable Highly Dissipative Divertor Plasma Regime on the Wendelstein 7-X Stellarator’

D. ZHANG et al.

Physical Review Letters, Vol. 123.2 (July 2019), DOI: 10.1103/PhysRevLett.123.025002

This article describes the first observation of highly stable power dissipation on the island divertors at the W7-X stellarator experiment. This observation shows that the island divertor concept, which can be a potential promising candidate to exhaust option for a stellarator type reactor, works as expected. I have provided the tomographic inversion of the radiation power given line integrated measurements of radiative power from the bolometer system, which is one of the major pieces of evidence supporting this article. I have been continuously developing and maintaining the Bayesian bolometer tomography model, which is originally

developed by Dr Jakob Svensson, who is one of the coauthors of this article.

Coauthor Article XI

‘Radiative edge cooling experiments in Wendelstein 7-X start-up limiter campaign’

T. BARBUI et al.

Nuclear Fusion, Vol. 59.7 (July 2019), DOI: 10 . 1088 / 1741 - 4326 / ab18c5

This article describes impurity seeding experiments related to the radiation distribution and cooling effect in the edge region of the plasma at the W7-X experiment. Nitrogen and neon impurities, which were seeded into the plasma, affect the radiation distribution and cooling effect in the edge region with a substantial electron temperature reduction at downstream limiter. I have provided the tomographic inversion of the radiation power given line integrated measurements of radiative power from the bolometer system, which is one of the major pieces of evidence supporting this article. I have been continuously developing and maintaining the Bayesian bolometer tomography model, which is originally developed by Dr Jakob Svensson, who is one of the coauthors of this article.

4.1 Article I¹

‘Bayesian modelling of the emission spectrum of the Joint European Torus Lithium Beam Emission Spectroscopy system’

S. KWAK, J. SVENSSON, M. BRIX and Y.-C. GHIM

Review of Scientific Instruments, Vol. 87.2 (2nd Feb. 2016), DOI: 10 . 1063 / 1 . 4940925

¹Reproduced from S. KWAK et al. ‘Bayesian modelling of the emission spectrum of the Joint European Torus Lithium Beam Emission Spectroscopy system’. In: *Review of Scientific Instruments*, Vol. 87.2 (2nd Feb. 2016), page 023501. DOI: 10 . 1063 / 1 . 4940925, with the permission of AIP Publishing.

Bayesian modelling of the emission spectrum of the Joint European Torus Lithium Beam Emission Spectroscopy system

Sehyun Kwak^{1,2†}, J. Svensson^{2,‡}, M. Brix³, Y.-c. Ghim^{1*} and JET Contributors[‡]

EUROfusion Consortium, JET, Culham Science Centre, Abingdon, OX14 3DB, United Kingdom

¹ Department of Nuclear and Quantum Engineering, KAIST, Daejeon 34141, South Korea

² Max-Planck-Institut für Plasmaphysik, 17491 Greifswald, Germany

³ Culham Centre for Fusion Energy, Culham Science Centre, Abingdon OX14 3DB, United Kingdom

E-mail: [†]slayer313@kaist.ac.kr, [‡]jakobsemail@gmail.com,

*ycghim@kaist.ac.kr

Postprint

Abstract. A Bayesian model of the emission spectrum of the JET lithium beam has been developed to infer the intensity of the Li I (2p-2s) line radiation and associated uncertainties. The detected spectrum for each channel of the lithium beam emission spectroscopy system is here modelled by a single Li line modified by an instrumental function, Bremsstrahlung background, instrumental offset, and interference filter curve. Both the instrumental function and the interference filter curve are modelled with non-parametric Gaussian processes. All free parameters of the model, the intensities of the Li line, Bremsstrahlung background, and instrumental offset, are inferred using Bayesian probability theory with a Gaussian likelihood for photon statistics and electronic background noise. The prior distributions of the free parameters are chosen as Gaussians. Given these assumptions, the intensity of the Li line and corresponding uncertainties are analytically available using a Bayesian linear inversion technique. The proposed approach makes it possible to extract the intensity of Li line without doing a separate background subtraction through modulation of the Li beam.

1. Introduction

In fusion research, lithium beam emission spectroscopy (Li-BES) is widely used to measure edge electron density profiles in various machines such as TEXTOR [1, 2],

[‡] See the Appendix of F. Romanelli et al., Proceedings of the 25th IAEA Fusion Energy Conference 2014, Saint Petersburg, Russia

ASDEX Upgrade [3] and JET [4, 5, 6]. When the neutral lithium beam is injected into the plasma both the beam attenuation and emission processes occur due to collisions between lithium atoms and plasma particles. The JET Li-BES system measures the emission spectrum from the spontaneous emission following those collisions. The intensity of the measured Li line depends primarily on the electron density. The relationship between the intensity of the Li line and the electron density can be expressed analytically by a multi-state model [1, 7], which describes excitation and de-excitation reactions caused by the particle impacts including electrons, protons, and impurity ions, and spontaneous emissions.

The Li-BES system is used to infer edge electron density profiles based on intensity profiles of Li line, hence the intensity profiles must be evaluated as precise as possible. Currently, intensity profiles of Li line from JET Li-BES data are obtained via a fitting procedure [5] with seven fitting parameters: a multiplication factor for background line radiation as measured by beam modulation (one parameter), a quadratic polynomial for the filtered background (three parameters) and a Gaussian function for lithium line radiation with its width, position and intensity (three parameters).

In this paper we show that improved intensity profiles of Li line can be obtained by modelling both the instrumental function and the interference filter curve for each channel based on Gaussian processes. Bayesian probability theory is used to infer the intensity of the Li line, Bremsstrahlung background, and instrumental offset with associated uncertainties. The instrumental offset can be differentiated from the plasma Bremsstrahlung level since the former is not influenced by the filter function. Thus, the method allows for the separation of signal and background without performing a separate background radiation measurement through a beam modulation procedure. In short, our method allows one to (1) generalize the fitting procedure using non-parametric Gaussian process by taking into account of instrumental effects, (2) estimate intensities and uncertainties of Li line consistently and (3) make the separate background measurements obsolete in case of no overlapping impurity lines. The usage of Gaussian processes to model instrumental effects can be applied generally, as described in Section 3, to improve spectral fitting also for other systems. A brief overview of the experimental setup of the JET Li-BES system and a description of the measured emission spectrum are given in Section 2. In Section 3 the Bayesian spectral model is described, including the modelling of the instrumental effects with Gaussian processes. The section also shows results from inference on line radiation, Bremsstrahlung background and instrumental effects using these models. A summary is provided in Section 4.

2. Spectral modelling

The JET Li-BES system consists of 26 spatial channels along the neutral lithium beam, with a typical energy of ~ 55 keV vertically penetrating into the plasma as shown in Figure 1. The 26 line of sights are not perpendicular to the beam direction, causing Doppler shifts of the lithium beam emission. As each line of sight has a different angle

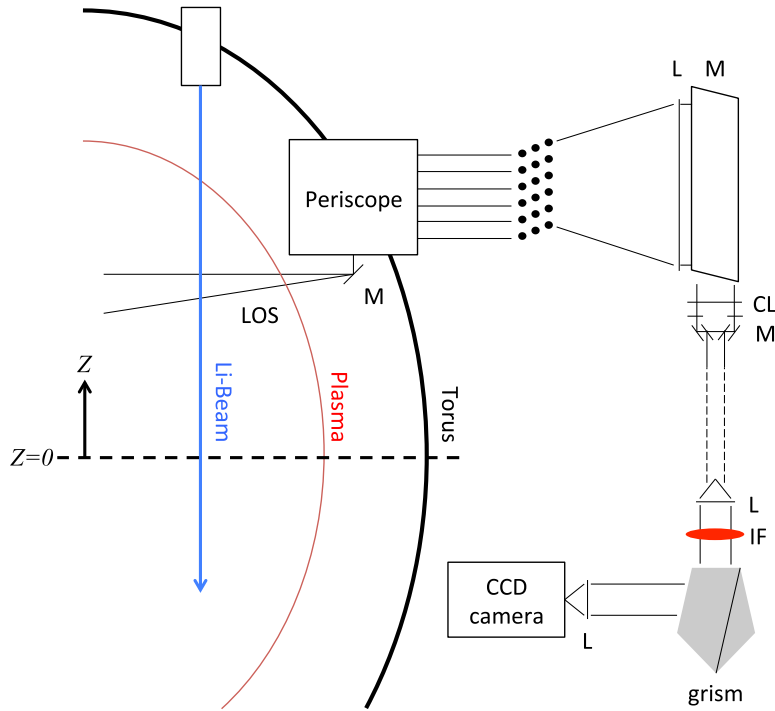


Figure 1. Schematic image of the Li-BES system on JET. In the figure L stands for a spherical lens, CL for a cylindrical lens, IF for an interference filter, M for a mirror and grism for a high resolution transmission grating prism. Z is the coordinate of the system where $Z = 0$ is at the midplane of JET.

to the beam line, the amount of the Doppler shifts are different for different channels. This fact is used to calibrate the spatial positions of the 26 channels. The spectrometer and charge coupled device (CCD) camera are thus required to obtain not only intensities but spectra of the beam emission as well. A detailed description of the system can be found elsewhere [5, 6].

The measured intensity at the m^{th} channel denoted as s_m in the CCD camera as a function of x can be expressed as

$$s_m(x) = d_m(x) [c_m(x) a_m + b_m] + z_m, \quad (1)$$

where x is the pixel number, corresponding to wavelength, $c_m(x)$ the instrumental function, $d_m(x)$ the interference filter curve, a_m the intensity of Li line, b_m Bremsstrahlung background, and z_m instrumental offset. We treat Bremsstrahlung radiation as a constant within a channel because it is almost constant within a narrow wavelength range of ~ 5 nm set by the interference filter. Note that we measure $s_m(x)$, and based on this measurement we wish to estimate a_m , b_m and z_m among which a_m being the most important quantity, allowing us to infer the local electron density.

Since the spectral width of the Li line is below the resolving capacity of the instrument, the shape of the line on the CCD chip is determined solely by instrumental

effects. The filter curve of the system can be independently measured (see in Section 3.1), and so we separate the instrumental effects into an instrument function $c_m(x)$, the shape of an infinitely narrow line on the detector, and the interference filter curve $d_m(x)$.

3. Bayesian inference with Gaussian processes

In order to fit the whole spectrum, the instrumental function $c_m(x)$ and the interference filter curve $d_m(x)$ must be known. The functional shape of these are not known a priori, so we here use non-parametric Gaussian processes to model them.

A Gaussian process [8], defined on a one dimensional domain, is defined by a covariance function and a mean function, where the covariance function specifies the covariance between any two points in the domain. This restricts the variability of the function to be inferred and can be used instead of a parameterization. Gaussian processes were introduced in the fusion community in reference [9] and is the default way of representing profile quantities in the Minerva framework [10]. It has been used for modelling the current distribution [9, 11, 12], soft-x ray tomography [13], and for representing profile quantities [9, 14, 15]. The covariance function of the Gaussian process is usually defined through families of covariance functions where a few so called *hyperparameters*, such as overall scale and length scale of the function, define the shape of the covariance function and thus the variability of the function.

Denoting the instrumental function of the m^{th} channel $c_m(x)$, and the interference filter function $d_m(x)$, as a vector $\mathbf{y}_* = [y_{*i}]$ where y_{*i} corresponds to $c_m(x_i)$ or $d_m(x_i)$, the representation of these functions as Gaussian processes corresponds to the y_{*i} having a multivariate normal distribution

$$\mathbf{y}_* \sim \mathcal{N}(\mathbf{0}, \mathbf{K}(\mathbf{x}, \mathbf{x})), \quad (2)$$

so

$$p(\mathbf{y}_*) = \frac{1}{\sqrt{(2\pi)^N |\mathbf{K}|}} \times \exp \left[-\frac{1}{2} (\mathbf{y}_* - \mathbf{0})^T \mathbf{K}^{-1}(\mathbf{x}, \mathbf{x}) (\mathbf{y}_* - \mathbf{0}) \right]. \quad (3)$$

Here, $p(\mathbf{y}_*)$ is the probability density function of \mathbf{y}_* , N is the number of elements in \mathbf{y}_* which is the total number of pixels within each channel. \mathbf{K} is a $N \times N$ covariance matrix whose ij^{th} component is determined as

$$K_{ij} = \sigma_f^2 \exp \left(-\frac{1}{2l^2} |x_i - x_j|^2 \right) + \sigma_n^2 \delta_{ij}, \quad (4)$$

where σ_f^2 is the signal variance which regulates the overall scale, σ_n^2 is the noise variance controlling the noise level of the signal, and l is the length scale governing how fast the function can change significantly. σ_f , σ_n and l together are the hyperparameters. δ_{ij} is the Kronecker delta. To determine the instrumental function, we use Bayesian probability

theory with Equation (3) as the prior, where the hyperparameters are determined based on the measured data by maximizing the evidence as described in Appendix A. Maximization of the evidence has previously been done in references [9, 11, 16], all implemented in the Minerva framework.

The prior distribution Equation (3) is then used in Bayes formula

$$p(\mathbf{y}_*|\mathbf{y}) = \frac{p(\mathbf{y}|\mathbf{y}_*)p(\mathbf{y}_*)}{p(\mathbf{y})}, \quad (5)$$

to find the posterior Gaussian process $p(\mathbf{y}_*|\mathbf{y})$ where \mathbf{y} is the measured data. The likelihood, $p(\mathbf{y}|\mathbf{y}_*)$, is a probabilistic model of the observations, and includes the noise characteristics.

In the following section, we provide a detailed description of how the likelihood and the prior are applied for emission spectrum modelling of the JET Li-BES system.

3.1. Instrumental function and interference filter curve inference

We infer the instrumental function and filter curve \mathbf{y}_* , i.e., $c_m(x)$ or $d_m(x)$ in Equation (1), by maximizing the posterior in Equation (5) where the prior is defined using Gaussian processes as described above. The instrumental function $c_m(x)$, can be derived from the emission spectrum data during the beam-into-gas calibration measurements, using separate interference filter curve measurements for $d_m(x)$. During the beam-into-gas calibration measurement, neutral lithium is injected into the D_2 gas. The lack of Bremsstrahlung background, makes the Li line dominant, and so the instrumental function can be inferred directly for each channel. The interference filter curve is measured separately by putting a uniform intensity light emission diode (LED) in front of the spectrometer. Both the instrumental function and the interference filter curve must be determined for each channel since they can be different for different channels due to fiber geometry, lens contamination, etc.

For constructing the likelihood, we need to model the uncertainties in the system. There are two major sources of uncertainties: (1) Poisson noise $\sigma_{ph} = \sqrt{n_{ph}}$ from the photon statistics and (2) the electronic noise σ_e . For Poisson noise the number of measured photons, n_{ph} , is calculated from the number of photoelectrons in the signal using the CCD camera's photons to photoelectron ratio. When the number of photons is sufficiently large the Poisson noise can be approximated by a Gaussian distribution. The variance of the Gaussian distributed electronic noise is estimated from measurements without exposure, i.e., the fluctuation level of the background signal. This gives the following likelihood

$$p(\mathbf{y}|\mathbf{y}_*) = \frac{1}{\sqrt{(2\pi)^N |\Sigma|}} \exp\left(-\frac{1}{2}(\mathbf{y} - \mathbf{y}_*)^T \Sigma^{-1} (\mathbf{y} - \mathbf{y}_*)\right), \quad (6)$$

where the $N \times N$ diagonal matrix Σ provides the associated uncertainties for N pixels

in a channel defined as $\Sigma = \Sigma_{ph} + \Sigma_e$. Σ_{ph} and Σ_e are

$$\begin{aligned} \Sigma_{ph} &= \begin{bmatrix} \sigma_{ph1}^2 & & & \\ & \sigma_{ph2}^2 & & \\ & & \dots & \\ & & & \sigma_{phN}^2 \end{bmatrix}, \\ \Sigma_e &= \begin{bmatrix} \sigma_{e1}^2 & & & \\ & \sigma_{e2}^2 & & \\ & & \dots & \\ & & & \sigma_{eN}^2 \end{bmatrix}, \end{aligned} \quad (7)$$

where the subscript $\{1, 2, \dots, N\}$ corresponds to the pixel index of a channel in the CCD camera. Notice that the only unknown in Equation (6) is \mathbf{y}_* .

The prior $p(\mathbf{y}_*)$, defined in Equation (3) contains the three hyperparameters σ_f , σ_n and l . Since the noise of the signal is captured by the likelihood, we do not need to include the noise variance σ_n in the prior Equation (4). However, for the sake of numerical stability we choose σ_n such that $\sigma_n/\sigma_f \ll 1$, i.e., $\sigma_n^2/\sigma_f^2 = 10^{-2}$ for both the instrumental function and the interference filter curve. The hyperparameters, both the overall scale σ_f and the length scale l , are determined by maximizing the evidence $p(\mathbf{y})$ in the denominator of Bayes formula Equation (5). We choose the hyperparameters such that $p(\mathbf{y}|\sigma_f, l)$ is maximized, where $p(\mathbf{y}|\sigma_f, l)$ can be found from the marginalization of the joint distribution of data and free parameters

$$p(\mathbf{y}|\sigma_f, l) = \int p(\mathbf{y}|\mathbf{y}_*, \sigma_f, l) p(\mathbf{y}_*|\sigma_f, l) d\mathbf{y}_*. \quad (8)$$

Appendix A discusses the rationale behind choosing hyperparameters that maximizes the evidence. Note that the right hand side of Equation (8) contains the likelihood and the prior for which we have well defined expressions, Equation (6) and Equation (3), respectively. Figure 2 and Figure 3 show the $p(\mathbf{y}|\sigma_f, l)$ of interference filter curves and instrumental function, respectively, as a function of the scale length l and the overall scale σ_f for the spatial channel of (a) $m = 4$, (b) 8, (c) 12 and (d) 16.

Since both the prior and the likelihood are multivariate Gaussian, and the forward model is linear, the posterior distribution is also a multivariate Gaussian distribution over \mathbf{y}_* . The posterior mean and covariance can thus be calculated explicitly via a Bayesian linear Gaussian inversion [17]. Figure 4 shows (a) the measured (blue) and the best Gaussian process estimation (red) of interference filter curve $d_m(x)$ for channel number 5, i.e., $m = 5$, and (b) normalized best Gaussian process estimation of the interference filter curve for all channels as a function of pixel (x) of the CCD camera. The best Gaussian process estimation is in good agreement with the measured data. In addition, Figure 4 shows (c) the measured (blue), a simple Gaussian fit (yellow) and the best Gaussian process estimation (red) of instrumental function $c_m(x)$ for channel number 18, i.e., $m = 18$, and (d) the best Gaussian process estimation of the instrumental functions for all channels. Each pixel (x) corresponds to a specific wavelength where the wavelength

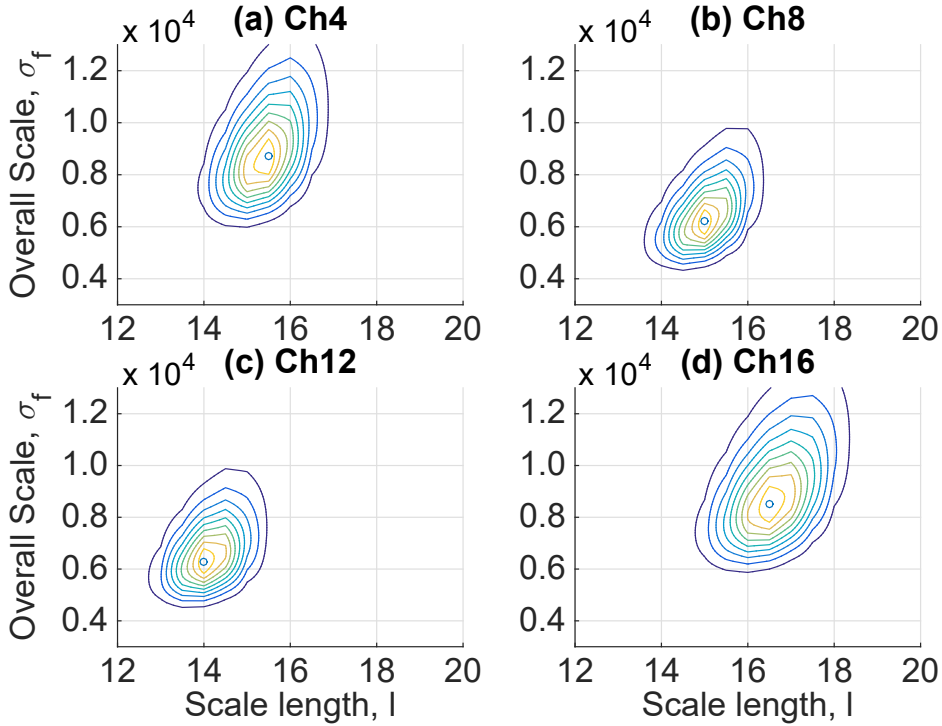


Figure 2. Contour of the evidence probability density for the interference filter curve calculated by Equation (8) as a function of the length scale l and the overall scale σ_f for the spatial channel of (a) $m = 4$, (b) 8, (c) 12 and (d) 16. Both the overall scale and the length scale of the corresponding spatial channel of the interference filter curve in Equation (4) are the values that maximize the evidence.

calibration is performed with neon and xenon lamps [5]. Note that typical values of Σ_e are 100 – 200; while $\Sigma_{ph} \sim \mathcal{O}(10^4)$ and $\sim \mathcal{O}(10^2) - \mathcal{O}(10^3)$ for interference filter curve and instrumental function measurements, respectively.

3.2. Intensity profile inference

In this part, we obtain the intensities in Equation (1), i.e., the intensity of Li line a_m , Bremsstrahlung background b_m and instrumental offset z_m from the JET Li-BES data of each channel. Again, Bayesian probability theory is utilized to determine these three quantities:

$$p(\mathcal{I}_m | \mathcal{D}_m) \propto p(\mathcal{D}_m | \mathcal{I}_m) p(\mathcal{I}_m), \quad (9)$$

where $\mathcal{I}_m = [a_m, b_m, z_m]$ is a vector of the free parameters for the m^{th} channel, and \mathcal{D}_m is the measured data.

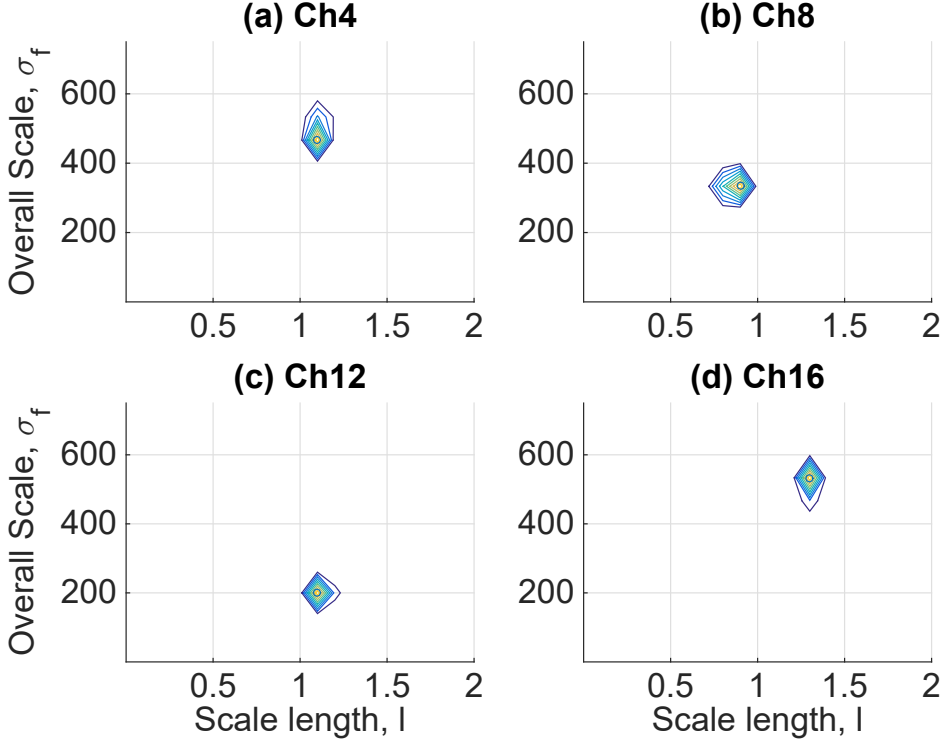


Figure 3. Same as Figure 2 for the instrumental function.

As priors for a_m , b_m and z_m we use

$$\begin{aligned}
 p(a_m) &= \frac{1}{\sigma_{a_m} \sqrt{2\pi}} \exp \left[-\frac{(a_m - 0)^2}{2\sigma_{a_m}^2} \right] \\
 p(b_m) &= \frac{1}{\sigma_{b_m} \sqrt{2\pi}} \exp \left[-\frac{(b_m - 0)^2}{2\sigma_{b_m}^2} \right] \\
 p(z_m) &= \frac{1}{\sigma_{z_m} \sqrt{2\pi}} \exp \left[-\frac{(z_m - 0)^2}{2\sigma_{z_m}^2} \right], \tag{10}
 \end{aligned}$$

giving $p(\mathcal{I}_m) = p(a_m)p(b_m)p(z_m)$. We choose very large prior standard deviations 10^6 , making the Gaussians effective flat. Although a_m and b_m need to be restricted to non-negative values, we use full Gaussian priors (rather than truncated ones) because (1) it makes the computation much simpler, (2) our measured data are good enough to make sure that they are positive numbers even with such inimical priors and (3) we set them to be zero if they turn out to be negative numbers. The likelihood $p(\mathcal{D}_m|\mathcal{I}_m)$ is multivariate Gaussian

$$\begin{aligned}
 p(\mathcal{D}_m|\mathcal{I}_m) &= \frac{1}{\sqrt{(2\pi)^N |\Sigma|}} \times \tag{11} \\
 &\exp \left(-\frac{1}{2} (\mathcal{D}_m - s_m)^T \Sigma^{-1} (\mathcal{D}_m - s_m) \right),
 \end{aligned}$$

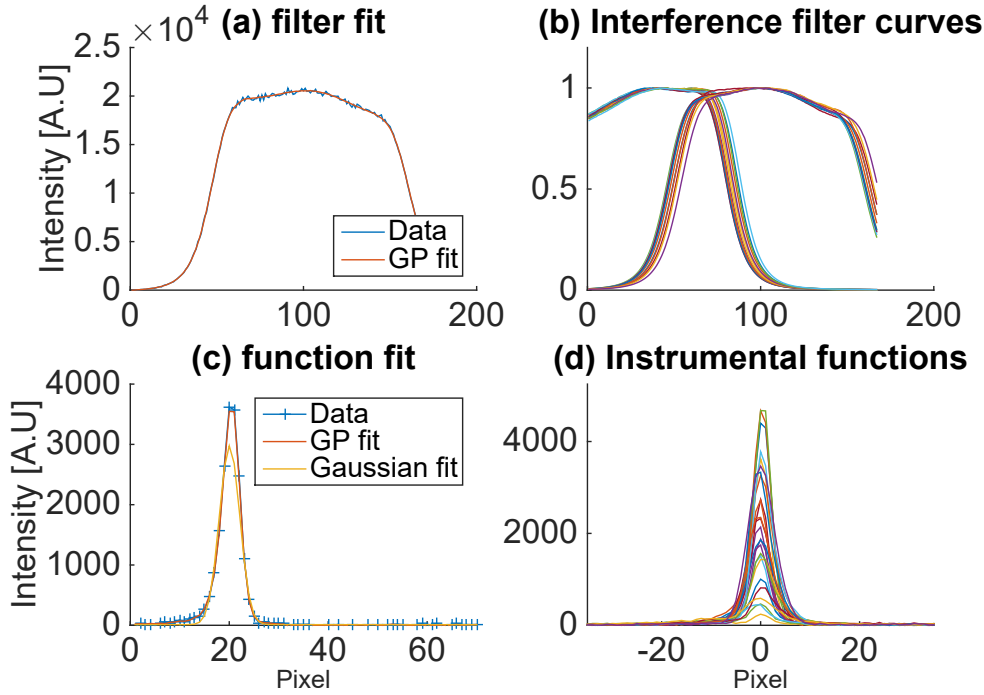


Figure 4. The best Gaussian process estimation (red) of (a) interference filter curve for channel number 5 and (c) instrumental function for channel number 18 and the measured data (blue). A simple Gaussian fit for the instrumental function (yellow) in (c) shows that Gaussian process is better than a simple Gaussian fit. The best Gaussian process estimation of (b) normalized interference filter curves and (d) instrumental functions for all channels are shown with different colors. The pixel can be converted to wavelength, the dispersion being approximately 0.04 nm/pixel.

where the covariance matrix Σ is given by Equation (7) and s_m by Equation (1) which is a function of \mathcal{I}_m .

Having a well defined prior and likelihood, the posterior distribution is obtained by a Bayesian linear Gaussian inversion. Figure 5 shows the intensity of lithium line radiation a_m , profile as a function of Z , the distance of the channel location from the midplane (Figure 1). Here we only have 25 channels since the interference filter curve of one channel could not be measured due to a technical problem. The numbers in the figure are the channel numbers of the JET Li-BES system. Note that this intensity profile is subsequently used to reconstruct the electron density profile at the plasma edge. We do not include inference of the electron density profile since it is outside the scope of this paper.

Having determined all the quantities on the right hand side of Equation (1) in a consistent way based on Bayesian inference and Gaussian processes, in Figure 6(a)-(d) shows the estimated spectra $s_m(x)$ (red) and the measured data (blue) for channel numbers $m = 4, 8, 12$ and 16 . They show that the lithium line shape and its absolute intensity, background radiation and electronic offsets are well reconstructed. In Figure 6(c), we illustrate the intensity of lithium line radiation a_{12} , background radiation

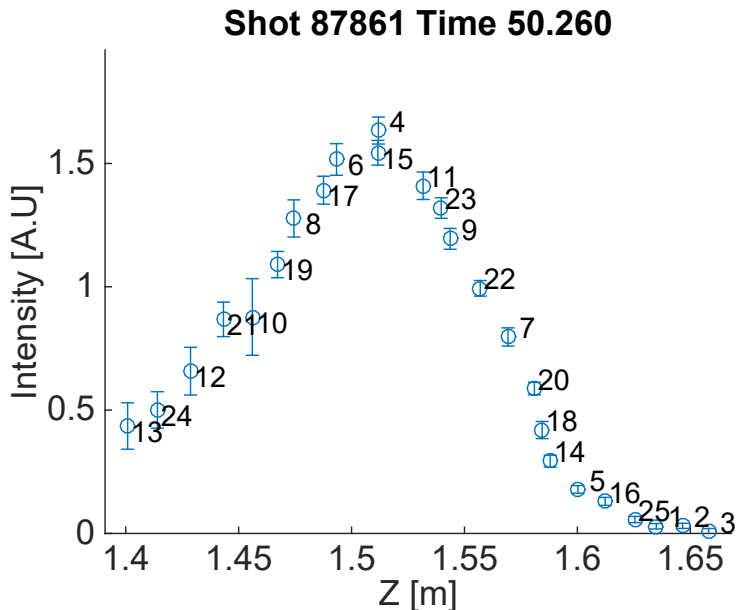


Figure 5. The intensity of lithium line radiation a_m , profile as a function of Z (distance from the midplane) with channel numbers. Circles are the intensities at their maximum posterior, and vertical bars represent 3σ ranges.

b_{12} and offset z_{12} for $m = 12$. For the case of channel $m = 16$, i.e., Figure 6(d), there exists an extra peak in the measurement caused by impurity line radiation [5]. The estimated s_m does not capture the impurity lines as they are not included in our model. As a simple consistency check on estimated uncertainties of a_m in Figure 5, we can see that the larger the signal-to-noise ratio, the higher the intensity of lithium line radiation a_m as shown in Figure 6(e).

We have mentioned earlier that our newly developed method allows one to remove the required separate measurement of Bremsstrahlung background radiation. Figure 7 shows the measured data with Li-beam on (yellow) and with Li-beam off (blue) corresponding to the background signal. The inferred background spectrum (red) based on the measured data during the Li-beam-on time frame agrees well with the measured background signal attesting that our method can capture background signal without performing separate background measurements. Note that the measured background signal is obtained during the nearest Li-beam-off time frame from the Li-beam-on time frame. Furthermore, as the model can provide the background signal level which is likely to be proportional to Bremsstrahlung radiation and its uncertainty for every channel, it conceivably could be used to infer the profile of effective charge Z_{eff} . Having stated this, we point out that if certain, i.e., neon (Ne) or nitrogen (N), impurities have large densities as are the cases for Ne or N seeded plasmas [5], the impurity line radiation may overlap with lithium line radiation for some channels with comparable intensities resulting in possible overestimation of the intensity of lithium line radiation. For this case, we need to either perform the separate background measurement or develop more sophisticated analysis

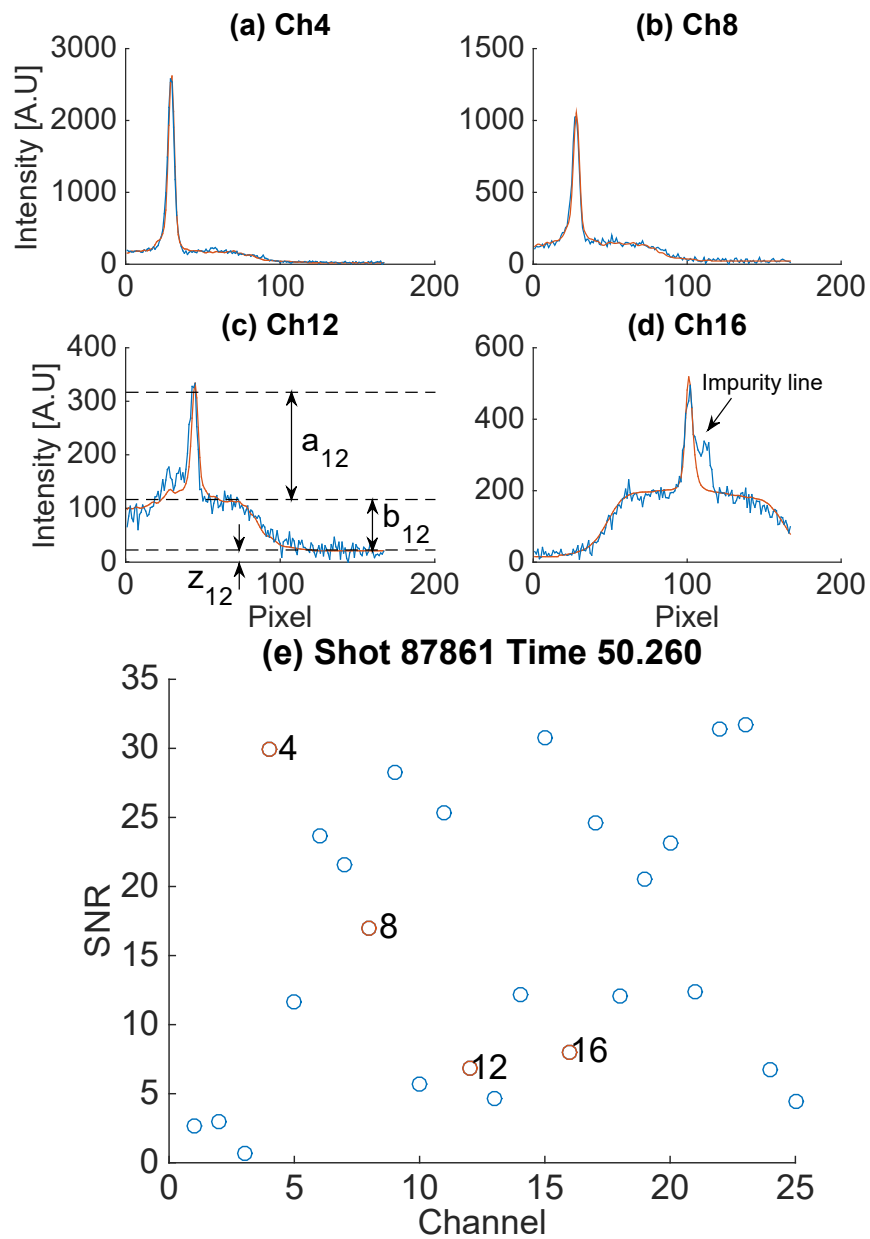


Figure 6. Estimated spectrum s_m (red) as a function of pixel (wavelength) for channel numbers (a) $m = 4$, (b) 8, (c) 12 and (d) 16 and the measured spectrum (blue). An example of estimated intensity of lithium line radiation a_m , background radiation b_m and offset z_m for $m = 12$ is shown in (c). Signal-to-noise ratio of each channel is shown in (e). The red circles in (e) are the channels shown in (a)-(d).

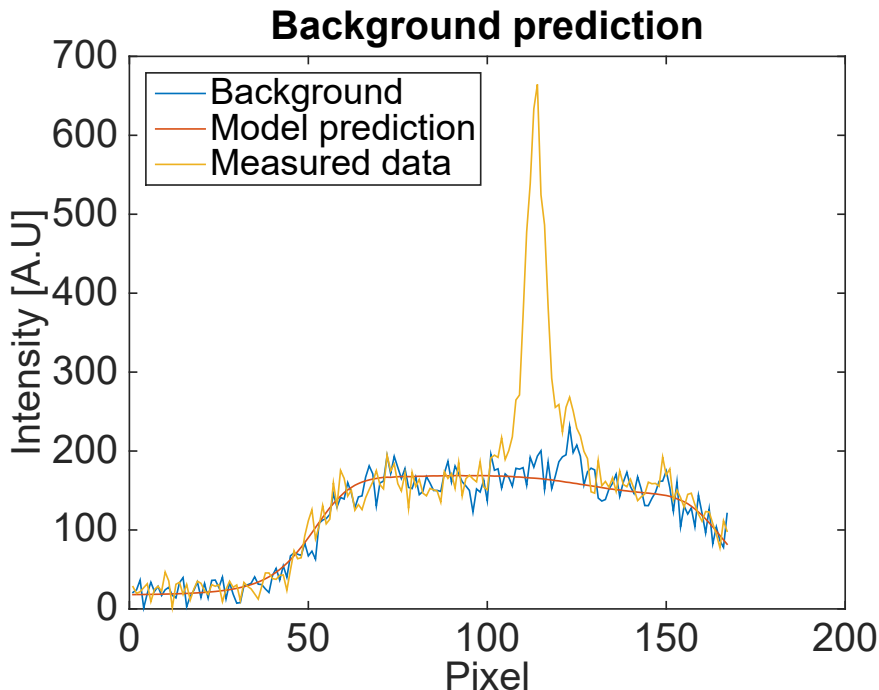


Figure 7. Measured data during the Li-beam-on time frame (yellow) and during the Li-beam-off time frame (blue) corresponding to the background spectrum for channel number $m = 14$ for the same shot number and time as shown in Figure 5, and the inferred, i.e., model predicted, background spectrum (red) based on the measured data during the Li-beam-on time frame only. The inferred background signal agrees well with the measured one.

technique which is left as a future work.

4. Summary

As Li-BES systems are widely used to reconstruct the electron density profile at the edge of plasmas based on the intensity of Li line, being able to resolve the measured spectrum data into the intensity of Li line, Bremsstrahlung background and instrumental offset is a substantial improvement on the conventional method of using background subtraction through beam modulation, and a Gaussian fit of the line shape. To obtain these parameters, we also need to know the instrumental function and interference filter curve.

The instrumental function and interference filter curve are both modelled with Gaussian processes, separately for each channel. The length scales and overall scales of the curves have been determined directly from the data through maximization of the evidence. The reconstructed spectra agree well with the measured spectra. In addition, the associated uncertainties of the data are also obtained consistently.

Apart from the improvement in fitting quality, another major advantage of this approach is that independent measurements of the background signals do not need to be

done. The method of background measurements is done by modulating the beam with an electrostatic deflection plate which increases hardware complexity and loses some temporal information. The Bremsstrahlung background signal that is simultaneously inferred could give additional information on for example effective charge Z_{eff} .

5. Acknowledgement

This work is supported by National R&D Program through the National Research Foundation of Korea (NRF) funded by the Ministry of Science, ICT & Future Planning (grant number 2014M1A7A1A01029835) and the KUSTAR-KAIST Institute, KAIST, Korea. This work has been carried out within the framework of the EUROfusion Consortium and has received funding from the Euratom research and training programme 2014-2018 under grant agreement No 633053. The views and opinions expressed herein do not necessarily reflect those of the European Commission.

Appendix A. Rationale behind maximizing the evidence probability

The posterior for the instrumental function or interference filter curve can be written as

$$p(\mathbf{y}_*|\mathbf{y}) \propto \exp\left[-\frac{1}{2}(\mathbf{y} - \mathbf{y}_*)^T \boldsymbol{\Sigma}^{-1}(\mathbf{y} - \mathbf{y}_*)\right] \times \exp\left[-\frac{1}{2}(\mathbf{y}_* - \mathbf{0})^T \mathbf{K}^{-1}(\mathbf{y}_* - \mathbf{0})\right], \quad (\text{A.1})$$

using Equation (6) and Equation (3). In addition to our main unknown \mathbf{y}_* , note that \mathbf{K} is a function of the hyperparameters σ_f and l , which are also not known. This suggests that we should integrate out these hyperparameters to get the marginal posterior:

$$\begin{aligned} p(\mathbf{y}_*|\mathbf{y}) &= \int \int p(\mathbf{y}_*, \sigma_f, l|\mathbf{y}) d\sigma_f dl \\ &= \int \int p(\mathbf{y}_*|\sigma_f, l, \mathbf{y}) p(\sigma_f, l|\mathbf{y}) d\sigma_f dl \\ &\approx p(\mathbf{y}_*|\sigma_{f0}, l_0, \mathbf{y}), \end{aligned} \quad (\text{A.2})$$

where the approximation is realized by setting $p(\sigma_f, l|\mathbf{y}) = \delta(\sigma_f - \sigma_{f0}) \delta(l - l_0)$, which is valid if the posterior distribution over the hyperparameters is narrowly centered around their most probable values.

The posterior for the hyperparameters σ_{f0} and l_0 is given by

$$p(\sigma_f, l|\mathbf{y}) \propto p(\mathbf{y}|\sigma_f, l) p(\sigma_f, l), \quad (\text{A.3})$$

where $p(\sigma_f, l|\mathbf{y})$ is given by Equation (8). Using a uniform prior over σ_f and l , the maximum posterior corresponds to the maximum of the marginal likelihood (Equation (8)).

References

- [1] Schweinzer J, Wolfrum E, Aumayr F, Pockl M, Winter H, Schorn R P, Hintz E and Unterreiter A 1992 *Plasma Physics and Controlled Fusion* **34** 1173–1183 ISSN 0741-3335 URL <http://stacks.iop.org/0741-3335/34/i=7/a=001?key=crossref.e4b9c6ae537d1b369f9bde3eda4a299b>
- [2] Wolfrum E, Aumayr F, Wutte D, Winter H, Hintz E, Rusbüldt D and Schorn R P 1993 *Review of Scientific Instruments* **64** 2285–2292 ISSN 0034-6748 URL <http://aip.scitation.org/doi/10.1063/1.1144460>
- [3] Fischer R, Wolfrum E and Schweinzer J 2008 *Plasma Physics and Controlled Fusion* **50** 085009 ISSN 0741-3335 URL <http://stacks.iop.org/0741-3335/50/i=8/a=085009?key=crossref.66dc3a9cef01c87d8417ae7a2c0d3d6a>
- [4] Pietrzyk Z A, Breger P and Summers D D R 1993 *Plasma Physics and Controlled Fusion* **35** 1725–1744 ISSN 0741-3335 URL <http://stacks.iop.org/0741-3335/35/i=12/a=006?key=crossref.ca847185a7856a170f0b1b1af27e0fa8>
- [5] Brix M, Dodt D, Korotkov A, Morgan P, Dunai D, Fischer R, Meigs A, Nedzelskiy I S, Schweinzer J, Vince J and Zoletnik S 2010 *Review of Scientific Instruments* **81** 10D733 ISSN 0034-6748 URL <http://aip.scitation.org/doi/10.1063/1.3502320>
- [6] Brix M, Dodt D, Dunai D, Lupelli I, Marsen S, Melson T F, Meszaros B, Morgan P, Petravich G, Refy D I, Silva C, Stamp M, Szabolics T, Zastrow K D and Zoletnik S 2012 *Review of Scientific Instruments* **83** 10D533 ISSN 00346748 URL <http://aip.scitation.org/doi/10.1063/1.4739411>
- [7] Schorn R P, Hintz E, Rusbüldt D, Aumayr F, Schneider M, Unterreiter E and Winter H 1991 *Applied Physics B Photophysics and Laser Chemistry* **52** 71–78 ISSN 0721-7269 URL <http://link.springer.com/10.1007/BF00357658>
- [8] Rasmussen C E and Williams C K I 2006 *Gaussian Processes for Machine Learning* (MIT Press)
- [9] Svensson J 2011 *JET report, EFDA-JET-PR(11)24* URL <http://www.euro-fusionscipub.org/wp-content/uploads/eurofusion/EFDP11024.pdf>
- [10] Svensson J and Werner A 2007 Large Scale Bayesian Data Analysis for Nuclear Fusion Experiments *2007 IEEE International Symposium on Intelligent Signal Processing* (IEEE) pp 1–6 ISBN 978-1-4244-0829-0 URL <http://ieeexplore.ieee.org/document/4447579/>
- [11] von Nessi G T, Hole M J, Svensson J and Appel L 2012 *Physics of Plasmas* **19** 012506 ISSN 1070-664X URL <http://aip.scitation.org/doi/10.1063/1.3677362>
- [12] Romero J and Svensson J 2013 *Nuclear Fusion* **53** 033009 ISSN 0029-5515 URL <http://stacks.iop.org/0029-5515/53/i=3/a=033009?key=crossref.e63bc2641d1ea5a6766bf4b0dc1db9ee>
- [13] Li D, Svensson J, Thomsen H, Medina F, Werner A and Wolf R 2013 *Review of Scientific Instruments* **84** 083506 ISSN 0034-6748 URL <http://aip.scitation.org/doi/10.1063/1.4817591>
- [14] Schmuck S, Svensson J, De La Luna E, Figini L, Johnson T, Alper B, Beurskens M, Fessey J, Gerbaud T and Sirinelli A 2011 Bayesian derivation of electron temperature profile using jet ece diagnostics *38th EPS Conference on Plasma Physics 2011, EPS 2011 : Europhysics Conference Abstracts (Europhysics Conference Abstracts no 35:2)* pp 1512–1515 qC 20140828
- [15] Chilenski M, Greenwald M, Marzouk Y, Howard N, White A, Rice J and Walk J 2015 *Nuclear Fusion* **55** 023012 ISSN 0029-5515 URL <http://stacks.iop.org/0029-5515/55/i=2/a=023012?key=crossref.b22d32b1ac570adef0ea0869bc2c1789>
- [16] von Nessi G T and Hole M J 2013 *Journal of Physics A: Mathematical and Theoretical* **46** 185501 ISSN 1751-8113 URL <http://stacks.iop.org/1751-8121/46/i=18/a=185501?key=crossref.085e8f9015638d2a9f8beb329833774a>
- [17] Svensson J and Werner A 2008 *Plasma Physics and Controlled Fusion* **50** 085002 ISSN 07413335 URL <http://stacks.iop.org/0741-3335/50/i=8/a=085002?key=crossref.8b9e7d2d10e66d8a740fcec9ab77227d>

4.2 Article II

'Bayesian electron density inference from JET lithium beam emission spectra using Gaussian processes'

S. KWAK, J. SVENSSON, M. BRIX and Y.-C. GHIM

Nuclear Fusion, Vol. 57:3 (11th Jan. 2017), DOI: 10.1088/1741-4326/aa5072

Bayesian electron density inference from JET lithium beam emission spectra using Gaussian processes

Sehyun Kwak^{1,2†}, J. Svensson^{2,‡}, M. Brix³, Y.-c. Ghim^{1*} and JET Contributors[‡]

EUROfusion Consortium, JET, Culham Science Centre, Abingdon, OX14 3DB, UK

¹ Department of Nuclear and Quantum Engineering, KAIST, Daejeon 34141, Republic of Korea

² Max-Planck-Institut für Plasmaphysik, 17491 Greifswald, Germany

³ Culham Centre for Fusion Energy, Culham Science Centre, Abingdon OX14 3DB, UK

E-mail: [†]slayer313@kaist.ac.kr, [‡]jakobsemail@gmail.com,

*ycghim@kaist.ac.kr

Postprint

Abstract. A Bayesian model to infer edge electron density profiles is developed for the JET lithium beam emission spectroscopy (Li-BES) system, measuring Li I (2p-2s) line radiation using 26 channels with ~ 1 cm spatial resolution and 10 \sim 20 ms temporal resolution. The density profile is modelled using a Gaussian process prior, and the uncertainty of the density profile is calculated by a Markov Chain Monte Carlo (MCMC) scheme. From the spectra measured by the transmission grating spectrometer, the Li I line intensities are extracted, and modelled as a function of the plasma density by a multi-state model which describes the relevant processes between neutral lithium beam atoms and plasma particles. The spectral model fully takes into account interference filter and instrument effects, that are separately estimated, again using Gaussian processes. The line intensities are inferred based on a spectral model consistent with the measured spectra within their uncertainties, which includes photon statistics and electronic noise. Our newly developed method to infer JET edge electron density profiles has the following advantages in comparison to the conventional method: (i) providing full posterior distributions of edge density profiles, including their associated uncertainties, (ii) the available radial range for density profiles is increased to the full observation range (~ 26 cm), (iii) an assumption of monotonic electron density profile is not necessary, (iv) the absolute calibration factor of the diagnostic system is automatically estimated overcoming the limitation of the conventional technique and allowing us to infer the electron density profiles for all pulses without preprocessing the data or an additional boundary condition, and (v) since the full spectrum is modelled, the procedure of modulating the beam to measure the background signal is only necessary for the case of overlapping of the Li I line with impurity lines.

[‡] See the Appendix of F. Romanelli et al., Proceedings of the 25th IAEA Fusion Energy Conference 2014, Saint Petersburg, Russia

Keywords: Bayesian inference, Forward modelling, Gaussian processes, Plasma diagnostics, Joint European Torus, Beam emission spectroscopy

1. Introduction

Edge electron density profiles have been recognised as one of the key physical quantities in magnetic confinement devices for controlling and understanding edge plasma phenomena, such as edge localised modes (ELMs) [1], L-H transitions [2] and turbulence transport [3]. Lithium beam emission spectroscopy (Li-BES) systems, capable of providing the profiles of edge electron density, have thus been widely used at various devices (TEXTOR [4, 5], ASDEX Upgrade [6, 7], W7-AS [6], and JET [8, 9, 10]). Li-BES system is a type of beam diagnostics that injects neutral lithium atoms into the plasma and measures Li I (2p-2s) line radiation caused by spontaneous emission processes from the first excited state (1s2 2p1) to the ground state (1s2 2s1) of the neutral lithium beam atoms. The Li I line intensity can be expressed as a function of the plasma density by a multi-state model [11] which describes the relevant processes between lithium atoms and plasma particles. The profiles of edge electron density can be inferred from the measured profiles of the Li I line intensity.

The integral expression of the multi-state model which calculates a profile of electron density [4] from the measured Li-BES data has been used conventionally at many devices [5, 6, 8, 9]. This method, however, has a limitation that profiles of absolute electron density (based on the absolute calibration factor) can be obtained only if either a *singular point*§ is found or an additional boundary condition is provided in the data. Consequently, this method involves some weaknesses: (i) preprocessing of the data is usually required to find the singular point, (ii) the singular point cannot be found accurately, (iii) a small change of the location of the singular point can cause a large difference of the density profile and iv) an additional boundary condition, which is required if the singular point does not exist, cannot be properly fixed because of the difficulty of obtaining all the populations of the different states of the neutral Li beam atoms. Another method utilising Bayesian probability theory to analyse the Li-BES data was reported at ASDEX Upgrade [7], using non-spectral APD (Avalanche Photo Diode) detectors and made impressive progress. Our method fits the full Li beam emission spectrum and uses Gaussian processes to model and regularise the electron density profiles, rather than using the non-spectral data and the combination of splines with a regularising *weak* monotonicity constraint used in [7]. Our proposed method requires neither preprocessing of the data, inner boundary information nor a profile monotonicity regulariser.

The method comprises two parts. The first part is obtaining the profile of the Li I line intensity. The JET Li beam emission spectrum is here modelled as a single Li I emission line and a background signal, convolved with an instrument function and filtered through an interference filter. The interference filter and instrument function need to be

§ This is a specific spatial point where both the numerator and the denominator of the integral expression of the multi-state model (see Eq.(4) in [4]) for the electron density become zero.

separately estimated and the uncertainties on the spectra are modelled by taking into account photon statistics and electronic noise. We infer interference filter and instrument functions based on separate measurements (which are required only once in a while as they do not vary much shot-to-shot base) using Gaussian processes. We use Gaussian processes because we do not know the parametric form, i.e., analytical expression of these functions. Having the interference filter and instrument functions, we then infer intensities of the Li I line radiation, background and the offset simultaneously. This provides the advantage of removing the necessity of beam modulations to obtain separate background measurements within a plasma shot. Furthermore, as the fitted background intensity is likely to be dominated by Bremsstrahlung radiation, our method opens a possibility to obtain the effective charge Z_{eff} . The second part of our method infers the profile of edge electron density based on the intensity profile of Li I line radiation using the multi-state model. During this second part, the absolute calibration factor of the system is inferred directly from the measurements, removing the need for the singular-point method mentioned above. All modelling and analyses are performed using a Bayesian scheme within the Minerva framework [12].

Section 2 describes the models we use: the multi-state model describing how to obtain electron density information from the Li I line radiation intensity and the spectral model of the raw data, forming together the forward model of the JET Li-BES system. Section 3 explains how the interference filter and instrument functions are inferred and the procedure for obtaining the intensity of the Li I line radiation and electron density profile. Conclusions are presented in Section 4.

2. Models

2.1. Multi-state model

Li-BES system measures the intensities of the Li I (2p-2s) line radiation from the neutral lithium beam penetrating into the plasma. The Li I line radiation is produced by spontaneous emission processes from the first excited state (1s2 2p1) to the ground state (1s2 2s1) of the neutral lithium beam atoms. The Li I line intensity is a function of a population of the first excited state which can be expressed in terms of a plasma density via a multi-state model.

The change of relative populations in time using the multi-state (collisional-radiative) model [4] is

$$\frac{dN_i(t)}{dt} = \sum_{j=1}^{M_{\text{Li}}} \left[\sum_s n_s a_{ij}^s(v_r^s) + b_{ij} \right] N_j, \quad (1)$$

which describes population and de-population of states of the neutral lithium atoms caused by processes between lithium beam atoms and plasma particles in addition to spontaneous emissions. N_i is a *relative* population of the i^{th} state with respect to the total number of the neutral lithium beam atoms at the position where the lithium beam enters the vacuum vessel. For instance, $N_1 = 0.7$ and $N_2 = 0.1$ mean that 70 % and 10

% of the initial neutral lithium beam atoms are in the ground and first excited states, respectively. M_{Li} is the number of states of the neutral lithium atoms, and we consider nine different states in this paper; thus, $M_{\text{Li}} = 9$. n_s is a plasma density of species s where $s = e$ and $s = p$ denote electron and proton, respectively. a_{ij}^s ($i \neq j$) > 0 is a net population rate coefficient by the plasma species s from the j^{th} state to the i^{th} state increasing the relative population of the i^{th} state, while $a_{ii}^s < 0$ is a net de-population rate coefficients including excitation, de-excitation and ionisation effects leaving the i^{th} state. All population and de-population rate coefficients caused by plasma species s depend on the relative speed between the neutral lithium beam atoms and plasma species s which is denoted as v_r^s . b_{ij} is the spontaneous emission rate coefficient or Einstein coefficient.

It becomes easier to solve Equation (1) if it is expressed in terms of the beam coordinate z : $d/dt = d/dz \cdot dz/dt$. Realising that dz/dt is the velocity of the neutral lithium beam atoms v_{Li} , we obtain

$$\frac{dN_i(z)}{dz} = \frac{1}{v_{\text{Li}}} \sum_{j=1}^{M_{\text{Li}}} \left[\sum_s n_s(z) a_{ij}^s(v_r^s(z)) + b_{ij} \right] N_j(z). \quad (2)$$

Here, we assume that v_{Li} is constant over the penetration range of the beam into plasmas.

The relative speed $v_r^s(z)$ is not directly measured but can be approximated using other quantities. The relative speed between the neutral lithium beam atoms and electrons $v_r^e(z)$ is dominated by the electron temperature T_e since the typical (thermal) speed of electrons is much faster than that of the neutral lithium beam atoms. The relative speed between the neutral lithium beam atoms and protons $v_r^p(z)$ can be approximated to the lithium beam velocity in case of JET Li-BES since the lithium beam energy is ~ 55 keV which is much higher than the ion temperature. Other species are not considered in this work. Thus, the multi-state model becomes

$$\frac{dN_i(z)}{dz} = \frac{1}{v_{\text{Li}}} \sum_{j=1}^{M_{\text{Li}}} [n_e(z) a_{ij}^e(T_e(z)) + n_p(z) a_{ij}^p(v_{\text{Li}}) + b_{ij}] N_j(z), \quad (3)$$

$$N_i(z=0) = \delta_{1i}, \quad (4)$$

with the initial condition Equation (4) where we assume that all the lithium beam atoms are neutral and in the ground state ($i = 1$) at the initial position where the beam enters the tokamak vacuum vessel corresponding to $z = 0$, i.e., $N_1(z=0) = 1$.^{||} The rate coefficients have been obtained from the Atomic Data Analysis Structure (ADAS) [13] and the reference [14]. Figure 1 shows an example of steady-state relative populations for the first excited state N_2 as a function of electron density and temperature with a beam energy of 50 keV.

^{||} As discussed in [7] where a sensitivity of the reconstructed density profile on the initial condition has been examined, less than 2% discrepancy on the initial condition does not significantly alter the density profile, i.e., changes are within the uncertainties of the profile. Furthermore, larger discrepancies on the initial condition cannot explain the observed data [7]; thereby providing us a mean to reject a certain initial condition.

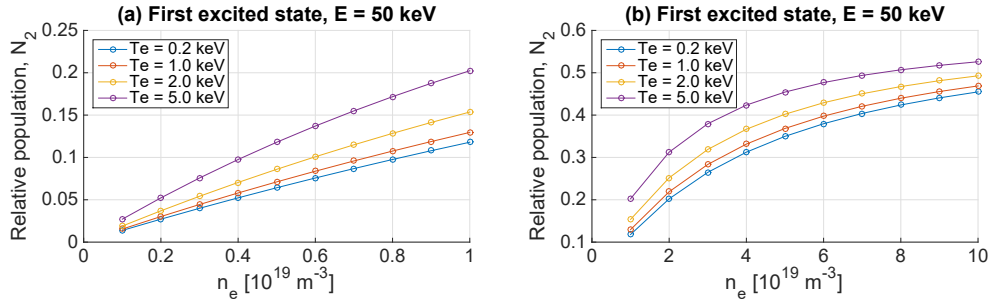


Figure 1. Steady-state relative populations of the first excited state (N_2) of the neutral lithium beam atoms as a function of the electron density and temperature with a beam energy of 50 keV in the range of (a) $0.1 \times 10^{19} < n_e < 1.0 \times 10^{19}$ and (b) $1.0 \times 10^{19} < n_e < 10.0 \times 10^{19}$.

Note that this multi-state model does not consider the population of ionised lithium atoms, which leave the beam due to a strong magnetic field of JET. Therefore, electron loss processes such as ionisation and charge-exchange simply attenuate the total population of the neutral lithium beam atoms, i.e., $\sum_{j=1}^{M_{\text{Li}}} N_j (z > 0) < 1$.

2.2. Spectral model

The JET Li-BES system measures spectra, including the Doppler shifted Li I line radiation from the 26 different spatial positions, covering a few nanometres in wavelength using the transmission grating spectrometer (dual entrance slit with interference filter for preselection of passband, details in [10]). A charge coupled device (CCD) camera detects the photons for integration time of approximately 10 ms. More detailed description of the JET Li-BES system can be found elsewhere [9, 10].

A spectrum from each spatial position contains four types of signals (in addition to noise): (i) Li I line, (ii) a background dominated by Bremsstrahlung radiation, (iii) an offset and (iv) impurity lines. Doppler broadening of the Li I line radiation is negligible since the lithium beam is a mono-energetic beam (~ 0.02 nm broadening occurs for the beam temperature of ~ 10 eV, and the dispersion of the CCD pixel is ~ 0.04 nm/pixel), therefore we treat the Li I line as a delta function in the spectrum. A measured spectrum $S(\lambda)$ from each spatial position can be expressed as

$$S(\lambda) = F(\lambda) [C(\lambda) A + B] + Z, \quad (5)$$

where A is the intensity of Li I line radiation, B the background level and Z the offset, which are all inferred together with their uncertainties through Bayesian inference. The instrument function $C(\lambda)$ and interference filter function $F(\lambda)$ are inferred through a Bayesian scheme using Gaussian processes from separate measurements [15]. Here, λ is the wavelength corresponding to a CCD pixel index [9].

Gaussian processes are probabilistic functions defined by a multivariate Gaussian distribution, generalization of a multivariate normal distribution to function space, whose

mean and covariance function specify the expected values and relationship between any two points on the domain [16]. This constrains the variability of the function without any analytic specification, i.e., in a non-parametric way. Gaussian processes were introduced in the fusion community in [17] and are implemented as a standard representation of profile quantities in the Minerva framework [12]. It has been used for current tomography [17, 18], soft x-ray tomography [19], and representing profile quantities [17, 20, 21]. The covariance function of a Gaussian process is defined as a parametrised function whose parameters, so called *hyperparameters*, determine aspects of the function such as overall scale and length scale. The hyperparameters are selected based on the measurements by maximising the *evidence* through Bayesian model selection. A detailed description of the Bayesian inference and modelling of the JET Li-BES data with Gaussian process can be found elsewhere [15].

2.3. Forward model

Our goal is to find all possible profiles of the edge electron density n_e consistent with the spectral observations. For this, we consider the forward model as shown in Figure 2. The edge electron density profile n_e is modelled as a set of values at given positions, with a prior given by a Gaussian process with given overall scale and length scale hyperparameters, discussed in more detail in Section 3.3. Edge n_e profiles are mapped onto flux surface coordinates ψ calculated by the EFIT equilibrium code [22]. Electron temperature T_e , required for the rate coefficients a_{ij}^s , is measured by the High Resolution Thomson Scattering (HRTS) system [23] and mapped onto the same flux surface coordinates. This will allow us to calculate a relative population of the first excited state of the neutral lithium beam atoms, i.e., N_2 , based on the multi-state model Equation (3) with a quasi-neutrality condition, i.e., $n_e = n_p$. Here, we assume that impurity densities are low enough to be ignored¶.

Once we have N_2 , we can predict the Li I line radiation intensity, A in Equation (5), where the detailed procedure is provided in Section 2.3.1. This model provides a prediction of the measured Li I line radiation A_* , given the free parameters of an electron density n_e and an absolute calibration factor α , by

$$p(A_*|n_e, \alpha) = \frac{1}{\sqrt{2\pi}\sigma} \exp \left[-\frac{(A_* - A(n_e, \alpha))^2}{2\sigma^2} \right], \quad (6)$$

where $A(n_e, \alpha)$ is a model prediction with specific values of the free parameters, n_e and α . σ is the uncertainty associated with the observation A_* . This is our basic form of the forward model in this paper and is the *likelihood* in Bayes formula (Equation (16)). We assume that deviations of the observation from predictions have a Gaussian distribution. We discuss how we estimate σ and rationale to form Gaussian distributed deviations in Section 2.3.2.

¶ If impurities are non-negligible, then our measured spectra may show strong impurity line radiation in which case our assumption is not valid.

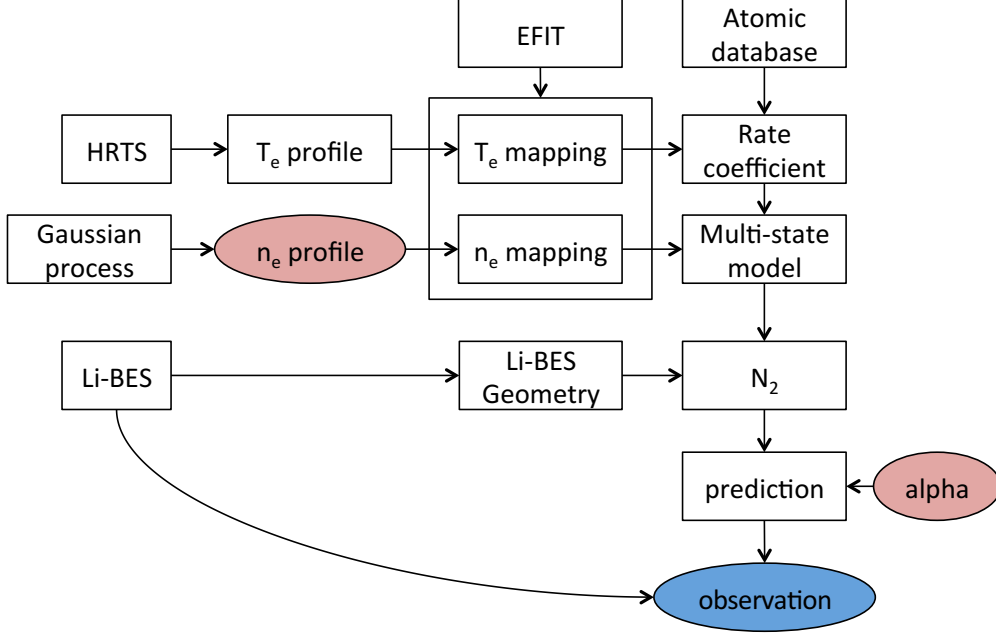


Figure 2. A simplified graphical representation of the JET Li-BES forward model as implemented in the Minerva Bayesian modelling framework [12]. The free parameters are shown with red circles and observations as a blue circle. The rectangular boxes represent operations or constants. The electron density n_e and temperature T_e are mapped onto the EFIT estimated flux surfaces. The relative populations of the neutral lithium beam atoms are calculated from the multi-state model, and profiles of the Li I line radiation intensities are predicted given edge n_e profiles and an absolute calibration factor, alpha (α). All the possible edge n_e profiles whose predicted Li I line intensity profile agree with the observation (blue circle) within their uncertainties are found through a MCMC scheme.

2.3.1. Detected number of photons The Li I line intensity, A in Equation (5), is proportional to the relative population of the first excited state N_2 , i.e., $A \propto b_{12}N_2$ where b_{12} is the spontaneous emission rate coefficient from the first state to the ground state. Change of the relative population of the first excited state due to the spontaneous emission as the beam travels a distance of Δz denoted as $|\Delta N_2|$ is

$$|\Delta N_2(z)| = \frac{|b_{12}|}{v_{\text{Li}}} \Delta z N_2(z), \quad (7)$$

where Δz can be considered as the observation length. Since one spontaneous emission produces one photon, the total number of emitted photons $N_{\text{ph}}^{\text{em}}$ corresponding to Li I

line radiation over the integration time Δt with the lithium beam current I_{Li} is

$$N_{\text{ph}}^{\text{em}}(z) = I_{\text{Li}} \Delta t |\Delta N_2(z)| = I_{\text{Li}} \Delta t \frac{|b_{12}|}{v_{\text{Li}}} \Delta z N_2(z). \quad (8)$$

The emitted photons falling into the solid angle of the collection optics pass through various mirrors, lens and grism before being detected by the CCD camera. We denote all these effects of optics including the solid angle as an effective transmittance of the system, T . Then, the number of photons detected by (or arrived to) the CCD camera $N_{\text{ph}}^{\text{det}}(z)$ is

$$N_{\text{ph}}^{\text{det}}(z) = T N_{\text{ph}}^{\text{em}}(z) = T I_{\text{Li}} \Delta t \frac{|b_{12}|}{v_{\text{Li}}} \Delta z N_2(z). \quad (9)$$

Also, we define Q as the count per photon of the CCD camera. Q describes the number of counts produced by the CCD camera when one photon arrives at the CCD detector. Then, the CCD output count due to the Li I line radiation $N_{\text{CCD}}^{\text{Li}}$ which we measure is

$$\begin{aligned} N_{\text{CCD}}^{\text{Li}}(z) &= Q N_{\text{ph}}^{\text{det}}(z) = Q T I_{\text{Li}} \Delta t \frac{|b_{12}|}{v_{\text{Li}}} \Delta z N_2(z) \\ &= A(z) \int F(\lambda) C(\lambda) d\lambda, \end{aligned} \quad (10)$$

and this is, by definition, equal to the Li I line intensity A multiplied by the spectrally integrated signal of the instrument function $C(\lambda)$ and the interference filter function $F(\lambda)$ in Equation (5).

We finally obtain

$$A(z) = \underbrace{\frac{Q T I_{\text{Li}} \Delta t \frac{|b_{12}|}{v_{\text{Li}}} \Delta z}{\int F(\lambda) C(\lambda) d\lambda}}_{\equiv \alpha} N_2(z) = \alpha N_2(z), \quad (11)$$

where α is the absolute calibration factor which is taken as a free parameter in our forward model in addition to the n_e profile as shown in Figure 2. Note that we have included the magnitude of the relative calibration factors in the instrument function $C(\lambda)$.

2.3.2. Uncertainties The main measurement error is due to the Poisson distributed photon statistics. On top of that, there is an additional electronic noise which is measured before a pulse starts and is here taken as a Gaussian distribution.

To be able to determine a level of photon noise, it is necessary to find the value of Q in Equation (10) so that the measured $N_{\text{CCD}}^{\text{Li}}$ can be converted to the detected number of photons $N_{\text{ph}}^{\text{det}}$ which is the quantity following a Poisson distribution. With an aim of determining the value of Q , we shine a uniform intensity light-emitting diode (LED) to the CCD camera while varying the intensity of the LED with all other conditions fixed as if it were actual measurements of the Li-BES during plasma discharges. The arithmetic mean of CCD output counts \bar{N}_{CCD} and its associated variance σ_{CCD}^2 are

$$\bar{N}_{\text{CCD}} = Q \bar{N}_{\text{ph}} + \bar{N}_{\text{CCD}}^{\text{DC}} + \bar{Z}_{\text{CCD}}, \quad (12)$$

$$\sigma_{\text{CCD}}^2 = Q^2 \sigma_{\text{ph}}^2 + \sigma_e^2 \quad (13)$$

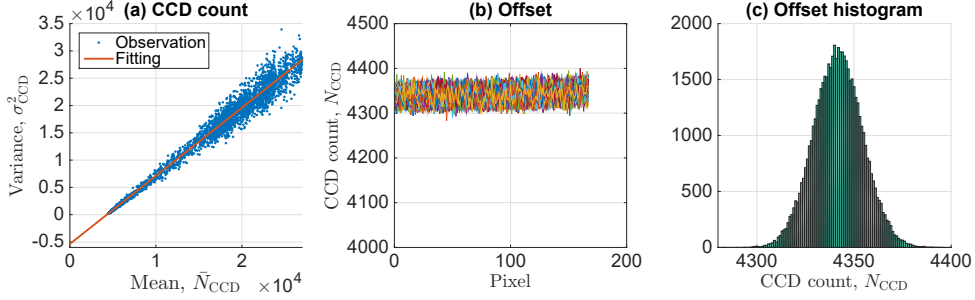


Figure 3. (a) The variance σ_{CCD}^2 vs. the mean counts \bar{N}_{CCD} of the CCD output with varying LED intensities. The slope of the fitted linear line is the value of Q which is 1.247 ± 0.005 . (b) Measurements of the CCD output counts as a function of the CCD pixel with all the electronics switched on and no input photons to the CCD, and (c) the histogram of the CCD output counts from (b). The histogram shows that (i) the variance is 160, i.e., $\sigma_e^2 \approx 160$, with the mean value of 4342 and (ii) it has a Gaussian shape.

where \bar{N}_{ph} is the mean of the number of photons detected by (arrived to) the CCD camera and $\bar{N}_{\text{CCD}}^{\text{DC}}$ the mean CCD output counts due to the dark current of the CCD. Here, \bar{Z}_{CCD} is the mean CCD offset. σ_{ph}^2 and σ_e^2 are the variances due to photon statistics and electronic noises, respectively. Note that we treat fluctuations in the dark current as a part of the electronic noise because they exist in the absence of detected photons.

With $\bar{N}_{\text{ph}} = (\bar{N}_{\text{CCD}} - \bar{N}_{\text{CCD}}^{\text{DC}} - \bar{Z}_{\text{CCD}}) / Q$ from Equation (12) and $\bar{N}_{\text{ph}} = \sigma_{\text{ph}}^2$ owing to a Poisson distribution, recasting Equation (13), we get

$$\sigma_{\text{CCD}}^2 = Q\bar{N}_{\text{CCD}} - (Q\bar{N}_{\text{CCD}}^{\text{DC}} + Q\bar{Z}_{\text{CCD}} - \sigma_e^2). \quad (14)$$

Notice that \bar{N}_{CCD} and σ_{CCD}^2 can be directly measured with the LED on, and by varying the intensity of the LED we can determine the value of Q . Figure 3(a) shows a graph of the measured σ_{CCD}^2 vs. \bar{N}_{CCD} , using a total of 4,175 (167 pixels from 25 channels) independent data points, the variances and the means which are estimated using 332 independent time points. The slope is the value of Q we seek, and we find that $Q = 1.247 \pm 0.005$.

To find the electronic noise level σ_e^2 , we switch on all the electronics and measure fluctuations in N_{CCD} without any photons to the CCD, i.e., $N_{\text{ph}} = 0$. Here, N_{CCD} and N_{ph} are individual measurements rather than their means. Figure 3(b) shows such measurements for all 26 spatial channels (different colours). Figure 3(c) is the histogram of the N_{CCD} . The variance is estimated to be 160 with a mean of 4342. Therefore, $\sigma_e^2 \approx 160$. As can be seen from the histogram, the dark current fluctuations are approximately Gaussian shaped. Furthermore, as we find the mean value of the offset, i.e., 4342, appears constantly for all channels, we always subtract this offset value from the measured signal before performing any analyses on the data. Any residual offset is captured by Z in Equation (5).

When the number of counts is large a Poisson distribution can be approximated with a Gaussian distribution. Since the detected number of photons $N_{\text{ph}}^{\text{det}}$ is larger than 100, we take the photon statistics to follow a Gaussian distribution as well. Therefore,

Expression style	Example	Meaning
Boldface	\mathbf{y}, \mathbf{S}	Column vector
Boldface with a check accent	$\check{\mathbf{K}}, \check{\mathbf{\Sigma}}$	Matrix
Plain	S, x	Scalar
Superscript index	\mathbf{y}^i, x^i	Quantity of the i^{th} channel out of the total 26 spatial positions (channels) of the JET Li-BES system
Subscript index	\mathbf{y}_i, x_i	Quantity at the i^{th} wavelength in the CCD camera

Table 1. Notations used in Section 3.

the variance σ^2 in Equation (6) is

$$\sigma^2 = \sigma_{\text{ph}}^2 + \sigma_{\text{e}}^2. \quad (15)$$

3. Bayesian inference

For our case, we have a spectrum $S(\lambda)$ described by three free parameters: the Li I line radiation intensity A , the background B dominated by Bremsstrahlung radiation, and the offset Z . The instrument function $C(\lambda)$ and the interference filter $F(\lambda)$ in Equation (5) are inferred separately using Gaussian processes.

In the Bayesian scheme, we calculate the probability distribution of a free parameter \mathcal{W} given observation \mathcal{D} known as the *posterior* $p(\mathcal{W}|\mathcal{D})$. The posterior is given by Bayes formula

$$p(\mathcal{W}|\mathcal{D}) = \frac{p(\mathcal{D}|\mathcal{W})p(\mathcal{W})}{p(\mathcal{D})}, \quad (16)$$

where $p(\mathcal{D}|\mathcal{W})$, $p(\mathcal{W})$ and $p(\mathcal{D})$ are the *likelihood*, *prior* and *evidence*, respectively. The likelihood is a model for observations given free parameters as described in Equation (6). The prior quantifies our assumptions on the free parameters before we have observations. The evidence is typically used for a model selection and is irrelevant if one is only interested in estimating the free parameters. A detailed description of Bayesian inference can be found elsewhere [24].

To minimise possible confusion, we define our notations used in this section in Table 1. As the JET Li-BES system obtains spectra from 26 different spatial positions, the channel index corresponds to the spatial position and the pixel index to the wavelength. The predicted signal at the i^{th} channel and j^{th} pixel is denoted as S_j^i , and D_j^i represents the observed signal.

Using these notations, we will find the most probable prediction of the line intensity, background and offset at i^{th} channel by calculating the posterior $p(A^i, B^i, Z^i|\mathbf{D}^i)$ where the predicted signal at the i^{th} channel and j^{th} pixel is

$$S_j^i = F_j^i (C_j^i A^i + B^i) + Z^i. \quad (17)$$

In the following subsections, we describe how to infer two unknown functions, the interference filter and instrument functions ($\mathbf{F}^i, \mathbf{C}^i$), and the free parameters (A^i, B^i, Z^i).

3.1. Interference filter and instrument functions

To infer the i^{th} channel interference filter function \mathbf{F}^i , we illuminate uniform LED light to the fibres. Since there is no Li I line radiation (A^i) with a negligible offset (Z^i) as shown in Figure 4, the predicted signal is

$$S_j^i = F_j^i (C_j^i A^i + B^i) + Z^i = F_j^i B^i, \quad (18)$$

where B^i is uniform LED light intensity. According to Bayes formula, the posterior is

$$p(\mathbf{F}^i | \mathbf{D}^i) \propto p(\mathbf{D}^i | \mathbf{F}^i) p(\mathbf{F}^i), \quad (19)$$

where the likelihood is

$$p(\mathbf{D}^i | \mathbf{F}^i) = \frac{1}{\sqrt{(2\pi)^{N_{\text{pixel}}} |\check{\Sigma}|}} \exp \left[-\frac{1}{2} (\mathbf{D}^i - \mathbf{S}^i)^T \check{\Sigma}^{-1} (\mathbf{D}^i - \mathbf{S}^i) \right]. \quad (20)$$

Here, $\mathbf{S}^i = \mathbf{F}^i B^i$ as in Equation (18), and N_{pixel} is the total number of CCD pixels for the i^{th} channel. $\check{\Sigma}$ is an $N_{\text{pixel}} \times N_{\text{pixel}}$ square diagonal matrix containing variances of the measured signal at each pixel of the CCD camera as in

$$\check{\Sigma} = \begin{bmatrix} \sigma_1^2 & & & & & \\ & \sigma_2^2 & & & & \\ & & \dots & & & \\ & & & \sigma_j^2 & & \\ & & & & \dots & \\ & & & & & \sigma_{N_{\text{pixel}}}^2 \end{bmatrix}, \quad (21)$$

where $\sigma_j^2 = \sigma_{\text{ph},j}^2 + \sigma_{\text{e},j}^2$ at the j^{th} pixel as Equation (15) is used in Equation (6). $\sigma_{\text{ph},j}^2$ and $\sigma_{\text{e},j}^2$ can be estimated as described in Section 2.3.2. Note that $\check{\Sigma}$ is different for different channels.

The prior $p(\mathbf{F}^i)$ in Equation (19) needs to be specified. Since we do not know the parametric form, i.e., analytical form, describing the interference filter of the i^{th} channel, \mathbf{F}^i , as a function of wavelength (pixel index), we use a Gaussian process prior for \mathbf{F}^i :

$$p(\mathbf{F}^i) = \frac{1}{\sqrt{(2\pi)^{N_{\text{pixel}}} |\check{\mathbf{K}}|}} \exp \left[-\frac{1}{2} (\mathbf{F}^i - \mathbf{0})^T \check{\mathbf{K}}^{-1} (\mathbf{F}^i - \mathbf{0}) \right]. \quad (22)$$

Here, $\mathbf{0}$ is a column vector whose entries are all zeros. The $N_{\text{pixel}} \times N_{\text{pixel}}$ matrix $\check{\mathbf{K}}$, which varies channel by channel, is defined as a squared exponential covariance function with the value at the j^{th} row and k^{th} column of

$$K_{jk} = \sigma_f^2 \exp \left[-\frac{1}{2\ell^2} |x_j - x_k|^2 \right] + \sigma_n^2 \delta_{jk}. \quad (23)$$

δ_{jk} is the Kronecker delta. \mathbf{x} is a vector of the CCD pixel index, thus $|x_j - x_k|$ is the difference in pixel index between the j^{th} and k^{th} pixels. σ_f^2 is the signal variance

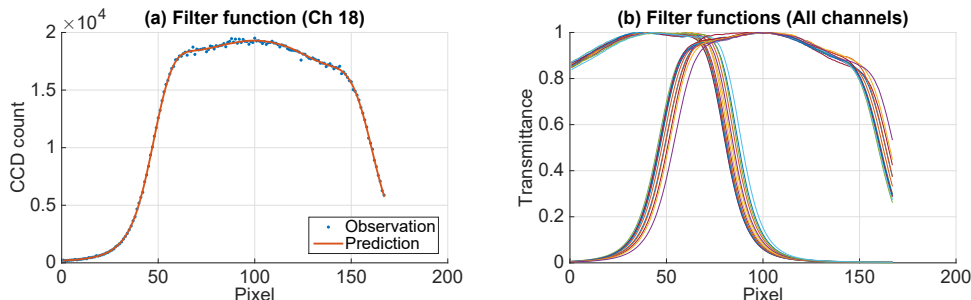


Figure 4. (a) The observation (dots) and the MAP estimate of the filter function (red line) for channel 18 using Bayes formula with the Gaussian process prior, showing a good agreement between the two. (b) Normalised filter functions (MAP) for all channels shown in different colours.

and ℓ the length scale. σ_n^2 is a small number for the numerical stability during matrix inversion. The hyperparameters σ_f^2 and ℓ govern the characteristic of the Gaussian process Equation (22), and we find their values by maximising the evidence $p(\mathbf{D}^i)$, more explicitly $p(\mathbf{D}^i|\sigma_f, \ell)$. More detailed description can be found elsewhere [15].

Figure 4(a) shows the comparison between the observation \mathbf{D}^i and the maximum a posteriori (MAP) estimate of \mathbf{F}^i for channel 18. Figure 4(b) shows the MAP estimates of the filter functions for all channels of the JET Li-BES system. Note that we normalise all the filter functions to have the maximum value of one as what we need is the *shape* of the filter functions in the wavelength (pixel index) domain. This does not create any problems because relative sensitivities among the channels are captured by the instrument functions as relative calibration factors, while α in Equation (11) takes care of the absolute calibration factor.

To infer the i^{th} channel instrument function \mathbf{C}^i , we use beam-into-gas shots. During the beam-into-gas shots, neutral lithium beam atoms are injected into the tokamak filled with a neutral deuterium gas whose pressure is less than 10^{-4} mbar. Because there is no plasma, there exists a negligible background signal caused by Bremsstrahlung ($B^i = 0$). For this case, the posterior is $p(\mathbf{C}^i|\mathbf{D}^i)$ with

$$S_j^i = F_j^i (C_j^i A^i + B^i) + Z^i = F_j^i C_j^i A^i + Z^i, \quad (24)$$

where the interference filter function \mathbf{F}^i is set to be the MAP estimation of $p(\mathbf{F}^i|\mathbf{D}^i)$ in Equation (19). Due to the small deuterium pressure inside the tokamak during the beam-into-gas experiments, a strong beam attenuation is not expected. According to [9], there is no indication of any beam attenuation, so the emitted photons N_{ph}^{em} should not vary along the beam. The variation of the observed intensities must therefore be due to differences in T , Q , and Δz in Equation (11). Assuming the Li I line emission is constant over the beam, \mathbf{C}^i will give us these relative calibration factors. Since the offset is not negligible for some channels as shown in Figure 5, i.e., a few channels have maximum amplitudes of less than 500 with the offset level of approximately 20, we calculate posterior of both instrument function and offset $p(\mathbf{C}^i, Z^i|\mathbf{D}^i)$.

The likelihood $p(\mathbf{D}^i|\mathbf{C}^i, Z^i)$ is taken as the Gaussian with the mean given by

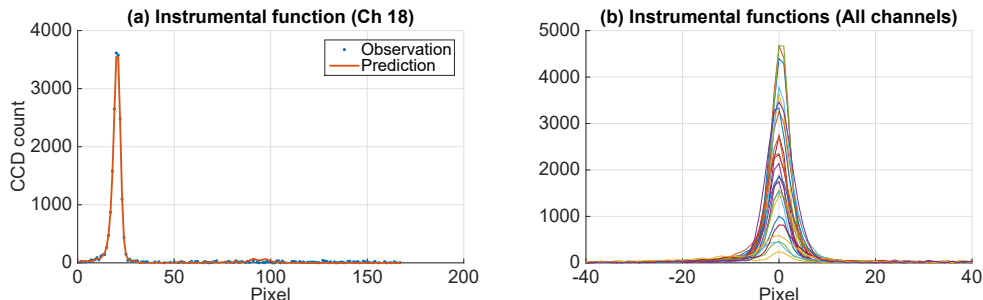


Figure 5. (a) The observation (dots) and the MAP estimate of the instrumental function (red line) for the channel 18. (b) The instrument functions (MAP) for all channels shown in different colours. Note that the instrument functions are not normalised in order to capture the relative sensitivities.

Equation (24). We let the prior $p(\mathbf{C}^i)$ to have the form of Equation (22) with the covariance function Equation (23). Again, the hyperparameters are set such that the evidence is maximised. The prior $p(Z^i)$ is a normal distribution with a zero mean and a very large variance (10^6). Figure 5(a) compares the observation and instrument function (MAP) for channel 18. Figure 5(b) shows the instrument functions (MAP) for all channels, which also capture the relative calibration factors.

3.2. Line intensities

We inferred \mathbf{F}^i and \mathbf{C}^i from Section 3.1 and are left with three free parameters A^i , B^i and Z^i in Equation (17). The posterior $p(A^i, B^i, Z^i | \mathbf{D}^i)$ is calculated using a Gaussian likelihood $p(\mathbf{D}^i | A^i, B^i, Z^i)$ with the mean of $S_j^i = F_j^i (C_j^i A^i + B^i) + Z^i$. As we have three independent free parameters, the prior $p(A^i, B^i, Z^i)$ is

$$p(A^i, B^i, Z^i) = p(A^i) p(B^i) p(Z^i), \quad (25)$$

where all three priors are Gaussian distributions with a zero mean and very large variance (10^6) effectively making them flat priors (our status of complete ignorance on these parameters) as much as possible while keeping a Gaussian form for a sake of computing algorithm.

A comparison between the Li I line and background intensities (MAP) and observation at 50.260 sec of the JET shot number 87861 for channel 8 is shown in Figure 6(a). Figure 6(b) and (c) show the profiles of the Li I line and background intensities with their uncertainties (the shortest 95 % confidence interval), respectively. The edge n_e profiles are directly inferred from the Li I line intensities. The profile of background radiation in Figure 6(c) is most likely dominated by Bremsstrahlung emission, so could be used for inferring the effective charge Z_{eff} , since Bremsstrahlung intensities are proportional to Z_{eff} ($I_{\text{Brem}} \propto Z_{\text{eff}}^2 n_e^2 T_e^{1/2}$).

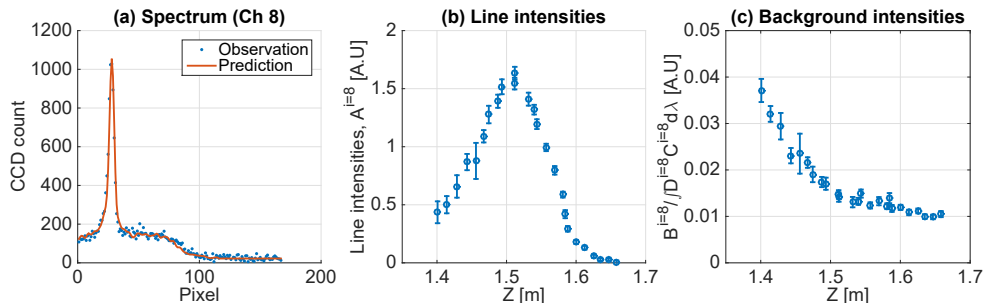


Figure 6. (a) The measured spectrum (dots) and its MAP estimate at 50.260 sec of the shot number 87861 for channel 8. The profile of (b) Li I line and (c) background intensities (MAP) with their variances.

3.3. Edge electron density profiles

To infer the electron density profile, we take the MAP estimate of the Li I line intensities with their variances ($\mathbf{A} \pm \sigma_{\mathbf{A}}$). The posterior is given by

$$p(\mathbf{n}_{\mathbf{e}}, \alpha | \mathbf{A}, \sigma_{\mathbf{A}}) \propto p(\mathbf{A} | \sigma_{\mathbf{A}}, \mathbf{n}_{\mathbf{e}}, \alpha) p(\mathbf{n}_{\mathbf{e}}, \alpha), \quad (26)$$

where the absolute calibration factor α and the edge electron density profile $\mathbf{n}_{\mathbf{e}}$ are the free parameters.

The likelihood $p(\mathbf{A} | \sigma_{\mathbf{A}}, \mathbf{n}_{\mathbf{e}}, \alpha)$ is given by

$$p(\mathbf{A} | \sigma_{\mathbf{A}}, \mathbf{n}_{\mathbf{e}}, \alpha) = \frac{1}{\sqrt{(2\pi)^{N_{\text{ch}}} |\check{\Sigma}_{\mathbf{A}}|}} \exp \left[-\frac{1}{2} (\mathbf{A} - \alpha \mathbf{N}_2)^T \check{\Sigma}_{\mathbf{A}}^{-1} (\mathbf{A} - \alpha \mathbf{N}_2) \right], \quad (27)$$

where $N_{\text{ch}} = 26$ is the total number of the channels. $\check{\Sigma}_{\mathbf{A}}$ is the $N_{\text{ch}} \times N_{\text{ch}}$ diagonal matrix with the entry of $(\sigma_{\mathbf{A}}^i)^2$ at the i^{th} row and i^{th} column. We calculate \mathbf{N}_2 using the Runge-Kutta method (RK4) from the model Equation (3) with the initial condition Equation (4).

We give n_e and α independent priors, where $p(\alpha)$ is uniform between 1 and 1000.⁺ For $p(\mathbf{n}_{\mathbf{e}})$, based on a large database of existing profiles, we can estimate the hyperparameters for the Gaussian process prior. From this we set the hyperparameters σ_f and ℓ for the covariance matrix $\check{\mathbf{K}}$ to be 20.0 and 0.025, respectively. We note that these values for the hyperparameters are not rigorously obtained by maximising the evidence due to the requirement of too much computation time. Nevertheless, these values give good fit to the data. A possible improvement would be to marginalise over these hyperparameters as in [17].

The posterior of $\mathbf{n}_{\mathbf{e}}$ and α is explored by a Markov Chain Monte Carlo (MCMC) sampling scheme. Figure 7(a) and (c) show the MAP estimate of the edge electron

⁺ This range covers most, if not all, of cases. Note that we strictly choose a uniform distribution for α as this is one of the key parameters to obtain absolute density profiles. Furthermore, being able to infer α based on the observed data is one of the key features of our model. Therefore, we are being as unbiased as possible by using a wide uniform distribution.

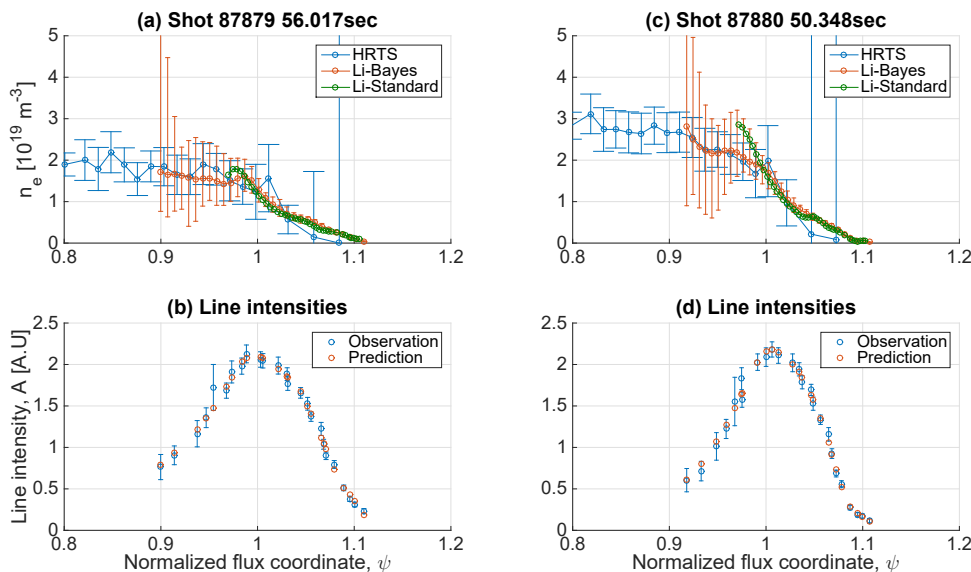


Figure 7. (a) The MAP estimate of the edge electron density profile (red) and the associated uncertainties (shortest 95% interval) together with the n_e profiles from the HRTS system (blue) and conventional Li-BES analysis (yellow). (b) the MAP estimate of the Li I intensities (blue), i.e., \mathbf{A} in Equation (26), and the prediction (red), i.e., $\alpha\mathbf{N}_2(\mathbf{n}_e)$ for the shot #87879 at 56.017 sec. (b) and (d) are same as (a) and (c) for the shot #87880 at 50.348 sec.

density profiles (red) with their associated uncertainties, which cover 95% of the samples from posterior, i.e., the shortest 95% interval. For the sake of comparison, n_e profiles from the HRTS system (blue) and results from the conventional analysis of the JET Li-BES system (yellow) [9, 10] are also shown in the same figures. Figure 7(b) and (d) show the MAP estimates of the Li I line intensities from the previous section (blue), i.e., \mathbf{A} in Equation (26), and prediction (red), i.e., $\alpha\mathbf{N}_2$, for Figure 7(a) and (c), respectively.

It is clear from these results that we have inferred a proper absolute calibration factor α even though we have not used the singular point method [4]. The range of the density profile inference has been extended to the full observation range which was not possible with the conventional data analysis method. We stress that we have not used a separate background measurement via Li neutral beam modulations because our method is capable of providing intensities of Li I line and background radiations simultaneously. Finally, we also have not made an assumption of monotonic profile, either.

In some cases, we observe a difference between the profiles inferred from the Li-BES and HRTS systems (Figure 8). Calibration of the spatial position for the Li-BES may be questioned. However, this calibration is performed with relatively high reliability [9]. We do suspect that it may have been caused by the EFIT reconstruction. The Li-BES system injects neutral lithium beam atoms vertically from the top of the JET at major radius $R = 3.25$ m and covering the vertical position $Z = 1.67 \sim 1.40$ m approximately; whereas

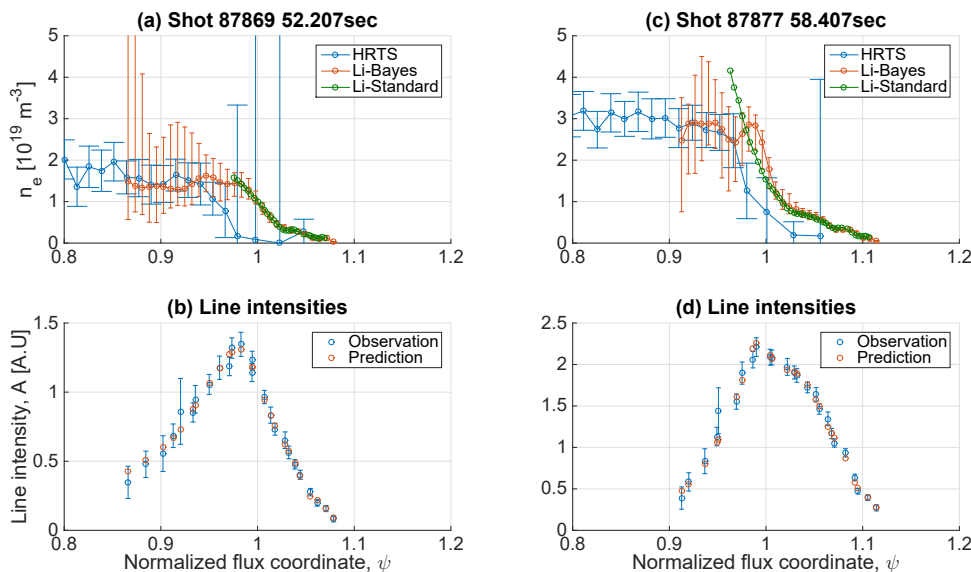


Figure 8. Same as Figure 7 for a different time and shot number, showing disagreement between the Li-BES and HRTS analysis although the prediction of the Li line intensities matches well with their MAP estimate.

the HRTS system observes electron density along the laser penetrating horizontally at the midplane ($R = 2.9 \sim 3.9$ m and $Z = 0.06 \sim 0.11$ m). The flux coordinate mapping provided through EFIT may well be inaccurate when comparing the midplane with the top of the vessel. We leave further investigation of this issue to future work.

In Figure 7(a) and (c) and Figure 8(a) and (c) we can see that the uncertainties of the electron densities in the inner region is larger than those of the outer region. This result cannot be explained solely by the number of detected photons as attested by Figure 7(b) and (d) and Figure 8(b) and (d). This trend of larger uncertainties in the inner region is also observed in ASDEX Upgrade [7, 25]. Here, we provide two qualitative reasons to explain this trend. As shown in Figure 1, the relative population of the first excited state N_2 becomes less sensitive to the change of n_e as it increases. Typically, n_e is larger in the inner region than the outer region, therefore the similar level of uncertainty in N_2 corresponds to a larger uncertainty of n_e in the inner region. In addition, the neutral Li beam attenuation as it penetrates into the plasmas can cause this trend of increasing uncertainties: consider two separate measurements of the absolute number of the first excited state which both give the same value of 200 ± 20 where the total number of neutral beam atoms is 500 in one case and 1000 in another case. Then, the relative population N_2 is $(200 \pm 20)/500 = 0.4 \pm 0.04$ for the former case and $(200 \pm 20)/1000 = 0.2 \pm 0.02$ for the latter case. It is evident that the former case has the larger uncertainty than the latter case even if the absolute numbers of the first excited state are the same for both cases. Therefore, the beam attenuation, i.e., decrease of the total number of beam atoms, can cause the larger uncertainty of n_e in the inner region [25]. Finally, we note that there can be additional effects from the uncertainties

of the absolute calibration factor [4, 8].

4. Conclusion

In this paper, we have presented a Bayesian model to obtain edge electron density profiles based on the measured JET Li-BES spectra. The model has been implemented in the Minerva Bayesian modelling framework. Our scheme includes uncertainties due to photon statistics and electric noise estimated from the measured data obtained with the transmission grating spectrometer. The instrument effects such as the interference filter function and instrument function are inferred from separate measurements using Gaussian processes whose hyperparameters are selected by evidence maximisation. Also the electron density profiles are modelled using Gaussian processes, whose hyperparameters are determined from the JET historical electron density profiles. Inference is done through maximisation of the posterior (MAP) and Markov Chain Monte Carlo Method (MCMC) sampling. The Li I line and background intensities are simultaneously inferred as well as their associated uncertainties, thereby eliminating extra effort of measuring background intensity via Li neutral beam modulations.

5. Acknowledgement

This work is supported by National R&D Program through the National Research Foundation of Korea (NRF) funded by the Ministry of Science, ICT and Future Planning (Grant No. 2014M1A7A1A01029835) and the KUSTAR-KAIST Institute, KAIST, Korea. This work has been carried out within the framework of the EUROfusion Consortium and has received funding from the Euratom research and training programme 2014-2018 under Grant Agreement No. 633053. The views and opinions expressed herein do not necessarily reflect those of the European Commission.

References

- [1] Zohm H 1996 *Plasma Physics and Controlled Fusion* **38** 105–128 ISSN 0741-3335 URL <https://iopscience.iop.org/article/10.1088/0741-3335/38/2/001>
- [2] Wagner F, Fussmann G, Grave T, Keilhacker M, Kornherr M, Lackner K, McCormick K, Müller E R, Stäbler A, Becker G, Bernhardt K, Ditte U, Eberhagen A, Gehre O, Gernhardt J, Gierke G v, Glock E, Gruber O, Haas G, Hesse M, Janeschitz G, Karger F, Kissel S, Klüber O, Lisitano G, Mayer H M, Meisel D, Mertens V, Murmann H, Poschenrieder W, Rapp H, Röhr H, Ryter F, Schneider F, Siller G, Smeulders P, Söldner F, Speth E, Steuer K H, Szymanski Z and Vollmer O 1984 *Physical Review Letters* **53** 1453–1456 ISSN 0031-9007 URL <https://link.aps.org/doi/10.1103/PhysRevLett.53.1453>
- [3] Carreras B 1997 *IEEE Transactions on Plasma Science* **25** 1281–1321 ISSN 00933813 URL <http://ieeexplore.ieee.org/document/650902/>
- [4] Schweinzer J, Wolfrum E, Aumayr F, Pockl M, Winter H, Schorn R P, Hintz E and Unterreiter A 1992 *Plasma Physics and Controlled Fusion* **34** 1173–1183 ISSN 0741-3335 URL <http://stacks.iop.org/0741-3335/34/i=7/a=001?key=crossref.e4b9c6ae537d1b369f9bde3eda4a299b>

- [5] Wolfrum E, Aumayr F, Wutte D, Winter H, Hintz E, Rusbüldt D and Schorn R P 1993 *Review of Scientific Instruments* **64** 2285–2292 ISSN 0034-6748 URL <http://aip.scitation.org/doi/10.1063/1.1144460>
- [6] McCormick K, Fiedler S, Kocsis G, Schweinzer J and Zoletnik S 1997 *Fusion Engineering and Design* **34-35** 125–134 ISSN 09203796 URL <https://linkinghub.elsevier.com/retrieve/pii/S0920379696006850>
- [7] Fischer R, Wolfrum E and Schweinzer J 2008 *Plasma Physics and Controlled Fusion* **50** 085009 ISSN 0741-3335 URL <http://stacks.iop.org/0741-3335/50/i=8/a=085009?key=crossref.66dc3a9cef01c87d8417ae7a2c0d3d6a>
- [8] Pietrzyk Z A, Breger P and Summers D D R 1993 *Plasma Physics and Controlled Fusion* **35** 1725–1744 ISSN 0741-3335 URL <http://stacks.iop.org/0741-3335/35/i=12/a=006?key=crossref.ca847185a7856a170f0b1b1af27e0fa8>
- [9] Brix M, Dodt D, Korotkov A, Morgan P, Dunai D, Fischer R, Meigs A, Nedzelskiy I S, Schweinzer J, Vince J and Zoletnik S 2010 *Review of Scientific Instruments* **81** 10D733 ISSN 0034-6748 URL <http://aip.scitation.org/doi/10.1063/1.3502320>
- [10] Brix M, Dodt D, Dunai D, Lupelli I, Marsen S, Melson T F, Meszaros B, Morgan P, Petravich G, Refy D I, Silva C, Stamp M, Szabolics T, Zastrow K D and Zoletnik S 2012 *Review of Scientific Instruments* **83** 10D533 ISSN 00346748 URL <http://aip.scitation.org/doi/10.1063/1.4739411>
- [11] Schorn R P, Hintz E, Rusbüldt D, Aumayr F, Schneider M, Unterreiter E and Winter H 1991 *Applied Physics B Photophysics and Laser Chemistry* **52** 71–78 ISSN 0721-7269 URL <http://link.springer.com/10.1007/BF00357658>
- [12] Svensson J and Werner A 2007 Large Scale Bayesian Data Analysis for Nuclear Fusion Experiments *2007 IEEE International Symposium on Intelligent Signal Processing (IEEE)* pp 1–6 ISBN 978-1-4244-0829-0 URL <http://ieeexplore.ieee.org/document/4447579/>
- [13] Summers H P 2004 The ADAS manual, 2nd Edition, Version 2.7 URL <http://www.adas.ac.uk/manual.php>
- [14] Schweinzer J, Brandenburg R, Bray I, Hoekstra R, Aumayr F, Janev R and Winter H 1999 *Atomic Data and Nuclear Data Tables* **72** 239–273 ISSN 0092640X URL <https://linkinghub.elsevier.com/retrieve/pii/S0092640X9990815X>
- [15] Kwak S, Svensson J, Brix M and Ghim Y c 2016 *Review of Scientific Instruments* **87** 023501 ISSN 0034-6748 URL <http://aip.scitation.org/doi/10.1063/1.4940925>
- [16] Rasmussen C E and Williams C K I 2006 *Gaussian Processes for Machine Learning* (MIT Press)
- [17] Svensson J 2011 *JET report, EFDA-JET-PR(11)24* URL <http://www.euro-fusionscipub.org/wp-content/uploads/eurofusion/EFDP11024.pdf>
- [18] Romero J and Svensson J 2013 *Nuclear Fusion* **53** 033009 ISSN 0029-5515 URL <http://stacks.iop.org/0029-5515/53/i=3/a=033009?key=crossref.e63bc2641d1ea5a6766bf4b0dc1db9ee>
- [19] Li D, Svensson J, Thomsen H, Medina F, Werner A and Wolf R 2013 *Review of Scientific Instruments* **84** 083506 ISSN 0034-6748 URL <http://aip.scitation.org/doi/10.1063/1.4817591>
- [20] Schmuck S, Svensson J, De La Luna E, Figini L, Johnson T, Alper B, Beurskens M, Fessey J, Gerbaud T and Sirinelli A 2011 Bayesian derivation of electron temperature profile using jet ece diagnostics *38th EPS Conference on Plasma Physics 2011, EPS 2011 : Europhysics Conference Abstracts (Europhysics Conference Abstracts no 35:2)* pp 1512–1515 qC 20140828
- [21] Chilenski M, Greenwald M, Marzouk Y, Howard N, White A, Rice J and Walk J 2015 *Nuclear Fusion* **55** 023012 ISSN 0029-5515 URL <http://stacks.iop.org/0029-5515/55/i=2/a=023012?key=crossref.b22d32b1ac570adef0ea0869bc2c1789>
- [22] Lao L, St John H, Stambaugh R, Kellman A and Pfeiffer W 1985 *Nuclear Fusion* **25** 1611–1622 ISSN 0029-5515 URL <http://stacks.iop.org/0029-5515/25/i=11/a=007?key=crossref.382b4e7e430c8741af0f7248e9a56c09>
- [23] Pasqualotto R, Nielsen P, Gowers C, Beurskens M, Kempenaars M, Carlstrom T and Johnson D 2004 *Review of Scientific Instruments* **75** 3891–3893 ISSN 00346748 URL <http://aip.scitation.org/doi/10.1063/1.1544460>

- org/doi/10.1063/1.1787922
- [24] Devinderjit Sivia J S 2006 *Data Analysis: A Bayesian Tutorial* (Oxford University Press) ISBN 0-198-56831-2
- [25] Willensdorfer M, Birkenmeier G, Fischer R, Laggner F M, Wolfrum E, Veres G, Aumayr F, Carralero D, Guimarãis L and Kurzan B 2014 *Plasma Physics and Controlled Fusion* **56** 025008 ISSN 0741-3335 URL <http://stacks.iop.org/0741-3335/56/i=2/a=025008?key=crossref.95b11a9241c7a2bc86f341bd85807a09>

4.3 Article III

‘Bayesian modelling of Thomson scattering and multichannel interferometer diagnostics using Gaussian processes’

S. KWAK, J. SVENSSON, S. BOZHENKOV, J. FLANAGAN, M. KEMPENAARS, A. BOBOC and Y.-c. GHIM

Nuclear Fusion, Vol. 60.4 (26th Feb. 2020), DOI: 10.1088/1741-4326/ab686e

Bayesian modelling of Thomson scattering and multichannel interferometer diagnostics using Gaussian processes

Sehyun Kwak^{1,2†}, J. Svensson², S. Bozhakov², J. Flanagan³,
M. Kempenaars^{3,4}, A. Boboc³, Y.-c. Ghim^{1*} and
JET Contributors[‡]

EUROfusion Consortium, JET, Culham Science Centre, Abingdon, OX14 3DB,
United Kingdom of Great Britain and Northern Ireland

¹Department of Nuclear and Quantum Engineering, KAIST, Daejeon 34141,
Korea, Republic of

²Max-Planck-Institut für Plasmaphysik, 17491 Greifswald, Germany

³Culham Centre for Fusion Energy, Culham Science Centre, Abingdon, OX14 3DB,
United Kingdom of Great Britain and Northern Ireland

⁴ITER Organization, Route de Vinon-sur-Verdon, CS 90 046, 13067 St Paul Lez
Durance Cedex, France

E-mail: [†]slayer313@kaist.ac.kr, *ycghim@kaist.ac.kr

Postprint

Abstract. Electron temperature and density profiles consistent with JET high resolution Thomson scattering (HRTS) and far infrared (FIR) interferometer data are inferred by a Bayesian joint model using Gaussian processes. Forward models predicting diagnostic data including instrument effects such as optics and electronics are developed independently for both diagnostic systems in the Minerva framework, and combined as one joint model. The full joint posterior distribution of the electron temperature and density profiles, the hyperparameters of the Gaussian processes and calibration factor is explored by Markov chain Monte Carlo (MCMC) sampling. The posterior distribution of the electron density(temperature) profile is obtained by marginalising all the possible combinations of the electron temperature(density) profile, the hyperparameters and calibration factor. Therefore, the method removes profile dependency on the hyperparameters completely in addition to eliminating often-used avoidable constraints such as monotonicity and parametrisation on the profiles. The posterior distribution of the calibration factor is also calculated explaining both the HRTS and the FIR interferometer data simultaneously. Thus, absolute electron density can be obtained from the HRTS without additional experiments measuring the calibration factor.

Keywords: Thomson scattering diagnostic, FIR interferometer, JET, Bayesian inference,

[‡] See the author list of E. Joffrin et al. accepted for publication in Nuclear Fusion Special issue 2019, <https://doi.org/10.1088/1741-4326/ab2276>

Gaussian process

1. Introduction

Consistent inference on physics parameters is arguably one of the most important and fundamental issues in any scientific field. Since large-scale magnetic confinement fusion experiments such as Joint European Torus (JET) [1] and Wendelstein 7-X (W7-X) [2] have multiple sophisticated diagnostics, it is inevitable to use a framework that is capable of handling and keeping track of parameters, data, assumptions, forward models and analysis codes in order to achieve consistent scientific inference. Resolving discrepancies among various measurements, if they exist, is challenging at least for the following reasons: i) forward models and analysis codes for a complex system, e.g., plasma diagnostics, often contain many hidden assumptions and depend on various uncertain information such as measurement positions, calibration factors and instrument effects as well as our insufficient understanding of physics, and ii) even if an individual forward model, for instance, is well managed, creating a joint model with other diagnostics or physics models can be difficult due to lack of a standardised interface.

The Minerva framework [3, 4] allows us to perform a consistent data analysis for complex experiments as it provides a standardised format (modularisation) for forward models and analysis codes, so called Minerva models, and a standardised interface to connect all of them in a systematic way. For instance, a Minerva (forward) model for a Thomson scattering system is built as an independent module depending on lasers, collecting optics, polychromators, data acquisition systems and physics parameters, i.e., electron temperature and density. Once the Minerva model is created, the input, e.g., laser energy and wavelength, polychromator details, electron temperature and density, and the output, e.g., predicted Thomson scattered signals, can be connected to/from other Minerva models and/or data sources. Minerva thus standardises scientific modelling and represents such joint models as joint probabilities and provides their graphical representation as shown in Figure 1. Some examples of implemented Minerva models are interferometer [5], magnetic sensor [6, 7, 8], Thomson scattering [9], beam emission spectroscopy [10, 11], soft X-ray [12], electron cyclotron emission [13], x-ray imaging crystal spectroscopy [14] and effective ion charge [15] diagnostics. We also note that data analysis based on Minerva models can be accelerated by field-programmable gate arrays (FPGAs) [16] and neural networks [17].

The conventional analysis for the high resolution Thomson scattering (HRTS) and the far infrared (FIR) interferometer diagnostics at JET are carried out individually. The HRTS can provide electron temperature and density profiles with the spatial resolutions of 0.8 – 1.6 cm [20, 21]. It is well known that electron density measurements with Thomson scattering systems require information on the calibration factors of the system [22]. The FIR interferometer diagnostic system provides line integrated electron densities, i.e., no spatial resolution, without such calibration factors [23, 24, 25, 26]. Bayesian analysis for Thomson scattering [9, 27, 28], interferometer [5, 29] systems and joint

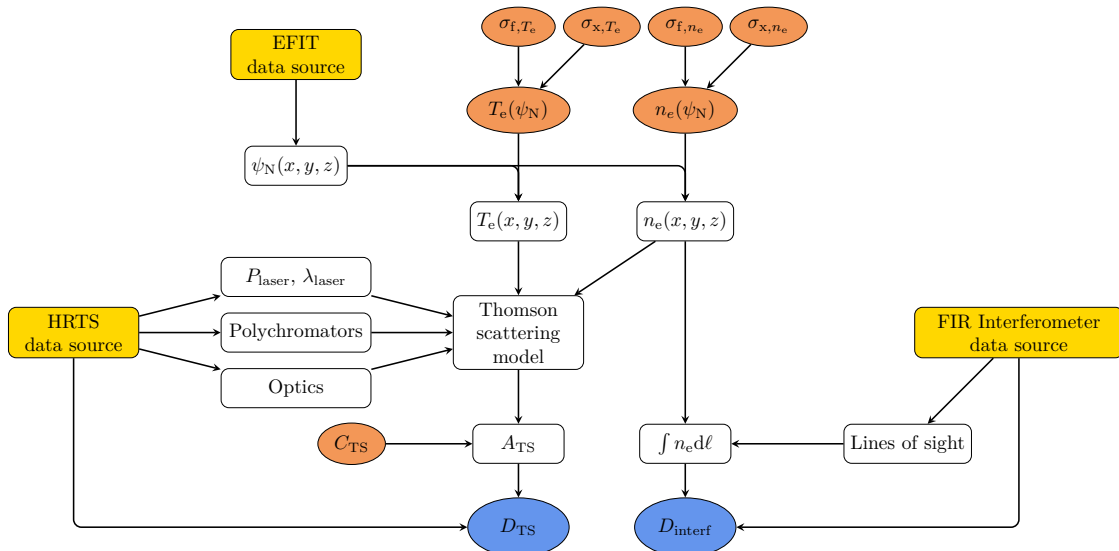


Figure 1. A simplified version of the Minerva graph representing the joint model of the high resolution Thomson scattering (HRTS) and the far infrared (FIR) interferometer systems at JET. The unknown parameters, i.e., the parameters we wish to determine, and observations are shown as red and blue circles, respectively. Note that the observations can be taken from previous inference, e.g., an *observed* Thomson scattered amplitude D_{TS} is taken from the inference results described in Section 3.1. The electron temperature T_e and density n_e are given as a function of the normalised poloidal flux ψ_N and mapped to Cartesian coordinates x, y, z in real space by using the equilibrium fitting (EFIT) code [18, 19]. The predicted Thomson scattered amplitude A_{TS} are calculated by the Minerva model of the Thomson scattering system with the calibration factor C_{TS} treated as an unknown parameter, and they are compared with the observed data. Line integrated electron densities are calculated by the lines of sight integration model mimicking the FIR interferometer system and compared with the observed data. Note that σ_{f, T_e} , σ_{x, T_e} , σ_{f, n_e} and σ_{x, n_e} are the hyperparameters of Gaussian processes which are explained in Section 2.3.

analysis [30] have been previously reported. They made impressive progress, especially evaluating uncertainties of electron temperature and density. This joint analysis [30] made use of spline models for the electron temperature and density profiles with additional monotonicity assumptions, which our method avoids. We use Gaussian processes, with a smoothness determined by a marginalisation over different length scales, thus providing an objective smoothness criterion.

In this work, we present a Bayesian joint model of the HRTS and the FIR interferometer systems at JET to combine the advantages of each diagnostic system while eliminating the disadvantages of them. We have developed Minerva (forward) models for both diagnostics individually and combine them as one joint model with an additional unknown parameter, the HRTS electron density calibration factor C_{TS} , as shown in Figure 1. The conventional analysis for the HRTS system uses a single interferometer chord (channel 3) to calibrate electron density for each discharge, if the

data from the chord 3 is available. It calculates an electron density correction factor (a single value per discharge) for the HRTS system as the ratio of line integrated density from the chord 3 to the predicted line integrated density from a linearly interpolated HRTS density profile with the EFIT mapping. The method in this work infers C_{TS} with uncertainties, self consistently for each time slice. This means that we can automatically and explicitly obtain the posterior distribution of C_{TS} explaining all the HRTS and the FIR interferometer data simultaneously, thereby getting rid of generally required extra calibration procedures, e.g., Raman calibration, to measure C_{TS} .

Electron temperature and density profiles are formulated by Gaussian processes [5, 31], a non-parametric model that can adopt the complexity of profiles within a Bayesian framework. Specifically, we use the hyperparameter model developed by [32] (denoted as σ_{f,T_e} , σ_{x,T_e} , σ_{f,n_e} and σ_{x,n_e} in Figure 1) whose details are explained in Section 2.3. Since we use a non-parametric model, our method does not depend on any predefined parametric model [20, 21, 33, 34, 35, 36] such as a modified hyperbolic tangent function [33] which often limit our *knowledge* on the profiles from measurements. Moreover, Gaussian processes avoid imposing assumptions such as monotonicity [30, 37].

We explore the joint posterior distribution of the electron temperature and density profiles, their hyperparameters and the HRTS electron density calibration factor by using Markov chain Monte Carlo (MCMC) sampling, specifically, we use an adaptive Metropolis-Hastings algorithm [38, 39, 40] implemented in Minerva. Finally, we obtain electron temperature(density) profiles with the associated uncertainties by marginalising out electron density(temperature) profiles, their hyperparameters and the calibration factor. In other words, our final result on the temperature and density profile does not depend on a specific set of values of all the other unknown parameters.

Section 2 describes the forward models of the HRTS and the FIR interferometer systems, and explains Gaussian processes for the electron temperature and density profile modelling. The details on Bayesian inference for electron temperature and density profiles and their results are discussed in Section 3. Our conclusions are provided in Section 4.

2. The forward model

2.1. JET high resolution Thomson scattering system

The HRTS diagnostic [20] measures the electron temperature and density from 63 spatial locations along the laser beam across the low-field side of JET from the major radius of $R = 3.0$ m to 3.9 m near the middle plane ($Z \sim 0.1$ m) with spatial resolutions of 0.8 – 1.6 cm. The laser wavelength of 1064 nm and typical energy level of 5.0 J with 20 ns pulse duration and 20 Hz repetition rate are used. The laser photons are scattered off of electrons via Thomson scattering, and the Thomson scattered spectra are broadened by the Doppler effect due to the thermal motions of the electrons. Electron temperature T_e and density n_e determine the width and the area, respectively, of a Thomson scattered

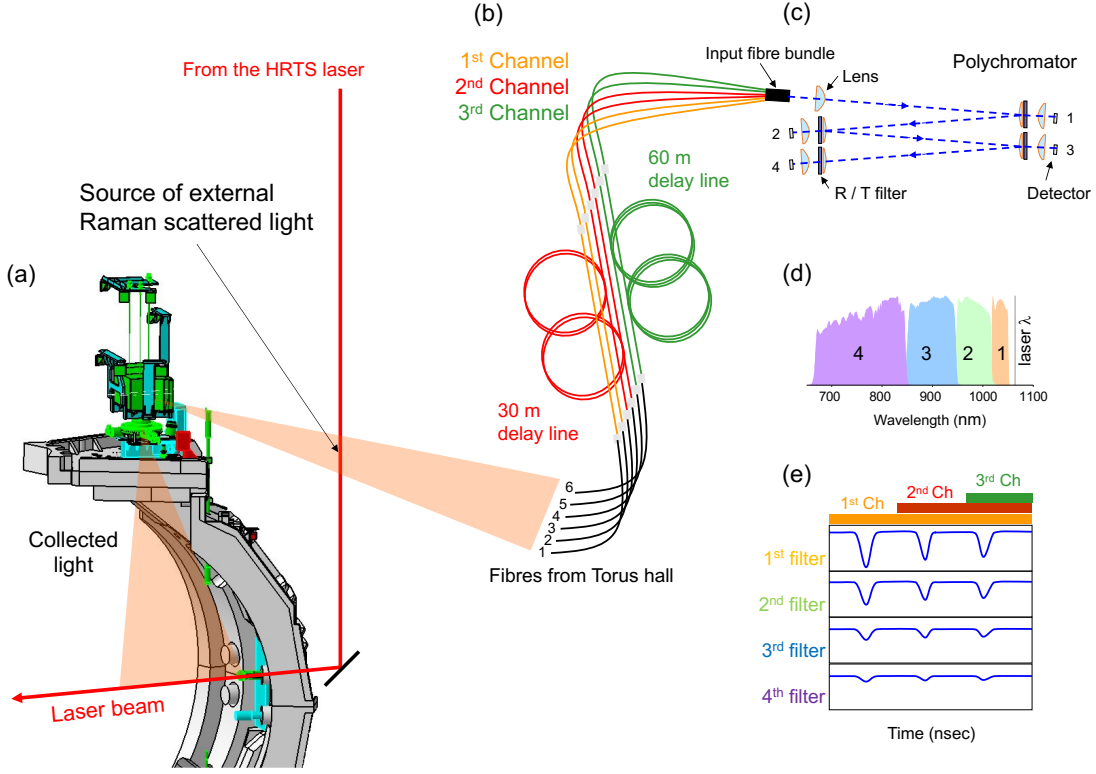


Figure 2. A schematic diagram of the HRTS system showing (a) the geometry of the laser beam and collecting optics, (b) three spatial locations covered by a polychromator with three sets of fibres (in this case, two optical fibres per location), (c) a polychromator with four reflection/transmission interference filters and detectors, and (d) an example of spectral response functions $\phi(\lambda)$. (e) Four filtered signals (cartoon drawings) detected by a polychromator from three different spatial locations are distinguished by time delays. External Raman scattered signals are originated from where the laser beam crosses the optical path between the collecting optics and the fibres.

spectrum. The predicted Thomson scattered signal amplitude A_{TS} is given as a function of T_e , n_e and the HRTS electron density calibration factor C_{TS} including the electronics, optics and geometric effects:

$$A_{\text{TS}} = C_{\text{TS}} n_e E_{\text{laser}} \int \frac{\phi(\lambda)}{\phi^{1,1}(\lambda_N)} \frac{\lambda}{hc} r_e^2 \frac{S(\lambda, \theta, T_e)}{\lambda_{\text{laser}}} d\lambda, \quad (1)$$

where E_{laser} is the laser energy, $\phi(\lambda)$ are spectral response functions of the HRTS system, $\phi^{1,1}(\lambda_N)$ is a normalisation factor for the spectral response functions (the value of the spectral response function of the first spectral channel of the first spatial position at the wavelength $\lambda_N = 1020$ nm), λ a scattered wavelength, h the Planck constant, c the speed of light, r_e the classical electron radius, $S(\lambda, \theta, T_e)$ the spectral density function [41], θ a scattering angle and λ_{laser} the laser wavelength. Further details of the Thomson scattering model are described in Appendix A.

Each polychromator detects Thomson scattered signals from three spatial locations

collected by three or six fibres, i.e., one or two fibres per location. The fibres for the second and third locations are set to be 30 m and 60 m longer than the first location, respectively, to separate these signals by time delays (Figure 2). This allows 63 spatial locations to be addressed by 21 polychromators.

Thomson scattered signals from each spatial location are resolved over time by the detectors as shown in Figure 2(e). The shape of the Thomson scattered signals depends on the shape of the laser pulses and detector electronics. By assuming that the HRTS system has Gaussian-shaped laser pulses and low-pass filter electronics [42], the Thomson scattered signals as a function of time $V_{\text{TS}}(t)$ are formulated as

$$V_{\text{TS}}(t) = A_{\text{TS}} \int_0^t \frac{1}{\sqrt{2\pi}\tau_{\text{laser}}} \frac{1}{\tau_{\text{electronics}}} \exp\left[-\frac{(t' - t_{\text{TS}})^2}{\tau_{\text{laser}}^2}\right] \exp\left(-\frac{t - t'}{\tau_{\text{electronics}}}\right) dt', \quad (2)$$

where A_{TS} is the amplitude (see Equation (1)), τ_{laser} is the width of Gaussian-shaped laser pulses, $\tau_{\text{electronics}}$ is the characteristic time of the electronics, and t_{TS} is the time when the laser energy is the maximum for Thomson scattered signals.

Raman scattered photons also get into the polychromators as the laser beam crosses the optical path between the collecting optics and fibres outside of the JET vacuum vessel (Figure 2(a)) in addition to stray light signals. These unintended *external* Raman scattered and stray light signals, which we call *parasitic* signals, are occasionally overlapping the Thomson scattered signals, therefore they must be separated out. The parasitic signals can be measured separately by firing laser pulses into the vessel before every JET discharge. While the temporal evolution of the parasitic signals is not changing, the amplitudes of the signals may slightly change over plasma discharges due to the changes of gas pressure and the laser energy. As the parasitic signals are collected by the same polychromators and fibres we can use Equation (2) to express these signals as

$$V_{\text{PS}}(t) = A_{\text{PS,R}} \int_0^t \frac{1}{\sqrt{2\pi}\tau_{\text{laser}}} \frac{1}{\tau_{\text{electronics}}} \exp\left[-\frac{(t' - t_{\text{PS,R}})^2}{\tau_{\text{laser}}^2}\right] \exp\left(-\frac{t - t'}{\tau_{\text{electronics}}}\right) dt' \\ + A_{\text{PS,S}} \int_0^t \frac{1}{\sqrt{2\pi}\tau_{\text{laser}}} \frac{1}{\tau_{\text{electronics}}} \exp\left[-\frac{(t' - t_{\text{PS,S}})^2}{\tau_{\text{laser}}^2}\right] \exp\left(-\frac{t - t'}{\tau_{\text{electronics}}}\right) dt', \quad (3)$$

where $A_{\text{PS}} = [A_{\text{PS,R}}, A_{\text{PS,S}}]$ is the amplitude, and $t_{\text{PS}} = [t_{\text{PS,R}}, t_{\text{PS,S}}]$ is the time when the laser energy is the maximum for these parasitic signals (external Raman scattered and stray light signals with the subscript R or S, respectively).

By taking account of the Thomson scattered signals $V_{\text{TS}}(t)$, the parasitic signals $V_{\text{PS}}(t)$ and the constant background offset V_{B} , we can express the predicted HRTS signals $V_{\text{HRTS}}(t)$ as

$$V_{\text{HRTS}}(t) = V_{\text{TS}}(t) + V_{\text{PS}}(t) + V_{\text{B}}. \quad (4)$$

Our method infers the Thomson scattered and parasitic signals simultaneously, and results of the method are discussed in Section 3.1.

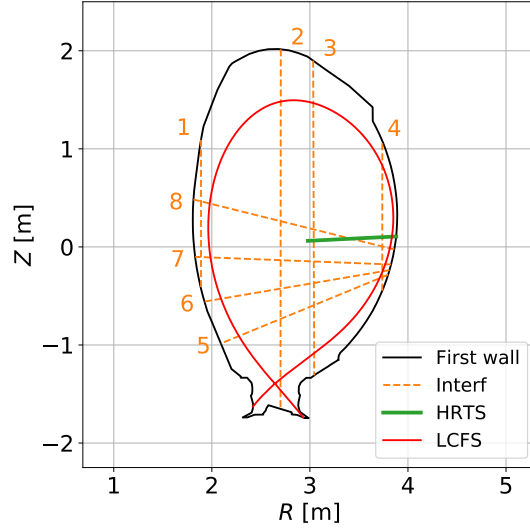


Figure 3. The lines (dashed orange) of sight of the FIR interferometer (Interf) system and the spatial positions of the HRTS system (green). The HRTS system measures the electron temperature and density along the green line with spatial resolutions of 0.8–1.6 cm, and the FIR interferometer system measures line integrated densities along the dashed orange lines. Red line indicates the plasma boundary of a typical JET plasma discharge.

2.2. JET far infrared (FIR) interferometer system

The JET far infrared (FIR) interferometer [23, 24, 25, 26] diagnostic measures line integrated electron densities along the eight lines of sight (four vertical and four lateral directions as shown in Figure 3) with an approximately 10–200 μs temporal resolution (depending on the channels). The 1st and 4th channels measure the line integrated densities near the first wall, constraining the electron density at the edge, and the other lines of sight cover the plasma core. Our forward model calculates the line integrated electron density of the i^{th} channel V_{interf}^i as:

$$V_{\text{interf}}^i = \int n_e(x, y, z) d\ell, \quad (5)$$

where the integration path $\int d\ell$ is all the way along the lines of sight inside the vacuum vessel.

2.3. Gaussian process prior

A Gaussian process [31] is a probabilistic function that associates each element of a domain to a single element of a random vector following a multivariate Gaussian distribution whose mean at every point and covariance between any two points within the domain are defined. Thus, the function that is modelled by a Gaussian process is

not constrained by any specific parametric representation, but properties given by their mean and covariance functions.

Zero mean, which does not usually limit the inference solutions [31], and squared exponential covariance functions are one of the most common specifications of a Gaussian process, and they are given as

$$\mu(x) = 0 \quad (6)$$

$$\Sigma(x^i, x^j) = \sigma_f^2 \exp\left(-\frac{(x^i - x^j)^2}{2\sigma_x^2}\right) + \sigma_y^2 \delta^{ij}, \quad (7)$$

where μ is the mean function, and x is a scalar or vector input, e.g., time or space. x^i and x^j denote i^{th} and j^{th} elements of the input domain, respectively. Σ is the covariance function with an overall scale σ_f , a length scale σ_x and a noise scale σ_y . These scales are hyperparameters, and σ_f and σ_x determine the smoothness of the function. σ_y is chosen to be a relatively small number with respect to the overall scale, i.e., $\sigma_y/\sigma_f = 10^{-3}$ in this work, to avoid any numerical instability [10]. δ^{ij} is the Kronecker delta function.

We note that Gaussian processes have been introduced to the fusion community with a non-parametric tomography for the JET FIR interferometer data [5] and used for current tomography [6, 7, 43, 44], beam emission spectroscopy [10, 11], soft X-ray spectroscopy [12], X-ray imaging crystal spectroscopy [14] and profile regressions [32]. In this work, Gaussian processes are used to model electron temperature and density profiles to constrain their smoothness (gradient scale length) without imposing any specific profile shapes or assumptions such as monotonicity.

Electron temperature and density profiles can have substantially different gradients in the core and edge regions [45]. In order to represent such spatially varying gradients, we choose non-stationary covariance functions [46], given as

$$\Sigma(x^i, x^j) = \sigma_f^2 \left(\frac{2\sigma_x(x^i)\sigma_x(x^j)}{\sigma_x(x^i)^2 + \sigma_x(x^j)^2}\right)^{\frac{1}{2}} \exp\left(-\frac{(x^i - x^j)^2}{\sigma_x(x^i)^2 + \sigma_x(x^j)^2}\right) + \sigma_y^2 \delta^{ij}, \quad (8)$$

where the length scale σ_x is an arbitrary function of the input x . The length scale function σ_x specifies the smoothness at any point on the domain. We need a function with different length scales in the core and edge regions and a smooth transition between the two. For this reason, we choose a hyperbolic tangent function [32],

$$\sigma_x(x^i) = \frac{\sigma_x^{\text{core}} + \sigma_x^{\text{edge}}}{2} - \frac{\sigma_x^{\text{core}} - \sigma_x^{\text{edge}}}{2} \tanh\left(\frac{x^i - x_0}{\sigma_x^{\text{width}}}\right), \quad (9)$$

where σ_x^{core} and σ_x^{edge} are the core and edge length scales, respectively. x_0 is the transition position of the length scale, and σ_x^{width} determines how fast the transition occurs. With this length scale function, the smoothness (gradient scale length) of the profiles is changing gradually from the core to the edge.

The Gaussian processes of electron temperature and density profiles are set as a function of the normalised poloidal flux, i.e., $x = \psi_N$, as shown in the Figure 1. By using

the equilibrium fitting (EFIT) code [18, 19] with only the magnetic diagnostics, electron temperature and density profiles are mapped onto Cartesian coordinates x, y, z in real space. The forward models of the HRTS and the FIR interferometer systems access values of T_e and n_e at their corresponding spatial positions and calculate the predictions, A_{TS} and V_{interf}^i , given by Equation (1) and (5), respectively. These predictions are directly compared to the observations for inference.

3. Bayesian inference

In Bayesian probability theory, we express a probability of generating (observing) experimental data D given parameter values H as a conditional probability $P(D|H)$, a likelihood. Our state of knowledge on the parameters H before any observations are taken into account is formulated as a prior probability $P(H)$. For instance, $P(T_e)$ may be a uniform distribution from zero to some maximum, e.g., 100 keV. Note that the parameters H are what we wish to infer by conducting experiments. Bayes' formula states that our state of knowledge on the parameters H given the observed data D is the posterior probability $P(H|D)$, expressed as

$$P(H|D) = \frac{P(D|H)P(H)}{P(D)}, \quad (10)$$

where the denominator is a normalisation factor $P(D)$ (also called the model evidence). A more detailed description of Bayesian inference can be found in [47, 48].

The posterior distribution is high dimensional if there exist many parameters of interest. Thus, to calculate lower dimensional distributions of parameters of interest, a marginalisation has to be carried out:

$$P(H_1) = \int P(H_1, H_2) dH_2. \quad (11)$$

The marginal distributions provide full information of the parameters of interest by taking into account all possible values of the other parameters. We can perform this integration by collecting values of the parameters of interest H_1 from joint samples $[H_1, H_2]$ of the joint distribution $P(H_1, H_2)$. These collected values of H_1 are equivalent to samples drawn from the marginal distribution $P(H_1)$.

In this work, the parameters are electron temperature and density profiles at 50 normalised poloidal flux surfaces, $\mathbf{T}_e = [T_e(\psi_N^{i=1}), T_e(\psi_N^{i=2}), \dots, T_e(\psi_N^{i=s})]$ and $\mathbf{n}_e = [n_e(\psi_N^{i=1}), n_e(\psi_N^{i=2}), \dots, n_e(\psi_N^{i=s})]$ with $s = 50$, the calibration factor C_{TS} and the hyperparameters $\mathbf{M}_{T_e} = [\sigma_{f, T_e}, \sigma_{x, T_e}]$ and $\mathbf{M}_{n_e} = [\sigma_{f, n_e}, \sigma_{x, n_e}]$ (the red circles in Figure 1). σ_{x, T_e} and σ_{x, n_e} are given by Equation (9) with two sets of four parameters σ_x^{core} , σ_x^{edge} , σ_x^{width} , and x_0 . The data are obtained by the HRTS and the FIR interferometer diagnostics. With \mathbf{D}_{TS} denoting the amplitudes of Thomson scattered signals from all the spatial locations and $\mathbf{D}_{\text{interf}}$ standing for the line integrated electron densities from all the lines

of sight, the posterior is expressed as

$$\begin{aligned}
& P(\mathbf{T}_e, \mathbf{n}_e, C_{\text{TS}}, \mathbf{M}_{T_e}, \mathbf{M}_{n_e} | \mathbf{D}_{\text{TS}}, \mathbf{D}_{\text{interf}}) \\
&= \frac{P(\mathbf{D}_{\text{TS}}, \mathbf{D}_{\text{interf}} | \mathbf{T}_e, \mathbf{n}_e, C_{\text{TS}}, \mathbf{M}_{T_e}, \mathbf{M}_{n_e}) P(\mathbf{T}_e, \mathbf{n}_e, C_{\text{TS}}, \mathbf{M}_{T_e}, \mathbf{M}_{n_e})}{P(\mathbf{D}_{\text{TS}}, \mathbf{D}_{\text{interf}})} \\
&= \frac{P(\mathbf{D}_{\text{TS}} | \mathbf{T}_e, \mathbf{n}_e, C_{\text{TS}}) P(\mathbf{D}_{\text{interf}} | \mathbf{n}_e) P(\mathbf{T}_e | \mathbf{M}_{T_e}) P(\mathbf{n}_e | \mathbf{M}_{n_e}) P(\mathbf{M}_{T_e}) P(\mathbf{M}_{n_e}) P(C_{\text{TS}})}{P(\mathbf{D}_{\text{TS}}) P(\mathbf{D}_{\text{interf}})}. \tag{12}
\end{aligned}$$

Notice that Figure 1 exactly expresses Equation (12) which is automatically generated by the Minerva framework such that conditional dependences among the parameters and observations can be easily verified.

Raw data from the HRTS system contain the parasitic signals, i.e., the external Raman scattered and stray light signals as explained in Section 2.1. In order to proceed the profile inference, we have to first extract the Thomson scattered signals from the raw HRTS data which is discussed in Section 3.1. Then, we present how electron temperature and density profiles are inferred in Section 3.2.

3.1. Inference on the amplitudes of the Thomson scattered signals

We assume that the time series of raw HRTS data from the i^{th} spatial position (total of 63 spatial positions with 21 polychromators, $i = 1, 2, \dots, 63$) and the j^{th} spectral channel (four spectral channels for each polychromator $j = 1, \dots, 4$) denoted as $\mathbf{D}_{\text{HRTS}}^{i,j}$ § is following a multivariate Gaussian distribution whose mean is the HRTS predicted signals $\mathbf{V}_{\text{HRTS}}^{i,j}$ given by Equation (4) with the covariance $\Sigma_{\text{HRTS}}^{i,j}$ as a combination of the electronics and photon noises. Thus, the probability $P(\mathbf{D}_{\text{HRTS}}^{i,j} | A_{\text{TS}}^{i,j}, A_{\text{PS}}^{i,j}, V_{\text{B}}^{i,j}, t_{\text{TS}}^{i,j}, t_{\text{PS}}^{i,j}, \tau_{\text{laser}}^{i,j}, \tau_{\text{electronics}}^{i,j})$ is written as

$$\begin{aligned}
& P(\mathbf{D}_{\text{HRTS}}^{i,j} | A_{\text{TS}}^{i,j}, A_{\text{PS}}^{i,j}, V_{\text{B}}^{i,j}, t_{\text{TS}}^{i,j}, t_{\text{PS}}^{i,j}, \tau_{\text{laser}}^{i,j}, \tau_{\text{electronics}}^{i,j}) = \\
& \frac{1}{\sqrt{(2\pi)^m |\Sigma_{\text{HRTS}}^{i,j}|}} \exp\left(-\frac{1}{2} (\mathbf{D}_{\text{HRTS}}^{i,j} - \mathbf{V}_{\text{HRTS}}^{i,j})^{\text{T}} \Sigma_{\text{HRTS}}^{i,j}{}^{-1} (\mathbf{D}_{\text{HRTS}}^{i,j} - \mathbf{V}_{\text{HRTS}}^{i,j})\right). \tag{13}
\end{aligned}$$

$\mathbf{D}_{\text{HRTS}}^{i,j}$ and $\mathbf{V}_{\text{HRTS}}^{i,j}$ are time series vectors, e.g., $\mathbf{D}_{\text{HRTS}}^{i,j} = [D_{\text{HRTS}}^{i,j}(t = t_1), \dots, D_{\text{HRTS}}^{i,j}(t = t_m)]$ with $m = 500$ covering 500 ns. The covariance $\Sigma_{\text{HRTS}}^{i,j}$ is given as a diagonal matrix assuming no correlation with other time points, that is

$$\Sigma_{\text{HRTS}}^{i,j} = \begin{pmatrix} (\sigma_{\text{HRTS}}^{i,j}(t = t_1))^2 & 0 & \dots & 0 \\ 0 & (\sigma_{\text{HRTS}}^{i,j}(t = t_2))^2 & \dots & 0 \\ \vdots & \vdots & \ddots & \vdots \\ 0 & 0 & \dots & (\sigma_{\text{HRTS}}^{i,j}(t = t_m))^2 \end{pmatrix}, \tag{14}$$

§ Note that \mathbf{D}_{TS} in Equation (12) are the amplitudes of the Thomson scattered signals *extracted* from the raw HRTS data \mathbf{D}_{HRTS} .

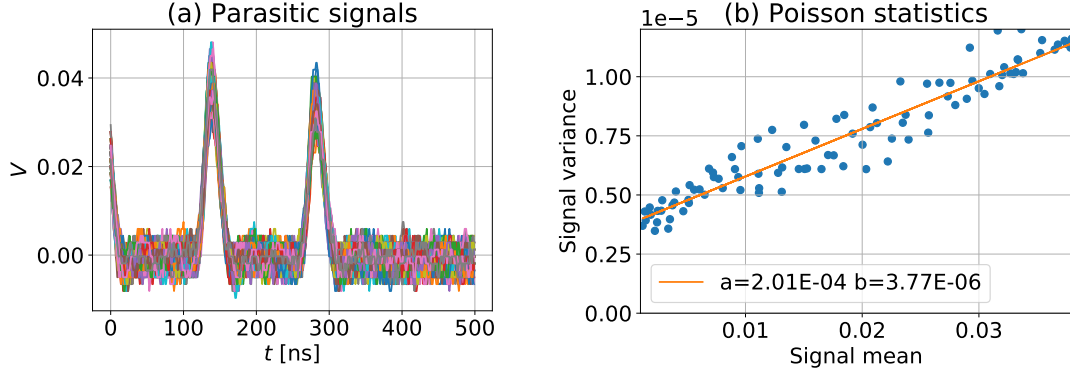


Figure 4. (a) An example of the parasitic signals obtained by firing the laser pulses before a plasma discharge. Different signal levels from different laser pulses (different colours) at a fixed time are dominated by the photon noise. (b) Poisson statistics are calculated from the linear relation between the signal mean and variance from the different parasitic signals, and we find that $\sigma_{\text{photon}}^2 = aV_{\text{HRTS}}$ with $a = 2.01 \times 10^{-4}$ in this example.

where $(\sigma_{\text{HRTS}}^{i,j}(t))^2 = (\sigma_{\text{electronics}}^{i,j})^2 + (\sigma_{\text{photon}}^{i,j}(t))^2$ is the uncertainty of the raw HRTS data.

The electronics noise $\sigma_{\text{electronics}}^{i,j}$ is set as a zero mean Gaussian noise whose standard deviation is estimated from the electronics noise signals measured before the laser pulses and plasma discharges, i.e., without the laser pulses and plasmas, and assumed not to vary over time.

The photon noise is estimated from the mean and variance of the parasitic signals. Figure 4(a) shows an example of the parasitic signals obtained by firing many laser pulses (different colours) before a single plasma discharge, and (b) shows the linear relation between the signal mean and the variance over many laser pulses with the estimated slope of $a = 2.01 \times 10^{-4}$. Here, the photon noise is assumed to be the dominant contribution to the signal fluctuation [36]. Once we have the value of a , then the photon noise can be estimated as

$$(\sigma_{\text{photon}}^{i,j}(t))^2 = aV_{\text{HRTS}}^{i,j}(t). \quad (15)$$

More details on the method of the photon noise estimation can be found in [10].

Assuming that a prior probability of each parameter ($A_{\text{TS}}^{i,j}$, $A_{\text{PS}}^{i,j}$, $V_{\text{B}}^{i,j}$, $t_{\text{TS}}^{i,j}$, $t_{\text{PS}}^{i,j}$, $\tau_{\text{laser}}^{i,j}$ and $\tau_{\text{electronics}}^{i,j}$) is given as a uniform distribution, the posterior probability is written as

$$\frac{P(A_{\text{TS}}^{i,j}, A_{\text{PS}}^{i,j}, V_{\text{B}}^{i,j}, t_{\text{TS}}^{i,j}, t_{\text{PS}}^{i,j}, \tau_{\text{laser}}^{i,j}, \tau_{\text{electronics}}^{i,j} | \mathbf{D}_{\text{HRTS}}^{i,j})}{P(\mathbf{D}_{\text{HRTS}}^{i,j})} = \frac{P(\mathbf{D}_{\text{HRTS}}^{i,j} | A_{\text{TS}}^{i,j}, A_{\text{PS}}^{i,j}, V_{\text{B}}^{i,j}, t_{\text{TS}}^{i,j}, t_{\text{PS}}^{i,j}, \tau_{\text{laser}}^{i,j}, \tau_{\text{electronics}}^{i,j}) \times P(A_{\text{TS}}^{i,j}) P(A_{\text{PS}}^{i,j}) P(V_{\text{B}}^{i,j}) P(t_{\text{TS}}^{i,j}) P(t_{\text{PS}}^{i,j}) P(\tau_{\text{laser}}^{i,j}) P(\tau_{\text{electronics}}^{i,j})}{P(\mathbf{D}_{\text{HRTS}}^{i,j})}. \quad (16)$$

The posterior distribution of $A_{\text{TS}}^{i,j}$, $A_{\text{PS}}^{i,j}$, $V_{\text{B}}^{i,j}$, $t_{\text{TS}}^{i,j}$, $t_{\text{PS}}^{i,j}$, $\tau_{\text{laser}}^{i,j}$ and $\tau_{\text{electronics}}^{i,j}$ is explored by Markov chain Monte Carlo (MCMC) sampling, specifically, we use the adaptive

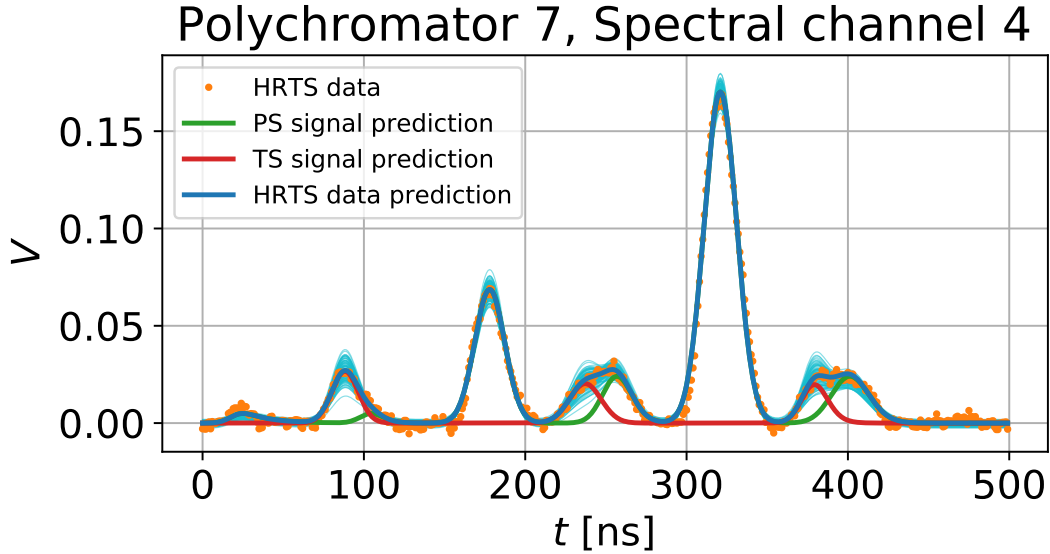


Figure 5. An example of the measured raw HRTS data $\mathbf{D}_{\text{HRTS}}^{i,j}$ (orange dots) and the mean of predicted HRTS signals $\mathbf{V}_{\text{HRTS}}^{i,j}$ (dark blue line) from the fourth spectral channel ($j = 4$) of the seventh polychromator (corresponding to $i = 19, 20$ and 21) during a plasma discharge over one laser pulse. The light blue lines show samples of the posterior (Equation (16)) explored by the MCMC method. The red and green lines are the predicted Thomson scattered signals $\mathbf{V}_{\text{TS}}^{i,j}$ and the predicted parasitic signals $\mathbf{V}_{\text{PS}}^{i,j}$ calculated through Equations (2) and (3), respectively, given the posterior mean. There are three peaks of Thomson scattered signals as one polychromator receives the signals from three different spatial positions as described in Section 2.1

Metropolis-Hastings algorithm [38, 39, 40]. The mechanism of this algorithm is: i) to propose a random sample x' in parameter space from a proposal distribution $Q(x'|x_t)$ given a previous sample x_t and ii) to accept the candidate if $P(x')/P(x_t) \geq u$, otherwise reject it ($P(x)$ is the posterior probability of x , and u is a random number from a uniform distribution on $[0, 1]$). After some iterations, the algorithms will collect a set of samples, which are drawn from the posterior distribution [38, 39]. We use an adaptive rule [40] to modify the proposal distribution Q in every iteration to sample the posterior distribution effectively.

The samples drawn from the posterior distribution given by Equation (16) are shown in Figure 5. The orange dots are the measured raw HRTS data $\mathbf{D}_{\text{HRTS}}^{i,j}$ (the fourth spectral channel of the seventh polychromator in this example) during a plasma discharge over one laser pulse. The dark blue line is the mean of predicted HRTS signals $\mathbf{V}_{\text{HRTS}}^{i,j}$, whereas the light blue lines are samples of the posterior. The red and green lines are the predicted Thomson scattered signals $\mathbf{V}_{\text{TS}}^{i,j}$ and the predicted parasitic signals $\mathbf{V}_{\text{PS}}^{i,j}$ calculated through Equations (2) and (3), respectively, given the posterior mean.

As electron temperature and density profiles are inferred based on the *observed*||

|| As a matter of fact, \mathbf{D}_{TS} is an inferred quantity (rather than being an observed quantity) from the

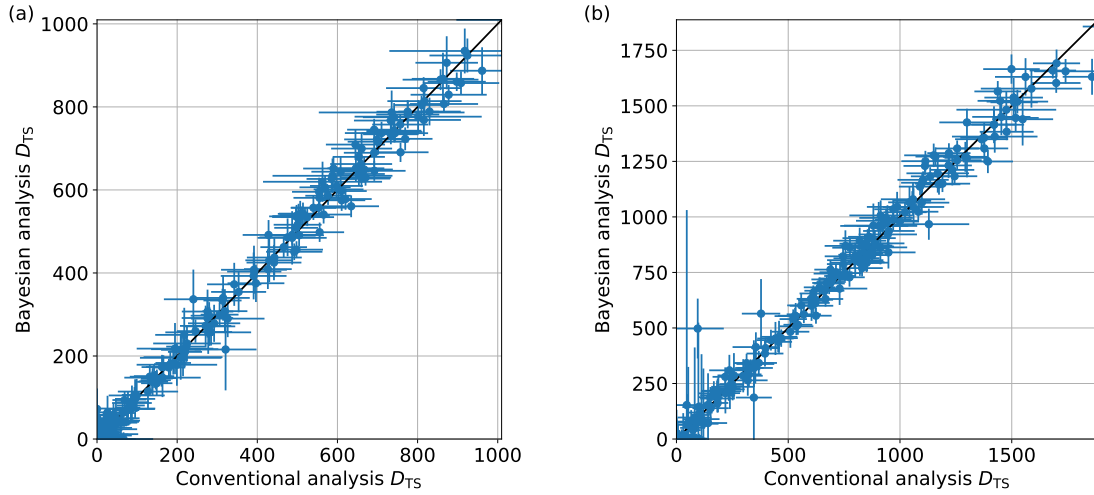


Figure 6. Comparisons between the mean values of the Thomson scattered amplitudes with one standard deviation error bars from the Bayesian approach and the conventional method for (a) JET discharge #88630 at 8.024s and (b) JET discharge #89380 at 11.776s. The black line is: $y = x$.

amplitudes of the Thomson scattered signals \mathbf{D}_{TS} from all the spatial locations, we need to obtain \mathbf{A}_{TS} given the measured raw HRTS data (see Equation (2)). Thus, we marginalise out all the other parameters except $A_{\text{TS}}^{i,j}$ from the posterior as

$$P(A_{\text{TS}}^{i,j} | \mathbf{D}_{\text{HRTS}}^{i,j}) = \int P(A_{\text{TS}}^{i,j}, A_{\text{PS}}^{i,j}, V_{\text{B}}^{i,j}, t_{\text{TS}}^{i,j}, t_{\text{PS}}^{i,j}, \tau_{\text{laser}}^{i,j}, \tau_{\text{electronics}}^{i,j} | \mathbf{D}_{\text{HRTS}}^{i,j}) dA_{\text{PS}}^{i,j} dV_{\text{B}}^{i,j} dt_{\text{TS}}^{i,j} dt_{\text{PS}}^{i,j} d\tau_{\text{laser}}^{i,j} d\tau_{\text{electronics}}^{i,j}. \quad (17)$$

We perform the marginalisation by collecting the values of $A_{\text{TS}}^{i,j}$ from sample vectors $[A_{\text{TS}}^{i,j}, A_{\text{PS}}^{i,j}, V_{\text{B}}^{i,j}, t_{\text{TS}}^{i,j}, t_{\text{PS}}^{i,j}, \tau_{\text{laser}}^{i,j}, \tau_{\text{electronics}}^{i,j}]$ of the posterior given by Equation (16). The collected values of $A_{\text{TS}}^{i,j}$ are equivalent to samples drawn from the marginal posterior distribution $P(A_{\text{TS}}^{i,j} | \mathbf{D}_{\text{HRTS}}^{i,j})$ given by Equation (17). Finally, we define the mean and variance of the amplitudes of the Thomson scattered signal from the j^{th} spectral channel of the i^{th} spatial position as $D_{\text{TS}}^{i,j}$ and $(\sigma_{\text{TS}}^{i,j})^2$ for profile inference in the following section, respectively, which are calculated as

$$D_{\text{TS}}^{i,j} = \int A_{\text{TS}}^{i,j} P(A_{\text{TS}}^{i,j} | \mathbf{D}_{\text{HRTS}}^{i,j}) dA_{\text{TS}}^{i,j}, \quad (18)$$

$$(\sigma_{\text{TS}}^{i,j})^2 = \int (A_{\text{TS}}^{i,j} - D_{\text{TS}}^{i,j})^2 P(A_{\text{TS}}^{i,j} | \mathbf{D}_{\text{HRTS}}^{i,j}) dA_{\text{TS}}^{i,j}. \quad (19)$$

We emphasise that our method infers the amplitudes of the Thomson scattered signals $A_{\text{TS}}^{i,j}$ by taking into account all possible values of all the other parameters $A_{\text{PS}}^{i,j}$, $V_{\text{B}}^{i,j}$, $t_{\text{TS}}^{i,j}$, $t_{\text{PS}}^{i,j}$, $\tau_{\text{laser}}^{i,j}$ and $\tau_{\text{electronics}}^{i,j}$. As discussed in Section 2.1, the parasitic signals measured raw data \mathbf{D}_{HRTS} . We treat the inferred \mathbf{D}_{TS} as an observed one for the profile inference.

might change over laser pulses during plasma discharges, and our method takes that into account by marginalisation, to arrive at a proper distribution of $A_{\text{TS}}^{i,j}$ from the raw HRTS measurements. In addition, our method uses a more realistic signal model for the Thomson scattered and parasitic signals (Equations (2) and (3)) and uncertainty model which takes into account electronics and Photon noises. In contrast, the conventional method uses a Gaussian signal model and does not perform the marginalisation to calculate $A_{\text{TS}}^{i,j}$. The mean values of the Thomson scattered amplitudes with one standard deviation error bars from the Bayesian approach and the conventional method are compared as shown in Figure 6. In general, the two results are comparable to each other, but there are notable differences on the size of error bars, especially when the signal level is low.

3.2. Inference on the electron temperature and density profiles

3.2.1. Likelihood. To obtain the posterior probability of electron temperature and density profiles, \mathbf{T}_e and \mathbf{n}_e , the calibration factor C_{TS} , and the hyperparameters, \mathbf{M}_{T_e} and \mathbf{M}_{n_e} , given \mathbf{D}_{TS} and $\mathbf{D}_{\text{interf}}$, we need to model two likelihoods, i.e., one for the Thomson scattered data $P(\mathbf{D}_{\text{TS}}|\mathbf{T}_e, \mathbf{n}_e, C_{\text{TS}})$ and the other for the FIR interferometer data $P(\mathbf{D}_{\text{interf}}|\mathbf{n}_e)$ as described in Equation (12).

We assume that the conditional probability of the Thomson scattered data $P(\mathbf{D}_{\text{TS}}|\mathbf{T}_e, \mathbf{n}_e, C_{\text{TS}})$ is a multivariate Gaussian distribution whose mean is $\mathbf{D}_{\text{TS}} = \{D_{\text{TS}}^{i,j}|i = 1, 2, \dots, 63, j = 1, \dots, 4\} = [D_{\text{TS}}^{1,1}, D_{\text{TS}}^{1,2}, \dots, D_{\text{TS}}^{63,3}, D_{\text{TS}}^{63,4}]$ (63 spatial positions and four spectral channels for each polychromator resulting in total of $63 \times 4 = 252$ amplitudes) with the covariance Σ_{TS} as

$$\Sigma_{\text{TS}} = \begin{pmatrix} (\sigma_{\text{TS}}^{1,1})^2 & 0 & \dots & 0 & 0 \\ 0 & (\sigma_{\text{TS}}^{1,2})^2 & \dots & 0 & 0 \\ \vdots & \vdots & \ddots & \vdots & \vdots \\ 0 & 0 & \dots & (\sigma_{\text{TS}}^{63,3})^2 & 0 \\ 0 & 0 & \dots & 0 & (\sigma_{\text{TS}}^{63,4})^2 \end{pmatrix}. \quad (20)$$

We have calculated $D_{\text{TS}}^{i,j}$ and $(\sigma_{\text{TS}}^{i,j})^2$ in Section 3.1. Thus, we have

$$P(\mathbf{D}_{\text{TS}}|\mathbf{T}_e, \mathbf{n}_e, C_{\text{TS}}) = \frac{1}{\sqrt{(2\pi)^k |\Sigma_{\text{TS}}|}} \exp\left(-\frac{1}{2}(\mathbf{D}_{\text{TS}} - \mathbf{A}_{\text{TS}\star})^T \Sigma_{\text{TS}}^{-1} (\mathbf{D}_{\text{TS}} - \mathbf{A}_{\text{TS}\star})\right), \quad (21)$$

where $\mathbf{A}_{\text{TS}\star} = \{A_{\text{TS}\star}^{i,j}|i = 1, 2, \dots, 63, j = 1, \dots, 4\} = [A_{\text{TS}\star}^{1,1}, A_{\text{TS}\star}^{1,2}, \dots, A_{\text{TS}\star}^{63,3}, A_{\text{TS}\star}^{63,4}]$ is a *predicted* quantity (denoted with an additional subscript \star) calculated by Equation (1) given the parameters of \mathbf{T}_e , \mathbf{n}_e and C_{TS} . Notice the difference between $\mathbf{A}_{\text{TS}\star}$ and \mathbf{A}_{TS} , where the latter is an *observed* quantity from the raw HRTS data. Here, k is the total number of Thomson scattered amplitudes, i.e. $k = 63 \times 4 = 252$. We formulate the likelihood for the Thomson scattered data as a multivariate Gaussian distribution for computational efficiency.

With the same argument, the conditional probability of the FIR interferometer data $P(\mathbf{D}_{\text{interf}}|\mathbf{n}_e)$ is

$$P(\mathbf{D}_{\text{interf}}|\mathbf{n}_e) = \frac{1}{\sqrt{(2\pi)^l |\boldsymbol{\Sigma}_{\text{interf}}|}} \exp\left(-\frac{1}{2}(\mathbf{D}_{\text{interf}} - \mathbf{V}_{\text{interf}})^T \boldsymbol{\Sigma}_{\text{interf}}^{-1} (\mathbf{D}_{\text{interf}} - \mathbf{V}_{\text{interf}})\right), \quad (22)$$

where $\mathbf{V}_{\text{interf}} = \{V_{\text{interf}}^i | i = 1, 2, \dots, 8\} = [V_{\text{interf}}^{i=1}, V_{\text{interf}}^{i=2}, \dots, V_{\text{interf}}^{i=8}]$ is a set of the predicted line integrated densities calculated by Equation (5) given the parameter of \mathbf{n}_e . Here, $l = 8$ representing the eight lines of sight. The covariance matrix $\boldsymbol{\Sigma}_{\text{interf}}$ is an $l \times l$ diagonal matrix, where the diagonal elements describe the uncertainties, i.e., variance, of the eight channels of the FIR interferometer system. Relevant measured quantities $\mathbf{D}_{\text{interf}}$ and $\boldsymbol{\Sigma}_{\text{interf}}$ are retrieved from the data source [5, 29], i.e., JET database.

3.2.2. Prior. We now turn our attention to model the prior probabilities, which are $P(\mathbf{T}_e|\mathbf{M}_{T_e})$, $P(\mathbf{n}_e|\mathbf{M}_{n_e})$, $P(\mathbf{M}_{T_e})$, $P(\mathbf{M}_{n_e})$ and $P(C_{\text{TS}})$, in Equation (12).

The prior probabilities of \mathbf{T}_e and \mathbf{n}_e are modelled by using the Gaussian processes with the zero mean function (Equation (6)) and the covariance function $\Sigma(\psi_N^i, \psi_N^j)$ (Equation (8)). We form the Gaussian process priors as

$$P(\mathbf{T}_e|\mathbf{M}_{T_e}) = \frac{1}{\sqrt{(2\pi)^s |\boldsymbol{\Sigma}_{\mathbf{T}_e}|}} \exp\left(-\frac{1}{2}(\mathbf{T}_e - \mathbf{0})^T \boldsymbol{\Sigma}_{\mathbf{T}_e}^{-1} (\mathbf{T}_e - \mathbf{0})\right), \quad (23)$$

$$P(\mathbf{n}_e|\mathbf{M}_{n_e}) = \frac{1}{\sqrt{(2\pi)^s |\boldsymbol{\Sigma}_{\mathbf{n}_e}|}} \exp\left(-\frac{1}{2}(\mathbf{n}_e - \mathbf{0})^T \boldsymbol{\Sigma}_{\mathbf{n}_e}^{-1} (\mathbf{n}_e - \mathbf{0})\right), \quad (24)$$

where $s = 50$ denotes the number of flux surfaces we use to infer the profiles in this work. $\mathbf{0}$ is the zero vector, and the covariance matrix $\boldsymbol{\Sigma}_{\oplus}$ (where the subscript \oplus representing either \mathbf{T}_e or \mathbf{n}_e) is defined as

$$\boldsymbol{\Sigma}_{\oplus} = \begin{pmatrix} \Sigma_{\oplus}(\psi_N^{i=1}, \psi_N^{i=1}) & \Sigma_{\oplus}(\psi_N^{i=1}, \psi_N^{i=2}) & \cdots & \Sigma_{\oplus}(\psi_N^{i=1}, \psi_N^{i=s}) \\ \Sigma_{\oplus}(\psi_N^{i=2}, \psi_N^{i=1}) & \Sigma_{\oplus}(\psi_N^{i=2}, \psi_N^{i=2}) & \cdots & \Sigma_{\oplus}(\psi_N^{i=2}, \psi_N^{i=s}) \\ \vdots & \vdots & \ddots & \vdots \\ \Sigma_{\oplus}(\psi_N^{i=s}, \psi_N^{i=1}) & \Sigma_{\oplus}(\psi_N^{i=s}, \psi_N^{i=2}) & \cdots & \Sigma_{\oplus}(\psi_N^{i=s}, \psi_N^{i=s}) \end{pmatrix}. \quad (25)$$

We set the prior probabilities of the hyperparameters $P(\mathbf{M}_{T_e})$ and $P(\mathbf{M}_{n_e})$ to be uniform distributions. Likewise, the prior of the calibration factor $P(C_{\text{TS}})$ is set to be a uniform distribution.

3.2.3. Posterior. Equation (12) provides us the joint posterior probability of \mathbf{T}_e , \mathbf{n}_e , C_{TS} , \mathbf{M}_{T_e} and \mathbf{M}_{n_e} with the likelihoods, i.e., Equations (21) and (22), and the prior probabilities, i.e., Equations (23) and (24) together with the uniform distributions for C_{TS} , \mathbf{M}_{T_e} and \mathbf{M}_{n_e} . The joint posterior distribution of \mathbf{T}_e , \mathbf{n}_e , C_{TS} , \mathbf{M}_{T_e} and \mathbf{M}_{n_e} is explored by MCMC sampling with the adaptive Metropolis-Hastings algorithm [38, 39, 40]. The inference results for JET discharge #88630 at 10.526 s (L-mode) are shown in Figure 7:

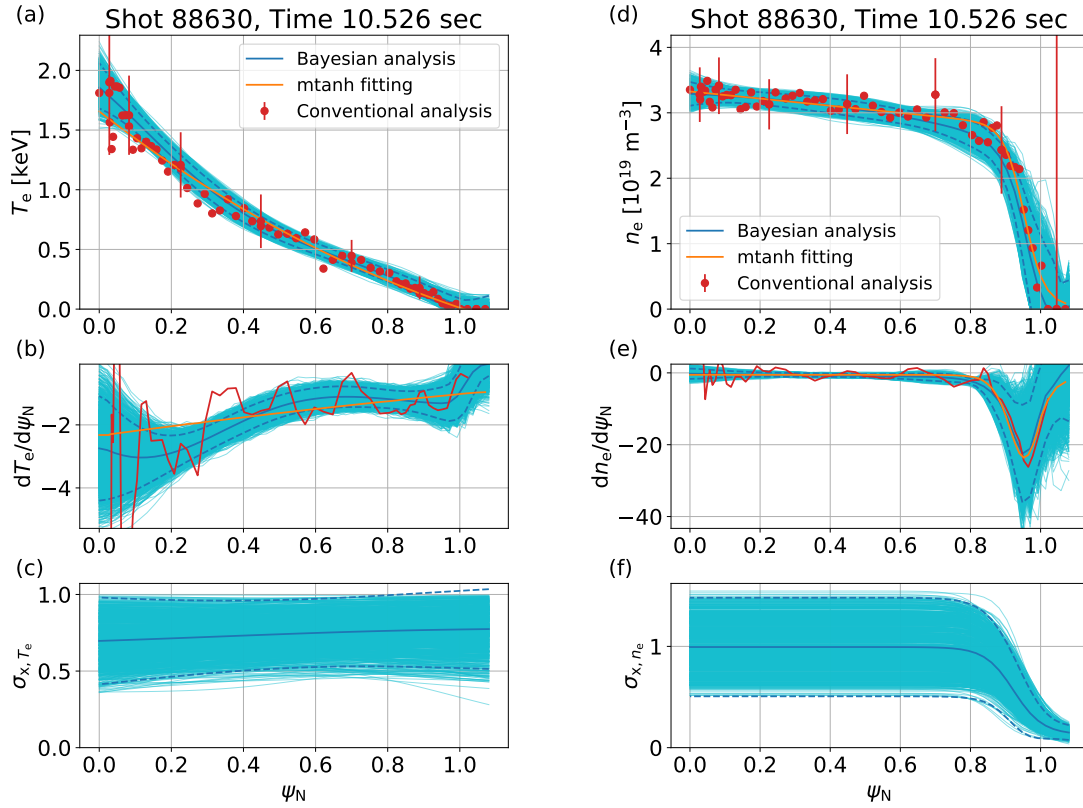


Figure 7. Inference results for JET discharge #88630 at 10.526 s (L-mode): (a) T_e profiles, (b) T_e gradient, (c) length scale of T_e profiles, (d) n_e profiles, (e) n_e gradient and (f) length scale of n_e profiles. The thick and light blue lines are the mean and samples, respectively, of the marginal joint posterior distributions. The blue dashed lines are the lower and upper boundaries of two standard deviation ($\pm 2\sigma$) marginal posterior uncertainty bands. For comparison, the electron temperature and density profiles (red dots with $\pm 2\sigma$ error bars on a few points) and gradients (red lines) from the conventional analysis of the HRTS system [20] are shown. The results (orange lines) of a fitted modified hyperbolic tangent function [33] to the conventional analysis are also presented here. The red vertical line in (d) indicates a large uncertainty of the conventional analysis outside of the last closed flux surface due to a small signal-to-noise ratio.

(a) T_e profiles, (b) T_e gradient, (c) length scale of T_e profiles, (d) n_e profiles, (e) n_e gradient and (f) length scale of n_e profiles. The electron temperature(density) profiles are obtained by marginalising over the electron density(temperature) profiles, the calibration factor C_{TS} and hyperparameters \mathbf{M}_{T_e} and \mathbf{M}_{n_e} . Similarly, the length scale profiles of T_e and n_e are obtained by marginalising over all the other parameters. The gradient profiles are calculated numerically from these marginalised T_e and n_e profiles. The thick and light blue lines are the mean and samples, respectively, of the marginal joint posterior distributions. The blue dashed lines are the lower and upper boundaries of two standard deviation ($\pm 2\sigma$) marginal posterior uncertainty bands.

For comparison, we show, in Figure 7, the electron temperature and density profiles

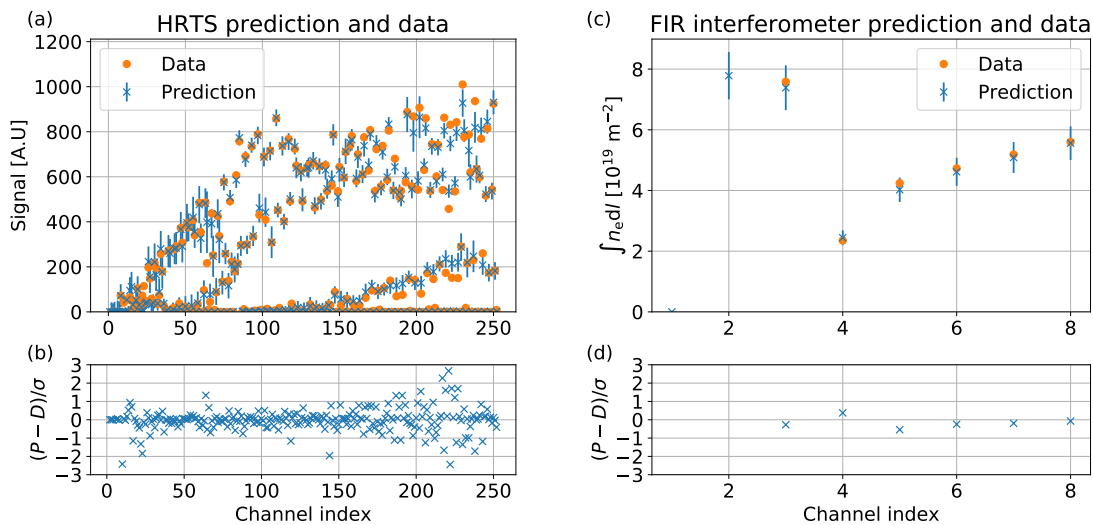


Figure 8. The data (orange dots) and predictions (blue crosses with $\pm 1\sigma$ error bars) of (a) the HRTS and (c) the FIR interferometer systems for JET discharge #88630 at 10.526s. The differences between the predictions P and data D divided by the uncertainties σ are shown in (b) and (d). Note that the channels #1 and #2 of the FIR interferometer system were not available for this discharge, hence no measured line integrated densities for these channels.

(red dots with $\pm 2\sigma$ error bars on a few points) and T_e and n_e gradient profiles (red lines) from the conventional analysis of the HRTS system [20]. The gradient profiles from the conventional analysis are calculated from two neighbouring points then smoothed by a simple moving mean with five points. We also present the results (orange lines) of a fitted modified hyperbolic tangent function [33] to the conventional analysis. The Bayesian method reproduces the gradient profiles which agree with those from the conventional method within the marginal posterior uncertainties.

The data (orange dots) and predictions (blue crosses with $\pm 1\sigma$ error bar) of the HRTS and the FIR interferometer systems are shown in Figure 8 (a) and (c). The predictions are calculated through Equations (1) and (5) given the mean of the joint posterior distribution. The differences between the predictions P and data D divided by the uncertainties σ are also shown in Figure 8 (b) and (d). The data and predictions agree within the uncertainties.

An example of the electron temperature and density profiles of a JET H-mode discharge (#89380 at 11.776s) is shown in Figure 9. The Gaussian processes infer the pedestal gradients of the electron temperature and density profiles by taking account of all possible hyperparameter values and marginalising them out. Note that we have not included the spatial instrument response of the HRTS system because all the HRTS data used in this work are obtained from the present HRTS configuration that affects the pedestal gradient minimally [21].

We emphasise that our method inferring profiles of electron temperature and density

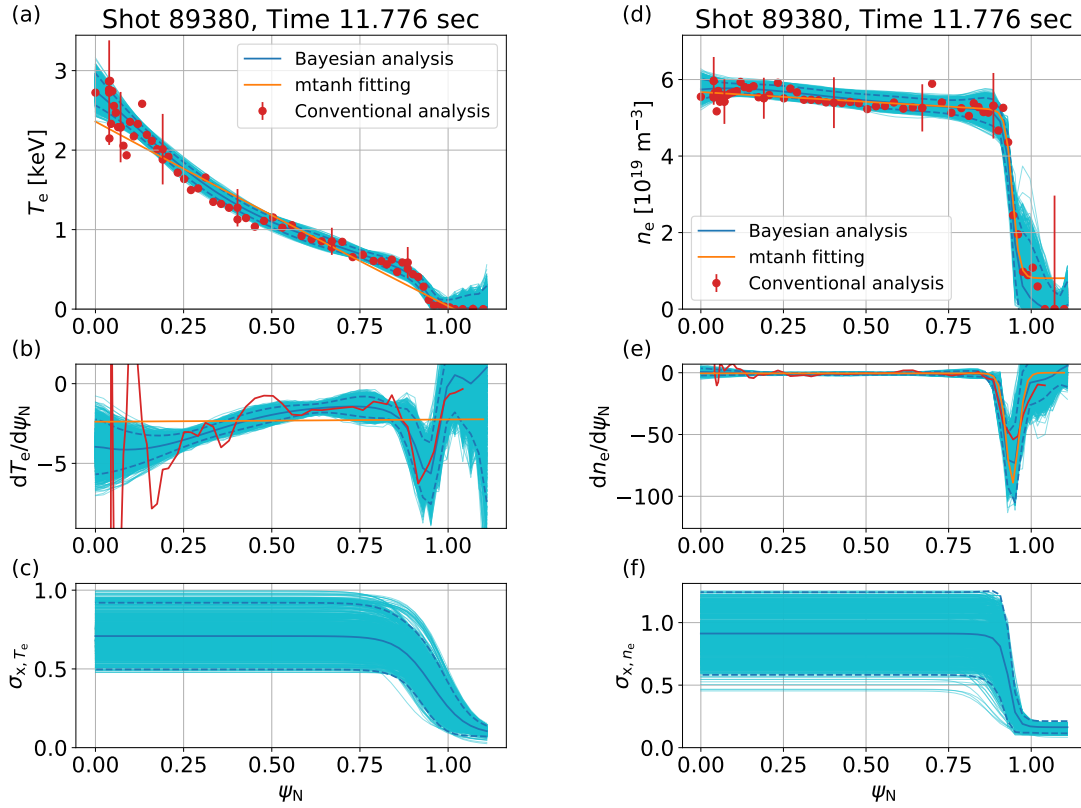


Figure 9. Same as Figure 7 for a JET H-mode discharge (#89380 at 11.776 s).

do not depend on any parametrisation due to the usage of non-parametric Gaussian processes with the hyperparameters. The choice of Gaussian process class will result in different prior probabilities for different profile shapes. At the same time, the Gaussian process is still a universal approximator, so given enough data the actual underlying profile would be recovered. It is very hard to estimate, even define, the bias introduced by the choice of Gaussian process family, but within a family the marginalisation over hyperparameters should objectively choose proper smoothnesses. The choice of Gaussian process family (in this case the hyperbolic tangent function) will in the end correspond to a physics assumption, though a much weaker one than a strict parameterised function. In no case though will the shape be related (not even weakly) to a hyperbolic tangent curve. Thus, non-hyperbolic tangent profile shapes, e.g., hollow profiles, can be inferred as shown in Figure 10 where the profile shapes are fully determined by the data, taking account of all possible combinations of C_{TS} , \mathbf{M}_{T_e} and \mathbf{M}_{n_e} .

This Gaussian process family well reproduces all profile shapes we have examined including highly non-monotonic profiles. Nevertheless, there might be cases which are not well represented by this Gaussian process family. Extensive usage of our method will show how versatile this Gaussian process parameterisation is.

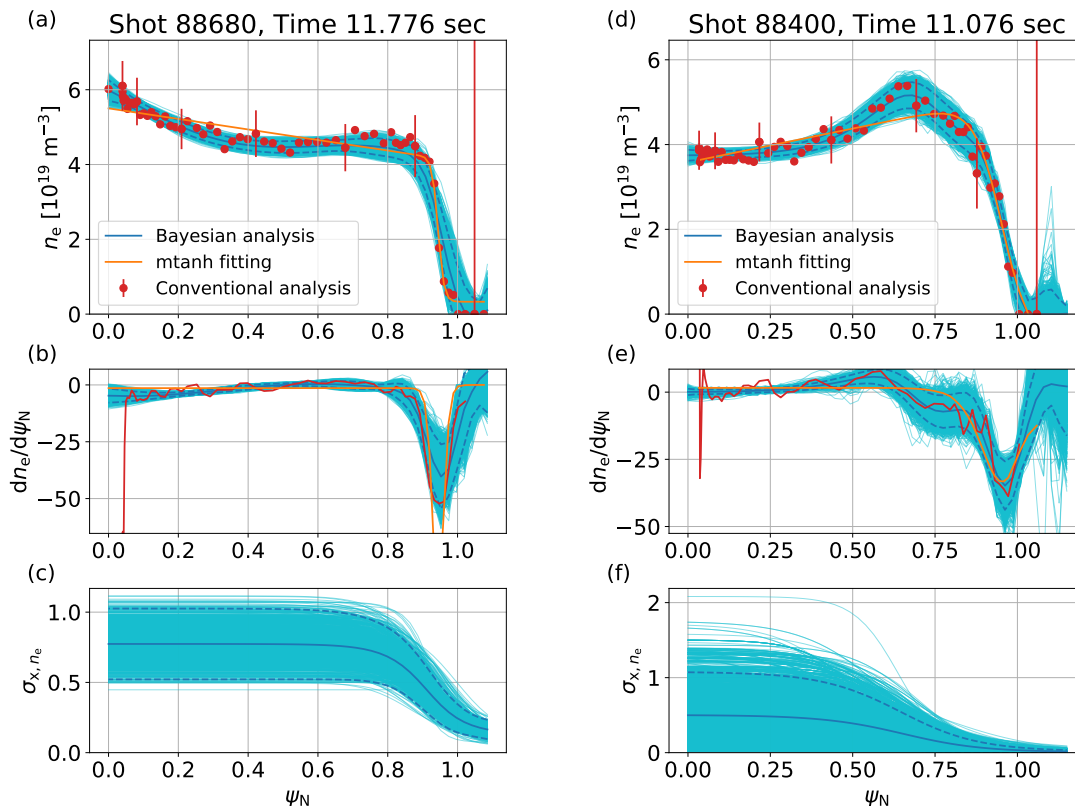


Figure 10. Same as Figure 7 for n_e inference results for (a), (b) and (c) JET discharge #88680 at 11.776 s (H-mode plasma with 6 MW neutral beam injection) and (d), (e) and (f) #88400 at 11.076 s (H-mode plasma with pellet injection).

3.3. Discussion on the calibration factor C_{TS}

The electron density calibration factor C_{TS} for the HRTS system is set as a single unknown parameter for all the spectral channels of all the polychromators and inferred by sampling the joint posterior distribution, i.e., Equation (12), that can explain both the measured HRTS and FIR interferometer data. Figure 11 shows the mean (thick segmented blue lines) and the samples (light blue lines) from the marginalised C_{TS} posterior distribution over all the other parameters which are electron temperature, density and their associated hyperparameters for multiple time points of several JET discharges.

The inferred calibration factor may provide us useful information on the HRTS system. For instance, relatively large variation of the calibration factor within a single discharge, e.g., JET discharge #88380 in Figure 11, may be caused by: i) a fluctuation of the laser energy, ii) a laser misalignment or iii) over/under-estimation of the plasma volume via the EFIT code. The overall trend of the calibration factor over many discharges may suggest us unforeseen slow aberration of the instruments such as contamination on the collecting optics (by dust for example). Our method can handle the temporal

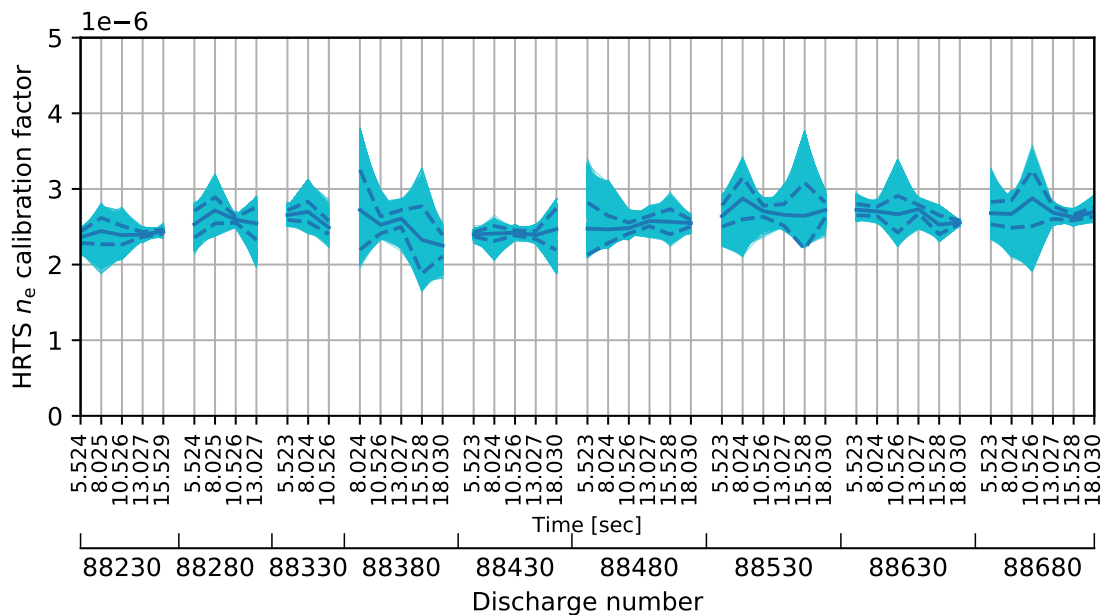


Figure 11. Evolution of the electron density calibration factor C_{TS} over multiple JET discharges. The upper and lower labels on the abscissa are the time points and the discharge numbers, respectively. The thick segmented blue lines show the mean of the samples (light blue lines) from the marginalised C_{TS} posterior distribution. Evolution of C_{TS} may provide us how the HRTS system vary over time. The blue dashed lines are the lower and upper boundaries of one standard deviation marginal posterior uncertainty bands.

variation of C_{TS} as well as the uncertainties of C_{TS} and its influence on the profile quantities.

4. Conclusions

We have developed and presented a Bayesian inference scheme for electron temperature and density profiles using non-parametric Gaussian processes consistent with the high resolution Thomson scattering (HRTS) and the far infrared (FIR) interferometer data from JET. The forward models of both systems are constructed within the Minerva framework, individually and combined together. Our method consists of two steps: i) extracting the amplitudes of the Thomson scattered signals from the raw HRTS measurements, and ii) inferring the electron temperature and density profiles.

The raw HRTS measurements contain not only the Thomson scattered but also the parasitic signals which are external Raman scattered and stray light signals. These signals are carefully modelled by taking account of the instrument effects with the associated uncertainties which are electronics and photon noises. The joint posterior distribution of the Thomson scattered and the parasitic signals are explored by Markov chain Monte Carlo (MCMC) sampling, and the amplitudes of the Thomson scattered signals are

obtained by marginalising out all the other parameters. The mean and variance of the amplitudes define the observed quantities for the profile inference.

The electron temperature and density profiles are modelled by non-parametric Gaussian processes. The profiles are inferred from the observed amplitudes of the Thomson scattered signals and the FIR interferometer data by exploring (with MCMC sampling) the joint posterior distribution of the electron temperature and density profiles, the electron density calibration factor of the HRTS system and the hyperparameters. The electron temperature and density profiles are obtained by marginalising out all the other parameters. Therefore, these profiles do not depend on a specific value of hyperparameters nor any parametric regressions which may restrain the shape of the profiles significantly. In addition, combining the HRTS and the FIR interferometer data allows us to infer the calibration factor and its uncertainty, and it may provide us knowledge on unforeseen aberration of the diagnostic systems over time.

These inference results, including the profile samples, can be used for further advanced investigation such as transport analysis with TRANSP [49]. Samples of gradient profiles can be fed to transport codes to extract uncertainty information on calculated physics parameters.

5. Acknowledgement

This work is supported by National R&D Program through the National Research Foundation of Korea (NRF) funded by the Ministry of Science and ICT (Grant No. 2017M1A7A1A01015892 and 2017R1C1B2006248) and the the KAI-NEET, KAIST, Korea. This work has been carried out within the framework of the EUROfusion Consortium and has received funding from the Euratom research and training programme 2014-2018 and 2019-2020 under grant agreement No 633053. The views and opinions expressed herein do not necessarily reflect those of the European Commission.

Appendix A. Details on the Thomson scattering model, i.e., Equation (1)

Thomson scattered energy E per unit solid angle Ω per unit wavelength λ that depends on the electron temperature T_e and density n_e is given by Naito formula [41]

$$\frac{\partial^2 E}{\partial \Omega \partial \lambda} = r_e^2 n_e E_{\text{laser}} L \frac{S(\lambda, \theta, T_e)}{\lambda_{\text{laser}}}, \quad (\text{A.1})$$

where r_e is the classical electron radius, E_{laser} the energy of incident laser, L a scattering length, S the spectral density function which depends on scattering wavelength λ and angle θ in addition to the electron temperature T_e . Since $N = \frac{\lambda}{hc} E$ where N is the number of photons at the wavelength λ , Equation (A.1) can be rewritten as

$$\frac{\partial^2 N}{\partial \Omega \partial \lambda} = \frac{\lambda}{hc} \frac{\partial^2 E}{\partial \Omega \partial \lambda}, \quad (\text{A.2})$$

where h is the Planck constant and c the speed of light.

Taking account of spectral response functions of Thomson scattering diagnostic systems (in this case, the HRTS system) $\phi(\lambda)$, which include the transmittance of optics and polychromator filter functions, the number of collected photons N_{TS} is

$$\begin{aligned} N_{\text{TS}} &= \iint \phi(\lambda) \frac{\partial^2 N}{\partial \Omega \partial \lambda} d\Omega d\lambda \\ &= \iint \phi(\lambda) \frac{\lambda}{hc} r_e^2 n_e E_{\text{laser}} L \frac{S(\lambda, \theta, T_e)}{\lambda_{\text{laser}}} d\Omega d\lambda \\ &\approx L \Delta \Omega n_e E_{\text{laser}} \int \phi(\lambda) \frac{\lambda}{hc} r_e^2 \frac{S(\lambda, \theta, T_e)}{\lambda_{\text{laser}}} d\lambda, \end{aligned} \quad (\text{A.3})$$

and the last line is obtained by approximating $\int d\Omega$ to $\Delta \Omega$.

Detectors convert the collected photons to an electronics signal A_{TS} with their gain factor G , thus we have

$$A_{\text{TS}} = G L \Delta \Omega \phi^{1,1}(\lambda_N) n_e E_{\text{laser}} \int \frac{\phi(\lambda)}{\phi^{1,1}(\lambda_N)} \frac{\lambda}{hc} r_e^2 \frac{S(\lambda, \theta, T_e)}{\lambda_{\text{laser}}} d\lambda, \quad (\text{A.4})$$

where $\phi^{1,1}(\lambda_N)$ is a normalisation factor for the spectral response functions (the value of the spectral response function of the first spectral channel of the first spatial position at the wavelength $\lambda_N = 1020$ nm in our case).

Equation (1) is obtained by letting the electron density calibration factor $C_{\text{TS}} = G L \Delta \Omega \phi^{1,1}(\lambda_N)$, that is

$$A_{\text{TS}} = C_{\text{TS}} n_e E_{\text{laser}} \int \frac{\phi(\lambda)}{\phi^{1,1}(\lambda_N)} (\lambda) \frac{\lambda}{hc} r_e^2 \frac{S(\lambda, \theta, T_e)}{\lambda_{\text{laser}}} d\lambda. \quad (\text{A.5})$$

References

- [1] Litaudon X *et al.* 2017 *Nuclear Fusion* **57** 102001 ISSN 0029-5515 URL <http://stacks.iop.org/0029-5515/57/i=10/a=102001?key=crossref.17a0f33a13c4a2bbaafb54b4eb7df30>
- [2] Wolf R *et al.* 2017 *Nuclear Fusion* **57** 102020 URL <https://doi.org/10.1088%2F1741-4326%2F57/10/10/102020>
- [3] Seed eScience Research *The Minerva framework* URL <https://seed-escience.org/>
- [4] Svensson J and Werner A 2007 Large Scale Bayesian Data Analysis for Nuclear Fusion Experiments *2007 IEEE International Symposium on Intelligent Signal Processing (IEEE)* pp 1–6 ISBN 978-1-4244-0829-0 URL <http://ieeexplore.ieee.org/document/4447579/>
- [5] Svensson J 2011 *JET report, EFDA-JET-PR(11)24* URL <http://www.euro-fusionscipub.org/wp-content/uploads/eurofusion/EFDP11024.pdf>
- [6] Svensson J and Werner A 2008 *Plasma Physics and Controlled Fusion* **50** 085002 ISSN 0741-3335 URL <http://stacks.iop.org/0741-3335/50/i=8/a=085002?key=crossref.8b9e7d2d10e66d8a740fcec9ab77227d>
- [7] von Nessi G T, Hole M J, Svensson J and Appel L 2012 *Physics of Plasmas* **19** 012506 ISSN 1070-664X URL <http://aip.scitation.org/doi/10.1063/1.3677362>
- [8] von Nessi G T and Hole M J 2014 *Plasma Physics and Controlled Fusion* **56** 114011 ISSN 0741-3335 URL <http://stacks.iop.org/0741-3335/56/i=11/a=114011?key=crossref.d58e08b3c9223c89bab07f760e99229e>

- [9] Bozhenkov S, Beurskens M, Molin A D, Fuchert G, Pasch E, Stoneking M, Hirsch M, Höfel U, Knauer J, Svensson J, Mora H T and Wolf R 2017 *Journal of Instrumentation* **12** P10004–P10004 ISSN 1748-0221 URL <http://stacks.iop.org/1748-0221/12/i=10/a=P10004?key=crossref.21c7d556bea6caf012906a098b133ef0>
- [10] Kwak S, Svensson J, Brix M and Ghim Y c 2016 *Review of Scientific Instruments* **87** 023501 ISSN 0034-6748 URL <http://aip.scitation.org/doi/10.1063/1.4940925>
- [11] Kwak S, Svensson J, Brix M and Ghim Y C 2017 *Nuclear Fusion* **57** 036017 ISSN 0029-5515 URL <http://stacks.iop.org/0029-5515/57/i=3/a=036017?key=crossref.78317e8d5c69c0d93e4bfd4af120a500>
- [12] Li D, Svensson J, Thomsen H, Medina F, Werner A and Wolf R 2013 *Review of Scientific Instruments* **84** 083506 ISSN 0034-6748 URL <http://aip.scitation.org/doi/10.1063/1.4817591>
- [13] Schmuck S, Svensson J, De La Luna E, Figini L, Johnson T, Alper B, Beurskens M, Fessey J, Gerbaud T and Sirinelli A 2011 Bayesian derivation of electron temperature profile using jet ece diagnostics *38th EPS Conference on Plasma Physics 2011, EPS 2011 : Europhysics Conference Abstracts (Europhysics Conference Abstracts no 35:2)* pp 1512–1515 qC 20140828
- [14] Langenberg A, Svensson J, Thomsen H, Marchuk O, Pablant N A, Burhenn R and Wolf R C 2016 *Fusion Science and Technology* **69** 560–567 ISSN 15361055 URL <https://www.tandfonline.com/doi/full/10.13182/FST15-181>
- [15] Krychowiak M 2016 *Review of Scientific Instruments* **87** 11D304 ISSN 10897623 URL <http://scitation.aip.org/content/aip/journal/rsi/87/11/10.1063/1.4964376>
- [16] Mora H T, Bozhenkov S, Knauer J, Kornejew P, Kwak S, Ford O, Fuchert G, Pasch E, Svensson J, Werner A, Wolf R and Timmermann D 2017 FPGA acceleration of Bayesian model based analysis for time-independent problems *2017 IEEE Global Conference on Signal and Information Processing (GlobalSIP) (IEEE)* pp 774–778 ISBN 978-1-5090-5990-4 URL <http://ieeexplore.ieee.org/document/8309065/>
- [17] Pavone A, Svensson J, Langenberg A, Pablant N, Hoefel U, Kwak S, Wolf R C and Team W X 2018 *Review of Scientific Instruments* **89** 10K102 ISSN 0034-6748 URL <http://aip.scitation.org/doi/10.1063/1.5039286>
- [18] Lao L, St John H, Stambaugh R, Kellman A and Pfeiffer W 1985 *Nuclear Fusion* **25** 1611–1622 ISSN 0029-5515 URL <http://stacks.iop.org/0029-5515/25/i=11/a=007?key=crossref.382b4e7e430c8741af0f7248e9a56c09>
- [19] O'Brien D, Lao L, Solano E, Garribba M, Taylor T, Cordey J and Ellis J 1992 *Nuclear Fusion* **32** 1351–1360 URL <https://doi.org/10.1088%2F0029-5515%2F32%2F8%2Fi05>
- [20] Pasqualotto R, Nielsen P, Gowers C, Beurskens M, Kempenaars M, Carlstrom T and Johnson D 2004 *Review of Scientific Instruments* **75** 3891–3893 ISSN 0034-6748 URL <http://aip.scitation.org/doi/10.1063/1.1787922>
- [21] Frassinetti L, Beurskens M N A, Scannell R, Osborne T H, Flanagan J, Kempenaars M, Maslov M, Pasqualotto R and Walsh M 2012 *Review of Scientific Instruments* **83** 013506 ISSN 0034-6748 URL <http://aip.scitation.org/doi/10.1063/1.3673467>
- [22] Scannell R 2007 *Investigation of H-mode edge profile behaviour on MAST using Thomson scattering* Ph.D. thesis University College Cork
- [23] Braithwaite G, Gottardi N, Magyar G, O'Rourke J, Ryan J and Véron D 1989 *Review of Scientific Instruments* **60** 2825–2834 ISSN 0034-6748 URL <http://aip.scitation.org/doi/10.1063/1.1140666>
- [24] Boboc A, Gelfusa M, Murari A and Gaudio P 2010 *Review of Scientific Instruments* **81** 10D538 ISSN 0034-6748 URL <http://aip.scitation.org/doi/10.1063/1.3478146>
- [25] Boboc A, Gil C, Pastor P, Spuig P, Edlington T and Dorling S 2012 *Review of Scientific Instruments* **83** 10E341 ISSN 0034-6748 URL <http://aip.scitation.org/doi/10.1063/1.4737420>
- [26] Boboc A, Bieg B, Felton R, Dalley S and Kravtsov Y 2015 *Review of Scientific Instruments* **86** 091301 ISSN 0034-6748 URL <http://aip.scitation.org/doi/10.1063/1.4929443>
- [27] Fischer R, Wendland C, Dinklage A, Gori S, Dose V and Teams W A 2002 *Plasma Physics and*

- Controlled Fusion* **44** 1501–1519 ISSN 07413335 URL <http://stacks.iop.org/0741-3335/44/i=8/a=306?key=crossref.90d7ee0715d647125b222b2bd64bea16>
- [28] Park K R, Kim K h, Kwak S, Svensson J, Lee J and Ghim Y c 2017 *Journal of Instrumentation* **12** C11022–C11022 ISSN 1748-0221 URL <http://stacks.iop.org/1748-0221/12/i=11/a=C11022?key=crossref.3a526848b7d41b2c69eed8b828346290>
- [29] Ford O P 2010 *Tokamak plasma analysis through Bayesian diagnostic modelling* Ph.D. thesis Imperial College London
- [30] Fischer R, Fuchs C J, Kurzan B, Suttrop W and Wolfrum E 2010 *Fusion Science and Technology* **58** 675–684 ISSN 1536-1055 URL <https://www.tandfonline.com/doi/full/10.13182/FST10-110>
- [31] Rasmussen C E and Williams C K I 2006 *Gaussian Processes for Machine Learning* (MIT Press)
- [32] Chilenski M, Greenwald M, Marzouk Y, Howard N, White A, Rice J and Walk J 2015 *Nuclear Fusion* **55** 023012 ISSN 0029-5515 URL <http://stacks.iop.org/0029-5515/55/i=2/a=023012?key=crossref.b22d32b1ac570a0def0ea0869bc2c1789>
- [33] Groebner R J, Mahdavi M A, Leonard A W, Osborne T H and Porter G D 2002 *Plasma Physics and Controlled Fusion* **44** 326 ISSN 07413335 URL <http://stacks.iop.org/0741-3335/44/i=5A/a=326?key=crossref.ab9f87434e30708c202f3d17568e5cc5>
- [34] Carlstrom T, Burrell K, Groebner R, Leonard A, Osborne T and Thomas D 1999 *Nuclear Fusion* **39** 1941–1947 URL <https://doi.org/10.1088%2F0029-5515%2F39%2F11%2F338>
- [35] Connor J W and Wilson H R 1999 *Plasma Physics and Controlled Fusion* **42** R1–R74 URL <https://doi.org/10.1088%2F0741-3335%2F42%2F1%2F201>
- [36] Leyland M J, Beurskens M N A, Flanagan J C, Frassinetti L, Gibson K J, Kempenaars M, Maslov M and Scannell R 2016 *Review of Scientific Instruments* **87** 013507 ISSN 0034-6748 URL <http://aip.scitation.org/doi/10.1063/1.4939855>
- [37] Fischer R, Wolfrum E and Schweinzer J 2008 *Plasma Physics and Controlled Fusion* **50** 085009 ISSN 0741-3335 URL <http://stacks.iop.org/0741-3335/50/i=8/a=085009?key=crossref.66dc3a9cef01c87d8417ae7a2c0d3d6a>
- [38] Metropolis N, Rosenbluth A W, Rosenbluth M N, Teller A H and Teller E 1953 *The Journal of Chemical Physics* **21** 1087–1092 ISSN 0021-9606 URL <http://aip.scitation.org/doi/10.1063/1.1699114>
- [39] Hastings W K 1970 *Biometrika* **57** 97–109 ISSN 1464-3510 URL <https://academic.oup.com/biomet/article/57/1/97/284580>
- [40] Haario H, Saksman E and Tamminen J 2001 *Bernoulli* **7** 223 ISSN 13507265 URL <https://www.jstor.org/stable/3318737?origin=crossref>
- [41] Naito O, Yoshida H and Matoba T 1993 *Physics of Fluids B: Plasma Physics* **5** 4256–4258 ISSN 0899-8221 URL <http://aip.scitation.org/doi/10.1063/1.860593>
- [42] Kurzan B, Jakobi M, Murmann H and Team A U 2004 *Plasma Physics and Controlled Fusion* **46** 299–317 ISSN 0741-3335 URL <http://stacks.iop.org/0741-3335/46/i=1/a=019?key=crossref.90ae7dc904113006bcfc986aa1ddac7a>
- [43] Romero J and Svensson J 2013 *Nuclear Fusion* **53** 033009 ISSN 0029-5515 URL <http://stacks.iop.org/0029-5515/53/i=3/a=033009?key=crossref.e63bc2641d1ea5a6766bf4b0dc1db9ee>
- [44] Romero J A, Dettrick S A, Granstedt E, Roche T and Mok Y 2018 *Nature Communications* **9** 691 ISSN 2041-1723 URL <http://www.nature.com/articles/s41467-018-03110-5>
- [45] ASDEX Team 1989 *Nuclear Fusion* **29** 1959–2040 ISSN 17414326 URL <http://stacks.iop.org/0029-5515/29/i=11/a=010?key=crossref.f8eff2d027380946fd88742ac88d929c>
- [46] Higdon D, Swall J and Kern J 1999 Non-stationary spatial modeling *Bayesian Statistics 6 Proceedings of the Sixth Valencia International Meeting* pp 761–768
- [47] Devinderjit Sivia J S 2006 *Data Analysis: A Bayesian Tutorial* (Oxford University Press) ISBN 0-198-56831-2
- [48] Jaynes E T 2003 *Probability Theory: The Logic of Science* (Cambridge University Press) ISBN 0-521-59271-2

- [49] Hawryluk R 1981 AN EMPIRICAL APPROACH TO TOKAMAK TRANSPORT *Physics of Plasmas Close to Thermonuclear Conditions* (Elsevier) pp 19–46 URL <https://linkinghub.elsevier.com/retrieve/pii/B9781483283852500091>

4.4 Article IV

‘Bayesian modelling of multiple diagnostics at Wendelstein 7-X’

S. KWAK, J. SVENSSON, S. BOZHENKOV, H. T. MORA, U. HOEFEL, A. PAVONE,
M. KRYCHOWIAK, A. LANGENBERG and Y.-C. GHIM

Plasma Physics and Controlled Fusion, (2020), in preparation

Bayesian modelling of multiple plasma diagnostics at Wendelstein 7-X

Sehyun Kwak^{1,2}, J. Svensson², S. Bozhnikov²,
H. Trimino Mora², U. Hoefel², A. Pavone², M. Krychowiak²,
A. Langenberg², Y.-c. Ghim¹ and W7-X Team

¹Department of Nuclear and Quantum Engineering, KAIST, Daejeon 34141, Korea, Republic of

²Max-Planck-Institut für Plasmaphysik, 17491 Greifswald, Germany

E-mail: sehyun.kwak@ipp.mpg.de

11 November 2020

Abstract. Consistent inference of the electron density and temperature has been carried out with multiple heterogeneous plasma diagnostic data sets at Wendelstein 7-X. The predictive models of the interferometer, Thomson scattering and helium beam emission spectroscopy systems have been developed in the Minerva framework and combined to a single joint model. The electron density and temperature profiles are modelled by Gaussian processes with their hyperparameters. The model parameters such as the calibration factor of the Thomson scattering system and the model predictive uncertainties are regarded as additional unknown parameters. The joint posterior probability distribution of the electron density and temperature profiles, hyperparameters of the Gaussian processes and model parameters is explored by Markov chain Monte Carlo algorithms. The posterior samples drawn from the joint posterior distribution are numerically marginalised over the hyperparameters and model parameters to obtain the marginal posterior distributions of the electron density and temperature profiles. The inference of these profiles is performed with different combinations of the interferometer and Thomson scattering data as well as either the empirical electron density and temperature constraints at the limiter/divertor positions introduced by *virtual observations* or the edge density and temperature from the helium beam emission data. Furthermore, the addition of the X-ray imaging crystal spectrometers to the joint model for the ion temperature profiles is demonstrated. All these profiles presented in this work are inferred with the optimal hyperparameters and model parameters by exploring the full joint posterior distribution which intrinsically embodies Bayesian Occam's razor.

Keywords: Interferometers, Thomson scattering diagnostics, Beam emission spectroscopy, X-ray imaging crystal spectrometers, Plasma diagnostics, Wendelstein 7-X, Minerva framework, Bayesian inference, Gaussian processes, Forward modelling, Occam's razor

Submitted to: *Plasma Phys. Control. Fusion*

1. Introduction

Consistent inference of physics parameters of fusion plasmas with their associated uncertainties is crucial to understand and to control the underlying physical phenomena in a large scale fusion experiment. Such an experiment as the Joint European Torus (JET) [1] and Wendelstein 7-X (W7-X) [2] typically employs several tens of sophisticated and complicated measurement techniques. The analysis of experimental data from each of the measurement instruments is substantially complex, therefore, to make full use of these heterogeneous data sets to refine physics parameters as rigorously as possible is challenging. In order to make this possible and practical, it is advantageous to use a framework that is capable of handling and keeping track of parameters, assumptions, predictive models and observations.

The Minerva framework has been developed to achieve consistent inference for a complex system by modularisation of models and standardisation of interfaces to connect them in a systematic way [3]. For example, a Minerva Thomson scattering (forward) model encapsulates physics and instrumental effects of a Thomson scattering system to calculate Thomson scattering signals given the laser power and wavelength, scattering angles, spectral response functions, data acquisition systems, physics parameters, i.e., electron density and temperature, and so on. These model dependencies can be fed from either other Minerva models or data sources (interfaces to databases), and model predictions such as predicted Thomson scattering signals can be directly compared to the corresponding observations. The Minerva framework automatically manages such integrations of Minerva models, and these Minerva models can be represented by a Bayesian graphical model [4], which is a transparent way of unfolding and handling the complexity of the models. These automatic model administration together with graphical representation make the joint analysis of multiple heterogeneous data sets achievable and practical. In nuclear fusion research, the Minerva framework has been used for a number of scientific applications to magnetic sensors [5], interferometers [6, 7], Thomson scattering systems [8, 9], soft X-ray spectroscopy [10], beam emission spectroscopy [11, 12], X-ray imaging crystal spectrometers [13], electron cyclotron emission [14] and effective ion charge diagnostics [15]. These Minerva models can be accelerated by a field-programmable gate array (FPGA) [16] or an artificial neural network [17, 18].

In this work, the Bayesian joint analysis of the interferometer, Thomson scattering and helium beam emission spectroscopy systems at W7-X has been carried out (followed by the addition of the X-ray imaging crystal spectrometers [13]). The conventional analysis of the interferometer [19], Thomson scattering [8] and helium beam emission spectroscopy [20] systems is typically carried out individually. The Thomson scattering system provides the local measurements of the electron density and temperature across the plasma, and the interferometer system measures line integrated electron density along the line of sight. When the calibration factor of the Thomson scattering system has not been fully identified, the electron density profiles from Thomson scattering data can be cross-calibrated with the interferometer data. For this reason, the line of sight of

the W7-X interferometer system is set to be approximately identical to the laser path of the Thomson scattering system. In order to perform the cross-calibration as precise as possible, the electron density and temperature in the edge region should be known. However, the Thomson scattering data does not typically provide a good quality of the electron density and temperature measurements in the edge region, where the electronics noise is much larger than the Thomson scattering signals. The conventional way of dealing with this problem is to assume that the electron density and temperature is zero outside the last closed magnetic flux surface (LCFS) given by the variational moments equilibrium code (VMEC) [21, 22]. The method developed in this work makes use of either the empirical electron density and temperature constraints at the limiter/divertor positions based on physics knowledge *a priori* introduced by *virtual observations* or the edge electron density and temperature measurements from the helium emission spectroscopy system. Furthermore, the X-ray imaging crystal spectrometers (XICS) [13] is integrated to the Bayesian joint model of the interferometer, Thomson scattering and helium beam emission spectroscopy systems in order to infer the electron density and temperature profiles as well as the ion temperature profiles consistent with all these measurements.

2. The model

In Bayesian inference [4, 23, 24], the probability of a hypothetical value of unknown parameters $P(H)$ can be updated to the *posterior probability* of the unknown parameters given observations $P(H|D)$ through Bayes formula:

$$P(H|D) = \frac{P(D|H)P(H)}{P(D)}. \quad (1)$$

The probability of the unknown parameters, also known as the prior probability $P(H)$, encodes the *prior knowledge* such as physics and empirical assumptions. For instance, the temperature must be positive by definition, thus, the probability of any negative temperature must be zero. The conditional probability of the observations $P(D|H)$ makes a *predictive distribution* over the observations given a hypothetical value of the unknown parameters. In other words, this predictive distribution expresses all possible values of the observations that can be measured given a hypothetical value of the unknown parameters. Typically, the mean of the predictive distribution is given by a function which encapsulates the processes happening during an experiment by taking into account physical phenomena as well as the experimental setup, for example, the instrument effects, calibrations, optics, electronics and so on, also known as a *forward model* $f(H)$. The marginal probability of the observations $P(D)$, also known as the *model evidence*, is a normalisation constant in this context.

When we have multiple heterogeneous data sets, which conditionally depend on the unknown parameters, Bayes formula can be written as:

$$P(H|\{D_i\}) = \frac{(\prod_i P(D_i|H))P(H)}{P(\{D_i\})}. \quad (2)$$

Each of the predictive distributions contains a forward model of the measurement instruments, which are typically sophisticated and complicated. They may include extra model parameters, for instance calibration factors, depending on the experimental setup. The prior distribution encodes the prior knowledge of the unknown parameters as well as hyperparameters (parameters of the prior distribution) and unknown model parameters. These prior and predictive distributions together constitute the joint probability distribution $P(H, D)$ which embodies the full relationship between all the unknown parameters and observations. This joint distribution is modelled in Minerva as a Bayesian graphical model [4].

The Minerva graph of the Bayesian joint model of the interferometer, Thomson scattering and helium beam emission spectroscopy systems is shown in Figure 1. Each node represents either a deterministic calculation (white box) or a probability function, a prior (blue circle) or a predictive probability (grey circle). Such deterministic nodes include a simple operation (e.g. `los`, a function for line integration along a line of sight), a physics model (e.g. `Thomson model`) and a data source (`ds`). The arrows indicate the conditional dependencies of these nodes. This graph represents the joint distribution of all the unknown parameters and observations which consists of all these prior and predictive distributions.

In this work, the electron density n_e and temperature T_e profiles are given as a function of the effective minor radius ρ_{eff} and modelled by Gaussian processes [25, 26, 27]. The Gaussian processes are *non-parametric* functions which associate any set of points in the domain of the functions with a random vector following a multivariate Gaussian distribution. The properties of the Gaussian processes are determined not by any parametric form but by the covariance function of the Gaussian distribution. The covariance function provides the covariance value between any two points, and the smoothness of the Gaussian processes is determined by these covariance values. In nuclear fusion research, Gaussian processes were first introduced by non-parametric tomography of the electron density and current distribution [7], and has since been used in a number of applications [9, 10, 11, 12, 13, 28].

The prior distribution of the electron temperature is given by a Gaussian process with the zero mean and squared exponential covariance function, which is one of the most common specifications of the Gaussian processes, which can be written as:

$$P(T_e | \sigma_{T_e}) = \mathcal{N}(\mu_{T_e}, \Sigma_{T_e}), \quad (3)$$

$$\mu_{T_e}(\rho_{\text{eff}}) = 0, \quad (4)$$

$$\Sigma_{T_e}(\rho_{\text{eff},i}, \rho_{\text{eff},j}) = \sigma_{f,T_e}^2 \exp\left(-\frac{(\rho_{\text{eff},i} - \rho_{\text{eff},j})^2}{2\sigma_{x,T_e}^2}\right) + \sigma_{y,T_e}^2 \delta_{ij}. \quad (5)$$

All the hyperparameters are denoted as $\sigma_{T_e} = [\sigma_{f,T_e}, \sigma_{x,T_e}]$, and σ_{y,T_e} is set to be relatively small number with respect to σ_{f,T_e} , for example $\sigma_{y,T_e}/\sigma_{f,T_e} = 10^{-3}$ to avoid numerical instabilities. The electron density can have substantially different smoothness (gradient) in the core and edge regions, and for this reason, the prior distribution of the electron

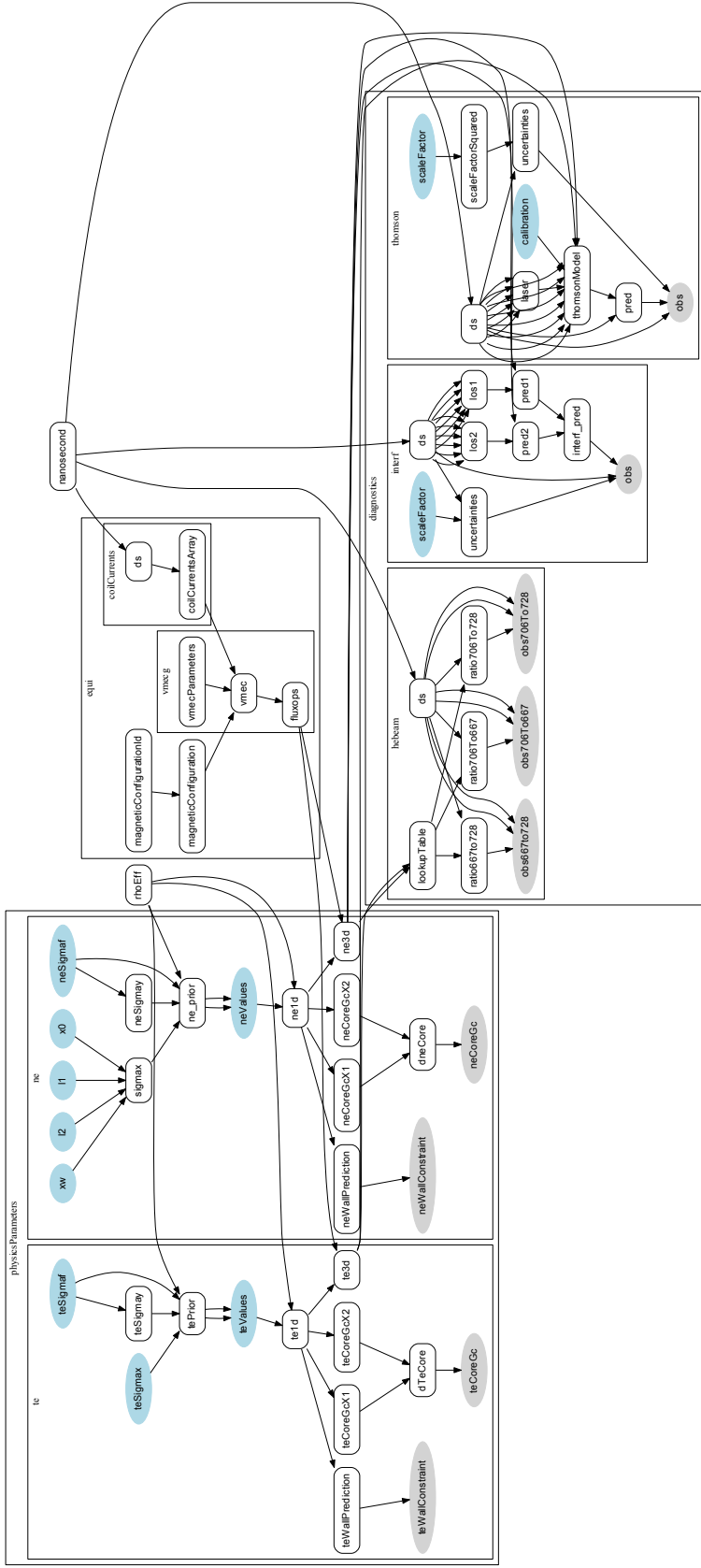


Figure 1. The Minerva graph of the Bayesian joint model of the interferometer, Thomson scattering and helium beam emission spectroscopy systems at Wendelstein 7-X. The unknown parameters and observations are shown as the blue and grey circles, respectively. The electron density n_e and temperature T_e are given as a function of the effective minor radius ρ_{eff} and mapped to x, y, z Cartesian coordinates through the coordinate transformations provided by the variational moments equilibrium code (VMEC) node. The electron density and temperature profiles are modelled by Gaussian processes with their hyperparameters, and each of the model predictions is calculated given all these unknown parameters. This graph represents the joint probability of all the unknown parameters and observations which consists of all these prior and predictive distributions.

density is modelled by a Gaussian process with the zero mean and non-stationary covariance function [29] which can be written as:

$$P(n_e | \sigma_{n_e}) = \mathcal{N}(\mu_{n_e}, \Sigma_{n_e}), \quad (6)$$

$$\mu_{n_e}(\rho_{\text{eff}}) = 0, \quad (7)$$

$$\begin{aligned} \Sigma_{n_e}(\rho_{\text{eff},i}, \rho_{\text{eff},j}) &= \sigma_{f,n_e}^2 \left(\frac{2\sigma_{x,n_e}(\rho_{\text{eff},i})\sigma_{x,n_e}(\rho_{\text{eff},j})}{\sigma_{x,n_e}(\rho_{\text{eff},i})^2 + \sigma_{x,n_e}(\rho_{\text{eff},j})^2} \right)^{\frac{1}{2}} \\ &\times \exp\left(-\frac{(\rho_{\text{eff},i} - \rho_{\text{eff},j})^2}{\sigma_{x,n_e}(\rho_{\text{eff},i})^2 + \sigma_{x,n_e}(\rho_{\text{eff},j})^2} \right) + \sigma_{y,n_e}^2 \delta_{ij}. \end{aligned} \quad (8)$$

The length scale function $\sigma_{x,n_e}(\rho_{\text{eff}})$ can be given by a hyperbolic tangent function, developed in [28] and also applied in [9], which is:

$$\sigma_{x,n_e}(\rho_{\text{eff}}) = \frac{\sigma_{x,n_e}^{\text{core}} + \sigma_{x,n_e}^{\text{edge}}}{2} - \frac{\sigma_{x,n_e}^{\text{core}} - \sigma_{x,n_e}^{\text{edge}}}{2} \tanh \frac{\rho_{\text{eff}} - \rho_{\text{eff},0,n_e}}{\rho_{\text{eff},w,n_e}}. \quad (9)$$

Again, all the hyperparameters are denoted as $\sigma_{n_e} = [\sigma_{f,n_e}, \sigma_{x,n_e}^{\text{core}}, \sigma_{x,n_e}^{\text{edge}}, \rho_{\text{eff},0,n_e}, \rho_{\text{eff},w,n_e}]$.

The electron density and temperature profiles can be mapped to x, y, z Cartesian coordinates through the coordinate transformations provided by the VMEC node. Given 3D fields of the electron density and temperature in real space, each of predictive distributions of the interferometer, Thomson scattering and helium beam emission spectroscopy data can be calculated. The interferometer system [19] is a single chord dispersion interferometer which measures the line integrated electron density along the line of sight. The forward model of the interferometer system predicts the line integral of the electron density, which is directly compared to the measurement stored in the W7-X database. The Thomson scattering system [8] collects Thomson scattered spectra from 10 to 79 spatial locations along the laser beam across the centre of the plasma. The physics model of Thomson scattering processes [30] is implemented in the Thomson scattering model [8, 9] which makes predictions of the Thomson scattered spectra given the electron density and temperature. The calibration factor of the Thomson scattering system has not been yet fully identified, thus the calibration factor is regarded as an additional unknown parameter. The interferometer system is designed to cross-calibrate the Thomson scattering system, and for this reason, the line of sight of the W7-X interferometer is set to be approximately identical to the laser path of the Thomson scattering system.

The joint posterior distribution of the Bayesian joint model of the interferometer

and Thomson scattering systems can be written as:

$$\begin{aligned}
& P(n_e, T_e, \sigma_{n_e}, \sigma_{T_e}, \sigma_{\text{DI}}, \sigma_{\text{TS}}, C_{\text{TS}} | D_{\text{DI}}, D_{\text{TS}}) \\
&= \frac{P(D_{\text{DI}}, D_{\text{TS}} | n_e, T_e, \sigma_{n_e}, \sigma_{T_e}, \sigma_{\text{DI}}, \sigma_{\text{TS}}, C_{\text{TS}}) P(n_e, T_e, \sigma_{n_e}, \sigma_{T_e}, \sigma_{\text{DI}}, \sigma_{\text{TS}}, C_{\text{TS}})}{P(D_{\text{DI}}, D_{\text{TS}})} \\
&= \frac{P(D_{\text{DI}} | n_e, \sigma_{\text{DI}}) P(D_{\text{TS}} | n_e, T_e, \sigma_{\text{TS}}, C_{\text{TS}}) P(n_e | \sigma_{n_e}) P(T_e | \sigma_{T_e}) P(\sigma_{n_e}) P(\sigma_{T_e})}{P(D_{\text{DI}}) P(D_{\text{TS}})} \\
&\times P(\sigma_{\text{DI}}) P(\sigma_{\text{TS}}) P(C_{\text{TS}}), \tag{10}
\end{aligned}$$

where σ_{n_e} and σ_{T_e} are the hyperparameters of the Gaussian processes of the electron density and temperature profiles. The predictive distributions $P(D_{\text{DI}} | n_e, \sigma_{\text{DI}})$ and $P(D_{\text{TS}} | n_e, T_e, \sigma_{\text{TS}})$ are modelled as Gaussian distributions whose mean and standard deviation are the predictions of the forward models and predictive uncertainties, which are proportional to the measurement uncertainties with scale factors σ_{DI} and σ_{TS} . These scale factors are regarded as additional unknown parameters due to our incomplete knowledge of measurement uncertainties. These model parameters and the hyperparameters of the Gaussian processes can be optimised to maximise the posterior probability of the model, which takes into account the principle of Occam's razor [31, 32].

The calibration factor of the Thomson scattering system C_{TS} is also treated as an additional unknown parameter, therefore, the Thomson scattering system will be automatically cross-calibrated with the interferometer data. Nevertheless, the electron density and temperature in the edge region play an important role in this cross-calibration, since the profile boundary depends on the observations in the edge region. Here, we utilise our physics and empirical knowledge to impose such observations in the edge region by assuming that the electron density and temperature are not significantly high enough to melt down the limiter and divertor of the W7-X experiment [2]. These low density and temperature constraints can be introduced by *virtual* observations at the limiter/divertor positions *a priori* as a part of the prior distributions, which can be written as:

$$P(D_{v,n_e} | n_e) = \mathcal{N}(n_e(x_{\text{wall}}, y_{\text{wall}}, z_{\text{wall}}), \sigma_{v,n_e}^2), \tag{11}$$

$$P(D_{v,T_e} | T_e) = \mathcal{N}(T_e(x_{\text{wall}}, y_{\text{wall}}, z_{\text{wall}}), \sigma_{v,T_e}^2), \tag{12}$$

where $x_{\text{wall}}, y_{\text{wall}}, z_{\text{wall}}$ are the spatial locations of the limiter/divertor. The density and temperature constraints at the limiter/divertor are set to be reasonably low: $D_{\text{wall},n_e} = 10^{15} \text{ m}^{-3}$, $\sigma_{\text{wall},n_e} = 10^{15} \text{ m}^{-3}$, $D_{\text{wall},T_e} = 0.1 \text{ eV}$ and $\sigma_{\text{wall},T_e} = 0.1 \text{ eV}$. In the same way, we also introduce the zero gradients of the electron density and temperature profiles at the magnetic axis. Given these virtual observations, the joint posterior

probability can be written as:

$$\begin{aligned}
& P(n_e, T_e, \sigma_{n_e}, \sigma_{T_e}, \sigma_{DI}, \sigma_{TS}, C_{TS} | D_{DI}, D_{TS}, D_{v,n_e}, D_{v,T_e}) \\
&= \frac{P(D_{DI}, D_{TS}, D_{v,n_e}, D_{v,T_e} | n_e, T_e, \sigma_{n_e}, \sigma_{T_e}, \sigma_{DI}, \sigma_{TS}, C_{TS}) P(n_e, T_e, \sigma_{n_e}, \sigma_{T_e}, \sigma_{DI}, \sigma_{TS}, C_{TS})}{P(D_{DI}, D_{TS}, D_{v,n_e}, D_{v,T_e})} \\
&= \frac{P(D_{DI} | n_e, \sigma_{DI}) P(D_{TS} | n_e, T_e, \sigma_{TS}, C_{TS}) P(D_{v,n_e} | n_e) P(D_{v,T_e} | T_e) P(n_e | \sigma_{n_e}) P(T_e | \sigma_{T_e})}{P(D_{DI}) P(D_{TS}) P(D_{v,n_e}) P(D_{v,T_e})} \\
&\times P(\sigma_{n_e}) P(\sigma_{T_e}) P(\sigma_{DI}) P(\sigma_{TS}) P(C_{TS}) \\
&= \frac{P(D_{DI} | n_e, \sigma_{DI}) P(D_{TS} | n_e, T_e, \sigma_{TS}, C_{TS}) P(n_e | D_{v,n_e}, \sigma_{n_e}) P(T_e | D_{v,T_e}, \sigma_{T_e})}{P(D_{DI}) P(D_{TS})} \\
&\times P(\sigma_{n_e}) P(\sigma_{T_e}) P(\sigma_{DI}) P(\sigma_{TS}) P(C_{TS}), \tag{13}
\end{aligned}$$

where $P(n_e | D_{v,n_e}, \sigma_{n_e})$ and $P(T_e | D_{v,T_e}, \sigma_{T_e})$ are the Gaussian process priors with the edge constraints introduced by these virtual observations. Remarkably, any physics/empirical law can be introduced by virtual observations, for example the left-hand and right-hand side of physics formula can be regarded as predictions and corresponding observations at any space and time. These physics/empirical priors based on virtual observations have been used for the Bayesian joint model at Wendelstein 7-AS [33] and the plasma equilibria at JET [6].

On the other hand, we can provide local measurements of the electron density and temperature in the edge region from the helium beam emission spectroscopy system. The helium beam emission spectroscopy system [20] injects helium gas into the plasma and collects three helium line emissions (667 nm, 706 nm and 728 nm lines). The electron density and temperature can be inferred from three line intensity ratios of 667 nm to 728 nm, 706 nm to 667 nm and 706 nm to 728 nm helium lines by the pre-calculated lookup tables based on the collisional-radiative model [12, 34]. The joint posterior probability of the Bayesian joint model of the interferometer, Thomson scattering and helium beam emission spectroscopy systems can be written as:

$$\begin{aligned}
& P(n_e, T_e, \sigma_{n_e}, \sigma_{T_e}, \sigma_{DI}, \sigma_{TS}, C_{TS} | D_{DI}, D_{TS}, D_{He}) \\
&= \frac{P(D_{DI}, D_{TS}, D_{He} | n_e, T_e, \sigma_{n_e}, \sigma_{T_e}, \sigma_{DI}, \sigma_{TS}, C_{TS}) P(n_e, T_e, \sigma_{n_e}, \sigma_{T_e}, \sigma_{DI}, \sigma_{TS}, C_{TS})}{P(D_{DI}, D_{TS}, D_{He})} \\
&= \frac{P(D_{DI} | n_e, \sigma_{DI}) P(D_{TS} | n_e, T_e, \sigma_{TS}, C_{TS}) P(D_{He} | n_e, T_e) P(n_e | \sigma_{n_e}) P(T_e | \sigma_{T_e})}{P(D_{DI}) P(D_{TS}) P(D_{He})} \\
&\times P(\sigma_{n_e}) P(\sigma_{T_e}) P(\sigma_{DI}) P(\sigma_{TS}) P(C_{TS}), \tag{14}
\end{aligned}$$

where D_{He} is the helium beam emission data. Again, the predictive distribution $P(D_{He} | n_e, T_e)$ is modelled as a Gaussian distribution whose mean and variance are the predictions of the lookup tables and the predictive uncertainties of these helium line ratios.

All these joint posterior distributions are explored by Markov chain Monte Carlo (MCMC) algorithms, specifically adaptive Metropolis-Hastings algorithms [35, 36, 37] implemented in Minerva. All the hyperparameters of the Gaussian processes and the

model parameters are marginalised out numerically in order to obtain the marginal posterior distributions of the electron density and temperature profiles. This means that these profiles are inferred by taking into account all the possible values of the hyperparameters and model parameters consistent with all the measurements simultaneously.

3. The inference

The electron density and temperature profiles are amongst the most important physics parameters to understand magnetohydrodynamic equilibrium, transport and performance of the fusion plasma. The Thomson scattering system provides the electron density and temperature profiles across half of the plasma (upgraded to the full range in the latest campaigns), and the dispersion interferometer system measures the line integrated electron density which can be used to infer the calibration factor and to cross-calibrate the Thomson scattering system since the calibration factor has not been yet fully identified. Nevertheless, the profile boundary plays an important role in this cross-calibration. Since the profile boundary can be determined by the information of the electron density and temperature in the edge region, this information can be provided by either the virtual observations at the limiter/divertor positions or the helium beam emission data. In this work, profile inference has been carried out with different combinations of the interferometer, Thomson scattering systems and helium beam emission data as well as the edge virtual observations.

Figure 2 shows the electron density and temperature profiles with respect to the effective minor radius ρ_{eff} inferred by exploring the joint posterior distribution given the interferometer and Thomson scattering data which is given by Equation (10). The blue and light blue lines are the marginal posterior mean and samples, respectively. The marginal posterior samples calculated by numerically integrating the joint posterior distribution over the hyperparameters and model parameters, which can be written as:

$$\begin{aligned} & P(n_e, T_e | D_{\text{DI}}, D_{\text{TS}}) \\ &= \int \int \int \int \int P(n_e, T_e, \sigma_{n_e}, \sigma_{T_e}, \sigma_{\text{DI}}, \sigma_{\text{TS}}, C_{\text{TS}} | D_{\text{DI}}, D_{\text{TS}}) d\sigma_{n_e} d\sigma_{T_e} d\sigma_{\text{DI}} d\sigma_{\text{TS}} dC_{\text{TS}}. \end{aligned} \tag{15}$$

The orange dots are the electron density and temperature with the error bars provided by the Thomson scattering analysis implemented in Minerva [8]. The green dots are the electron temperature from the electron cyclotron emission (ECE) analysis at the low field side [38]. The calibration factor of the Thomson scattering system is uncertain due to unknown factors during experiments such as laser misalignment, and the electron density profiles of the Thomson scattering analysis, therefore, might not be consistent with the line integrated electron density measurement from the interferometer. On the other hand, the joint model automatically calibrates the Thomson scattering data with the line integrated electron density measurement, thus the electron density profiles of

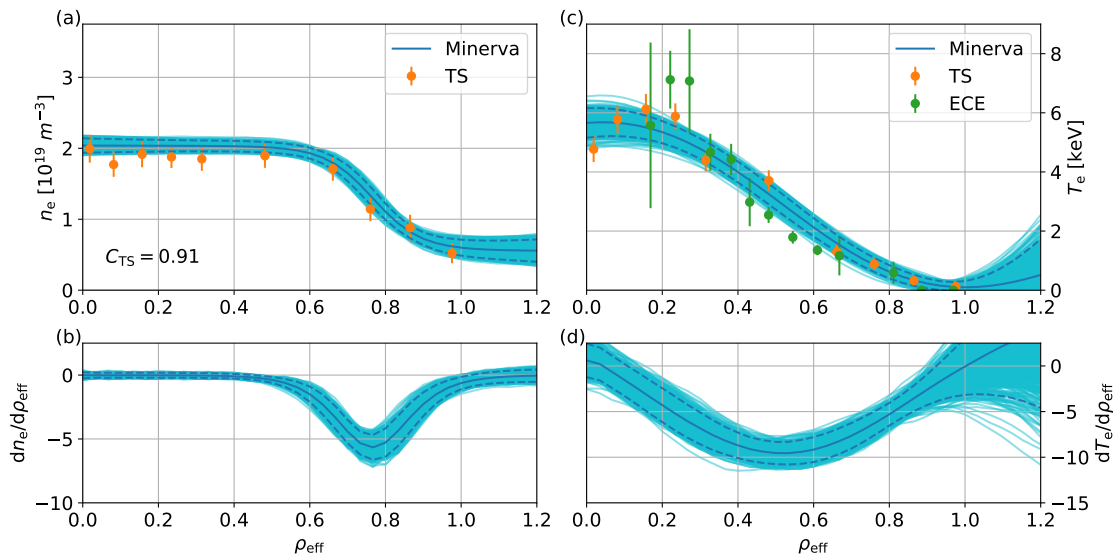


Figure 2. Inference results of the Bayesian joint model of the interferometer and Thomson scattering systems (experiment ID 20160309.013, $t = 0.43$ s): (a) the electron density and (b) temperature profiles and (c) n_e and (d) T_e gradient profiles. The blue and light blue lines are the marginal posterior mean and samples, respectively. The orange dots are the electron density and temperature with the error bars provided by the Bayesian Thomson scattering analysis [8]. The green dots are the electron temperature from the electron cyclotron emission (ECE) analysis at the low field side [38]. The Thomson scattering system is automatically cross-calibrated with the inferred calibration factor $C_{\text{TS}} = 0.91$ by the joint model. We note that, in this case, the electron density provided by the Thomson scattering system alone (the orange dots) is not consistent with the interferometer data due to some calibration uncertainties [8], whereas the profiles from the joint model (the blue lines) are consistent with both Thomson scattering and interferometer data.

the joint analysis are consistent with both Thomson scattering and interferometer data (the inferred calibration factor $C_{\text{TS}} = 0.91$). In other words, the Thomson scattering analysis might underestimate the electron density profiles by approximately 9% with respect to the interferometer data. The n_e and T_e gradient profiles are also presented in Figure 2(c) and Figure 2(d). We note that there is no measurement available outside the last closed magnetic flux surface (LCFS), i.e., $\rho_{\text{eff}} > 1.0$ so that the electron density and temperature can be purely determined by the Gaussian process priors.

The electron density and temperature are not expected to be significantly high at the limiter/divertor positions, and we can introduce this prior knowledge by making the virtual observations, as described in Section 2. The electron density and temperature profiles of the marginal posterior distribution given these virtual observations $P(n_e, T_e | D_{\text{DI}}, D_{\text{TS}}, D_{\text{v}, n_e}, D_{\text{v}, T_e})$ are shown in Figure 3. We remark that the mean values of the calibration factor of the Thomson scattering system with and without the virtual observations are substantially different ($C_{\text{TS}} = 0.83$ with the virtual observations and $C_{\text{TS}} = 0.91$ without the virtual observations). In other words, the calibration factor of

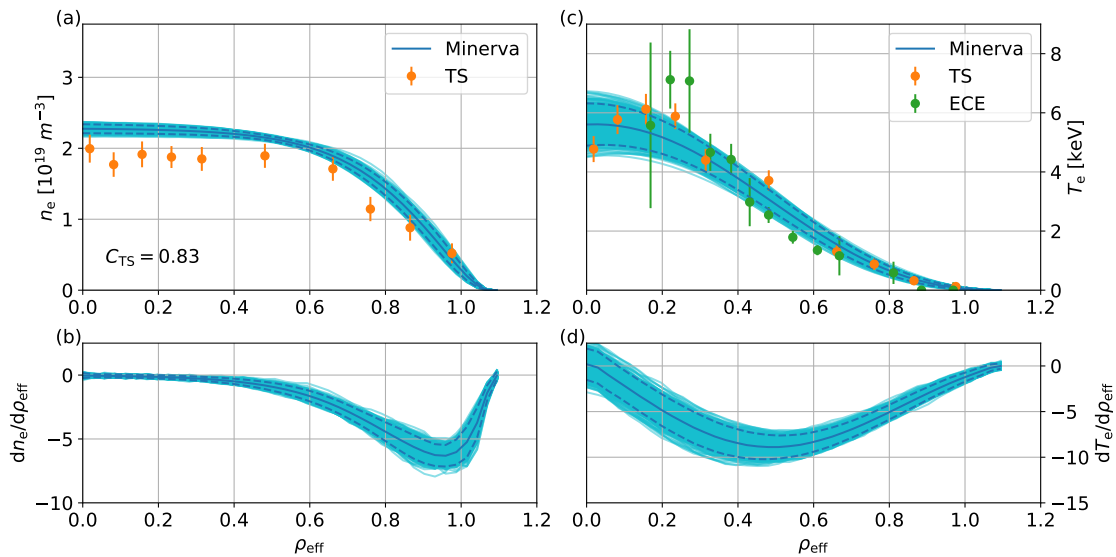


Figure 3. Same as Figure 2 for inference results of the Bayesian joint model of the interferometer and Thomson scattering systems with the electron density and temperature constraints at the limiter/divertor positions introduced by the virtual observations.

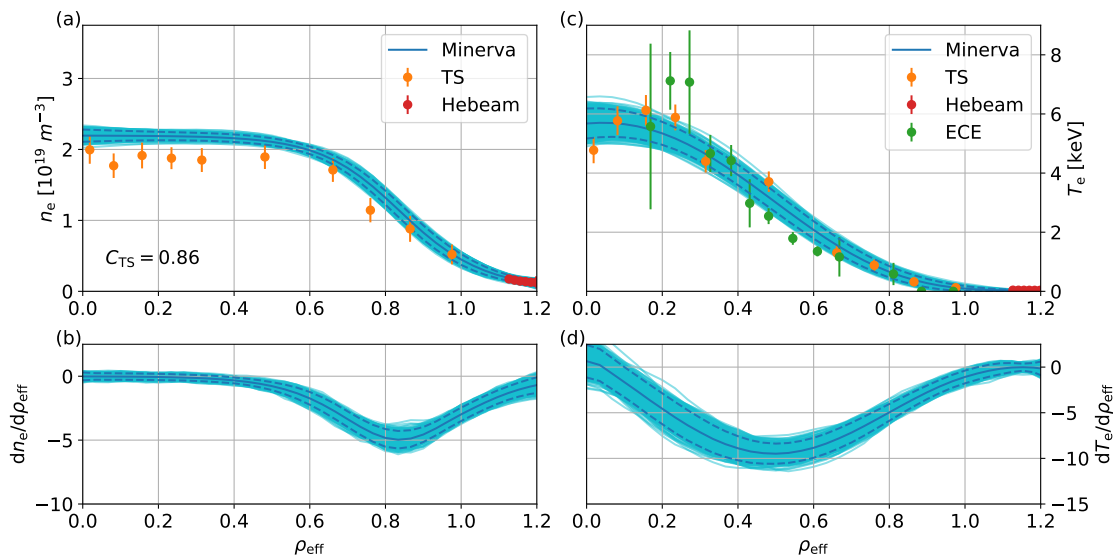


Figure 4. Same as Figure 2 for inference results of the Bayesian joint model of the interferometer, Thomson scattering, and helium beam emission spectroscopy systems. The red dots are the electron density and temperature of the stand-alone analysis of Bayesian helium beam model, developed in this work.

the Thomson scattering system can be substantially influenced by the information of the electron density and temperature in the edge region.

In order to compare the inference solutions of the joint model given the virtual and experimental observations in the edge region, the helium beam emission data is added to

the joint model instead of the virtual observations. The electron density and temperature profiles of the marginal posterior distribution given the helium beam emission data $P(n_e, T_e | D_{DI}, D_{TS}, D_{He})$ are shown in Figure 4. The mean value of the calibration factor with the helium beam emission data ($C_{TS} = 0.86$) is slightly different from the one with the virtual observations ($C_{TS} = 0.83$). The predictions given these marginal posterior mean and samples and the corresponding observations are compared in Figure 5. The helium beam emission spectroscopy system provides not only the density and temperature measurements but also their measurement uncertainties in the edge region which are critical to determining the optimal hyperparameters (smoothness) by Bayesian Occam's razor [31, 32]. Unlike the inference results given the virtual observations, the joint model of the interferometer, Thomson scattering and helium beam emission spectroscopy systems provides reasonable electron density and temperature profiles in the edge region. Nevertheless, the virtual observations could be another possible option to reinforce the model and exclude physically/empirically improbable solutions when the observations are not sufficiently available.

We emphasise that these profiles neither underfit nor overfit the data. Bayesian methods penalise underfitted and overfitted models automatically and quantitatively. Underfitted models, which propose over-simplified profiles, for example straight profiles, are not able to predict the data within their predictive uncertainties. On the other hand, overfitted model, which propose over-complex profiles, for example wiggly profiles, are able to predict the data better than simpler models. However, overfitted models can propose a greater variety of profiles than simpler models do, and each of them is almost equally probable. The probability of each proposed profile hence is lower than the probability of the profiles proposed by simpler models because the probability over the entire profile space must be equal to one. For this reason, over-complex models are automatically self-penalised by Bayesian Occam's razor [31, 32]. In this case, Gaussian processes with too small length scale (over-complex models) are able to propose profiles which predict the data accurately, i.e., high predictive probabilities $P(D_{DI} | n_e, \sigma_{DI})$, $P(D_{TS} | n_e, T_e, \sigma_{TS}, C_{TS})$ and $P(D_{He} | n_e, T_e)$, but the prior probabilities of these proposed profiles $P(n_e | \sigma_{n_e})$ and $P(T_e | \sigma_{T_e})$ are low since the Gaussian processes can propose many other candidates equally probable. Consequently, the joint posterior probability associated with over-complex models is low. The models with too large predictive uncertainties (over-complex models) are also self-penalised in the same way. By exploring the joint posterior distribution of the electron density and temperature profiles, hyperparameters and model parameters, we collect profiles with proper length scale (smoothness) and predictive uncertainties. Furthermore, these inference solutions provide marginal posterior samples and uncertainties which are obtained by taking into account all possible values of the hyperparameters and model parameters. In other words, these samples and uncertainties do not depend on specific values of hyperparameters and model parameters.

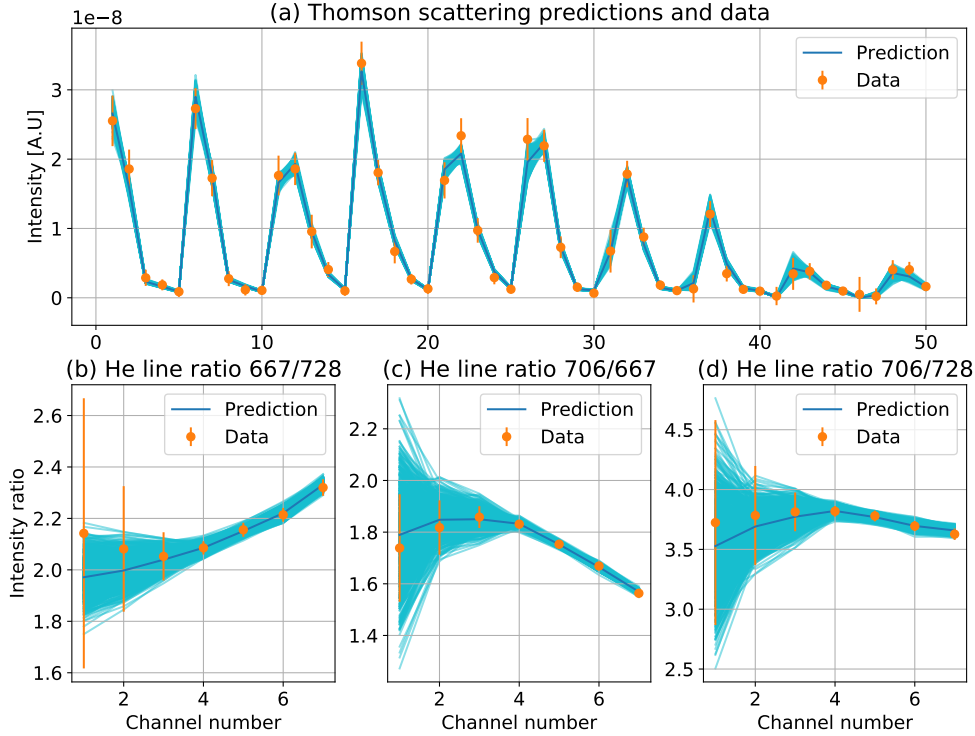


Figure 5. The predictions (in blue and light blue) and observations (in orange) of (a) the Thomson scattering data and (b,c,d) the three helium line intensity ratios given the posterior mean and samples shown in Figure 4. The Thomson scattering signals consists of 50 data points from ten spatial locations (five integrated signals over five different spectral ranges from each spatial location). The helium beam emission data are the three line intensity ratios of (a) 667 nm to 728 nm, (b) 706 nm to 667 nm and (c) 706 nm to 728 nm helium lines from eight spatial locations.

4. The addition of the X-ray Imaging Crystal Spectrometers

The X-ray imaging crystal spectrometers (XICS) [13] measure X-ray spectra of argon and iron impurities in different charge states within a wide range of electron temperature, from 0.3 keV to 6 keV. The XICS system collects line integrated spectra along 20 lines of sight, covering more than half of the plasma on the poloidal cross section at a toroidal angle of 159.09. The XICS forward model implemented previously in Minerva [13] is added to the Bayesian joint model of the interferometer, Thomson scattering and helium beam emission spectroscopy systems. The local X-ray spectra are calculated by taking into account a number of atomic processes such as excitation, recombination, ionisation and charge exchange and depend on the electron density and temperature as well as the ion temperature. The forward model integrates these predicted local spectra given these physics parameters along the lines of sight to calculate the line integrated X-ray spectra.

The ion temperature prior distribution is modelled by a Gaussian process with the zero mean and squared exponential covariance function. The joint posterior probability given the interferometer, Thomson scattering, helium beam emission and XICS data can be written as:

$$\begin{aligned}
& P(n_e, T_e, T_i, \sigma_{n_e}, \sigma_{T_e}, \sigma_{T_i}, \sigma_{DI}, \sigma_{TS}, C_{TS} | D_{DI}, D_{TS}, D_{He}, D_{XICS}) \\
&= \frac{P(D_{XICS} | n_e, T_e, T_i) P(T_i | \sigma_{T_i}) P(\sigma_{T_i}) P(n_e, T_e, \sigma_{n_e}, \sigma_{T_e}, \sigma_{DI}, \sigma_{TS}, C_{TS} | D_{DI}, D_{TS}, D_{He})}{P(D_{XICS})}
\end{aligned} \tag{16}$$

where T_i is the ion temperature, σ_{T_i} all the hyperparameters of the Gaussian process and D_{XICS} the XICS data. The predictive distribution $P(D_{XICS} | n_e, T_e, T_i)$ is modelled as a Gaussian distribution whose mean and variance are the predictions of the XICS forward model. The predictive uncertainties of the line integrated X-ray spectra. The electron density and temperature profiles as well as the ion temperature profiles are inferred tomographically given the interferometer, Thomson scattering, helium beam emission and XICS data.

The maximum *a posteriori* (MAP) solutions of the joint posterior probability of the electron density and temperature, ion temperature profiles are found by the pattern search algorithm [39] implemented in Minerva, as shown in Figure 6. The predictions and observations of the helium beam emission and line integrated X-ray spectra are shown in Figure 7. The XICS forward model is substantially complex and computationally expensive, thus full sampling from the joint posterior distribution is left for future work. This can be achieved by a neural network approximation of the XICS Minerva model [17].

Remarkably, we infer these profiles with the optimal values of the hyperparameters (smoothness) and model parameters by maximising the joint posterior probability. A conventional approach to finding the optimal hyperparameters and model parameters is to maximise the posterior probability of these hyperparameters and model parameters, which is proportional to a marginal predictive distribution of the observations, also known as the model evidence. Calculation of the model evidence is computationally challenging because it requires integration over a high dimensional parameter space, therefore this is a major obstacle to apply Bayesian Occam's razor to applications in the real world. On the other hand, calculation of the joint posterior probability does not involve such integration. The joint posterior distribution can be seen as the product of the conditional posterior distribution of the parameters and the posterior distribution of the hyperparameters and model parameters, which can be written as:

$$\begin{aligned}
& P(n_e, T_e, T_i, \sigma_{n_e}, \sigma_{T_e}, \sigma_{T_i}, \sigma_{DI}, \sigma_{TS}, C_{TS} | D_{DI}, D_{TS}, D_{He}, D_{XICS}) \\
&= P(n_e, T_e, T_i | \sigma_{n_e}, \sigma_{T_e}, \sigma_{T_i}, \sigma_{DI}, C_{TS}, \sigma_{TS}, D_{DI}, D_{TS}, D_{He}, D_{XICS}) \\
&\times P(\sigma_{n_e}, \sigma_{T_e}, \sigma_{T_i}, \sigma_{DI}, \sigma_{TS}, C_{TS} | D_{DI}, D_{TS}, D_{He}, D_{XICS}).
\end{aligned} \tag{17}$$

The joint posterior distribution intrinsically embodies Bayesian Occam's razor through the posterior probability of the hyperparameters and model parameters, and the MAP

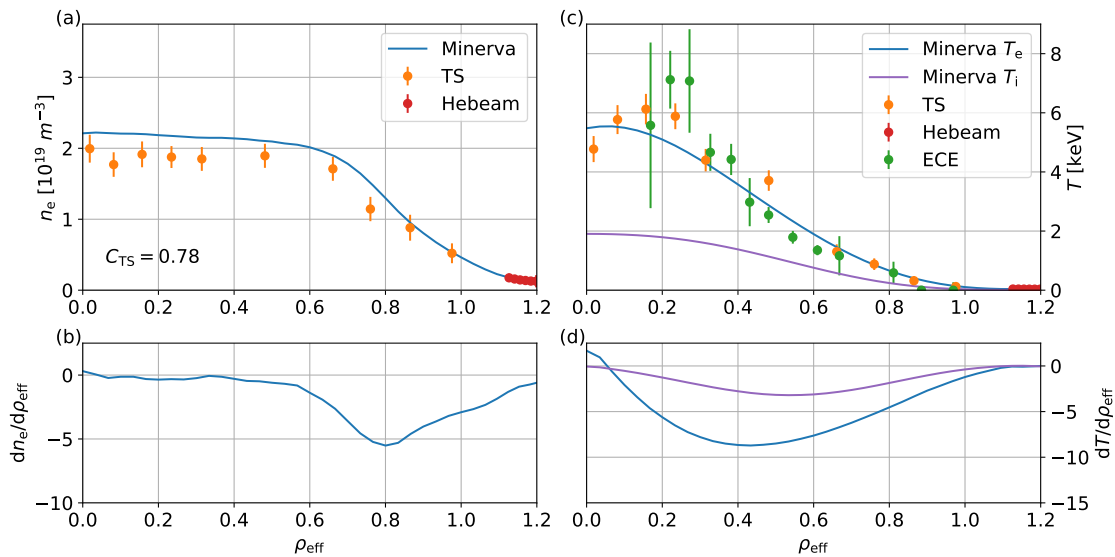


Figure 6. Same as Figure 2 for the inference results of the Bayesian joint model of the interferometer, Thomson scattering, helium beam emission spectroscopy and XICS systems. The ion temperature and T_i gradient profiles are shown as the purple lines in (c) and (d).

solution is therefore the optimal profiles with the optimal hyperparameters (smoothness) and model parameters. This does explain the reason why the profiles are not wiggly but optimally smooth in Figure 6.

5. Conclusions

The Bayesian joint model of the interferometer, Thomson scattering and helium beam emission spectroscopy systems has been developed at Wendelstein 7-X (W7-X). Each of the forward models has been implemented individually and combined together as a joint model in the Minerva framework. The electron density and temperature profiles are given as a function of the effective minor radius and modelled by Gaussian processes with their hyperparameters. The model parameters, for example the calibration factor of the Thomson scattering system, are regarded as additional unknown parameters. The joint posterior distribution of the electron density and temperature profiles, hyperparameters and model parameters is explored by Markov chain Monte Carlo (MCMC) algorithms.

The profile inference has been carried out with different combinations of the three different heterogeneous data sets and virtual observations. The electron density and temperature profiles are inferred with the Bayesian joint model of the interferometer and Thomson scattering system, and the Thomson scattering data is automatically cross-calibrated with the line integrated electron density from the interferometer. In order to exclude physically and empirically improbable solutions, the electron density and temperature are assumed to be not significantly high at the limiter/divertor positions

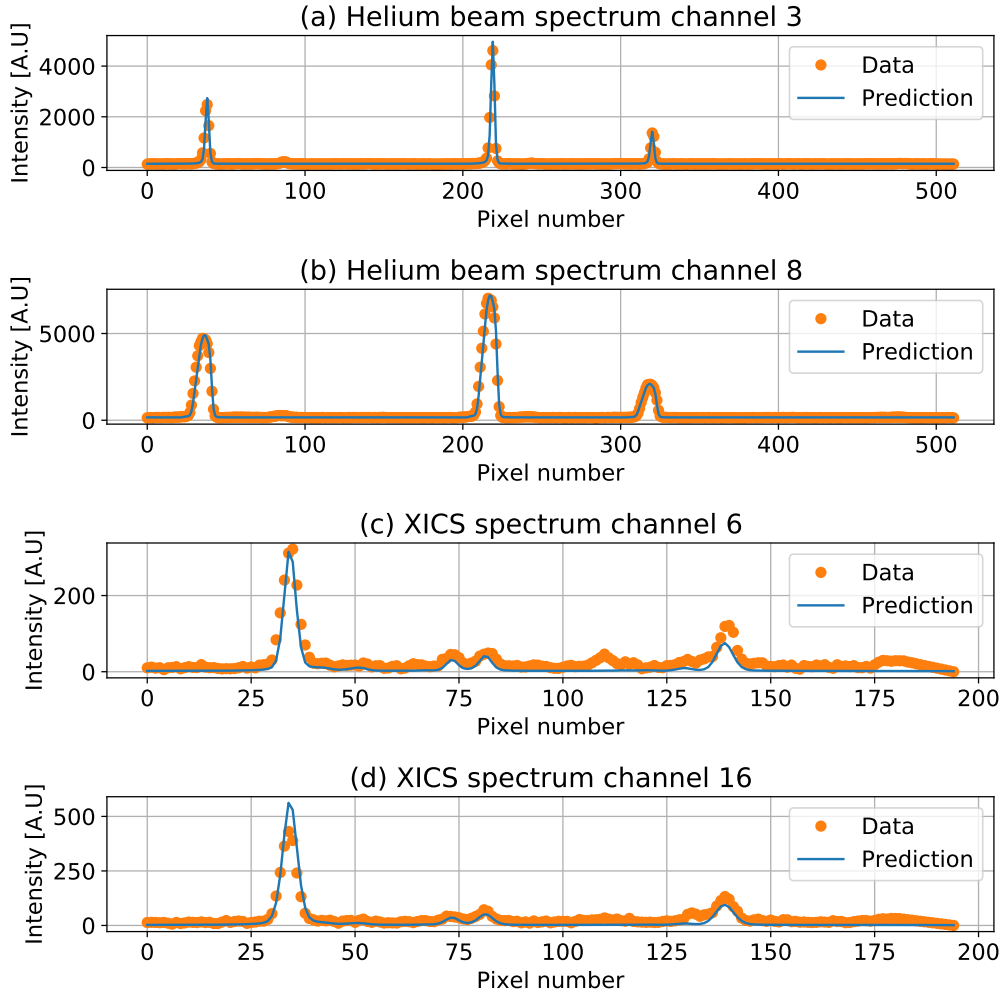


Figure 7. The predictions (in blue) and observations (in orange) of the helium beam spectra of the channel #3 (near to the divertor) and #8 (the innermost channel) and the XICS spectra of the channel #6 (in the edge region) and 16 # (in the core region) given the profiles shown in Figure 6.

by introducing the virtual observations as a part of the prior distributions. These inferred profiles and calibration factor from the joint posterior distribution with the virtual observations are physically and empirically reasonable and substantially different from those of the joint posterior distribution without the virtual observations due to lack of information of the electron density and temperature in the edge region. Furthermore, in order to compare the inference solutions with the virtual and experimental observations in the edge region, the helium beam emission data is added to the joint model instead of the virtual observations. The profiles inferred with the joint model of the interferometer, Thomson scattering system and helium beam emission spectroscopy systems are reasonable because the helium beam emission data provides the electron density and temperature measurements as well as their measurement uncertainties in

the edge region which are crucial to finding the optimal smoothness of the profiles by Bayesian Occam's razor. Nevertheless, when the observations are not sufficiently available, the virtual observations can be a good option to strengthen the model and exclude physically/empirically improbable inference solutions.

We emphasise that these inference solutions have been found with the optimal hyperparameters (smoothness) and model parameters by Bayesian Occam's razor which penalises over-complex models automatically and quantitatively. In other words, these inference solutions neither underfit nor overfit all the measurements. Furthermore, the marginal posterior samples are calculated to obtain the electron density and temperature profiles by taking into account all possible values of the hyperparameters and model parameters given the observations. Remarkably, the joint posterior distribution of the unknown parameters, hyperparameters and model parameters intrinsically embodies Bayesian Occam's razor. The joint posterior probability can be calculated relatively easier than the model evidence, therefore, Bayesian Occam's razor can be applied to the problems in the real world by exploring the joint posterior distribution easier than the model evidence. As shown in this work, the MAP solution of the joint posterior probability distribution given the interferometer, Thomson scattering, helium beam emission spectroscopy and XICS systems provides the electron density and temperature as well as the ion temperature profiles with appropriate model parameters and hyperparameters. Therefore the MAP solution does not either underfit or overfit the data.

6. Acknowledgement

This work is supported by National R&D Program through the National Research Foundation of Korea (NRF) funded by the Ministry of Science and ICT (Grant No. 2017M1A7A1A01015892 and 2017R1C1B2006248) and the the KAI-NEET, KAIST, Korea. This work has been carried out within the framework of the EUROfusion Consortium and has received funding from the Euratom research and training programme 2014-2018 and 2019-2020 under grant agreement No 633053. The views and opinions expressed herein do not necessarily reflect those of the European Commission.

References

- [1] Litaudon X *et al.* 2017 *Nuclear Fusion* **57** 102001 ISSN 0029-5515 URL <http://stacks.iop.org/0029-5515/57/i=10/a=102001?key=crossref.17a0f33a13c4a2bbaafb54b4eb7df30>
- [2] Klinger T *et al.* 2019 *Nuclear Fusion* **59** 112004 ISSN 0029-5515 URL <https://iopscience.iop.org/article/10.1088/1741-4326/ab03a7>
- [3] Seed eScience Research The Minerva framework URL <https://seed-escience.org/>
- [4] Pearl J 1988 *Probabilistic Reasoning in Intelligent Systems: Networks of Plausible Inference* (Morgan Kaufmann)
- [5] Svensson J and Werner A 2008 *Plasma Physics and Controlled Fusion* **50** 085002 ISSN 07413335 URL <http://stacks.iop.org/0741-3335/50/i=8/a=085002?key=crossref.8b9e7d2d10e66d8a740fcec9ab77227d>

- [6] Ford O P 2010 *Tokamak plasma analysis through Bayesian diagnostic modelling* Ph.D. thesis Imperial College London
- [7] Svensson J 2011 *JET report, EFDA-JET-PR(11)24* URL <http://www.euro-fusionscipub.org/wp-content/uploads/eurofusion/EFDP11024.pdf>
- [8] Bozhenkov S, Beurskens M, Molin A D, Fuchert G, Pasch E, Stoneking M, Hirsch M, Höfel U, Knauer J, Svensson J, Mora H T and Wolf R 2017 *Journal of Instrumentation* **12** P10004–P10004 ISSN 1748-0221 URL <http://stacks.iop.org/1748-0221/12/i=10/a=P10004?key=crossref.21c7d556bea6caf012906a098b133ef0>
- [9] Kwak S, Svensson J, Bozhenkov S A, Flanagan J, Kempenaars M, Boboc A and Ghim Y c 2020 *Nuclear Fusion* ISSN 0029-5515 URL <https://iopscience.iop.org/article/10.1088/1741-4326/ab686e>
- [10] Li D, Svensson J, Thomsen H, Medina F, Werner A and Wolf R 2013 *Review of Scientific Instruments* **84** 083506 ISSN 0034-6748 URL <http://aip.scitation.org/doi/10.1063/1.4817591>
- [11] Kwak S, Svensson J, Brix M and Ghim Y c 2016 *Review of Scientific Instruments* **87** 023501 ISSN 0034-6748 URL <http://aip.scitation.org/doi/10.1063/1.4940925>
- [12] Kwak S, Svensson J, Brix M and Ghim Y C 2017 *Nuclear Fusion* **57** 036017 ISSN 0029-5515 URL <http://stacks.iop.org/0029-5515/57/i=3/a=036017?key=crossref.78317e8d5c69c0d93e4bfd4af120a500>
- [13] Langenberg A, Svensson J, Thomsen H, Marchuk O, Pablant N A, Burhenn R and Wolf R C 2016 *Fusion Science and Technology* **69** 560–567 ISSN 1536-1055 URL <https://www.tandfonline.com/doi/full/10.13182/FST15-181>
- [14] Hoefel U, Hirsch M, Kwak S, Pavone A, Svensson J, Stange T, Hartfuß H J, Schilling J, Weir G, Oosterbeek J W, Bozhenkov S, Braune H, Brunner K J, Chaudhary N, Damm H, Fuchert G, Knauer J, Laqua H, Marsen S, Moseev D, Pasch E, Scott E R, Wilde F and Wolf R 2019 *Review of Scientific Instruments* **90** 043502 ISSN 0034-6748 URL <http://aip.scitation.org/doi/10.1063/1.5082542>
- [15] Pavone A, Hergenbahn U, Krychowiak M, Hoefel U, Kwak S, Svensson J, Kornejew P, Winters V, Koenig R, Hirsch M, Brunner K J, Pasch E, Knauer J, Fuchert G, Scott E, Beurskens M, Effenberg F, Zhang D, Ford O, Vanó L and Wolf R 2019 *Journal of Instrumentation* **14** C10003–C10003 ISSN 1748-0221 URL <https://iopscience.iop.org/article/10.1088/1748-0221/14/10/C10003>
- [16] Mora H T, Bozhenkov S, Knauer J, Kornejew P, Kwak S, Ford O, Fuchert G, Pasch E, Svensson J, Werner A, Wolf R and Timmermann D 2017 FPGA acceleration of Bayesian model based analysis for time-independent problems *2017 IEEE Global Conference on Signal and Information Processing (GlobalSIP)* (IEEE) pp 774–778 ISBN 978-1-5090-5990-4 URL <http://ieeexplore.ieee.org/document/8309065/>
- [17] Pavone A, Svensson J, Langenberg A, Pablant N, Hoefel U, Kwak S and Wolf R C 2018 *Review of Scientific Instruments* **89** 10K102 ISSN 0034-6748 URL <http://aip.scitation.org/doi/10.1063/1.5039286>
- [18] Pavone A, Svensson J, Langenberg A, Höfel U, Kwak S, Pablant N and Wolf R C 2019 *Plasma Physics and Controlled Fusion* **61** 075012 ISSN 0741-3335 URL <https://iopscience.iop.org/article/10.1088/1361-6587/ab1d26>
- [19] Knauer J, Kornejew P, Trimino Mora H, Hirsch M, Werner A, Wolf R C and the W7-X team A new dispersion interferometer for the stellarator wendelstein 7-x proceeding of the 43rd EPS Conference on Plasma Physics, P. Mantica ed., European Physical Society
- [20] Barbui T, Krychowiak M, König R, Schmitz O, Muñoz B, Schweer B and Terra A 2016 *Review of Scientific Instruments* **87** 11E554 ISSN 10897623 URL <http://aip.scitation.org/doi/10.1063/1.4962989>
- [21] Hirshman S, van RIJ W and Merkel P 1986 *Computer Physics Communications* **43** 143–155 ISSN 00104655 URL <https://linkinghub.elsevier.com/retrieve/pii/0010465586900585>
- [22] Geiger J, Beidler C, Drevlak M, Maaßberg H, Nührenberg C, Suzuki Y and Turkin Y 2010 *Contributions to Plasma Physics* **50** 770–774 ISSN 08631042 URL <http://doi.wiley.com/10.1088/0021-8995/50/7/070>

- 1002/ctpp.200900028
- [23] Jaynes E T 2003 *Probability Theory: The Logic of Science* (Cambridge University Press) ISBN 0-521-59271-2
 - [24] Devinderjit Sivia J S 2006 *Data Analysis: A Bayesian Tutorial* (Oxford University Press) ISBN 0-198-56831-2
 - [25] O'Hagan A 1978 *Journal of the Royal Statistical Society. Series B (Methodological)* **40** 1–42 ISSN 00359246 URL <http://www.jstor.org/stable/2984861>
 - [26] Neal R M 1995 *Bayesian learning for neural networks* Ph.D. thesis University of Toronto
 - [27] Rasmussen C E and Williams C K I 2006 *Gaussian Processes for Machine Learning* (MIT Press)
 - [28] Chilenski M, Greenwald M, Marzouk Y, Howard N, White A, Rice J and Walk J 2015 *Nuclear Fusion* **55** 023012 ISSN 0029-5515 URL <http://stacks.iop.org/0029-5515/55/i=2/a=023012?key=crossref.b22d32b1ac570adef0ea0869bc2c1789>
 - [29] Higdon D, Swall J and Kern J 1999 Non-stationary spatial modeling *Bayesian Statistics 6 Proceedings of the Sixth Valencia International Meeting* pp 761–768
 - [30] Naito O, Yoshida H and Matoba T 1993 *Physics of Fluids B: Plasma Physics* **5** 4256–4258 ISSN 0899-8221 URL <http://aip.scitation.org/doi/10.1063/1.860593>
 - [31] Gull S F 1988 Bayesian inductive inference and maximum entropy *Maximum-Entropy and Bayesian Methods in Science and Engineering: Foundations* ed Erickson G J and Smith C R (Springer Netherlands) pp 53–74 ISBN 978-94-009-3049-0 URL https://doi.org/10.1007/978-94-009-3049-0_4
 - [32] Mackay D J 1991 *Bayesian methods for adaptive models* Ph.D. thesis California Institute of Technology
 - [33] Svensson J, Dinklage A, Geiger J, Werner A and Fischer R 2004 *Review of Scientific Instruments* **75** 4219–4221 ISSN 0034-6748 URL <http://aip.scitation.org/doi/10.1063/1.1789611>
 - [34] Krychowiak M, Brix M, Dodt D, Feng Y, König R, Schmitz O, Svensson J and Wolf R 2011 *Plasma Physics and Controlled Fusion* **53** 035019 ISSN 0741-3335 URL <http://stacks.iop.org/0741-3335/53/i=3/a=035019?key=crossref.4b073280665d8e8d5df5658ce385f252>
 - [35] Metropolis N, Rosenbluth A W, Rosenbluth M N, Teller A H and Teller E 1953 *The Journal of Chemical Physics* **21** 1087–1092 ISSN 0021-9606 URL <http://aip.scitation.org/doi/10.1063/1.1699114>
 - [36] Hastings W K 1970 *Biometrika* **57** 97–109 ISSN 1464-3510 URL <https://academic.oup.com/biomet/article/57/1/97/284580>
 - [37] Haario H, Saksman E and Tamminen J 2001 *Bernoulli* **7** 223 ISSN 13507265 URL <https://www.jstor.org/stable/3318737?origin=crossref>
 - [38] Hirsch M, Höfel U, Oosterbeek J W, Chaudhary N, Geiger J, Hartfuss H J, Kasperek W, Marushchenko N, van Milligen B, Plaum B, Stange T, Svensson J, Tsuchiya H, Wagner D, McWeir G and Wolf R 2019 *EPJ Web of Conferences* **203** 03007 ISSN 2100-014X URL <https://www.epj-conferences.org/10.1051/epjconf/201920303007>
 - [39] Hooke R and Jeeves T A 1961 *Journal of the ACM* **8** 212–229 ISSN 00045411 URL <http://portal.acm.org/citation.cfm?doid=321062.321069>

4.5 Article V

'Bayesian equilibria of axisymmetric plasmas'

S. KWAK, J. SVENSSON, O. FORD, L. APPEL and Y.-C. GHIM

Nuclear Fusion, (2020), in preparation

Bayesian equilibria of axisymmetric plasmas

Sehyun Kwak^{1,2}, J. Svensson², O. Ford², L. Appel³, Y.-c. Ghim¹
and JET Contributors[‡]

EUROfusion Consortium, JET, Culham Science Centre, Abingdon, OX14 3DB,
United Kingdom of Great Britain and Northern Ireland

¹Department of Nuclear and Quantum Engineering, KAIST, Daejeon 34141,
Korea, Republic of

²Max-Planck-Institut für Plasmaphysik, 17491 Greifswald, Germany

³Culham Centre for Fusion Energy, Culham Science Centre, Abingdon, OX14 3DB,
United Kingdom of Great Britain and Northern Ireland

E-mail: sehyun.kwak@ipp.mpg.de

11 November 2020

Abstract. Bayesian models of axisymmetric plasmas using Gaussian processes and force balance equations have been developed. These models give the full joint posterior probability distributions over plasma current distributions and pressure profiles given the magnetic field and pressure measurements simultaneously. The toroidal currents such as plasma and magnetic field coil currents are modelled as a grid of toroidal current carrying solid beams. The plasma pressure and poloidal current flux profiles are given as a function of the poloidal magnetic flux surface, determined by the toroidal currents. Inference of all these physics parameters is a tomographic problem, thus, in order to exclude unreasonable solutions, two different prior distributions have been exploited: a Gaussian process prior and an equilibrium prior. The Gaussian process prior constrains the plasma current distributions by their covariance (smoothness) function whose hyperparameters have been optimally selected by Bayesian Occam's razor. On the other hand, the equilibrium prior imposes the magnetohydrodynamic force balance by introducing observations that the differences between the magnetic force and the plasma pressure gradient are almost zero at every plasma current beam. These *virtual* observations emphasise equilibrium solutions *a priori* as a part of the prior knowledge. These models with the two different priors employ predictive models of magnetic sensors and other plasma diagnostics in order to find all possible solutions consistent with all the measurements. The complex, high dimensional posterior distributions are explored by a new method based on the Gibbs sampling scheme.

Keywords: Plasma equilibria, Plasma diagnostics, JET, Bayesian inference, Physics priors, Virtual observations, Gaussian processes, Forward modelling, Occam's razor

Submitted to: *Nucl. Fusion*

[‡] See the author list of E. Joffrin et al. accepted for publication in Nuclear Fusion Special issue 2019, <https://doi.org/10.1088/1741-4326/ab2276>

1. Introduction

In magnetic confinement fusion research, inference of plasma current distributions is critical to control and to understand the underlying physics and the plasma [1, 2, 3]. The plasma current distributions determine the magnetic field geometry of the plasma that plays an important role in plasma control [4] and provide the canonical coordinate system [1], in which to express physics parameters and models for further research, for example energy transport. This magnetic field geometry can be represented as a set of poloidal magnetic flux surfaces often normalised to zero at the plasma centre, known as the magnetic axis, and to one at the plasma boundary, known as the last closed flux surface (LCFS).

The conventional approach to infer the plasma current distributions is to find a single solution to magnetohydrodynamic (MHD) force balance equations such as the Grad-Shafranov equation [5, 6] consistent with magnetic field measurements [7]. This approach has been providing a plasma equilibrium solution, nevertheless, it has the following limitations: typically it makes use of 1D parameterisations of the plasma pressure and poloidal current flux with a handful of parameters, which are often incapable of representing the shape of spatial profiles of them, and it usually takes into account only the magnetic measurements, thus this equilibrium solution might be inconsistent with plasma pressure and poloidal current measurements. Moreover, this approach finds only a single solution, not all possible solutions given the force balance equations and measurements. In other words, the conventional approach does not provide uncertainties of either the magnetic field geometry or the physics parameters such as the plasma current distributions or pressure profiles.

In this work, we will demonstrate Bayesian inference of axisymmetric plasma current distributions and pressure profiles consistent with a number of measurements from magnetic sensors and other plasma diagnostics in a large-scale fusion experiment. This Bayesian approach makes use of an axisymmetric current beam model [8], which represents all kind of toroidal currents, for example plasma and poloidal field coil currents, as a grid of toroidal current carrying solid beams. These toroidal current distributions determine the poloidal magnetic flux surface on which other physics parameters such as the plasma pressure and poloidal current flux are often assumed to be constant [3], thus they are given as a function of the magnetic flux surface. The plasma pressure and poloidal current flux are modelled by Gaussian processes, which are capable of representing a great variety of 1D spatial profiles of these physics parameters [9, 10]. Since inference of all these physics parameters is a tomographic problem, in order to exclude unreasonable solutions, we have introduced two different prior distributions: a Gaussian process prior and an equilibrium prior. The Gaussian process prior constrains the plasma current distributions by the covariance (smoothness) function which determines the covariance (smoothness) between any two plasma current beams. The parameters of the covariance function, also known as the *hyperparameters* of Gaussian processes, can be optimised to maximise the posterior probability of the model, which takes into account

the principle of Occam’s razor [11, 12, 13]. In other words, we can infer the plasma current distributions with the optimal smoothness from the measurements. On the other hand, the equilibrium prior imposes the force balance between the magnetic force and the plasma pressure gradient, given by the Grad-Shafranov equation, by introducing *virtual* observations that the differences between the two forces should be almost zero at every plasma current beam. These virtual observations emphasise equilibrium solutions as a part of the prior knowledge [14]. Here, the axisymmetric plasma model with the Gaussian process prior and the one with the equilibrium prior are called the current tomography model and the equilibrium model, respectively. In addition to these prior distributions, both models employ predictive models of magnetic sensors (pickup coils, saddle coils and flux loops) [8], polarimeters [14, 15], interferometers [14], lithium beam emission spectroscopy [16, 17] and high-resolution Thomson scattering (HRTS) systems [10] in order to find all possible plasma current distributions as well as pressure and poloidal current flux profiles consistent with all their measurements simultaneously at one of the large-scale fusion experiments, the Joint European Torus (JET) [18]. Since these models involve a large number of unknown parameters and observations as well as multiple predictive models of scientific instruments, it is, therefore, inevitable to use a framework that is capable of handling and keeping track of all these parameters, assumptions, predictive models and observations in such a complex model. For this reason, these models have been implemented in the Minerva framework.

The Minerva framework [19, 20] has been developed to achieve consistent scientific inference in a complex system by providing a standardised format for model components, for example probability and forward functions, and a standardised interface for component dependencies, input parameters, which can be connected from output of other model components. Minerva automatically manages all the model components and connections and represents them by a Bayesian graphical model [21], as shown in Figure 1. The modular structure, graphical representation and automatic model administration allow us to handle a complex model and to keep track of a large number of parameters, assumptions, predictive models and observations in a systematic way. Furthermore, we can easily build and compare models with different model specifications, for example various prior distributions. In this work, we present the two axisymmetric plasma models with different priors. The Minerva framework has been used for a number of scientific applications to magnetic sensors [8], interferometers [10, 13, 14], Thomson scattering systems [10, 22], soft X-ray spectroscopy [23], beam emission spectroscopy [16, 17], X-ray imaging crystal spectroscopy [24], electron cyclotron emission diagnostics [25] and effective ion charge diagnostics [26] in nuclear fusion research. These Bayesian models implemented in Minerva can be accelerated by a field-programmable gate array (FPGA) [27] and an artificial neural network [28, 29].

These Bayesian models of axisymmetric plasmas provide the full joint posterior distributions over the plasma current distributions, poloidal current flux and pressure profiles consistent with the magnetic field and pressure measurements simultaneously. However, exploration of such complex, high dimensional posterior distributions is

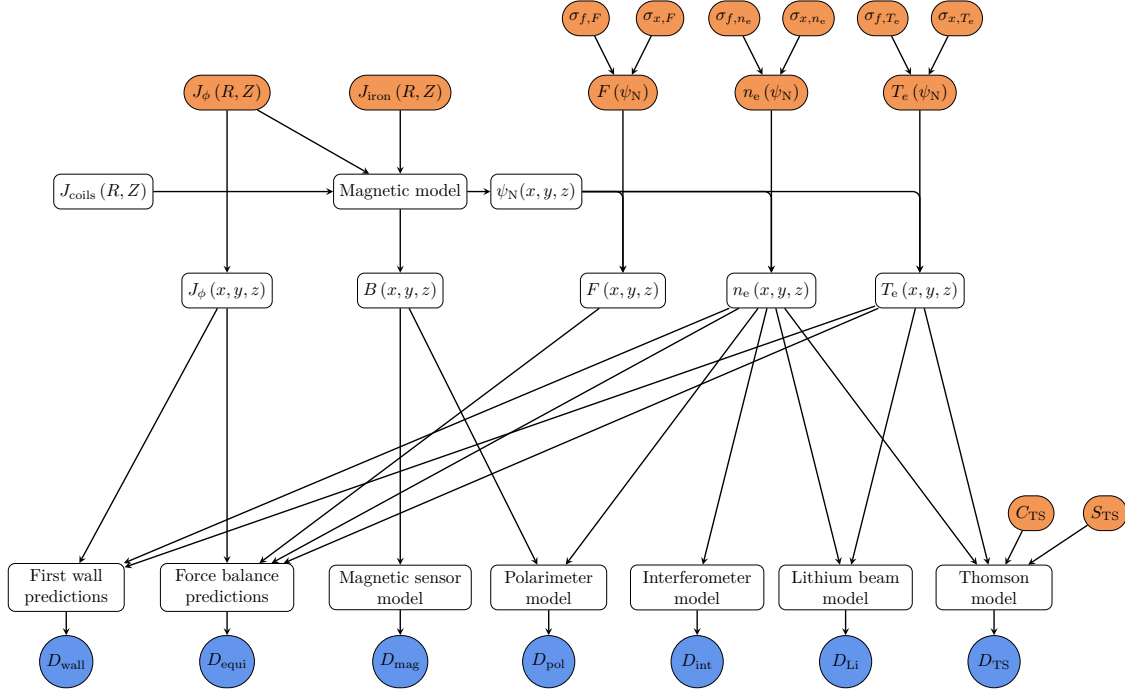


Figure 1. A simplified version of Minerva graph representing the Bayesian equilibrium model of axisymmetric plasmas at Joint European Torus (JET). The unknown parameters and observations are shown as the red and blue circles, respectively. The toroidal currents of the plasma J_{ϕ} , iron core J_{iron} and magnetic field coils J_{coils} are modelled as a 2D grid of toroidal current carrying solid beams in R, Z coordinates which determines the magnetic field B and the normalised poloidal magnetic flux surface ψ_N . The poloidal current flux F and electron density n_e and temperature T_e are modelled by Gaussian processes, whose hyperparameters are denoted as σ_f and σ_x . All these physics parameters are provided as 3D fields in x, y, z Cartesian coordinates, and given these 3D fields, the predictive models of the magnetic sensors, polarimeters, interferometers, lithium beam emission spectroscopy and high-resolution Thomson scattering (HRTS) systems make their predictions, which are directly compared to the corresponding observations. In order to emphasise equilibrium solutions, the model imposes the force balance between the magnetic force and the plasma pressure gradient, given by the Grad-Shafranov equation, at every plasma current beam by introducing the virtual observations that the differences between the two forces should be almost zero. In the same way, the model introduces empirical constraints that all the physics parameters should be almost zero at the first wall. The nodes in this graph represent larger, collapsed, subgraphs that model the internals of the different functions.

computationally challenging [14, 30, 31]. To overcome these problems, we have developed a new method to explore these posterior distributions based on the Gibbs sampling scheme [32]. In short, the method splits the full joint posterior distribution into several low dimensional conditional posterior distributions and sample them consecutively. These conditional posterior distributions are in general much simpler to sample, and some of them can be expressed in analytic functions obtained by the linear Gaussian inversion [8, 14]. The difficulty of sampling the full joint posterior distributions, therefore, can be substantially reduced by this method.

2. The model

In Bayesian inference [21, 33, 34], the model can be defined by a joint probability of unknown parameters and observations $P(H, D)$. The joint probability consists of the predictive probability $P(D|H)$ and the prior probability $P(H)$, which can be written as:

$$P(H, D) = P(D|H) P(H). \quad (1)$$

The prior probability $P(H)$ encodes the *prior knowledge* of the unknown parameters such as physical/empirical assumptions. For example, density or temperature must be positive, thus the probability of any negative density or temperature must be zero. Given a hypothetical value of the unknown parameters, a prediction can be made as a *predictive distributions* $P(D|H)$ over the observations. Typically, the mean of predictive distributions can be given as a function, which encapsulates the physical processes happening during an experiment by taking into account physics phenomena as well as experimental setup, known as a forward model $f(H)$. The prior probability of unknown parameters can be updated to the posterior probability $P(H|D)$ through Bayes formula:

$$P(H|D) = \frac{P(D, H)}{P(D)} = \frac{P(D|H) P(H)}{P(D)}, \quad (2)$$

where $P(D)$ is a marginal probability of the observation, also known as the model evidence, which is a normalisation constant in this context.

If the model contains a large number of unknown parameters and heterogeneous data sets, the model can be written as a product of individual prior and predictive distributions, conditional on their parent variables, also known as factorisation:

$$P(\{D_i\}, \{H_j\}) = \left(\prod_i P(D_i|H) \right) \left(\prod_i P(H_j) \right). \quad (3)$$

Each of the predictive distributions contains a forward model of the scientific instruments which includes model parameters, for example calibration factors. The prior distributions encode prior knowledge such as physics/empirical assumptions. The prior and predictive distributions together constitute the model, the joint distributions $P(\{D_i\}, \{H_j\})$. In other words, the model specification consists of not only the predictive distributions which make predictions over the observations but also the prior distributions in which

we reflect the prior knowledge and assumptions. All these model components and their conditional dependencies can be represented by a Bayesian graphical model, as shown in Figure 1, which is a transparent way of unfolding the complexity of the model.

In this work, we have developed Bayesian models of axisymmetric plasmas, the current tomography and equilibrium models, which involve a large number of unknown parameters, assumptions, predictive models and observations, as shown in Figure 1. The unknown parameters (the red circles) and observations (the blue circles) are connected via the forward models and functions (the white boxes), and the arrows visualise their dependencies. These two models share the following components: the axisymmetric current beam model (J_ϕ , J_{iron} , J_{coils} and **Magnetic model**), the Gaussian process priors of the poloidal current flux and pressure profiles (F , n_e and T_e), the wall constraints (D_{wall}) and the predictive distribution of all the plasma diagnostics (e.g. **Thomson model**). Given all these model components, the current tomography and equilibrium models employ the Gaussian process prior of the plasma current distributions and the equilibrium prior, respectively. All these model components are briefly described in the following subsections.

2.1. The axisymmetric current beam model

In an axisymmetric magnetic confinement fusion experiment, all kind of toroidal currents such as plasma and magnetic field coil currents can be modelled as a grid of toroidal solid beams with finite rectangular cross sections, each beam carrying a uniform current. This current beam model, previously developed in [8], has been implemented in the current tomography and equilibrium models. This current beam model takes into account the toroidal currents of the plasma J_ϕ , iron core J_{iron} and magnetic field coils J_{coils} of the JET fusion experiment, as shown in Figure 2.

Given these toroidal current distributions, the magnetic vector potential A at a spatial location $r = [x, y, z]$ generated by the toroidal current density J is given by the Biot-Savart law:

$$A(r) = \frac{\mu_0}{4\pi} \iiint \frac{J(r')}{|r - r'|} d^3r', \quad (4)$$

where μ_0 is the vacuum permeability. The magnetic field B can be derived from the vector potential, which is:

$$B = \nabla \times A. \quad (5)$$

The fast calculation of the magnetic vector potential and the magnetic field can be carried out by multiplying current density by a unit current response factor for an arbitrary fixed spatial location given the beam grids. These response factors are pre-calculated for all spatial locations where the model needs to determine the magnetic vector potential and the magnetic field, for instance the spatial locations of plasma current beams and magnetic sensors. From the magnetic vector potential, the poloidal magnetic flux ψ is given by:

$$\psi(x, y, z) = \oint A \cdot dl. \quad (6)$$

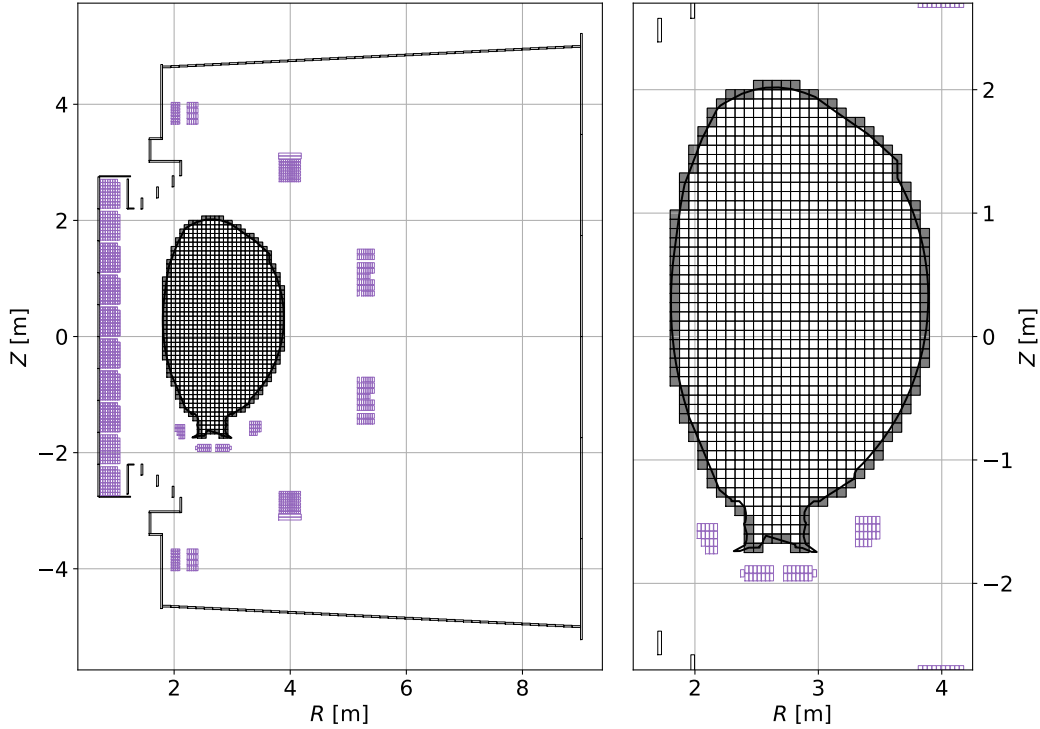


Figure 2. The JET toroidal current model. The beam grids of unknown toroidal currents of the plasma J_ϕ and iron core J_{iron} are shown in thin black lines. The beam grids of the poloidal magnetic field coil currents J_{coils} , which are retrieved from the JET database, are shown in thin purple lines. The equilibrium virtual observations D_{equi} , which impose the force balance constraints, are introduced at every plasma current beam. The wall virtual observations D_{wall} force the currents of the outermost beams (with grey shade) whose cross sections are intersected by the first wall of the JET machine (thick black line) to zero.

The poloidal magnetic flux can be represented as a set of flux surfaces, normalised to zero at the centre of plasma or the magnetic axis and to one at the boundary or the last closed flux surface (LCFS). These normalised poloidal magnetic flux surfaces ψ_N are often considered as the canonical coordinates, which plays an important role in diagnostic data analysis, physics studies and plasma control in nuclear fusion research. The current tomography and equilibrium models make use of the normalised flux ψ_N coordinates to express the other physics parameters, the poloidal current flux F and electron density n_e and temperature T_e by using Gaussian processes.

2.2. The Gaussian process prior

A Gaussian process [35, 36, 37] is a non-parametric function which associates any set of points of the domain of the function, for example space and time, with a random

vector following a multivariate Gaussian distribution. The properties of Gaussian process are specified by the mean and covariance function of the Gaussian distribution. The covariance function determines the covariance of output values at any two points which can be seen as smoothness of the Gaussian process. Unlike a parametric model, which might severely constrain the posterior distribution, the Gaussian process, not depending on any specific parameterisation, puts less constraints on the posterior distribution. In nuclear fusion research, Gaussian processes were introduced by non-parametric tomography of the electron density and current distribution [13], followed by a number of applications [9, 10, 16, 17, 23, 24, 38]. Gaussian processes are also the standard way to model profiles in Minerva.

The zero mean and squared exponential covariance function are one of the most common specifications of a Gaussian process $f(x)$, which can be given by:

$$f(x) \sim \mathcal{N}(\mu(x), \Sigma(x, x)), \quad (7)$$

$$\mu(x) = 0, \quad (8)$$

$$\Sigma(x_i, x_j) = \sigma_f^2 \exp\left(-\frac{(x_i - x_j)^2}{2\sigma_x}\right) + \sigma_y^2 \delta_{ij}, \quad (9)$$

where μ is the mean function and x is an arbitrary (scalar or vector) point in the domain. The covariance function $\Sigma(x_i, x_j)$ is defined between any two arbitrary points x_i and x_j . The parameters of the covariance function σ_f , σ_x and σ_y are the *hyperparameters* of the Gaussian process. The overall scale σ_f and the length scale σ_x determine smoothness of the function, and σ_y is chosen to be relatively small number with respect to σ_f , for example $\sigma_y/\sigma_f = 10^{-3}$ to avoid numerical instabilities. The overall and length scale (the smoothness) of this Gaussian process is constant over the domain. The prior distribution of the plasma current distributions J_ϕ is modelled by this Gaussian process, which is:

$$P(J_\phi | \sigma_{f, J_\phi}, \sigma_{x, J_\phi}) \sim \mathcal{N}(\mu_{J_\phi}(x), \Sigma_{J_\phi}(x, x)), \quad (10)$$

where the mean μ_{J_ϕ} and covariance function Σ_{J_ϕ} are given by Equation (8) and Equation (9), respectively. The domain of these functions is given in R, Z coordinates $x = [R, Z]$, and the length scale contains two components for R and Z direction $\sigma_{x, J_\phi} = [\sigma_{R, J_\phi}, \sigma_{Z, J_\phi}]$. The prior distributions of the hyperparameters σ_{f, J_ϕ} and σ_{x, J_ϕ} are given by uniform distributions. In a similar way, the prior distribution of the poloidal current flux F can be modelled by this Gaussian process as well, which is:

$$P(F | \sigma_{f, F}, \sigma_{x, F}) \sim \mathcal{N}(\mu_F(\psi_N), \Sigma_F(\psi_N, \psi_N)), \quad (11)$$

and the prior distributions of the hyperparameters $\sigma_{f, F}$ and $\sigma_{x, F}$ are given by uniform distributions.

The electron density and temperature can have substantially different smoothness (gradient) in the core and edge regions [39]. A non-stationary covariance function [40] is able to represent such spatially varying smoothness, which is given by:

$$\Sigma(x_i, x_j) = \sigma_f^2 \left(\frac{2\sigma_x(x_i)\sigma_x(x_j)}{\sigma_x(x_i)^2 + \sigma_x(x_j)^2} \right)^{\frac{1}{2}} \exp\left(-\frac{(x_i - x_j)^2}{\sigma_x(x_i)^2 + \sigma_x(x_j)^2}\right) + \sigma_y^2 \delta_{ij}, \quad (12)$$

where the length scale $\sigma_x(x)$ is given as an arbitrary function. We need a function with different smoothness (gradient) in the core and edge regions and a smooth transition between the two for the length scale, and for this reason, we choose a hyperbolic tangent function [9, 10], which is:

$$\sigma_x(x) = \frac{\sigma_x^{\text{core}} + \sigma_x^{\text{edge}}}{2} - \frac{\sigma_x^{\text{core}} - \sigma_x^{\text{edge}}}{2} \tanh\left(\frac{x - x_0}{x_w}\right), \quad (13)$$

where σ_x^{core} and σ_x^{edge} are the length scale value in the core and edge regions. The position and width of the transition are denoted as x_0 and x_w . The prior distributions of the electron density n_e and temperature T_e can be modelled by this Gaussian process, which is:

$$P(n_e | \sigma_{f,n_e}, \sigma_{x,n_e}) \sim \mathcal{N}(\mu_{n_e}(\psi_N), \Sigma_{n_e}(\psi_N, \psi_N)), \quad (14)$$

$$P(T_e | \sigma_{f,T_e}, \sigma_{x,T_e}) \sim \mathcal{N}(\mu_{T_e}(\psi_N), \Sigma_{T_e}(\psi_N, \psi_N)), \quad (15)$$

where their mean and covariance functions given by Equation (8) and Equation (12), respectively. The length scale functions σ_{x,n_e} and σ_{x,T_e} contain the four parameters of σ_x^{core} , σ_x^{edge} , x_0 and x_w . Again, the prior distributions of all these hyperparameters are given by uniform distributions.

All the physics parameters are modelled by either 2D beam grids in R, Z coordinates (J_ϕ and J_{iron}) or 1D Gaussian processes in the ψ_N coordinates (F , n_e and T_e). These physics parameters can be given by 3D fields in x, y, z coordinates through the coordinate transformations. Since we have such 3D fields of all these physics parameters, the predictions of observed quantities can be made at any point in space and time by the predictive models. Furthermore, physics/empirical laws can be predicted, for example the force balance equation. These predictions of the physics/empirical laws can be formally introduced as a part of the prior distributions by making virtual observations [14, 41].§

2.3. The equilibrium prior

A magnetic confinement fusion device confines the plasma particles with high kinetic energy by the magnetic force of the plasma currents and the magnetic field. This magnetic force counteracts the kinetic force of the plasma particles due to the plasma pressure gradient and keeps the plasma in a macroscopic equilibrium state, which can be described by the MHD force balance equation:

$$J \times B - \nabla p \simeq 0, \quad (16)$$

where J is the plasma current density, B is the magnetic field and p is the isotropic pressure of the plasma particles. For axisymmetric plasmas, this force balance can be

§ These observations are introduced to prescribe physics/empirical assumptions, not observed during the experiments.

given in term of the toroidal current density J_ϕ , poloidal current flux F and pressure p , by the Grad-Shafranov equation [5, 6], which can be written as:

$$J_\phi - Rp' - \frac{\mu_0}{R}FF' \simeq 0, \quad (17)$$

where $p' = \frac{\partial p}{\partial \psi}$ and $F' = \frac{\partial F}{\partial \psi}$. In this work, the isotropic pressure of plasma particles are assumed to be twice of the electron pressure $p = 2n_e T_e$.

In order to impose the MHD force balance, the model evaluates the integral of the Grad-Shafranov equation over cross section of every plasma current beam. These force balance constraints are introduced by *virtual* observations [14], which are given by:

$$P(D_{\text{equi}}|J_\phi, F, n_e, T_e) = \prod_i \mathcal{N} \left(\int_{Z_{\min,i}}^{Z_{\max,i}} \int_{R_{\min,i}}^{R_{\max,i}} J_\phi - Rp' - \frac{\mu_0}{R}FF' dR dZ, \sigma_{\text{equi}} \right), \quad (18)$$

where $R_{\min,i}$, $R_{\max,i}$, $Z_{\min,i}$ and $Z_{\max,i}$ are the minimum and maximum values of R and Z positions of the cross section of the i^{th} plasma current beam. All virtual measurements of the force balance constraints D_{equi} are set to be zero, which mean the force balance should be fulfilled. The standard deviation of these virtual observations σ_{equi} , to which we reflect the epistemic uncertainties of the force balance, is set to be 50 kA m^{-2} , a few per cent of the typical average plasma current density. These virtual observations together with the prior distributions of J_ϕ , F , n_e and T_e constitute the equilibrium prior [14], which can be written as:

$$P(J_\phi, F, n_e, T_e|D_{\text{equi}}) = \frac{P(D_{\text{equi}}|J_\phi, F, n_e, T_e) P(J_\phi) P(F) P(n_e) P(T_e)}{P(D_{\text{equi}})}. \quad (19)$$

Here, the prior distribution of the toroidal current density $P(J_\phi)$ is not given by Equation (10) but Gaussian distributions with large standard deviations, for instance $300 \times 10^6 \text{ kA m}^{-2}$, which is much higher than typical average plasma current density of the order of 10^3 kA m^{-2} at JET, thus these Gaussian priors are effectively uniform.

2.4. The wall constraints

The plasma current density J_ϕ and the electron density n_e and temperature T_e are not expected to be significantly high on the material surface facing the plasma inside the machine, also known as the first wall. These empirical expectations are taken into account by another set of virtual observations D_{wall} on the first wall. These virtual observations $D_{\text{wall}} = [D_{\text{wall},J_\phi}, D_{\text{wall},n_e}, D_{\text{wall},T_e}]$ are introduced at either the outermost plasma current beams whose cross section are intersected by the first wall (the beams with grey shade in Figure 2) or some spatial locations on the first wall except the divertor

regions (the black dots in Figure 3), which are given by:

$$P(D_{\text{wall}}|J_\phi, n_e, T_e) = P(D_{\text{wall}, J_\phi}|J_\phi) P(D_{\text{wall}, n_e}|n_e) P(D_{\text{wall}, T_e}|T_e), \quad (20)$$

$$P(D_{\text{wall}, J_\phi}|J_\phi) = \prod_i \mathcal{N}(J_\phi(R_i, Z_i), \sigma_{\text{wall}, J_\phi}), \quad (21)$$

$$P(D_{\text{wall}, n_e}|n_e) = \prod_i \mathcal{N}(n_e(x_i, y_i, z_i), \sigma_{\text{wall}, n_e}), \quad (22)$$

$$P(D_{\text{wall}, T_e}|T_e) = \prod_i \mathcal{N}(T_e(x_i, y_i, z_i), \sigma_{\text{wall}, T_e}), \quad (23)$$

where $J_\phi(R_i, Z_i)$ is the plasma current density of the i^{th} outermost current beam and $n_e(x_i, y_i, z_i)$ and $T_e(x_i, y_i, z_i)$ are the electron density and temperature at the i^{th} spatial location on the first wall. All the virtual observations and uncertainties at the first wall are set to be reasonably low: $D_{\text{wall}, J_\phi} = 0.0 \text{ kA m}^{-2}$, $\sigma_{\text{wall}, J_\phi} = 1.0 \text{ kA m}^{-2}$, $D_{\text{wall}, n_e} = 10^{15} \text{ m}^{-3}$, $\sigma_{\text{wall}, n_e} = 10^{15} \text{ m}^{-3}$, $D_{\text{wall}, T_e} = 0.1 \text{ eV}$ and $\sigma_{\text{wall}, T_e} = 0.1 \text{ eV}$.

2.5. The plasma diagnostics

In order to find all possible plasma current distributions as well as the poloidal current flux and pressure profiles consistent with magnetic field and pressure measurements simultaneously, the current tomography and equilibrium models employ a number of predictive models of the following plasma diagnostics: magnetic sensors (pickup coils, saddle coils and flux loops) [8], polarimeters [15], interferometers [10, 13, 14], lithium beam emission spectroscopy [16, 17] and high-resolution Thomson scattering (HRTS) systems [10]. All the lines of sight and observation positions of all these plasma diagnostics are shown in Figure 3. Each of these predictive models includes forward models of measurement techniques which encapsulate the relevant physical phenomena and experimental setup. These models make the predictions of these measurements given the 3D fields of these physics parameters in x, y, z coordinates. These 3D fields of the poloidal current flux F and electron density n_e and temperature T_e are transformed from the ψ_N coordinates, thus all the measurements related to those parameters from the polarimeters, interferometers, lithium beam emission spectroscopy and HRTS systems depend on the toroidal current distributions J_ϕ and J_{iron} as well as the coil currents J_{coils} , which are known and taken from the JET database.

2.5.1. The magnetic sensors The JET magnetic sensors consist of the pickup coils, saddle coils and flux loops (the red dots, lines and diamonds in Figure 3). These magnetic sensors measure the magnetic flux through the surrounding coils. The pickup coils, saddle coils and flux loops provide, respectively, local magnetic field measurements at the coil positions (the red dots), flux differences between the two R, Z positions (the two endpoints of the red lines) and poloidal magnetic flux through the toroidal loops

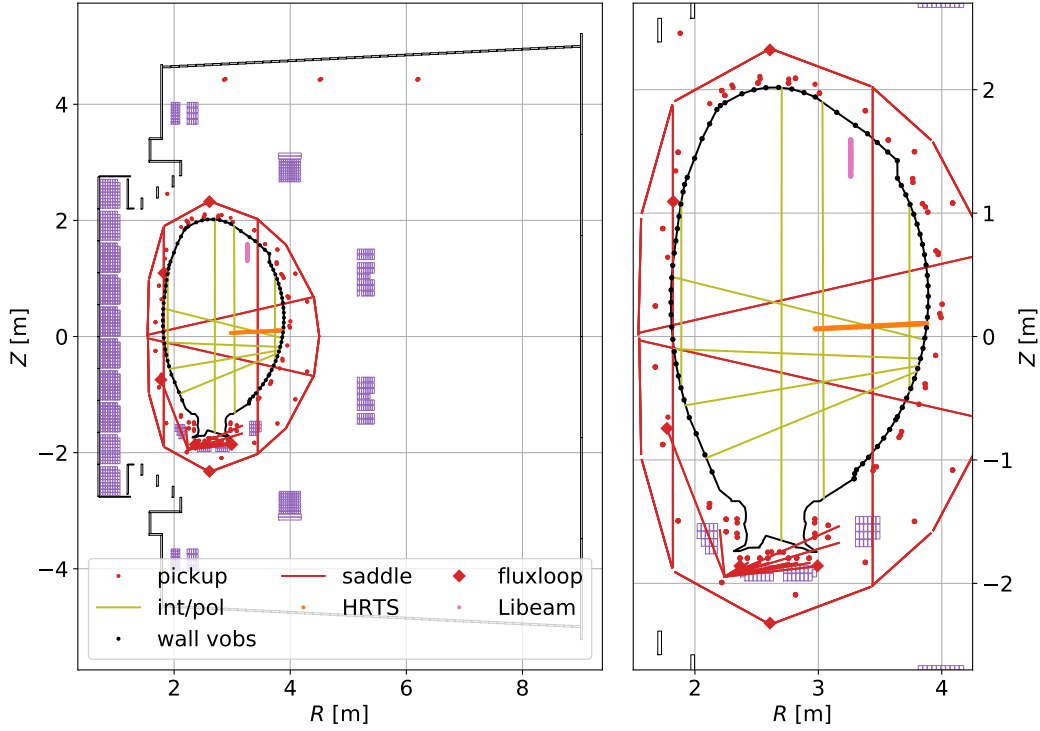


Figure 3. The lines of sight and observation positions, projected into the poloidal plane, of all the JET diagnostics in the model. The magnetic sensors (in red) consist of pickup coils, saddle coils and flux loops, which measure the magnetic field strength. The interferometers and polarimeters share the lines of sight (in yellow) and provide $\int n_e dl$ and $\int n_e B_{\parallel} dl$, respectively. The HRTS system measures the electron density and temperature at 63 spatial locations (in orange) along the horizontal injected laser path. The lithium beam emission spectroscopy system provides edge electron density at 26 spatial locations (in pink) along the vertically injected beam from the top of the machine. The first wall and the wall constraints are shown in the black line and dots.

(the red diamonds). The predictive model of all these magnetic sensors [8] is given by:

$$P(D_{\text{mag}}|J_{\phi}, J_{\text{iron}}) = P(D_{\text{pickup}}|J_{\phi}, J_{\text{iron}}) P(D_{\text{saddle}}|J_{\phi}, J_{\text{iron}}) P(D_{\text{fluxloop}}|J_{\phi}, J_{\text{iron}}), \quad (24)$$

$$P(D_{\text{pickup}}|J_{\phi}, J_{\text{iron}}) = \prod_i \mathcal{N}(B_R(R_i, Z_i) \cos \theta_i + B_Z(R_i, Z_i) \sin \theta_i, \sigma_{\text{pickup},i}), \quad (25)$$

$$P(D_{\text{saddle}}|J_{\phi}, J_{\text{iron}}) = \prod_i \mathcal{N}(G_{\text{saddle},i}(\psi(R_{2,i}, Z_{2,i}) - \psi(R_{1,i}, Z_{1,i})), \sigma_{\text{saddle},i}), \quad (26)$$

$$P(D_{\text{fluxloop}}|J_{\phi}, J_{\text{iron}}) = \prod_i \mathcal{N}(\psi(R_i, Z_i), \sigma_{\text{fluxloop},i}), \quad (27)$$

where $B_R(R_i, Z_i)$ and $B_Z(R_i, Z_i)$ are the R and Z direction of the magnetic field at the position of the i^{th} pickup coil with the angle of the normal vector θ_i , $\psi(R_{2,i}, Z_{2,i})$ and $\psi(R_{1,i}, Z_{1,i})$ are the poloidal magnetic flux at the two R, Z positions of the i^{th} saddle coil with the correction factor for the actual 3D coil geometry $G_{\text{saddle},i}$ and $\psi(R_i, Z_i)$ is the poloidal magnetic flux through the i^{th} flux loop. All the observations and uncertainties of all these magnetic sensors $D_{\text{mag}} = [D_{\text{pickup}}, D_{\text{saddle}}, D_{\text{fluxloop}}]$ and $\sigma_{\text{mag}} = [\sigma_{\text{pickup}}, \sigma_{\text{saddle}}, \sigma_{\text{fluxloop}}]$ are retrieved from the JET database.

2.5.2. The interferometers and polarimeters The JET far-infrared (FIR) interferometer-polarimeter system [42, 43, 44] launches electromagnetic waves into the plasma and measures the phase differences and polarisation angles between these injected waves and the reference wave. These phase differences and polarisation angles are proportional to the line integrated quantities $\int n_e d\ell$ and $\int n_e B_{\parallel} d\ell$, respectively, along four lateral and four vertical lines of sight (the yellow lines in Figure 3). These quantities are pre-calculated and stored in the JET database with their uncertainties. The predictive models of the JET interferometer-polarimeter system [14, 15] are given by:

$$P(D_{\text{int}} | n_e(\psi_N)) = \prod_i \mathcal{N}\left(\int n_e d\ell_i, \sigma_{\text{int},i}\right), \quad (28)$$

$$P(D_{\text{pol}} | J_\phi, n_e(\psi_N)) = \prod_i \mathcal{N}\left(\int n_e B_{\parallel} d\ell_i, \sigma_{\text{pol},i}\right), \quad (29)$$

where $\int d\ell_i$ is the line integral along the i^{th} line of sight and B_{\parallel} is the magnetic field strength parallel to the line of sight. All the observations and uncertainties of all these line integrated quantities $D_{\text{int}}, D_{\text{pol}}, \sigma_{\text{int}}, \sigma_{\text{pol}}$ are retrieved from the JET database.

2.5.3. The high-resolution Thomson scattering (HRTS) system The JET high-resolution Thomson scattering (HRTS) system [45] launches laser pulses into the plasma and collects Thomson scattered photons [46] with polychromators with four spectral channels from 63 spatial locations (the orange dots in Figure 3) with a spatial resolution of 0.8 cm to 1.6 cm and a temporal resolution of 20 Hz. The intensity and width of Thomson scattering spectra provide the electron density n_e and temperature T_e measurements. Since the electron density calibration factor C_{TS} and the position shift of all spatial channels along the laser path S_{TS} of the HRTS system are cross-calibrated with other plasma diagnostics, they are regarded as additional unknown parameters. The predictive model of the JET HRTS system [10] is given by:

$$P(D_{\text{TS}} | n_e(\psi_N), T_e(\psi_N), C_{\text{TS}}, S_{\text{TS}}) = \prod_i \prod_j \mathcal{N}(A_{\text{TS},i,j}(n_e(R_i, Z_i, S_{\text{TS}}), T_e(R_i, Z_i, S_{\text{TS}}), C_{\text{TS}}), \sigma_{\text{TS},i,j}), \quad (30)$$

where $A_{\text{TS},i,j}(n_e(R_i, Z_i, S_{\text{TS}}), T_e(R_i, Z_i, S_{\text{TS}}), C_{\text{TS}})$ is the amplitude of the Thomson scattering spectrum of the j^{th} spectral channel of the i^{th} spatial position and $\sigma_{\text{TS},i,j}$ is

the corresponding uncertainty. The electron density and temperature at the shifted position of the i^{th} spatial channel are given by:

$$n_e(R_i, Z_i, S_{\text{TS}}) = n_e(R_i + S_{\text{TS}} \cos \theta_{\text{TS}}, Z_i + S_{\text{TS}} \sin \theta_{\text{TS}}), \quad (31)$$

$$T_e(R_i, Z_i, S_{\text{TS}}) = T_e(R_i + S_{\text{TS}} \cos \theta_{\text{TS}}, Z_i + S_{\text{TS}} \sin \theta_{\text{TS}}), \quad (32)$$

where R_i and Z_i the R and Z position of the i^{th} spatial channel and θ_{TS} is the angle of the laser path. If the position shift S_{TS} is positive, the shifted positions will be closer to the first wall than the original positions. The range of S_{TS} is set not to allow any shifted position to be beyond the first wall. The amplitude of the Thomson scattering spectrum can be written as:

$$A_{\text{TS},i,j}(n_e, T_e, C_{\text{TS}}) = C_{\text{TS}} n_e E_{\text{laser}} \int \phi_{i,j}(\lambda) \frac{\lambda}{hc} r_e^2 \frac{S(\lambda, \theta, T_e)}{\lambda_{\text{laser}}} d\lambda, \quad (33)$$

where E_{laser} is the laser energy, $\phi_{i,j}(\lambda)$ spectral response function of the j^{th} spectral channel of the i^{th} spatial position, λ the scattered wavelength, h the Planck constant, c the speed of light, r_e the classical electron radius, $S(\lambda, \theta, T_e)$ the spectral density function [47], θ the scattering angle and λ_{laser} the laser wavelength. The prior distributions of C_{TS} and S_{TS} are given by uniform distributions.

2.5.4. The lithium beam emission spectroscopy system The JET lithium beam emission spectroscopy system [48, 49] injects lithium beam atoms into the plasma and collect line emission at 26 spatial locations (the pink dots in Figure 3) with a spatial resolution of approximately 1.0 cm and a temporal resolution of 10 ms to 20 ms. The lithium beam atoms interact with the plasma electrons and ions via collisions and produce spontaneous emission from the first excited state. The intensity of the line emission can provide the electron density and temperature measurements, but the JET lithium beam emission spectroscopy system is designed to provide only the electron density measurements in the edge region at the top of the machine. The predictive model of the JET lithium beam emission spectroscopy system [16, 17] is given by:

$$P(D_{\text{Li}} | n_e(\psi_N), T_e(\psi_N)) = \prod_i \mathcal{N}(A_{\text{Li},i}(n_e(R_i, Z_i), T_e(R_i, Z_i)), \sigma_{\text{Li},i}), \quad (34)$$

where $A_{\text{Li},i}(n_e(R_i, Z_i), T_e(R_i, Z_i))$ is the amplitude of the lithium line emission of the i^{th} spatial position and $\sigma_{\text{Li},i}$ is the corresponding uncertainty. The amplitude of the line emission is predicted by the collisional-radiative model which takes into account excitation and de-excitation, ionisation and spontaneous emission.

2.6. The joint distribution

All these prior and predictive distributions represent the prior knowledge of the unknown parameters and the predictions of the observations and together constitute the joint distribution which embodies the full relationship between the unknown parameters and the observations. Therefore, the model is defined as the joint distribution.

The axisymmetric plasma model with the Gaussian process prior of the plasma current distributions, the current tomography model, is given by:

$$\begin{aligned}
& P(J_\phi, \sigma_{J_\phi}, J_{\text{iron}}, n_e, \sigma_{n_e}, T_e, \sigma_{T_e}, C_{\text{TS}}, S_{\text{TS}}, D_{\text{mag}}, D_{\text{int}}, D_{\text{pol}}, D_{\text{Li}}, D_{\text{TS}}, D_{\text{wall}}) \\
& = P(D_{\text{mag}}|J_\phi, J_{\text{iron}}) P(D_{\text{int}}|n_e(\psi_N)) P(D_{\text{pol}}|J_\phi, n_e(\psi_N)) P(D_{\text{Li}}|n_e(\psi_N), T_e(\psi_N)) \\
& \times P(D_{\text{TS}}|n_e(\psi_N), T_e(\psi_N), C_{\text{TS}}, S_{\text{TS}}) P(C_{\text{TS}}) P(S_{\text{TS}}) P(D_{\text{wall}}|J_\phi, n_e(\psi_N), T_e(\psi_N)) \\
& \times P(J_\phi|\sigma_{f,J_\phi}, \sigma_{x,J_\phi}) P(\sigma_{f,J_\phi}) P(\sigma_{x,J_\phi}) P(J_{\text{iron}}) \\
& \times P(n_e|\sigma_{f,n_e}, \sigma_{x,n_e}) P(\sigma_{f,n_e}) P(\sigma_{x,n_e}) P(T_e|\sigma_{f,T_e}, \sigma_{x,T_e}) P(\sigma_{f,T_e}) P(\sigma_{x,T_e}), \quad (35)
\end{aligned}$$

where $\sigma_{J_\phi} = [\sigma_{f,J_\phi}, \sigma_{x,J_\phi}]$, $\sigma_F = [\sigma_{f,F}, \sigma_{x,F}]$, $\sigma_{n_e} = [\sigma_{f,n_e}, \sigma_{x,n_e}]$ and $\sigma_{T_e} = [\sigma_{f,T_e}, \sigma_{x,T_e}]$. The other model with the equilibrium prior shown in Figure 1, the equilibrium model, is given by:

$$\begin{aligned}
& P(J_\phi, J_{\text{iron}}, F, \sigma_F, n_e, \sigma_{n_e}, T_e, \sigma_{T_e}, C_{\text{TS}}, S_{\text{TS}}, D_{\text{mag}}, D_{\text{int}}, D_{\text{pol}}, D_{\text{Li}}, D_{\text{TS}}, D_{\text{equi}}, D_{\text{wall}}) \\
& = P(D_{\text{mag}}|J_\phi, J_{\text{iron}}) P(D_{\text{int}}|n_e(\psi_N)) P(D_{\text{pol}}|J_\phi, n_e(\psi_N)) P(D_{\text{Li}}|n_e(\psi_N), T_e(\psi_N)) \\
& \times P(D_{\text{TS}}|n_e(\psi_N), T_e(\psi_N), C_{\text{TS}}, S_{\text{TS}}) P(C_{\text{TS}}) P(S_{\text{TS}}) P(D_{\text{wall}}|J_\phi, n_e(\psi_N), T_e(\psi_N)) \\
& \times P(D_{\text{equi}}|J_\phi, n_e(\psi_N), T_e(\psi_N), F(\psi_N)) P(J_\phi) P(J_{\text{iron}}) P(F|\sigma_{f,F}, \sigma_{x,F}) P(\sigma_{f,F}) P(\sigma_{x,F}) \\
& \times P(n_e|\sigma_{f,n_e}, \sigma_{x,n_e}) P(\sigma_{f,n_e}) P(\sigma_{x,n_e}) P(T_e|\sigma_{f,T_e}, \sigma_{x,T_e}) P(\sigma_{f,T_e}) P(\sigma_{x,T_e}). \quad (36)
\end{aligned}$$

We emphasise that the main difference between these two models is the choice of the prior distribution to emphasise solutions based on either optimal hyperparameters based on Bayesian Occam's razor or the MHD force balance. The current tomography model makes use of the Gaussian process prior of the plasma current distributions with the optimal hyperparameters, and on the other hand, the equilibrium model imposes the MHD force balance by the equilibrium prior.

3. The inference

Given the joint distributions, when observations are made by an experiment, the posterior distributions can be calculated through Bayes formula, given by Equation (2). The full joint posterior distribution of the current tomography model is:

$$\begin{aligned}
& P(J_\phi, \sigma_{J_\phi}, J_{\text{iron}}, n_e, \sigma_{n_e}, T_e, \sigma_{T_e}, C_{\text{TS}}, S_{\text{TS}}, D_{\text{mag}}, D_{\text{int}}, D_{\text{pol}}, D_{\text{Li}}, D_{\text{TS}}, D_{\text{wall}}) \\
& = \frac{P(J_\phi, \sigma_{J_\phi}, J_{\text{iron}}, n_e, \sigma_{n_e}, T_e, \sigma_{T_e}, C_{\text{TS}}, S_{\text{TS}}|D_{\text{mag}}, D_{\text{int}}, D_{\text{pol}}, D_{\text{Li}}, D_{\text{TS}}, D_{\text{wall}})}{P(D_{\text{mag}}, D_{\text{int}}, D_{\text{pol}}, D_{\text{Li}}, D_{\text{TS}}, D_{\text{wall}})}, \quad (37)
\end{aligned}$$

and the one of the equilibrium model is:

$$\begin{aligned}
& P(J_\phi, J_{\text{iron}}, F, \sigma_F, n_e, \sigma_{n_e}, T_e, \sigma_{T_e}, C_{\text{TS}}, S_{\text{TS}}|D_{\text{mag}}, D_{\text{int}}, D_{\text{pol}}, D_{\text{Li}}, D_{\text{TS}}, D_{\text{equi}}, D_{\text{wall}}) \\
& = \frac{P(J_\phi, J_{\text{iron}}, F, \sigma_F, n_e, \sigma_{n_e}, T_e, \sigma_{T_e}, C_{\text{TS}}, S_{\text{TS}}, D_{\text{mag}}, D_{\text{int}}, D_{\text{pol}}, D_{\text{Li}}, D_{\text{TS}}, D_{\text{equi}}, D_{\text{wall}})}{P(D_{\text{mag}}, D_{\text{int}}, D_{\text{pol}}, D_{\text{Li}}, D_{\text{TS}}, D_{\text{equi}}, D_{\text{wall}})}, \quad (38)
\end{aligned}$$

where the denominators are a normalisation constant in this context. These posterior distributions can be explored by optimisation or sampling algorithms, for example pattern search [50] and Markov chain Monte Carlo (MCMC) algorithms [51, 52, 53], in order to find the optimal solution, which maximises the posterior probability, also known as the maximum *a posteriori* (MAP) solution or all possible solutions, which are drawn from the posterior distribution, also known as posterior samples. However, these posterior distributions are high dimensional (more than 1000 dimensions) and highly correlated through all these observations. In addition, these distributions involve all these forward models, which often require a significant amount of computation time. For this reason, exploration of such complex, high dimensional posterior distributions is computationally challenging [14, 30, 31]. A number of numerical recipes and algorithms has been applied to the equilibrium problem [14, 30, 31, 41, 54, 55], but, none of these algorithms manage to sample from these complex joint posterior distributions for cases such as H-mode plasmas.

In this work, we have developed a new method to explore these posterior distributions. The main idea of the new method is to separate a high dimensional target distribution $P(X_1, X_2, \dots, X_n)$ into a number of low dimensional conditional distributions $P(X_i | X_1, \dots, X_{i-1}, X_{i+1}, \dots, X_n)$ and to sample them consecutively based on the Gibbs sampling scheme [32] as follow:

- (i) Begin with initial values $X_1^{(k)}, X_2^{(k)}, \dots, X_n^{(k)}$.
- (ii) Sample the first parameter $X_1^{(k+1)}$ from $P(X_1^{(k+1)} | X_2^{(k)}, X_3^{(k)}, \dots, X_n^{(k)})$. Update the first parameter to $X_1^{(k+1)}$ and sample the second parameter $X_2^{(k+1)}$ from $P(X_2^{(k+1)} | X_1^{(k+1)}, X_3^{(k)}, \dots, X_n^{(k)})$. Update the second parameter to $X_2^{(k+1)}$ and sample the third parameter $X_3^{(k+1)}$ from $P(X_3^{(k+1)} | X_1^{(k+1)}, X_2^{(k+1)}, X_4^{(k)}, \dots, X_n^{(k)})$. Likewise, sample all the other parameters consecutively until to update all the parameters to $X_1^{(k+1)}, X_2^{(k+1)}, \dots, X_n^{(k+1)}$, which will be the $(k+1)^{\text{th}}$ sample.
- (iii) Repeat the above.

The samples approximate the target distribution $P(X_1, X_2, \dots, X_n)$. These conditional distributions are in general much simpler to sample than the target distribution, and for some of them, analytic expressions can be found. In this way, the difficulty of sampling the high dimensional target distribution can be substantially reduced.

For this reason, the current tomography model is divided by the following parts:

$$P(J_\phi, J_{\text{iron}} | n_e, \sigma_{n_e}, T_e, \sigma_{T_e}, C_{\text{TS}}, S_{\text{TS}}, D_{\text{mag}}, D_{\text{int}}, D_{\text{pol}}, D_{\text{Li}}, D_{\text{TS}}, D_{\text{wall}}), \quad (39)$$

$$P(n_e, \sigma_{n_e}, T_e, \sigma_{T_e}, C_{\text{TS}}, S_{\text{TS}} | J_\phi, J_{\text{iron}}, D_{\text{mag}}, D_{\text{int}}, D_{\text{pol}}, D_{\text{Li}}, D_{\text{TS}}, D_{\text{wall}}), \quad (40)$$

and the equilibrium model is divided by the following parts:

$$P(J_\phi, J_{\text{iron}} | F, \sigma_F, n_e, \sigma_{n_e}, T_e, \sigma_{T_e}, C_{\text{TS}}, S_{\text{TS}}, D_{\text{mag}}, D_{\text{int}}, D_{\text{pol}}, D_{\text{Li}}, D_{\text{TS}}, D_{\text{equi}}, D_{\text{wall}}), \quad (41)$$

$$P(n_e, \sigma_{n_e}, T_e, \sigma_{T_e}, C_{\text{TS}}, S_{\text{TS}} | J_\phi, J_{\text{iron}}, F, \sigma_F, D_{\text{mag}}, D_{\text{int}}, D_{\text{pol}}, D_{\text{Li}}, D_{\text{TS}}, D_{\text{equi}}, D_{\text{wall}}), \quad (42)$$

$$P(F, \sigma_F | J_\phi, J_{\text{iron}}, n_e, \sigma_{n_e}, T_e, \sigma_{T_e}, C_{\text{TS}}, S_{\text{TS}}, D_{\text{mag}}, D_{\text{int}}, D_{\text{pol}}, D_{\text{Li}}, D_{\text{TS}}, D_{\text{equi}}, D_{\text{wall}}). \quad (43)$$

In order to make analytic expressions available for the conditional posterior distributions of electron density and temperature, given by Equation (40) and Equation (42), through the linear Gaussian inversion [8, 14], the observations of the HRTS and lithium beam spectroscopy systems are given as electron density and temperature, which are pre-calculated from individual inference applications. In addition, the hyperparameters σ_F , σ_{n_e} and σ_{T_e} and the HRTS model parameters C_{TS} and S_{TS} are set to be the MAP solutions which are found through the inversion procedures, described in the next paragraph. These conditional posterior distributions of the current tomography model can be now written as:

$$P(J_\phi, J_{\text{iron}} | n_e, T_e, C_{\text{TS}}, S_{\text{TS}}, D_{\text{mag}}, D_{\text{int}}, D_{\text{pol}}, D_{\text{Li}}, D_{\text{TS}}, D_{\text{wall}}), \quad (44)$$

$$P(n_e, T_e | J_\phi, J_{\text{iron}}, \sigma_{n_e}, \sigma_{T_e}, C_{\text{TS}}, S_{\text{TS}}, D_{\text{int}}, D_{\text{pol}}, D_{\text{Li}}, D_{\text{TS}}, D_{\text{wall}}), \quad (45)$$

and those of the equilibrium model:

$$P(J_\phi, J_{\text{iron}} | F, n_e, T_e, C_{\text{TS}}, S_{\text{TS}}, D_{\text{mag}}, D_{\text{int}}, D_{\text{pol}}, D_{\text{Li}}, D_{\text{TS}}, D_{\text{equi}}, D_{\text{wall}}), \quad (46)$$

$$P(n_e, T_e | J_\phi, J_{\text{iron}}, F, \sigma_{n_e}, \sigma_{T_e}, C_{\text{TS}}, S_{\text{TS}}, D_{\text{int}}, D_{\text{pol}}, D_{\text{Li}}, D_{\text{TS}}, D_{\text{equi}}, D_{\text{wall}}), \quad (47)$$

$$P(F | J_\phi, J_{\text{iron}}, \sigma_F, n_e, T_e, D_{\text{equi}}). \quad (48)$$

Most of these conditional posterior distributions can be sampled from their analytic expressions through the linear Gaussian inversion. The conditional posterior distribution of the toroidal current distributions whose analytic forms are not available through the linear Gaussian inversion can be explored by MCMC algorithm, specifically the adaptive Metropolis–Hastings algorithm [51, 52, 53]. Still approximated analytic distribution functions are available for these distributions, the MCMC algorithm can use these approximated distribution functions as initial proposal distributions. The posterior samples of the full joint posterior distributions will be drawn by sampling these conditional posterior distributions consecutively.

The MAP solutions can be found by a set of optimisation steps to explore the conditional posterior distributions based on the same scheme. Here, the procedure makes use of the pattern search algorithm [50] and the linear Gaussian inversion as follow:

- (i) Infer the toroidal current density J_ϕ and J_{iron} by the current tomography [8] with Gaussian processes given the magnetic field measurements D_{mag} and the wall constraints D_{wall} through the linear Gaussian inversion. The optimal

hyperparameters are found through the pattern search algorithm that explores the model evidence, which can be analytically calculated through the linear Gaussian inversion.

- (ii) Calculate the magnetic flux surface ψ_N given the toroidal current density.
- (iii) Infer the electron density n_e and temperature T_e given the ψ_N coordinates as well as the electron density and temperature measurements D_{int} , D_{Li} , D_{TS} and the wall constraints D_{wall} through the linear Gaussian inversion. The hyperparameters σ_{n_e} and σ_{T_e} and the HRTS model parameters C_{TS} and S_{TS} are optimised through the pattern search algorithm with the linear Gaussian inversion to explore the model evidence.
- (iv) Infer the poloidal current flux F and the hyperparameters σ_F given all the other unknown parameters from the previous steps and equilibrium prior D_{equi} if the equilibrium model. Otherwise, skip this step.
- (v) Infer the toroidal current density J_ϕ and J_{iron} given all the other unknown parameters given the previous steps and the magnetic field measurements D_{mag} in addition to the polarimeter measurements D_{pol} as well as the wall constraints D_{wall} .
- (vi) Explore the full joint posterior distribution by the pattern search algorithm from these initial guesses.
- (vii) Repeat the above from (iii) until finding the (local) maximum.

The MAP solutions are relatively easier to be found than the posterior samples and can be used as inference solutions or initial guesses for further exploration. The new sampling method uses these MAP solutions as initial guesses in order to sample the full joint posterior distribution. In the following subsections, the MAP solutions and the posterior samples of the current tomography and equilibrium models found by these inversion procedures will be presented.

3.1. The current tomography inference

The full joint posterior distribution of the current tomography model are explored to find all possible plasma current distributions and electron pressure profiles, which are modelled by the Gaussian process priors, given all the measurements simultaneously through the new inversion procedures. The marginal posterior distributions of the normalised poloidal magnetic flux surfaces, the electron density and temperature profiles for typical JET L- and H-mode plasmas are shown in Figure 4 and Figure 5. The blue and light blue lines are the marginal posterior mean and samples, respectively. The blue dashed lines are the lower and upper boundaries of one standard deviation ($\pm 1\sigma$) marginal posterior uncertainty bands. The magnetic axis and the last closed flux surface (LCFS) are depicted as big dots and thick lines, and three different sets of thinner lines are the normalised flux surfaces which are corresponding to $\psi_N = 0.25, 0.50, 0.75$ in Figure 4(a) and Figure 5(a). For comparison, the normalised flux surfaces of the conventional equilibrium fitting (EFIT) code [7, 56] (in green), the electron density

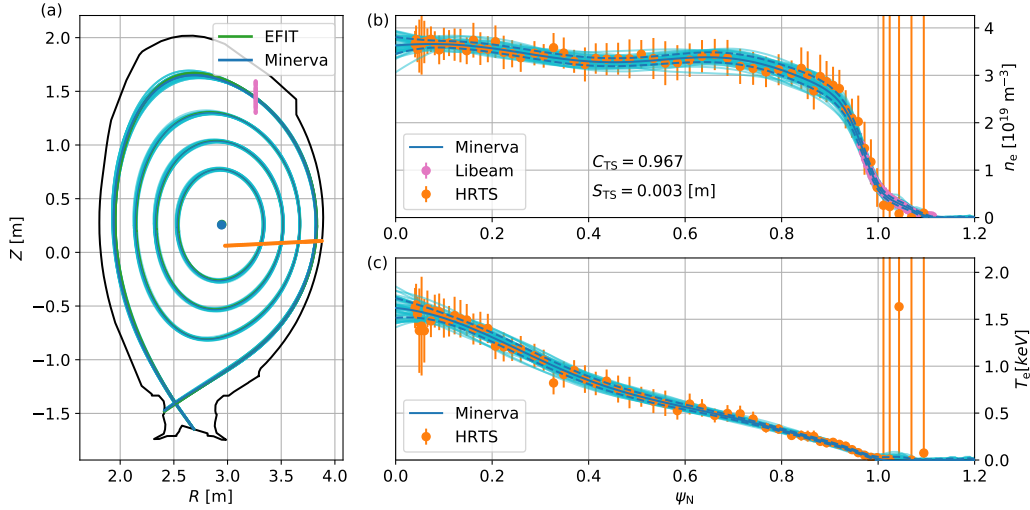


Figure 4. The inference results of the current tomography model for JET discharge #89709 at 8.0s (an L-mode plasma): (a) the normalised poloidal magnetic flux surfaces, (b) the electron density and (c) temperature profiles. For comparison, the results of the conventional analysis of the equilibrium fitting (EFIT) code (in green), the HRTS system (in orange) and the lithium beam spectroscopy (in pink) systems are shown here. The orange and pink dots in (a) are the measurement positions of the HRTS and lithium beam spectroscopy systems, respectively. The HRTS system is automatically calibrated with the inferred HRTS model parameters C_{TS} and S_{TS} given all the other measurements, and the posterior mean of C_{TS} and S_{TS} are presented. We note that these inferred HRTS model parameters C_{TS} and S_{TS} are also applied to the electron density profiles of the conventional analysis of the HRTS system (the orange dots), which means that the HRTS electron density profiles (the orange dots) are slightly lower (in this case 0.967 times lower) than the original analysis results.

and temperature profiles of the conventional analysis of the HRTS (in orange) and the lithium beam spectroscopy (in pink) systems are presented. The orange and pink dots in Figure 4(a) and Figure 5(a) are the measurement positions of the HRTS and lithium beam spectroscopy systems, respectively. The HRTS system is automatically calibrated with the inferred electron density calibration factor C_{TS} and the measurement position shift S_{TS} given all the other measurements during the inversion procedures. The posterior mean of C_{TS} and S_{TS} are presented in Figure 4(b) and Figure 5(b). We note that these inferred HRTS model parameters C_{TS} and S_{TS} are also applied to calibrate the electron density profiles of the conventional analysis of the HRTS system shown in Figure 4(b) and Figure 5(b) in order to make reasonable comparison and avoid confusion. This means that the HRTS electron density profiles (the orange dots) are 0.967 times lower than the original analysis results.

The hyperparameters of Gaussian processes of the plasma current distributions and electron density and temperature profiles are optimised by maximising the posterior distributions of the hyperparameters during the inversion procedures, and the marginal

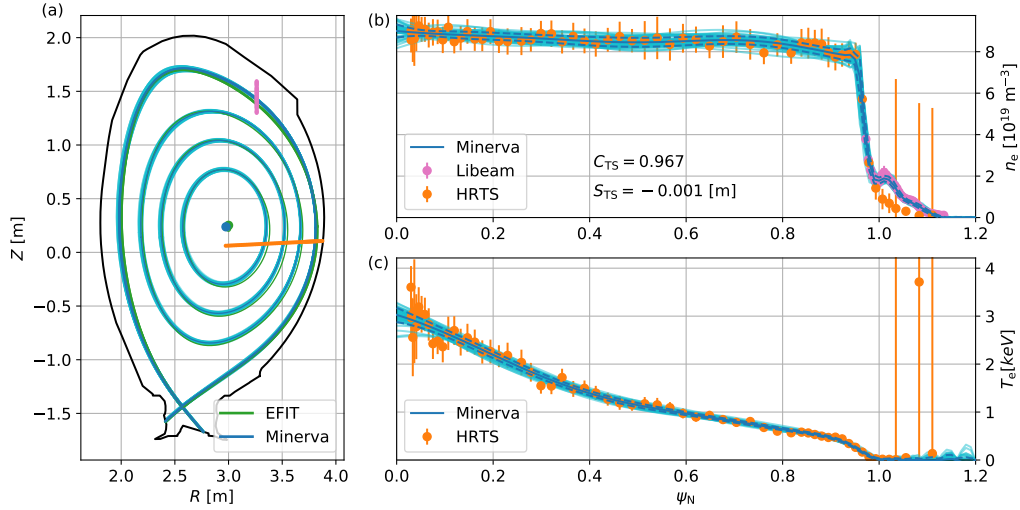


Figure 5. Same as Figure 4 for an H-mode plasma (JET discharge #89709 at 13.5 s).

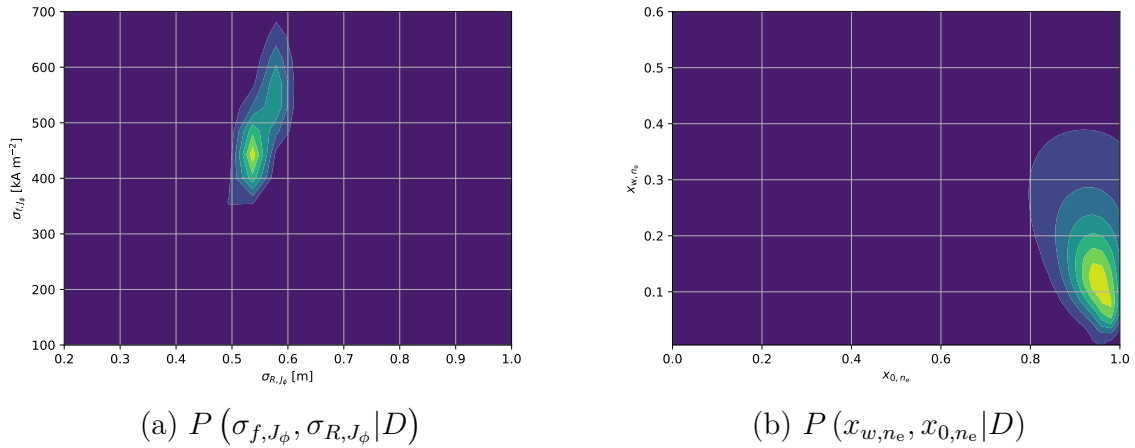


Figure 6. The marginal posterior distributions of the hyperparameters explored during the MAP inversion procedures: (a) the overall and length scale of the plasma current distributions and (b) the position and width of the transition of the smoothness of the electron density profiles.

posterior distributions of these hyperparameters are shown in Figure 6. These posterior distributions are proportional to the model evidence which embodies Bayesian Occam's razor [11, 12], and over-complex Gaussian processes are quantitative and automatically rejected. As shown in Figure 5, the Gaussian processes with the optimal hyperparameters are able to represent the low and steep gradient of the electron density and temperature profiles in the core and edge regions without problems of under- or over-fitting.

The comparison between the predictions and observations of the magnetic sensors, polarimeters and interferometers are shown in Figure 7. The blue and light blue lines

are the predictions given the posterior mean and samples, respectively. The valid and invalid observations are shown as the red and orange dots. Some of the magnetic sensors frequently suffer complete failure, for example systematic signal drift over time, the invalid magnetic sensors have been automatically detected by the magnetic diagnostic rejection procedure [14]. The normalised differences between the predictions and observations are presented. As shown in Figure 7, the predictions given the posterior samples well agree with the observations within their predictive uncertainties.

We emphasise that the inference results of the plasma current distributions and pressure profiles are consistent with all the measurements. Typically, the conventional analysis of the plasma diagnostics makes use of the normalised flux surfaces from the EFIT code with the magnetic field measurements in order to map the physics parameters, for example electron density profiles in the EFIT ψ_N coordinates. The results from the conventional analysis might very well be inconsistent with each other, because of not only the individual analysis but also the ψ_N coordinates. The inference solutions from the HRTS and lithium beam spectroscopy analysis codes are not consistent with each other in the EFIT ψ_N coordinates, as shown in Figure 8(c). In such cases, it would be very difficult to figure out which electron density (temperature) profiles is correct and should be used for further physics analysis. In contrast, the current tomography model takes into account all the magnetic field and pressure measurements simultaneously in order to find all possible *consistent solutions*, as shown in Figure 8(b). Furthermore, since the electron density and temperature are assumed to be constant on the normalised flux surfaces, thus they can give additional information on the normalised flux surfaces or the plasma current distributions. As shown in Figure 8(a), the normalised flux surfaces inferred with the current tomography model and the EFIT code are notably different, especially the LCFS near the top of the machine where the lithium beam spectroscopy system provides edge electron density profiles and the magnetic axis. The comparison of the current tomography n_e and conventional analysis n_e in the current tomography and EFIT ψ_N coordinates during a JET discharge are shown in Figure 9. The electron density profiles are consistent with those of the conventional analysis of the HRTS and lithium spectroscopy systems in the current tomography ψ_N coordinates, whereas not in the EFIT ψ_N coordinates.

We remark that, unlike the conventional EFIT code, all these inference results provide not only a single solution but also all possible solutions with their associated uncertainties. The full uncertainties of all the unknown parameters are calculated from the posterior samples, which can be used for quantification of uncertainties for further physics analysis such as transport analysis with TRANSP [57].

3.2. The equilibrium inference

In the previous subsection, we have explored the full joint posterior distributions of the current tomography model which does not take into account any further prior knowledge such as the MHD force balance. On the other hand, the equilibrium model introduces the

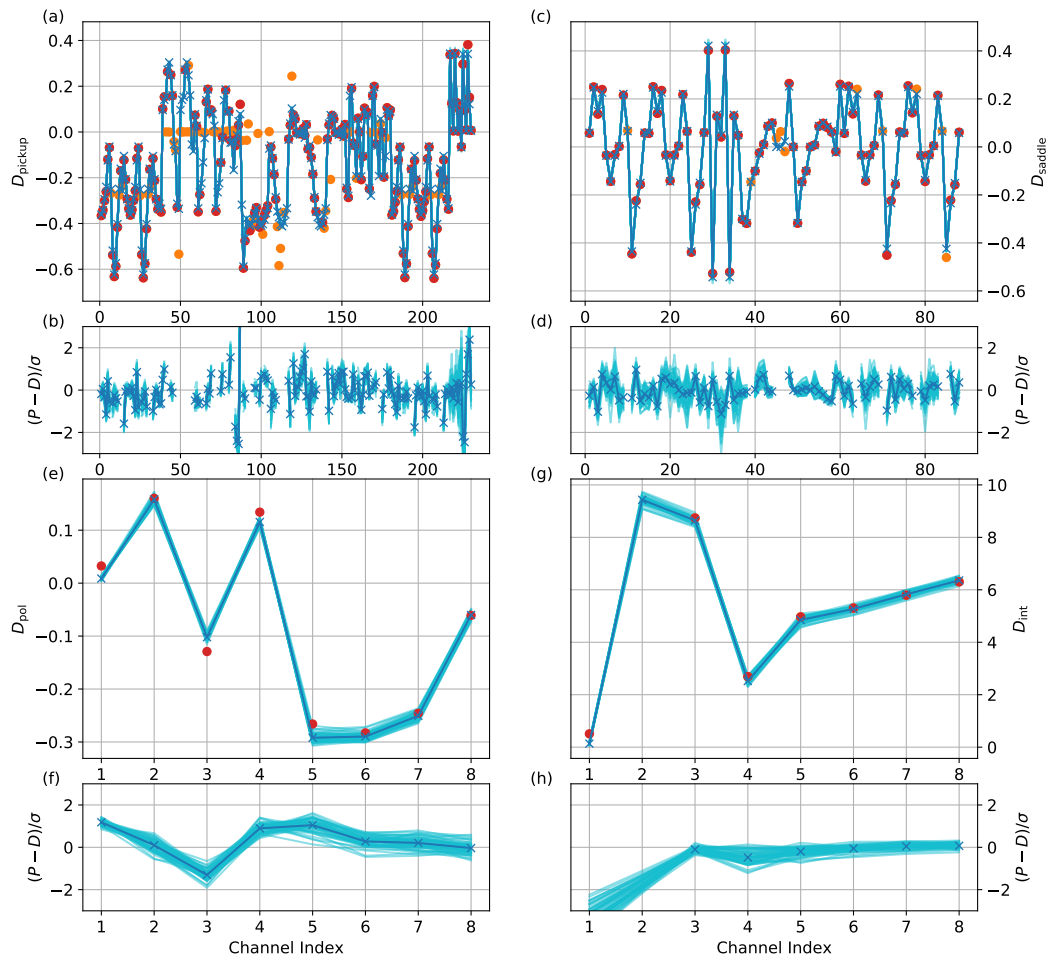


Figure 7. The predictions and observations of (a) the pickup coils, (c) saddle coils, (e) polarimeters and (g) interferometers. The valid and invalid data points are shown as the red and orange dots, respectively. The blue and light blue lines are the predictions given the posterior mean and samples. The normalised differences between the predictions and observations $(P - D)/\sigma$ are presented for (b) the pickup coils, (d) saddle coils, (f) polarimeters and (h) interferometers. We note that the line integrated electron density measurements from the second channel of the interferometers do not exist for this case, nevertheless, the model still makes the corresponding predictions.

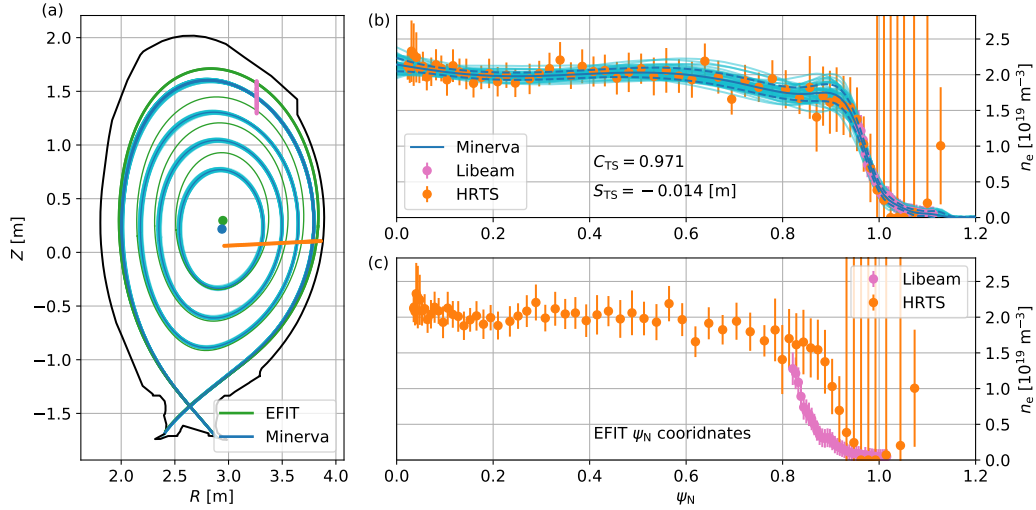


Figure 8. The comparison of the electron density profiles in the current tomography and EFIT ψ_N coordinates for JET discharge #92398 at 5.0 s (an L-mode plasma): (a) the normalised flux surfaces inferred with the current tomography model (in blue) and the conventional EFIT code (in green), (b) the electron density profiles in the current tomography ψ_N coordinates and (c) in the EFIT code ψ_N coordinates. The electron density profiles inferred with the current tomography model are consistent with all the measurements.

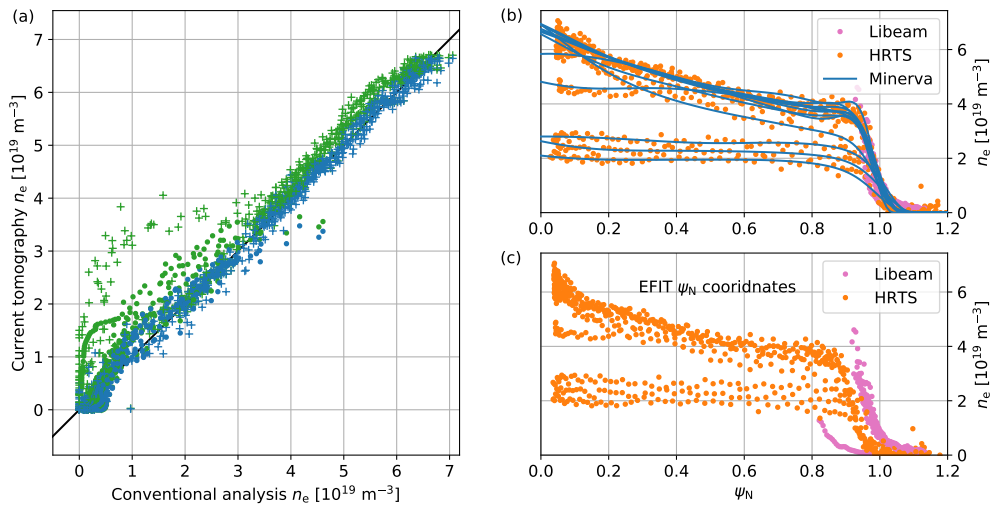


Figure 9. The comparison of the current tomography n_e and conventional analysis n_e in the current tomography and EFIT ψ_N coordinates during JET discharge #92398: (a) the comparison of the current tomography n_e and conventional analysis n_e of the HRTS (cross) and the lithium beam spectroscopy (dots) systems in the current tomography (in blue) and EFIT (in green) ψ_N coordinates and (b) the time evolution of the electron density profiles in the current tomography ψ_N coordinates and (c) in the EFIT ψ_N coordinates. The black line is $y = x$ in (a).

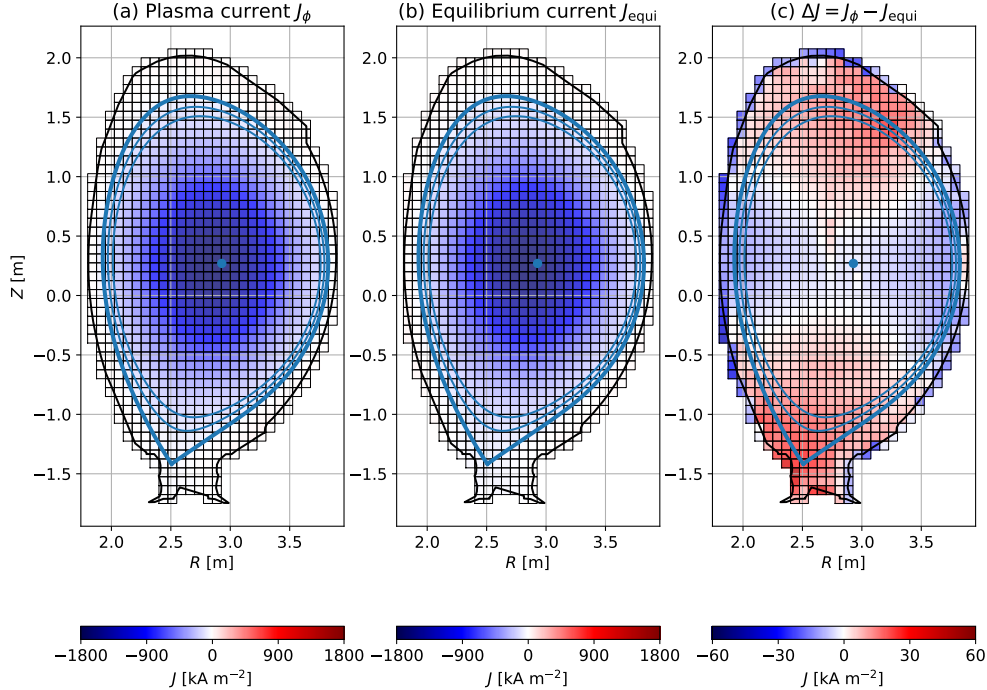


Figure 10. The plasma and equilibrium current distributions of the MAP solution for JET discharge #89709 at 8.0 s (an L-mode plasma): (a) the plasma and (b) equilibrium current distributions and (c) the difference between the two.

virtual observations which impose the MHD force balance constraints at every plasma current beam as a part of the prior. The full joint posterior distribution of the equilibrium model are explored through the new inversion procedure. The plasma and equilibrium current distributions of the MAP solution for typical JET L- and H-mode plasmas are shown in Figure 10 and Figure 11. The equilibrium current distributions are calculated given the poloidal current flux and pressure profiles ($p = 2n_e T_e$), and the difference between the two distributions are presented. The difference between these two current distributions are in general less than a few per cent of the typical plasma current values, therefore these solutions fulfil the MHD force balance.

The inference results of the equilibrium model propose a strong current in the edge region for an H-mode plasma, as shown in Figure 11. The electron density and temperature profiles of a typical H-mode plasma have a very steep gradient in the edge region ($\psi_N \sim 0.95$), as shown in Figure 12. The strong force due to the steep plasma pressure gradient in the edge region has to be balanced out by strong magnetic force due to high plasma currents. In other words, if the plasma in a stable, macroscopic MHD equilibrium state has steep pressure gradient in the edge region, then it might very well

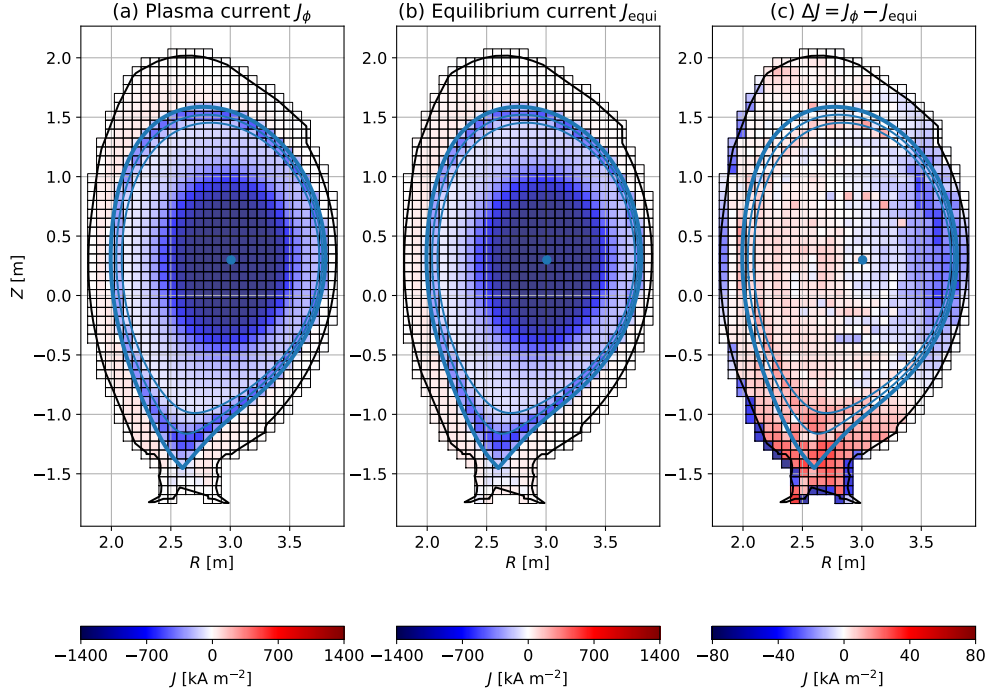


Figure 11. Same as Figure 10 for an H-mode plasma (JET discharge #92398 at 7.0 s).

be that the plasma currents are strong in the edge region. Typically, this inferred edge current density is around 5×10^2 kA, which is approximately one-third of the inferred core current density. The edge current density in the low field side is approximately two times higher than the one in the high field side. Furthermore, the normalised flux surfaces, especially near the X-point, are shrunk due to this strong edge current density, as shown in Figure 12.

We emphasise that the electron density and temperature profiles in the equilibrium ψ_N coordinates are consistent with all the measurements. For comparison, the electron density and temperature profiles of the conventional analysis of the HRTS system (in orange), the lithium beam spectroscopy (in pink) and reflectometer (in grey) systems are shown in Figure 12. The electron density and temperature profiles are inferred given the interferometer, HRTS and lithium beam spectroscopy measurements, nevertheless, these electron density profiles are also consistent with the reflectometer measurements. As explained in the previous subsection, the HRTS system is automatically calibrated with the inferred model parameters C_{TS} and S_{TS} given all the other measurements. In this case, the posterior mean of the electron density calibration factor C_{TS} is 0.897, which means that the conventional analysis of the HRTS system overestimates the electron density by around ten per cent. The electron density profiles of the HRTS measurements

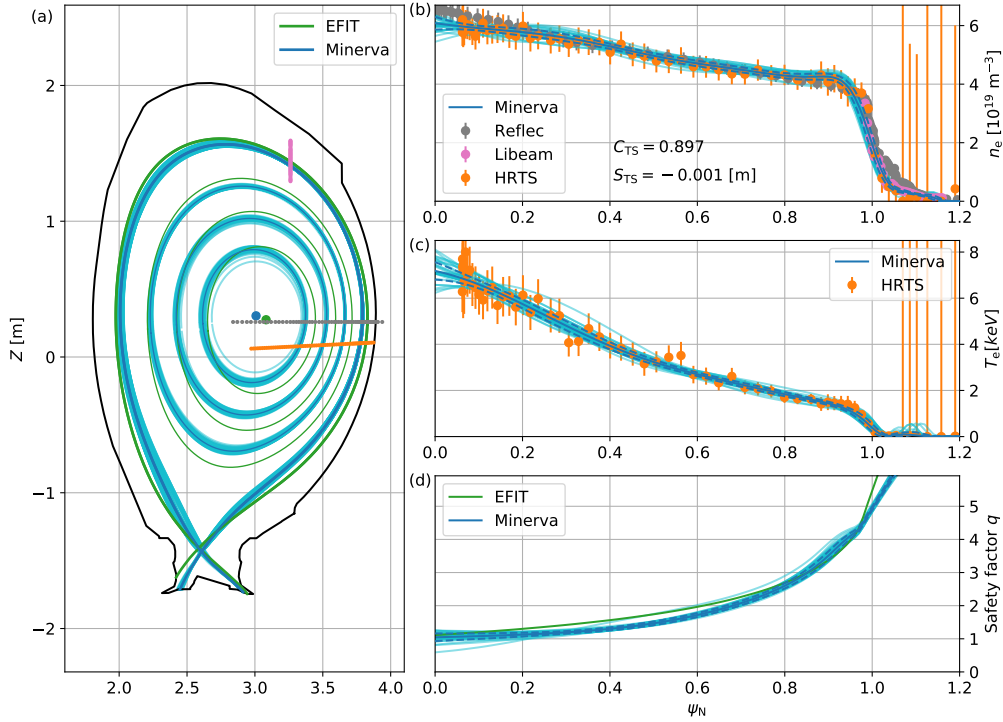


Figure 12. The inference results of the equilibrium model for JET discharge #92398 at 7.0s (an H-mode plasma): (a) the normalised poloidal magnetic flux surfaces, (b) the electron density, (c) temperature and (d) safety factor q profiles. For comparison, the results of the conventional analysis of the equilibrium fitting (EFIT) code (in green), the HRTS (in orange), the lithium beam spectroscopy (in pink) and the reflectometer (grey) systems are shown here. The orange and pink dots in (a) are the measurement positions of the HRTS and lithium beam spectroscopy systems. We note that the reflectometer measurements are not included in the model, nevertheless, the electron density profiles are consistent with the reflectometer measurements.

(the orange dots) shown in Figure 12(b) are calibrated with the inferred model parameters C_{TS} and S_{TS} in order to make reasonable comparison and avoid confusion, and these HRTS profiles are lower than the original analysis results. Importantly, the electron density profiles inferred with the equilibrium model are consistent with all the other measurements in the model as well as with the reflectometer measurements. In other words, the automatic calibration of the HRTS system has been carried out with all the other measurements in the model and confirmed by the reflectometer measurements. Furthermore, the equilibrium ψ_N coordinates map all these electron density profiles in a consistent way.

The safety factor q , which is the number of poloidal winding per a single toroidal winding of the magnetic field line, can be calculated given the poloidal current flux.

The safety factor q can be used to check certain stabilities of the plasma, which can be written as:

$$q = \frac{rB_\phi}{RB_\theta}, \quad (49)$$

where B_ϕ and B_θ are the toroidal and poloidal magnetic field, respectively, and r is the minor radius. The q profiles inferred with the equilibrium model are similar to the one of the EFIT code. In the core region, q profiles and their posterior uncertainties may be determined by the Gaussian process priors. Again, all these physics parameters are provided with their associated uncertainties which can be used for further physics analysis.

3.3. The equilibrium predictions given the current tomography solutions

The current tomography model does not impose further assumptions like the equilibrium model, which prescribes the MHD force balance. In this work, we do not have any poloidal current measurement technique such as motional Stark effect (MSE) diagnostics, thus the current tomography model has no information on the poloidal current distributions. Nevertheless, we can explore the joint posterior distribution of the poloidal current flux profiles and the other physics parameters drawn from the current tomography posterior distributions by using the equilibrium virtual observations:

$$\begin{aligned} & P(F, J_\phi, J_{\text{iron}}, n_e, T_e | \sigma_F, D_{\text{equi}}, D_{\text{CT}}) \\ &= \frac{P(D_{\text{equi}} | F, J_\phi, J_{\text{iron}}, n_e, T_e, \sigma_F, D_{\text{CT}}) P(F, J_\phi, J_{\text{iron}}, n_e, T_e | \sigma_F, D_{\text{CT}})}{P(D_{\text{equi}})} \\ &= \frac{P(D_{\text{equi}} | F, J_\phi, n_e, T_e) P(F | J_\phi, J_{\text{iron}}, n_e, T_e, \sigma_F) P(J_\phi, J_{\text{iron}}, n_e, T_e | D_{\text{CT}})}{P(D_{\text{equi}})} \\ &\simeq \frac{P(D_{\text{equi}} | F, J_\phi, n_e, T_e) P(F | \sigma_F) P(J_\phi, J_{\text{iron}}, n_e, T_e | D_{\text{CT}})}{P(D_{\text{equi}})}, \end{aligned} \quad (50)$$

where $P(J_\phi, J_{\text{iron}}, n_e, T_e | D_{\text{CT}})$ is the conditional posterior distributions of the current tomography model which has been already explored in Section 3.1 and all the measurements, which are taken into account the current tomography model, are denoted as $D_{\text{CT}} = [D_{\text{mag}}, D_{\text{int}}, D_{\text{pol}}, D_{\text{Li}}, D_{\text{TS}}, D_{\text{wall}}]$. Given the pre-calculated current tomography posterior samples, we can easily calculate Equation (50) and explore the joint posterior distribution of the poloidal current flux profiles and the other physics parameters. Here we make use of the same equilibrium virtual observations of the equilibrium model. We note that this is a new way to explore equilibrium solutions given the current tomography posterior samples.

The MHD force balance predictions given the current tomography posterior samples are shown in Figure 13. The difference between the plasma and equilibrium current density is small in general, but in the edge region, this difference can be notable. Interestingly, the equilibrium solutions of the current tomography model propose reverse bumps of the poloidal current flux profiles in the edge region, as shown in Figure 13(d), which attempt to

cancel out the strong equilibrium current contributions due to the steep pressure gradient (the brown reverse bumps) in the edge region as shown in Figure 13(a). These equilibrium current contributions $J_{p'} = Rp'$ can be seen as the toroidal current preconditions to balance out the plasma pressure gradient by the magnetic force of the plasma currents and the magnetic field. On the other hand, the equilibrium current contributions due to the poloidal current flux profiles $J_{FF'} = \frac{\mu_0}{R} FF'$ can cancel these toroidal current preconditions. In this case, the inference results of the current tomography model explain plasma equilibria without a strong current density in the edge region. In contrast, the inference results of the equilibrium model propose a strong toroidal current density in the edge region, approximately 4×10^2 kA, as shown in Figure 14. The plasma and equilibrium current distributions inferred with the equilibrium model are consistent with each other better than those with the current tomography model, therefore equilibrium model offers solutions consistent with the MHD force balance within small equilibrium prior uncertainties. Nevertheless, the predictions of both models consistent with all the measurements, therefore, the poloidal current measurement technique such as the MSE diagnostics would be crucial to understand these equilibrium solutions further. These current tomography and equilibrium models give different solutions for plasma equilibria because of the different model priors.

4. Conclusions

The Bayesian models of axisymmetric plasmas using Gaussian processes and magnetohydrodynamics force balance equations have been developed. These models give the full joint posterior distributions of the plasma current distributions and pressure profiles consistent with the magnetic field and pressure measurements from the following plasma diagnostics: the magnetic sensors, polarimeters, interferometers, high-resolution Thomson scattering and lithium beam emission spectroscopy systems. The plasma current distributions are modelled as a grid of toroidal solid beams carrying a uniform current, and the other physics parameters such as the plasma pressure and poloidal current flux profiles are given as a function of the normalised poloidal magnetic flux surfaces, determined by the toroidal currents. Since inference of all these physics parameters is a tomographic problem, in order to exclude unreasonable solutions, we have introduced two different prior distributions: the Gaussian process prior and the equilibrium prior. The current tomography model makes use of the Gaussian process prior with the optimal hyperparameters obtained by Bayesian Occam's razor. On the other hand, the equilibrium model imposes the Grad-Shafranov force balance constraints as a part of the equilibrium prior by introducing the virtual observations. These complex, high dimensional full joint posterior distributions have been explored by the new inversion procedures based on the Gibbs sampling scheme.

Unlike the conventional approach such as the EFIT code and the analysis code of each individual diagnostics, this approach provides the *consistent solutions* of the plasma current distributions as well as the poloidal current flux and electron density and

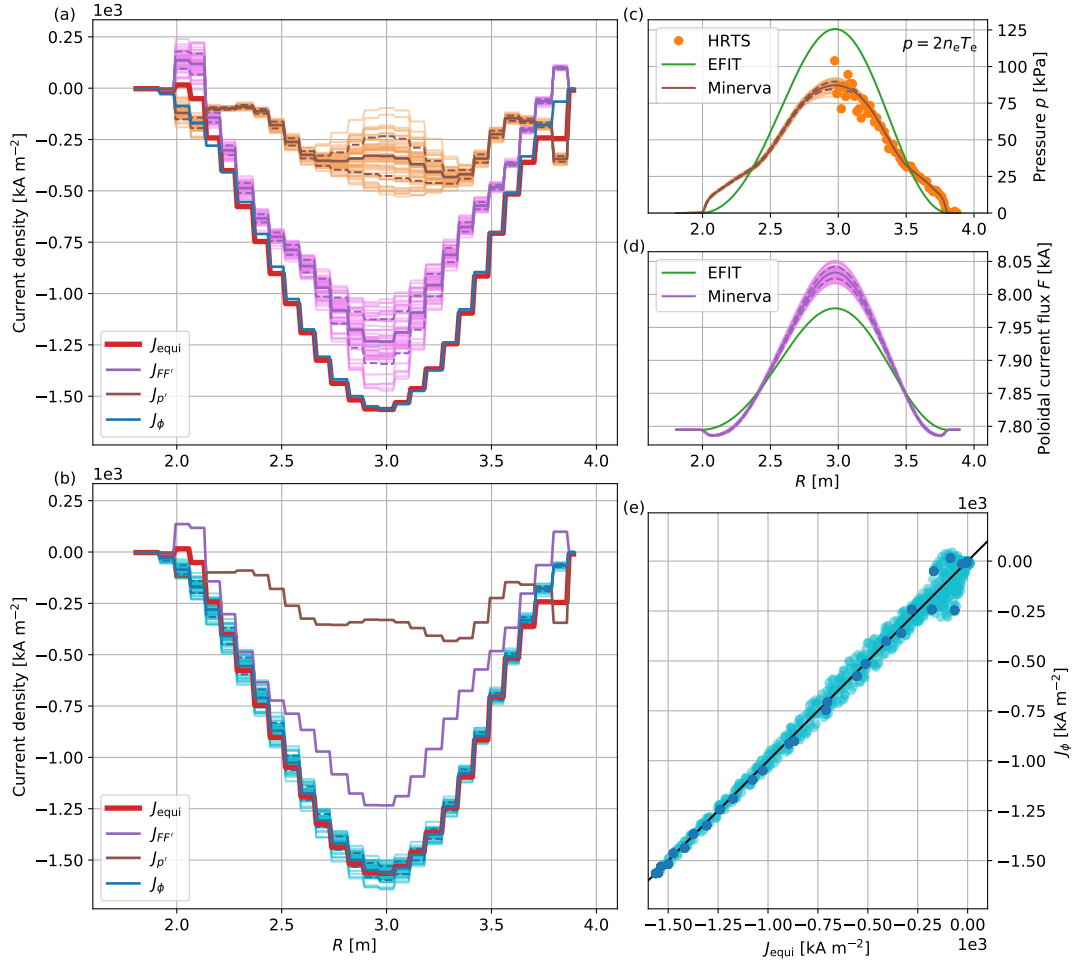


Figure 13. The MHD force balance predictions given the current tomography posterior samples for JET discharge #89709 at 13.5s (an H-mode plasma): (a) and (b) the plasma and equilibrium current distributions across the plasma, (c) the pressure and (d) poloidal current flux profiles and (e) the comparison between the plasma and equilibrium current density. The blue and thick red lines in (a) and (b) are the plasma and equilibrium current density, respectively. The brown and purple lines in (a) and (b) are the equilibrium current contributions $J_{p'} = R p'$ and $J_{F'} = \frac{\mu_0}{R} F F'$ due to the pressure and poloidal current flux profiles shown in (c) and (d). For comparison, the results of the EFIT code and the HRTS analysis are shown as the green lines and orange dots in (c) and (d). The black line is $y = x$ in (e).

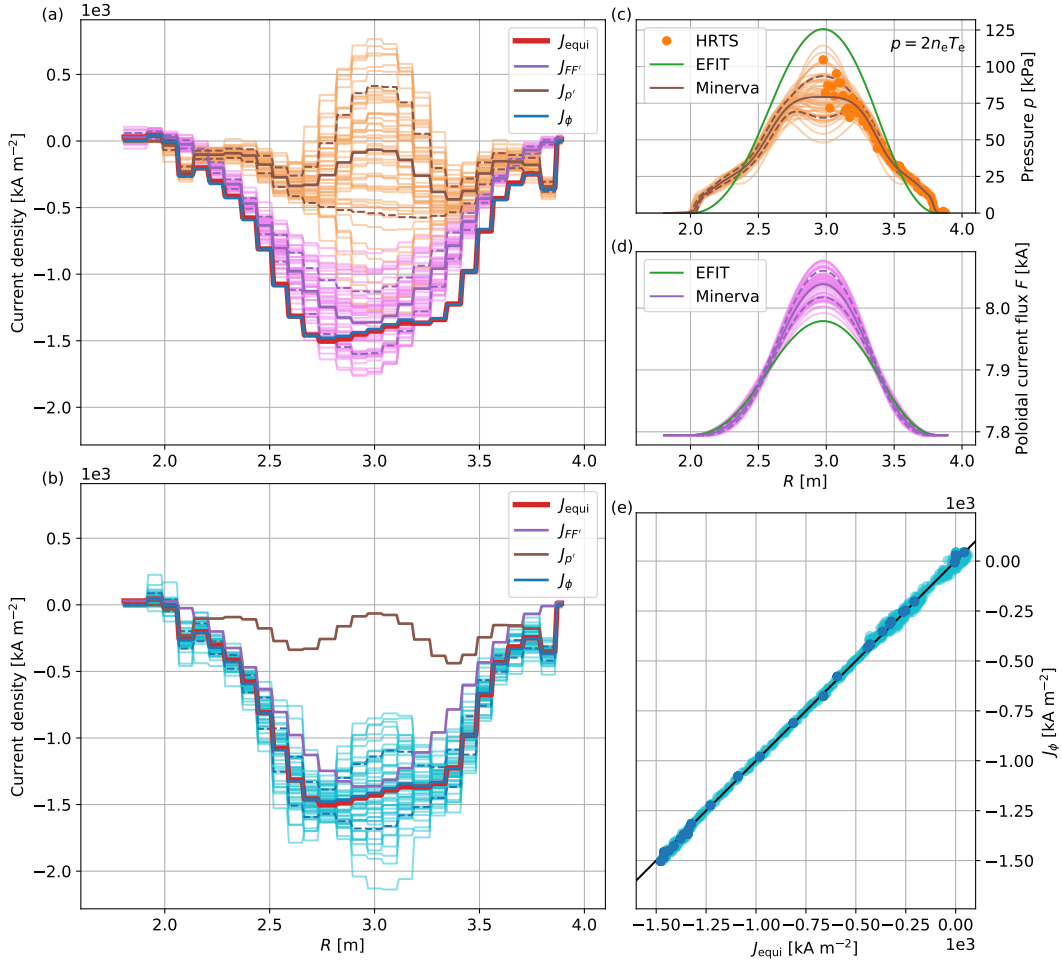


Figure 14. Same as Figure 10 for the inference results of the equilibrium model.

temperature profiles with all the magnetic field and pressure measurements simultaneously. The plasma current distributions and all the other physics parameters are optimally inferred from all the measurements. As a result, the plasma current distributions and all the other physics parameters such as the electron density and temperature expressed in the normalised flux coordinates are self-consistent with all the measurements. For this reason, these inference solutions provide extra information of the plasma current distributions from the electron density and temperature measurements and vice versa. Furthermore, the HRTS system is automatically calibrated with the inferred model parameters.

The equilibrium solutions inferred with the equilibrium model propose a strong toroidal current density in the edge region due to the steep pressure gradient of H-mode plasmas. This edge current density is approximately one-third of the core current density

and provides a strong magnetic force which can balance out the steep pressure gradient in a stable, macroscopic MHD equilibrium state. On the other hand, the equilibrium solutions predicted given the current tomography posterior samples propose the poloidal current flux hole (the reverse bumps) in the edge region which can strengthen the magnetic force to balance out the steep gradient without a strong toroidal current in the edge region. Nevertheless, the predictions of both models agree with all the measurements, therefore the poloidal current measurements would be crucial to understand these equilibrium solutions further.

All these solutions are provided with the optimal hyperparameters which are optimally chosen by Bayesian Occam's razor. Moreover, all these inferred physics parameters are provided with the full uncertainties, which can be used to explore all possible solutions of high-level physics parameters, for example the energy transport coefficient, in further physics studies.

5. Acknowledgement

This work is supported by National R&D Program through the National Research Foundation of Korea (NRF) funded by the Ministry of Science and ICT (Grant No. 2017M1A7A1A01015892 and 2017R1C1B2006248) and the the KAI-NEET, KAIST, Korea. This work has been carried out within the framework of the EUROfusion Consortium and has received funding from the Euratom research and training programme 2014-2018 and 2019-2020 under grant agreement No 633053. The views and opinions expressed herein do not necessarily reflect those of the European Commission.

References

- [1] Wesson J and Campbell D J 2004 *Tokamaks* (Clarendon Press)
- [2] Freidberg J P 2008 *Plasma Physics and Fusion Energy* (Cambridge University Press)
- [3] Freidberg J P 2008 *Ideal Magnetohydrodynamics* (Cambridge University Press)
- [4] Ferron J, Walker M, Lao L, John H S, Humphreys D and Leuer J 1998 *Nuclear Fusion* **38** 1055–1066 ISSN 0029-5515 URL <http://stacks.iop.org/0029-5515/38/i=7/a=308?key=crossref.b5cf5934bf8e0c7cb0753d1f2d80eddc>
- [5] Grad H and Rubin H 1958 *Journal of Nuclear Energy (1954)* **7** 284–285
- [6] Shafranov V D 1963 *Journal of Nuclear Energy. Part C, Plasma Physics, Accelerators, Thermonuclear Research* **5** 251–258 ISSN 0368-3281 URL <http://stacks.iop.org/0368-3281/5/i=4/a=307?key=crossref.f5194f3c35e44fecfc1e410c00983a4b>
- [7] Lao L, St John H, Stambaugh R, Kellman A and Pfeiffer W 1985 *Nuclear Fusion* **25** 1611–1622 ISSN 0029-5515 URL <http://stacks.iop.org/0029-5515/25/i=11/a=007?key=crossref.382b4e7e430c8741af0f7248e9a56c09>
- [8] Svensson J and Werner A 2008 *Plasma Physics and Controlled Fusion* **50** 085002 ISSN 07413335 URL <http://stacks.iop.org/0741-3335/50/i=8/a=085002?key=crossref.8b9e7d2d10e66d8a740fcec9ab77227d>
- [9] Chilenski M, Greenwald M, Marzouk Y, Howard N, White A, Rice J and Walk J 2015 *Nuclear Fusion* **55** 023012 ISSN 0029-5515 URL <http://stacks.iop.org/0029-5515/55/i=2/a=023012?key=crossref.b22d32b1ac570adef0ea0869bc2c1789>

- [10] Kwak S, Svensson J, Bozhenkov S A, Flanagan J, Kempenaars M, Boboc A and Ghim Y c 2020 *Nuclear Fusion* ISSN 0029-5515 URL <https://iopscience.iop.org/article/10.1088/1741-4326/ab686e>
- [11] Gull S F 1988 Bayesian inductive inference and maximum entropy *Maximum-Entropy and Bayesian Methods in Science and Engineering: Foundations* ed Erickson G J and Smith C R (Springer Netherlands) pp 53–74 ISBN 978-94-009-3049-0 URL https://doi.org/10.1007/978-94-009-3049-0_4
- [12] Mackay D J 1991 *Bayesian methods for adaptive models* Ph.D. thesis California Institute of Technology
- [13] Svensson J 2011 *JET report, EFDA-JET-PR(11)24* URL <http://www.euro-fusionscipub.org/wp-content/uploads/eurofusion/EFDP11024.pdf>
- [14] Ford O P 2010 *Tokamak plasma analysis through Bayesian diagnostic modelling* Ph.D. thesis Imperial College London
- [15] Ford O, Svensson J, Boboc A and McDonald D C 2008 *Review of Scientific Instruments* **79** 10F324 ISSN 0034-6748 URL <http://aip.scitation.org/doi/10.1063/1.2956880>
- [16] Kwak S, Svensson J, Brix M and Ghim Y c 2016 *Review of Scientific Instruments* **87** 023501 ISSN 0034-6748 URL <http://aip.scitation.org/doi/10.1063/1.4940925>
- [17] Kwak S, Svensson J, Brix M and Ghim Y C 2017 *Nuclear Fusion* **57** 036017 ISSN 0029-5515 URL <http://stacks.iop.org/0029-5515/57/i=3/a=036017?key=crossref.78317e8d5c69c0d93e4bfd4af120a500>
- [18] Litaudon X *et al.* 2017 *Nuclear Fusion* **57** 102001 ISSN 0029-5515 URL <http://stacks.iop.org/0029-5515/57/i=10/a=102001?key=crossref.17a0f33a13c4a2bbaafb54b4eb7df30>
- [19] Svensson J and Werner A 2007 Large Scale Bayesian Data Analysis for Nuclear Fusion Experiments *2007 IEEE International Symposium on Intelligent Signal Processing (IEEE)* pp 1–6 ISBN 978-1-4244-0829-0 URL <http://ieeexplore.ieee.org/document/4447579/>
- [20] Seed eScience Research The Minerva framework URL <https://seed-escience.org/>
- [21] Pearl J 1988 *Probabilistic Reasoning in Intelligent Systems: Networks of Plausible Inference* (Morgan Kaufmann)
- [22] Bozhenkov S, Beurskens M, Molin A D, Fuchert G, Pasch E, Stoneking M, Hirsch M, Höfel U, Knauer J, Svensson J, Mora H T and Wolf R 2017 *Journal of Instrumentation* **12** P10004–P10004 ISSN 1748-0221 URL <http://stacks.iop.org/1748-0221/12/i=10/a=P10004?key=crossref.21c7d556bea6caf012906a098b133ef0>
- [23] Li D, Svensson J, Thomsen H, Medina F, Werner A and Wolf R 2013 *Review of Scientific Instruments* **84** 083506 ISSN 0034-6748 URL <http://aip.scitation.org/doi/10.1063/1.4817591>
- [24] Langenberg A, Svensson J, Thomsen H, Marchuk O, Pablant N A, Burhenn R and Wolf R C 2016 *Fusion Science and Technology* **69** 560–567 ISSN 1536-1055 URL <https://www.tandfonline.com/doi/full/10.13182/FST15-181>
- [25] Hoefel U, Hirsch M, Kwak S, Pavone A, Svensson J, Stange T, Hartfuß H J, Schilling J, Weir G, Oosterbeek J W, Bozhenkov S, Braune H, Brunner K J, Chaudhary N, Damm H, Fuchert G, Knauer J, Laqua H, Marsen S, Moseev D, Pasch E, Scott E R, Wilde F and Wolf R 2019 *Review of Scientific Instruments* **90** 043502 ISSN 0034-6748 URL <http://aip.scitation.org/doi/10.1063/1.5082542>
- [26] Pavone A, Hergenbahn U, Krychowiak M, Hoefel U, Kwak S, Svensson J, Kornejew P, Winters V, Koenig R, Hirsch M, Brunner K J, Pasch E, Knauer J, Fuchert G, Scott E, Beurskens M, Effenberg F, Zhang D, Ford O, Vanó L and Wolf R 2019 *Journal of Instrumentation* **14** C10003–C10003 ISSN 1748-0221 URL <https://iopscience.iop.org/article/10.1088/1748-0221/14/10/C10003>
- [27] Mora H T, Bozhenkov S, Knauer J, Kornejew P, Kwak S, Ford O, Fuchert G, Pasch E, Svensson J, Werner A, Wolf R and Timmermann D 2017 FPGA acceleration of Bayesian model based analysis for time-independent problems *2017 IEEE Global Conference on Signal and Information Processing (GlobalSIP) (IEEE)* pp 774–778 ISBN 978-1-5090-5990-4 URL <http://ieeexplore.ieee.org/document/8309065/>

- [28] Pavone A, Svensson J, Langenberg A, Pablant N, Hoefel U, Kwak S and Wolf R C 2018 *Review of Scientific Instruments* **89** 10K102 ISSN 0034-6748 URL <http://aip.scitation.org/doi/10.1063/1.5039286>
- [29] Pavone A, Svensson J, Langenberg A, Höfel U, Kwak S, Pablant N and Wolf R C 2019 *Plasma Physics and Controlled Fusion* **61** 075012 ISSN 0741-3335 URL <https://iopscience.iop.org/article/10.1088/1361-6587/ab1d26>
- [30] von Nessi G T and Hole M J 2013 *Journal of Physics A: Mathematical and Theoretical* **46** 185501 ISSN 1751-8113 URL <http://stacks.iop.org/1751-8121/46/i=18/a=185501?key=crossref.085e8f9015638d2a9f8beb329833774a>
- [31] von Nessi G T and Hole M J 2014 *Plasma Physics and Controlled Fusion* **56** 114011 ISSN 0741-3335 URL <http://stacks.iop.org/0741-3335/56/i=11/a=114011?key=crossref.d58e08b3c9223c89bab07f760e99229e>
- [32] Geman S and Geman D 1984 *IEEE Transactions on Pattern Analysis and Machine Intelligence* **PAMI-6** 721–741 ISSN 0162-8828 URL <http://ieeexplore.ieee.org/document/4767596/>
- [33] Jaynes E T 2003 *Probability Theory: The Logic of Science* (Cambridge University Press) ISBN 0-521-59271-2
- [34] Devinderjit Sivia J S 2006 *Data Analysis: A Bayesian Tutorial* (Oxford University Press) ISBN 0-198-56831-2
- [35] O'Hagan A 1978 *Journal of the Royal Statistical Society. Series B (Methodological)* **40** 1–42 ISSN 00359246 URL <http://www.jstor.org/stable/2984861>
- [36] Neal R M 1995 *Bayesian learning for neural networks* Ph.D. thesis University of Toronto
- [37] Rasmussen C E and Williams C K I 2006 *Gaussian Processes for Machine Learning* (MIT Press)
- [38] Romero J A, Dettrick S A, Granstedt E, Roche T and Mok Y 2018 *Nature Communications* **9** 691 ISSN 2041-1723 URL <http://www.nature.com/articles/s41467-018-03110-5>
- [39] ASDEX Team 1989 *Nuclear Fusion* **29** 1959–2040 ISSN 17414326 URL <http://stacks.iop.org/0029-5515/29/i=11/a=010?key=crossref.f8eff2d027380946fd88742ac88d929c>
- [40] Higdon D, Swall J and Kern J 1999 Non-stationary spatial modeling *Bayesian Statistics 6 Proceedings of the Sixth Valencia International Meeting* pp 761–768
- [41] Svensson J, Dinklage A, Geiger J, Werner A and Fischer R 2004 *Review of Scientific Instruments* **75** 4219–4221 ISSN 0034-6748 URL <http://aip.scitation.org/doi/10.1063/1.1789611>
- [42] Boboc A, Gelfusa M, Murari A and Gaudio P 2010 *Review of Scientific Instruments* **81** 10D538 ISSN 00346748 URL <http://aip.scitation.org/doi/10.1063/1.3478146>
- [43] Boboc A, Gil C, Pastor P, Spuig P, Edlington T and Dorling S 2012 *Review of Scientific Instruments* **83** 10E341 ISSN 00346748 URL <http://aip.scitation.org/doi/10.1063/1.4737420>
- [44] Boboc A, Bieg B, Felton R, Dalley S and Kravtsov Y 2015 *Review of Scientific Instruments* **86** 091301 ISSN 10897623 URL <http://aip.scitation.org/doi/10.1063/1.4929443>
- [45] Pasqualotto R, Nielsen P, Gowers C, Beurskens M, Kempenaars M, Carlstrom T and Johnson D 2004 *Review of Scientific Instruments* **75** 3891–3893 ISSN 00346748 URL <http://aip.scitation.org/doi/10.1063/1.1787922>
- [46] Thomson J J 1906 *Conduction of Electricity Through Gases* (Cambridge University Press)
- [47] Naito O, Yoshida H and Matoba T 1993 *Physics of Fluids B: Plasma Physics* **5** 4256–4258 ISSN 0899-8221 URL <http://aip.scitation.org/doi/10.1063/1.860593>
- [48] Brix M, Dodt D, Korotkov A, Morgan P, Dunai D, Fischer R, Meigs A, Nedzelskiy I S, Schweinzer J, Vince J and Zoletnik S 2010 *Review of Scientific Instruments* **81** 10D733 ISSN 0034-6748 URL <http://aip.scitation.org/doi/10.1063/1.3502320>
- [49] Brix M, Dodt D, Dunai D, Lupelli I, Marsen S, Melson T F, Meszaros B, Morgan P, Petravich G, Refy D I, Silva C, Stamp M, Szabolics T, Zastrow K D and Zoletnik S 2012 *Review of Scientific Instruments* **83** 10D533 ISSN 00346748 URL <http://aip.scitation.org/doi/10.1063/1.4739411>
- [50] Hooke R and Jeeves T A 1961 *Journal of the ACM* **8** 212–229 ISSN 00045411 URL <http://portal.acm.org/citation.cfm?doid=321062.321069>

- [51] Metropolis N, Rosenbluth A W, Rosenbluth M N, Teller A H and Teller E 1953 *The Journal of Chemical Physics* **21** 1087–1092 ISSN 0021-9606 URL <http://aip.scitation.org/doi/10.1063/1.1699114>
- [52] Hastings W K 1970 *Biometrika* **57** 97–109 ISSN 1464-3510 URL <https://academic.oup.com/biomet/article/57/1/97/284580>
- [53] Haario H, Saksman E and Tamminen J 2001 *Bernoulli* **7** 223 ISSN 13507265 URL <https://www.jstor.org/stable/3318737?origin=crossref>
- [54] Hole M J, von Nessi G, Pretty D, Howard J, Blackwell B, Svensson J and Appel L C 2010 *Review of Scientific Instruments* **81** 10E127 ISSN 0034-6748 URL <http://aip.scitation.org/doi/10.1063/1.3491044>
- [55] Hole M, von Nessi G, Svensson J and Appel L 2011 *Nuclear Fusion* **51** 103005 ISSN 0029-5515 URL <http://stacks.iop.org/0029-5515/51/i=10/a=103005?key=crossref.392f9458f59be45b221081762d909675>
- [56] O'Brien D, Lao L, Solano E, Garribba M, Taylor T, Cordey J and Ellis J 1992 *Nuclear Fusion* **32** 1351–1360 ISSN 0029-5515 URL <http://stacks.iop.org/0029-5515/32/i=8/a=I05?key=crossref.8ebd91c19ae2a7832a295ae5c0455f48>
- [57] Hawryluk R 1981 AN EMPIRICAL APPROACH TO TOKAMAK TRANSPORT *Physics of Plasmas Close to Thermonuclear Conditions* (Elsevier) pp 19–46 URL <https://linkinghub.elsevier.com/retrieve/pii/B9781483283852500091>

5

A look ahead

If I have seen further, it is by standing upon
the shoulders of giants.

(Sir Isaac Newton)

As we are close to the end of this story, here again, I would like to emphasise that the principles and methods are indeed general and applicable to all kinds of scientific problems. As we have discussed previously, we have defined epistemic knowledge as the cost function of scientific problems. Given a model space and a parameter space, it is now straightforward for any human or machine to find inference solutions for models and their parameters simultaneously. The inference process, in principle, can be carried out autonomously. The principle of Occam's razor will guide any human or machine to find the optimal solutions for the model and the parameters with appropriate complexities given observations. Now, what could be the next step here? Perhaps, we can develop a *supermodel*, which includes all the data and parameter sets of the entire experiment and physical system. The supermodel of the W7-X experiment, which is now under construction, will take into account all the scientific instruments and physics models. By exploring the joint posterior distribution of the supermodel, we might be able to allow *a*-machines to find the ultimate consistent inference solution and achieve scientific discoveries autonomously. Nevertheless, we still have a number of unsolved questions towards the automation of science. How can we expand the model space or go beyond the model space? Or, in other words, how exactly have we been asking a question of *why*? To answer these questions, we have to find patterns of scientific inquiries and discoveries throughout the history of science. I believe that, no matter how difficult it is,

we will find a way to reveal patterns of the minds of giants in the light of the data, and we will lead ourselves beyond our imagination.

Statutory declaration

I hereby declare in accordance with the examination regulations that I myself have written this document, that no other sources as those indicated were used and all direct and indirect citations are properly designated, that the document handed in was neither fully nor partly subject to another examination procedure or published and that the content of the electronic exemplar is identical to the printing copy.

Greifswald, 25th November 2020

SEHYUN KWAK

List of Figures

1.1	Optimal solution by joint posterior distribution	5
2.1	Model, prediction and inference	12
2.2	Model complexity and evidence	18
2.3	Gaussian process prior	23
2.4	Gaussian process posterior	24
3.1	Fusion reaction rate	29
3.2	Tokamak and Stellarator	33

Publications as first author

Peer-reviewed articles

- [1] **S. KWAK**, J. SVENSSON, O. FORD, L. APPEL and Y.-C. GHIM. ‘Bayesian equilibria of axisymmetric plasmas’. In: *Nuclear Fusion*, (2020). In preparation.
- [2] **S. KWAK**, J. SVENSSON, S. BOZHENKOV, H. T. MORA, U. HOEFEL, A. PAVONE, M. KRYCHOWIAK, A. LANGENBERG and Y.-C. GHIM. ‘Bayesian modelling of multiple diagnostics at Wendelstein 7-X’. In: *Plasma Physics and Controlled Fusion*, (2020). In preparation.
- [3] **S. KWAK**, J. SVENSSON, S. BOZHENKOV, J. FLANAGAN, M. KEMPEN-AARS, A. BOBOC and Y.-C. GHIM. ‘Bayesian modelling of Thomson scattering and multichannel interferometer diagnostics using Gaussian processes’. In: *Nuclear Fusion*, Vol. 60.4 (26th Feb. 2020), page 046009. DOI: 10.1088/1741-4326/ab686e.
- [4] **S. KWAK**, J. SVENSSON, M. BRIX and Y.-C. GHIM. ‘Bayesian electron density inference from JET lithium beam emission spectra using Gaussian processes’. In: *Nuclear Fusion*, Vol. 57.3 (11th Jan. 2017), page 036017. DOI: 10.1088/1741-4326/aa5072.
- [5] **S. KWAK**, J. SVENSSON, M. BRIX and Y.-C. GHIM. ‘Bayesian modelling of the emission spectrum of the Joint European Torus Lithium Beam Emission Spectroscopy system’. In: *Review of Scientific Instruments*, Vol. 87.2 (2nd Feb. 2016), page 023501. DOI: 10.1063/1.4940925.

Talks

- [1] **S. KWAK** et al. ‘Bayesian modelling of multiple diagnostics at Wendelstein 7-X using the Minerva framework’. 82. Jahrestagung der DPG und DPG-Frühjahrstagung 2018. Erlangen, Germany, 5th Mar. 2018.
- [2] **S. KWAK** et al. ‘Bayesian modelling and inference of multiple diagnostic systems at Wendelstein 7-X in the Minerva framework’. KSTAR Conference 2018. Muju, Republic of Korea, 22nd Feb. 2018.
- [3] **S. KWAK** et al. ‘Bayesian modelling of multiple diagnostics at Wendelstein 7-X using the Minerva framework’. 59th Annual Meeting of the APS Division of Plasma Physics. Milwaukee, Wisconsin, USA, 24th Oct. 2017.
- [4] **S. KWAK**, J. SVENSSON, S. BOZHENKOV, J. FLANAGAN, M. KEMPEN-AARS, Y.-C. GHIM and JET CONTRIBUTORS. ‘Bayesian modelling of JET high resolution Thomson scattering system using the Minerva framework’. 58th Annual Meeting of the APS Division of Plasma Physics. San Jose, California, USA, 3rd Nov. 2016.
- [5] **S. KWAK**, J. SVENSSON, M. BRIX, Y.-C. GHIM and JET CONTRIBUTORS. ‘Bayesian inference for edge electron density profiles from the JET Li-BES data’. DPG-Frühjahrstagung 2016. Hannover, Germany, 4th Mar. 2016.
- [6] **S. KWAK**, J. SVENSSON, M. BRIX, Y.-C. GHIM and JET CONTRIBUTORS. ‘Bayesian modelling of spectrum data: JET Li-BES system (invited)’. KSTAR Conference 2016. Daejeon, Republic of Korea, 24th Feb. 2016.
- [7] **S. KWAK**, J. SVENSSON, M. BRIX, M. S. BAWA’ANEH, Y.-C. GHIM and JET CONTRIBUTORS. ‘Lithium BES Data Analysis via Bayesian Modelling at JET’. KPS Spring Meeting 2015. Daejeon, Republic of Korea, 22nd Apr. 2015.
- [8] **S. KWAK**, J. SVENSSON, M. BRIX, M. BAWA’ANEH, Y.-C. GHIM and JET CONTRIBUTORS. ‘Reconstruction of Electron Density Profile using Bayesian Inference on Lithium BES Data’. KSTAR Conference 2015. Daejeon, Republic of Korea, 25th Feb. 2015.

Posters

- [1] **S. KWAK**, J. SVENSSON, J. ABBATE, L. APPEL, J. HILLESHEIM, F. P. DIAZ, L. MENESES and JET CONTRIBUTORS. ‘Bayesian modelling of reflectometers at Joint European Torus using the Minerva framework’. DPG-Frühjahrstagung 2019. Munich, Germany, 21st Mar. 2019.
- [2] **S. KWAK** et al. ‘Wendelstein 7-X Bayesian Zeff inference in the Minerva framework’. 22th Topical Conference on High-Temperature Plasma Diagnostics. San Diego, California, USA, 16th Apr. 2018.
- [3] **S. KWAK**, J. SVENSSON, S. BOZHENKOV, J. FLANAGAN, M. KEMPEN-AARS, Y.-H. GHIM and JET CONTRIBUTORS. ‘Bayesian inference of electron temperature and density from JET high resolution Thomson scattering and interferometer data’. DPG-Frühjahrstagung 2017. Bremen, Germany, 13th Mar. 2017.
- [4] **S. KWAK**, J. SVENSSON, M. BRIX, Y.-C. GHIM and JET CONTRIBUTORS. ‘Bayesian modeling of JET Li-BES for edge electron density profiles using Gaussian processes’. 57th Annual Meeting of the APS Division of Plasma Physics. Savannah, Georgia, USA, 20th Oct. 2015.
- [5] **S. KWAK**, J. SVENSSON, M. BRIX, M. S. BAWA’ANEH, Y.-C. GHIM and JET CONTRIBUTORS. ‘Lithium BES Data Analysis via Bayesian Modelling at JET’. 42nd European Physical Society Conference on Plasma Physics. Lisbon, Portugal, 22nd June 2015.
- [6] **S. KWAK**, Y. JEON and Y.-C. GHIM. ‘Real-time EFIT data reconstruction based on neural network in KSTAR’. 56th Annual Meeting of the APS Division of Plasma Physics. New Orleans, Louisiana, USA, 27th Oct. 2014.
- [7] **S. KWAK**, Y. JEON and Y.-C. GHIM. ‘Equilibrium reconstruction based on the neural network algorithm in real time’. KSTAR Conference 2014. Gangwon-do, Republic of Korea, 24th Feb. 2014.

Publications as coauthor

Peer-reviewed articles

- [1] L. C. APPEL, **S. KWAK**, F. MILITELLO and J. SVENSSON. ‘A Bayesian model of filamentary dynamics in MAST’. In: *Plasma Physics and Controlled Fusion*, Vol. 62.12 (Oct. 2020), page 125002. DOI: 10.1088/1361-6587/ab8e1a.
- [2] S. SEREDA et al., amongst them **S. KWAK**. ‘Impact of boronizations on impurity sources and performance in Wendelstein 7-X’. In: *Nuclear Fusion*, Vol. 60.8 (Aug. 2020), page 086007. DOI: 10.1088/1741-4326/ab937b.
- [3] A. PAVONE, J. SVENSSON, **S. KWAK**, M. BRIX and R. C. WOLF. ‘Neural network approximated Bayesian inference of edge electron density profiles at JET’. In: *Plasma Physics and Controlled Fusion*, Vol. 62.4 (Mar. 2020), page 045019. DOI: 10.1088/1361-6587/ab7732.
- [4] S. JOUNG et al., amongst them **S. KWAK**. ‘Deep neural network Grad-Shafranov solver constrained with measured magnetic signals’. In: *Nuclear Fusion*, Vol. 60.1 (Jan. 2020), page 016034. DOI: 10.1088/1741-4326/ab555f.
- [5] T. KLINGER et al., amongst them **S. KWAK**. ‘Overview of first Wendelstein 7-X high-performance operation’. In: *Nuclear Fusion*, Vol. 59.11 (Nov. 2019), page 112004. DOI: 10.1088/1741-4326/ab03a7.
- [6] E. JOFFRIN et al., amongst them **S. KWAK**. ‘Overview of the JET preparation for deuterium–tritium operation with the ITER like-wall’. In: *Nuclear Fusion*, Vol. 59.11 (Nov. 2019), page 112021. DOI: 10.1088/1741-4326/ab2276.

- [7] F. EFFENBERG et al., amongst them **S. KWAK**. ‘First demonstration of radiative power exhaust with impurity seeding in the island divertor at Wendelstein 7-X’. In: *Nuclear Fusion*, Vol. 59.10 (Oct. 2019), page 106020. DOI: 10.1088/1741-4326/ab32c4.
- [8] A. PAVONE et al., amongst them **S. KWAK**. ‘Measurements of visible bremsstrahlung and automatic Bayesian inference of the effective plasma charge Z_{eff} at W7-X’. In: *Journal of Instrumentation*, Vol. 14.10 (Oct. 2019), pages C10003–C10003. DOI: 10.1088/1748-0221/14/10/C10003.
- [9] D. ZHANG et al., amongst them **S. KWAK**. ‘First Observation of a Stable Highly Dissipative Divertor Plasma Regime on the Wendelstein 7-X Stellarator’. In: *Physical Review Letters*, Vol. 123.2 (July 2019), page 025002. DOI: 10.1103/PhysRevLett.123.025002.
- [10] A. PAVONE, J. SVENSSON, A. LANGENBERG, U. HÖFEL, **S. KWAK**, N. PABLANT and R. C. WOLF. ‘Neural network approximation of Bayesian models for the inference of ion and electron temperature profiles at W7-X’. In: *Plasma Physics and Controlled Fusion*, Vol. 61.7 (July 2019), page 075012. DOI: 10.1088/1361-6587/ab1d26.
- [11] T. BARBUI et al., amongst them **S. KWAK**. ‘Radiative edge cooling experiments in Wendelstein 7-X start-up limiter campaign’. In: *Nuclear Fusion*, Vol. 59.7 (July 2019), page 076008. DOI: 10.1088/1741-4326/ab18c5.
- [12] U. HOEFEL et al., amongst them **S. KWAK**. ‘Bayesian modeling of microwave radiometer calibration on the example of the Wendelstein 7-X electron cyclotron emission diagnostic’. In: *Review of Scientific Instruments*, Vol. 90.4 (Apr. 2019), page 043502. DOI: 10.1063/1.5082542.
- [13] S. JOUNG et al., amongst them **S. KWAK**. ‘Imputation of faulty magnetic sensors with coupled Bayesian and Gaussian processes to reconstruct the magnetic equilibrium in real time’. In: *Review of Scientific Instruments*, Vol. 89.10 (Oct. 2018), 10K106. DOI: 10.1063/1.5038938.
- [14] A. PAVONE, J. SVENSSON, A. LANGENBERG, N. PABLANT, U. HOEFEL, **S. KWAK** and R. C. WOLF. ‘Bayesian uncertainty calculation in neural network inference of ion and electron temperature profiles at W7-X’. In: *Review of Scientific Instruments*, Vol. 89.10 (Oct. 2018), 10K102. DOI: 10.1063/1.5039286.

- [15] K.-R. PARK, K.-H. KIM, **S. KWAK**, J. SVENSSON, J. LEE and Y.-C. GHIM. 'Feasibility study of direct spectra measurements for Thomson scattered signals for KSTAR fusion-grade plasmas'. In: *Journal of Instrumentation*, Vol. 12.11 (Nov. 2017), pages C11022–C11022. DOI: 10.1088/1748-0221/12/11/C11022.
- [16] H. T. MORA et al., amongst them **S. KWAK**. 'FPGA acceleration of Bayesian model based analysis for time-independent problems'. In: *2017 IEEE Global Conference on Signal and Information Processing (GlobalSIP)*. IEEE, Nov. 2017, pages 774–778. DOI: 10.1109/GlobalSIP.2017.8309065.
- [17] R. WOLF et al., amongst them **S. KWAK**. 'Major results from the first plasma campaign of the Wendelstein 7-X stellarator'. In: *Nuclear Fusion*, Vol. 57.10 (Oct. 2017), page 102020. DOI: 10.1088/1741-4326/aa770d.
- [18] X. LITAUDON et al., amongst them **S. KWAK**. 'Overview of the JET results in support to ITER'. In: *Nuclear Fusion*, Vol. 57.10 (Oct. 2017), page 102001. DOI: 10.1088/1741-4326/aa5e28.

Acronyms

ECE electron cyclotron emission	LCFS last closed flux surface
EFIT equilibrium fitting	
FIR far infrared	MAP maximum a posteriori
FPGA field-programmable gate array	MC Monte Carlo
HRTS high-resolution Thomson scattering	MCMC Markov chain Monte Carlo
	MHD magnetohydrodynamic
ITER International Thermonuclear Experimental Reactor	PFC plasma facing component
JET Joint European Torus	W7-X Wendelstein 7-X
KSTAR Korea Superconducting Tokamak Advanced Research	XICS X-ray imaging crystal spectroscopy

Bibliography

- [1] J. SVENSSON. ‘Connecting theory and experiments in complex systems’. Culham Plasma Physics Summer School. 2008–2019.
- [2] E. T. JAYNES. *Probability Theory: The Logic of Science*. Cambridge University Press, 2003.
- [3] K. GÖDEL. ‘Über formal unentscheidbare Sätze der Principia Mathematica und verwandter Systeme I’. In: *Monatshefte für Mathematik und Physik*, Vol. 38-38.1 (Dec. 1931), pages 173–198. DOI: 10 . 1007 / BF01700692.
- [4] A. M. TURING. ‘On Computable Numbers, with an Application to the Entscheidungsproblem’. In: *Proceedings of the London Mathematical Society*, Vol. s2-42.1 (1937), pages 230–265. DOI: 10 . 1112 / plms / s2 - 42 . 1 . 230.
- [5] E. REITER and R. DALE. *Building Natural Language Generation Systems*. Cambridge University Press, 2000.
- [6] A. TOPIRCEANU, G. BARINA and M. UDRESCU. ‘MuSeNet: Collaboration in the Music Artists Industry’. In: *2014 European Network Intelligence Conference*. IEEE, Sept. 2014, pages 89–94. DOI: 10 . 1109 / ENIC . 2014 . 10.
- [7] D. SILVER et al. ‘Mastering the game of Go with deep neural networks and tree search’. In: *Nature*, Vol. 529.7587 (Jan. 2016), pages 484–489. DOI: 10 . 1038 / nature16961.
- [8] O. VINYALS et al. ‘Grandmaster level in StarCraft II using multi-agent reinforcement learning’. In: *Nature*, Vol. 575.7782 (Nov. 2019), pages 350–354. DOI: 10 . 1038 / s41586 - 019 - 1724 - z.
- [9] D. HUME. *An Inquiry Concerning Human Understanding*. Oxford University Press, 1748.

- [10] J. PEARL. *Causality: Models, Reasoning, and Inference*. Cambridge University Press, 2000.
- [11] F. BACON. *Novum Organum*. Longman & Co., London, 1620.
- [12] R. DESCARTES. *A Discourse on the Method of Rightly Conducting One's Reason and of Seeking Truth in the Sciences*. Oxford University Press, 1637.
- [13] G. GALILEI. *The Discourses and Mathematical Demonstrations Relating to Two New Sciences*. University of Wisconsin Press, 1638.
- [14] S. H. JEFFREYS. *Theory of Probability*. Oxford University Press, 1939.
- [15] K. POPPER. *The logic of scientific discovery*. Routledge, 1959.
- [16] R. T. COX. *The Algebra of Probable Inference*. Johns Hopkins University Press, 1961.
- [17] S. H. JEFFREYS. *Scientific Inference*. Oxford University Press, 1973.
- [18] J. PEARL. *Probabilistic Reasoning in Intelligent Systems: Networks of Plausible Inference*. Morgan Kaufmann, 1988.
- [19] S. F. GULL. 'Bayesian Inductive Inference and Maximum Entropy'. In: *Maximum-Entropy and Bayesian Methods in Science and Engineering: Foundations*. Edited by G. J. ERICKSON and C. R. SMITH. Springer Netherlands, 1988, pages 53–74. DOI: 10.1007/978-94-009-3049-0_4.
- [20] D. J. MACKAY. *Bayesian methods for adaptive models*. PhD thesis. California Institute of Technology, 1991.
- [21] J. SVENSSON and A. WERNER. 'Large Scale Bayesian Data Analysis for Nuclear Fusion Experiments'. In: *2007 IEEE International Symposium on Intelligent Signal Processing*. IEEE, 2007, pages 1–6. DOI: 10.1109/WISP.2007.4447579.
- [22] SEED eSCIENCE RESEARCH. 'The Minerva framework'. URL: <https://seed-escience.org/>.
- [23] T. BAYES. 'LII. An essay towards solving a problem in the doctrine of chances. By the late Rev. Mr. Bayes, F. R. S. communicated by Mr. Price, in a letter to John Canton, A. M. F. R. S'. In: *Philosophical Transactions of the Royal Society of London*, Vol. 53 (Jan. 1763), pages 370–418. DOI: 10.1098/rstl.1763.0053.

-
- [24] P.-S. LAPLACE. *A Philosophical Essay on Probabilities*. New York: Dover Publications Inc., 1814.
- [25] J. M. KEYNES. *A Treatise on Probability*. London: Macmillan & Co., 1921.
- [26] G. D'AGOSTINI. *Bayesian reasoning in high-energy physics: principles and applications*. CERN Yellow Reports: Monographs. Geneva: CERN, 1999. DOI: 10.5170/CERN-1999-003.
- [27] G. D'AGOSTINI. 'Bayesian inference in processing experimental data: principles and basic applications'. In: *Reports on Progress in Physics*, Vol. 66.9 (Aug. 2003), pages 1383–1419. DOI: 10.1088/0034-4885/66/9/201.
- [28] J. S. DEVINDERJIT SIVIA. *Data Analysis: A Bayesian Tutorial*. Oxford University Press, 2006.
- [29] R. M. NEAL. *Bayesian learning for neural networks*. PhD thesis. University of Toronto, 1995.
- [30] Y. GAL. *Uncertainty in deep learning*. PhD thesis. University of Cambridge, 2016.
- [31] Z. GHAHRAMANI. 'Probabilistic machine learning and artificial intelligence'. In: *Nature*, Vol. 521.7553 (May 2015), pages 452–459. DOI: 10.1038/nature14541.
- [32] G. A. COTTRELL. 'Maximum entropy and plasma physics'. In: (1990). URL: <http://www.euro-fusionscipub.org/wp-content/uploads/2014/11/JETP90004.pdf>.
- [33] J. SVENSSON. *Artificial neural network modelling in nuclear fusion research and engineering at the JET tokamak*. PhD thesis. KTH Royal Institute of Technology, 2000.
- [34] R. FISCHER, C. WENDLAND, A. DINKLAGE, S. GORI, V. DOSE and T. W.-A. TEAM. 'Thomson scattering analysis with the Bayesian probability theory'. In: *Plasma Physics and Controlled Fusion*, Vol. 44.8 (Aug. 2002), page 306. DOI: 10.1088/0741-3335/44/8/306.
- [35] J. SVENSSON, A. DINKLAGE, J. GEIGER, A. WERNER and R. FISCHER. 'Integrating diagnostic data analysis for W7-AS using Bayesian graphical models'. In: *Review of Scientific Instruments*, Vol. 75.10 (Oct. 2004), pages 4219–4221. DOI: 10.1063/1.1789611.

- [36] R. FISCHER, C. J. FUCHS, B. KURZAN, W. SUTTROP and E. WOLFRUM. ‘Integrated Data Analysis of Profile Diagnostics at ASDEX Upgrade’. In: *Fusion Science and Technology*, Vol. 58.2 (Oct. 2010), pages 675–684. DOI: 10.13182/FST10-110.
- [37] O. P. FORD. *Tokamak plasma analysis through Bayesian diagnostic modelling*. PhD thesis. Imperial College London, 2010.
- [38] J. SVENSSON. ‘Non-parametric Tomography Using Gaussian Processes’. In: *JET report, EFDA-JET-PR(11)24*, (2011). URL: <http://www.euro-fusionscipub.org/wp-content/uploads/eurofusion/EFDP11024.pdf>.
- [39] J. A. ROMERO, S. A. DETTRICK, E. GRANSTEDT, T. ROCHE and Y. MOK. ‘Inference of field reversed configuration topology and dynamics during Alfvénic transients’. In: *Nature Communications*, Vol. 9.1 (Dec. 2018), page 691. DOI: 10.1038/s41467-018-03110-5.
- [40] A. KOLMOGOROV. *Foundations of the Theory of Probability*. New York: Chelsea., 1933.
- [41] A. Y. NG and M. I. JORDAN. ‘On Discriminative vs. Generative Classifiers: A comparison of logistic regression and naive Bayes’. In: *Advances in Neural Information Processing Systems 14*. Edited by T. G. DIETTERICH, S. BECKER and Z. GHAHRAMANI. MIT Press, 2002, pages 841–848. URL: <http://papers.nips.cc/paper/2002-on-discriminative-vs-generative-classifiers-a-comparison-of-logistic-regression-and-naive-bayes.pdf>.
- [42] S. KULLBACK and R. A. LEIBLER. ‘On Information and Sufficiency’. In: *The Annals of Mathematical Statistics*, Vol. 22.1 (Mar. 1951), pages 79–86. DOI: 10.1214/aoms/1177729694.
- [43] B. RUSSELL. *History of Western Philosophy*. Allen & Unwin, 1945.
- [44] C. E. SHANNON. ‘A Mathematical Theory of Communication’. In: *Bell System Technical Journal*, Vol. 27.3 (July 1948), pages 379–423. DOI: 10.1002/j.1538-7305.1948.tb01338.x.
- [45] A. O’HAGAN. ‘Curve Fitting and Optimal Design for Prediction’. In: *Journal of the Royal Statistical Society. Series B (Methodological)*, Vol. 40.1 (1978), pages 1–42. URL: <http://www.jstor.org/stable/2984861>.

-
- [46] C. E. RASMUSSEN and C. K. I. WILLIAMS. *Gaussian Processes for Machine Learning*. MIT Press, 2006.
- [47] R. A. HORN and C. R. JOHNSON. *Matrix Analysis*. Cambridge University Press, 1985. DOI: 10.1017/CBO9780511810817.
- [48] N. J. HIGHAM. *Accuracy and Stability of Numerical Algorithms*. Second. Society for Industrial and Applied Mathematics, 2002. DOI: 10.1137/1.9780898718027.
- [49] D. LI, J. SVENSSON, H. THOMSEN, F. MEDINA, A. WERNER and R. WOLF. ‘Bayesian soft X-ray tomography using non-stationary Gaussian Processes’. In: *Review of Scientific Instruments*, Vol. 84.8 (Aug. 2013), page o83506. DOI: 10.1063/1.4817591.
- [50] M. CHILENSKI, M. GREENWALD, Y. MARZOUK, N. HOWARD, A. WHITE, J. RICE and J. WALK. ‘Improved profile fitting and quantification of uncertainty in experimental measurements of impurity transport coefficients using Gaussian process regression’. In: *Nuclear Fusion*, Vol. 55.2 (Feb. 2015), page o23012. DOI: 10.1088/0029-5515/55/2/023012.
- [51] A. LANGENBERG, J. SVENSSON, H. THOMSEN, O. MARCHUK, N. A. PABLANT, R. BURHENN and R. C. WOLF. ‘Forward Modeling of X-Ray Imaging Crystal Spectrometers Within the Minerva Bayesian Analysis Framework’. In: *Fusion Science and Technology*, Vol. 69.2 (Apr. 2016), pages 560–567. DOI: 10.13182/FST15-181.
- [52] H. GRAD and H. RUBIN. ‘Hydromagnetic equilibria and force-free fields’. In: *Journal of Nuclear Energy (1954)*, Vol. 7.3-4 (1958), pages 284–285.
- [53] V. D. SHAFRANOV. ‘Equilibrium of a toroidal plasma in a magnetic field’. In: *Journal of Nuclear Energy. Part C, Plasma Physics, Accelerators, Thermonuclear Research*, Vol. 5.4 (Jan. 1963), pages 251–258. DOI: 10.1088/0368-3281/5/4/307.
- [54] J. SVENSSON and A. WERNER. ‘Current tomography for axisymmetric plasmas’. In: *Plasma Physics and Controlled Fusion*, Vol. 50.8 (Aug. 2008), page o85002. DOI: 10.1088/0741-3335/50/8/085002.
- [55] R. HOOKE and T. A. JEEVES. ‘“Direct Search” Solution of Numerical and Statistical Problems’. In: *Journal of the ACM*, Vol. 8.2 (Apr. 1961), pages 212–229. DOI: 10.1145/321062.321069.

- [56] N. METROPOLIS, A. W. ROSENBLUTH, M. N. ROSENBLUTH, A. H. TELLER and E. TELLER. 'Equation of State Calculations by Fast Computing Machines'. In: *The Journal of Chemical Physics*, Vol. 21.6 (June 1953), pages 1087–1092. DOI: 10.1063/1.1699114.
- [57] W. K. HASTINGS. 'Monte Carlo sampling methods using Markov chains and their applications'. In: *Biometrika*, Vol. 57.1 (Apr. 1970), pages 97–109. DOI: 10.1093/biomet/57.1.97.
- [58] H. HAARIO, E. SAKSMAN and J. TAMMINEN. 'An Adaptive Metropolis Algorithm'. In: *Bernoulli*, Vol. 7.2 (Apr. 2001), page 223. DOI: 10.2307/3318737.
- [59] O. FORD, J. SVENSSON, A. BOBOC and D. C. McDONALD. 'Forward modeling of JET polarimetry diagnostic'. In: *Review of Scientific Instruments*, Vol. 79.10 (Oct. 2008), 10F324. DOI: 10.1063/1.2956880.
- [60] S. BOZHENKOV et al. 'The Thomson scattering diagnostic at Wendelstein 7-X and its performance in the first operation phase'. In: *Journal of Instrumentation*, Vol. 12.10 (Oct. 2017), P10004–P10004. DOI: 10.1088/1748-0221/12/10/P10004.
- [61] U. HOEFEL et al. 'Bayesian modeling of microwave radiometer calibration on the example of the Wendelstein 7-X electron cyclotron emission diagnostic'. In: *Review of Scientific Instruments*, Vol. 90.4 (Apr. 2019), page 043502. DOI: 10.1063/1.5082542.
- [62] A. PAVONE et al. 'Measurements of visible bremsstrahlung and automatic Bayesian inference of the effective plasma charge Z_{eff} at W7-X'. In: *Journal of Instrumentation*, Vol. 14.10 (Oct. 2019), pages C10003–C10003. DOI: 10.1088/1748-0221/14/10/C10003.
- [63] H. T. MORA et al. 'FPGA acceleration of Bayesian model based analysis for time-independent problems'. In: *2017 IEEE Global Conference on Signal and Information Processing (GlobalSIP)*. IEEE, Nov. 2017, pages 774–778. DOI: 10.1109/GlobalSIP.2017.8309065.
- [64] A. PAVONE, J. SVENSSON, A. LANGENBERG, N. PABLANT, U. HOEFEL, S. KWAK and R. C. WOLF. 'Bayesian uncertainty calculation in neural network inference of ion and electron temperature profiles at W7-X'. In: *Review of Scientific Instruments*, Vol. 89.10 (Oct. 2018), 10K102. DOI: 10.1063/1.5039286.

- [65] A. PAVONE, J. SVENSSON, A. LANGENBERG, U. HÖFEL, S. KWAK, N. PABLANT and R. C. WOLF. ‘Neural network approximation of Bayesian models for the inference of ion and electron temperature profiles at W7-X’. In: *Plasma Physics and Controlled Fusion*, Vol. 61.7 (July 2019), page 075012. DOI: 10.1088/1361-6587/ab1d26.
- [66] A. EINSTEIN. ‘Ist die Trägheit eines Körpers von seinem Energieinhalt abhängig?’ In: *Annalen der Physik*, Vol. 323.13 (1905), pages 639–641. DOI: 10.1002/andp.19053231314. eprint: <https://onlinelibrary.wiley.com/doi/pdf/10.1002/andp.19053231314>.
- [67] J. P. FREIDBERG. *Plasma Physics and Fusion Energy*. Cambridge University Press, 2008.
- [68] H. A. BETHE. ‘Energy Production in Stars’. In: *Physical Review*, Vol. 55.5 (Mar. 1939), pages 434–456. DOI: 10.1103/PhysRev.55.434.
- [69] J. NUCKOLLS, L. WOOD, A. THIESSEN and G. ZIMMERMAN. ‘Laser Compression of Matter to Super-High Densities: Thermonuclear (CTR) Applications’. In: *Nature*, Vol. 239.5368 (Sept. 1972), pages 139–142. DOI: 10.1038/239139a0.
- [70] A. S. RICHARDSON. *NRL Plasma Formulary*. Technical report. US Naval Research Laboratory, 2019. URL: https://www.nrl.navy.mil/ppd/sites/www.nrl.navy.mil/ppd/files/pdfs/NRL_Formulary_2019.pdf.
- [71] J. D. LAWSON. ‘Some Criteria for a Power Producing Thermonuclear Reactor’. In: *Proceedings of the Physical Society. Section B*, Vol. 70.1 (Jan. 1957), pages 6–10. DOI: 10.1088/0370-1301/70/1/303.
- [72] F. L. HINTON and R. D. HAZELTINE. ‘Theory of plasma transport in toroidal confinement systems’. In: *Reviews of Modern Physics*, Vol. 48.2 (Apr. 1976), pages 239–308. DOI: 10.1103/RevModPhys.48.239.
- [73] B. KADOMTSEV. ‘Plasma transport in tokamaks’. In: *Nuclear Fusion*, Vol. 31.7 (July 1991), pages 1301–1314. DOI: 10.1088/0029-5515/31/7/006.
- [74] P. HELANDER and D. J. SIGMAR. *Collisional Transport in Magnetized Plasmas*. Cambridge University Press, 2005.

- [75] B. COPPI and G. REWOLDT. ‘New Trapped-Electron Instability’. In: *Physical Review Letters*, Vol. 33.22 (Nov. 1974), pages 1329–1332. DOI: 10.1103/PhysRevLett.33.1329.
- [76] P. N. GUZDAR. ‘Ion-temperature-gradient instability in toroidal plasmas’. In: *Physics of Fluids*, Vol. 26.3 (1983), page 673. DOI: 10.1063/1.864182.
- [77] A. J. WOOTTON, B. A. CARRERAS, H. MATSUMOTO, K. MCGUIRE, W. A. PEEBLES, C. P. RITZ, P. W. TERRY and S. J. ZWEBEN. ‘Fluctuations and anomalous transport in tokamaks’. In: *Physics of Fluids B: Plasma Physics*, Vol. 2.12 (1990), pages 2879–2903. DOI: 10.1063/1.859358.
- [78] R. C. WOLF. ‘Internal transport barriers in tokamak plasmas*’. In: *Plasma Physics and Controlled Fusion*, Vol. 45.1 (Jan. 2003), R1–R91. DOI: 10.1088/0741-3335/45/1/201.
- [79] A. D. FOKKER. ‘Die mittlere Energie rotierender elektrischer Dipole im Strahlungsfeld’. In: *Annalen der Physik*, Vol. 348.5 (1914), pages 810–820. DOI: 10.1002/andp.19143480507.
- [80] M. PLANCK. ‘Über einen Satz der statistischen Dynamik und seine Erweiterung in der Quantentheorie’. In: Vol. 24 (1917), pages 324–341. URL: <https://www.biodiversitylibrary.org/item/92720>.
- [81] V. MUKHOVATOV and V. SHAFRANOV. ‘Plasma equilibrium in a Tokamak’. In: *Nuclear Fusion*, Vol. 11.6 (Dec. 1971), pages 605–633. DOI: 10.1088/0029-5515/11/6/005.
- [82] S. P. HIRSHMAN. ‘Steepest-descent moment method for three-dimensional magnetohydrodynamic equilibria’. In: *Physics of Fluids*, Vol. 26.12 (1983), page 3553. DOI: 10.1063/1.864116.
- [83] L. LAO, H. ST. JOHN, R. STAMBAUGH, A. KELLMAN and W. PFEIFFER. ‘Reconstruction of current profile parameters and plasma shapes in tokamaks’. In: *Nuclear Fusion*, Vol. 25.11 (1985), pages 1611–1622. DOI: 10.1088/0029-5515/25/11/007.
- [84] J. D. HANSON, S. P. HIRSHMAN, S. F. KNOWLTON, L. L. LAO, E. A. LAZARUS and J. M. SHIELDS. ‘V3FIT: a code for three-dimensional equilibrium reconstruction’. In: *Nuclear Fusion*, Vol. 49.7 (July 2009), page 075031. DOI: 10.1088/0029-5515/49/7/075031.

-
- [85] J. P. FREIDBERG. *Ideal Magnetohydrodynamics*. Cambridge University Press, 2008.
- [86] ASDEX TEAM. ‘The H-Mode of ASDEX’. In: *Nuclear Fusion*, Vol. 29.11 (Nov. 1989), pages 1959–2040. DOI: 10 . 1088 / 0029 - 5515 / 29 / 11 / 010.
- [87] J. WESSON. *THE SCIENCE OF JET*. Technical report. Nov. 1991. URL: <http://www.euro-fusionscipub.org/wp-content/uploads/2014/11/JETR99013.pdf>.
- [88] JET TEAM. ‘Physics of high performance JET plasmas in DT’. In: *Nuclear Fusion*, Vol. 39.9Y (Sept. 1999), pages 1227–1244. DOI: 10 . 1088 / 0029 - 5515 / 39 / 9y / 302.
- [89] A. IYOSHI et al. ‘Overview of the Large Helical Device project’. In: *Nuclear Fusion*, Vol. 39.9Y (Sept. 1999), pages 1245–1256. DOI: 10 . 1088 / 0029 - 5515 / 39 / 9Y / 313.
- [90] T. KLINGER et al. ‘Performance and properties of the first plasmas of Wendelstein 7-X’. In: *Plasma Physics and Controlled Fusion*, Vol. 59.1 (Jan. 2017), page 014018. DOI: 10 . 1088 / 0741 - 3335 / 59 / 1 / 014018.
- [91] R. WOLF et al. ‘Major results from the first plasma campaign of the Wendelstein 7-X stellarator’. In: *Nuclear Fusion*, Vol. 57.10 (Oct. 2017), page 102020. DOI: 10 . 1088 / 1741 - 4326 / aa770d.
- [92] T. KLINGER et al. ‘Overview of first Wendelstein 7-X high-performance operation’. In: *Nuclear Fusion*, Vol. 59.11 (Nov. 2019), page 112004. DOI: 10 . 1088 / 1741 - 4326 / ab03a7.
- [93] R. C. WOLF et al. ‘Performance of Wendelstein 7-X stellarator plasmas during the first divertor operation phase’. In: *Physics of Plasmas*, Vol. 26.8 (Aug. 2019), page 082504. DOI: 10 . 1063 / 1 . 5098761.
- [94] L. SPITZEB. ‘The stellarator concept’. In: *Physics of Fluids*, Vol. 1.4 (1958), pages 253–264. DOI: 10 . 1063 / 1 . 1705883.
- [95] J. WESSON and D. J. CAMPBELL. *Tokamaks*. Clarendon Press, 2004.
- [96] X. LITAUDON et al. ‘Overview of the JET results in support to ITER’. In: *Nuclear Fusion*, Vol. 57.10 (Oct. 2017), page 102001. DOI: 10 . 1088 / 1741 - 4326 / aa5e28.

- [97] E. JOFFRIN et al. ‘Overview of the JET preparation for deuterium–tritium operation with the ITER like-wall’. In: *Nuclear Fusion*, Vol. 59.11 (Nov. 2019), page 112021. DOI: 10.1088/1741-4326/ab2276.
- [98] M. KEILHACKER et al. ‘High fusion performance from deuterium-tritium plasmas in JET’. In: *Nuclear Fusion*, Vol. 39.2 (Feb. 1999), pages 209–234. DOI: 10.1088/0029-5515/39/2/306.
- [99] M. KEILHACKER. ‘Fusion physics progress on the Joint European Torus (JET)’. In: *Plasma Physics and Controlled Fusion*, Vol. 41.SUPPL. 12B (Dec. 1999), B1–B23. DOI: 10.1088/0741-3335/41/12B/301.
- [100] R. AYMAR, P. BARABASCHI and Y. SHIMOMURA. ‘The ITER design’. In: *Plasma Physics and Controlled Fusion*, Vol. 44.5 (May 2002), pages 519–565. DOI: 10.1088/0741-3335/44/5/304.
- [101] G. GRIEGER et al. ‘Physics optimization of stellarators’. In: *Physics of Fluids B: Plasma Physics*, Vol. 4.7 (Mar. 1992), pages 2081–2091. DOI: 10.1063/1.860481.
- [102] M. BRIX et al. ‘Upgrade of the lithium beam diagnostic at JET’. In: *Review of Scientific Instruments*, Vol. 81.10 (Oct. 2010), page 10D733. DOI: 10.1063/1.3502320.
- [103] M. BRIX et al. ‘Recent improvements of the JET lithium beam diagnostic’. In: *Review of Scientific Instruments*, Vol. 83.10 (Oct. 2012), page 10D533. DOI: 10.1063/1.4739411.
- [104] T. BARBUI, M. KRYCHOWIAK, R. KÖNIG, O. SCHMITZ, B. MUÑOZ, B. SCHWEER and A. TERRA. ‘Feasibility of line-ratio spectroscopy on helium and neon as edge diagnostic tool for Wendelstein 7-X’. In: *Review of Scientific Instruments*, Vol. 87.11 (Nov. 2016), 11E554. DOI: 10.1063/1.4962989.
- [105] T. BARBUI et al. ‘The He/Ne beam diagnostic for line-ratio spectroscopy in the island divertor of Wendelstein 7-X’. In: *Journal of Instrumentation*, Vol. 14.07 (July 2019), page C07014. DOI: 10.1088/1748-0221/14/07/C07014.
- [106] J. J. THOMSON. *Conduction of Electricity Through Gases*. Cambridge University Press, 1906.

-
- [107] R. PASQUALOTTO, P. NIELSEN, C. GOWERS, M. BEURSKENS, M. KEMPENAARS, T. CARLSTROM and D. JOHNSON. ‘High resolution Thomson scattering for Joint European Torus (JET)’. In: *Review of Scientific Instruments*, Vol. 75.10 II (Oct. 2004), pages 3891–3893. DOI: 10.1063/1.1787922.
- [108] A. BOBOC, M. GELFUSA, A. MURARI and P. GAUDIO. ‘Recent developments of the JET far-infrared interferometer-polarimeter diagnostic’. In: *Review of Scientific Instruments*, Vol. 81.10 (Oct. 2010), page 10D538. DOI: 10.1063/1.3478146.
- [109] A. BOBOC, C. GIL, P. PASTOR, P. SPUIG, T. EDLINGTON and S. DORLING. ‘Upgrade of the JET far infrared interferometer diagnostic’. In: *Review of Scientific Instruments*, Vol. 83.10 (Oct. 2012), 10E341. DOI: 10.1063/1.4737420.
- [110] A. BOBOC, B. BIEG, R. FELTON, S. DALLEY and Y. KRAVTSOV. ‘Invited Article: A novel calibration method for the JET real-time far infrared polarimeter and integration of polarimetry-based line-integrated density measurements for machine protection of a fusion plant’. In: *Review of Scientific Instruments*, Vol. 86.9 (Sept. 2015), page 091301. DOI: 10.1063/1.4929443.
- [111] J. KNAUER, P. KORNEJEW, H. TRIMINO MORA, M. HIRSCH, A. WERNER, R. C. WOLF and THE W7-X TEAM. ‘A new dispersion interferometer for the stellarator Wendelstein 7-X’. Proceeding of the 43rd EPS Conference on Plasma Physics, P. Mantica ed., European Physical Society. Leuven, Belgium, 4th July 2016.
- [112] S. KWAK, J. SVENSSON, M. BRIX and Y.-C. GHIM. ‘Bayesian modelling of the emission spectrum of the Joint European Torus Lithium Beam Emission Spectroscopy system’. In: *Review of Scientific Instruments*, Vol. 87.2 (2nd Feb. 2016), page 023501. DOI: 10.1063/1.4940925.
- [113] S. KWAK, J. SVENSSON, M. BRIX and Y.-C. GHIM. ‘Bayesian electron density inference from JET lithium beam emission spectra using Gaussian processes’. In: *Nuclear Fusion*, Vol. 57.3 (11th Jan. 2017), page 036017. DOI: 10.1088/1741-4326/aa5072.

- [114] S. KWAK, J. SVENSSON, S. BOZHENKOV, J. FLANAGAN, M. KEMPEN-
AARS, A. BOBOC and Y.-C. GHIM. ‘Bayesian modelling of Thomson
scattering and multichannel interferometer diagnostics using Gaussian
processes’. In: *Nuclear Fusion*, Vol. 60.4 (26th Feb. 2020), page 046009.
DOI: 10.1088/1741-4326/ab686e.
- [115] S. KWAK, J. SVENSSON, S. BOZHENKOV, H. T. MORA, U. HOEFEL, A.
PAVONE, M. KRYCHOWIAK, A. LANGENBERG and Y.-C. GHIM. ‘Bayesian
modelling of multiple diagnostics at Wendelstein 7-X’. In: *Plasma Phys-
ics and Controlled Fusion*, (2020). In preparation.
- [116] S. KWAK, J. SVENSSON, O. FORD, L. APPEL and Y.-C. GHIM. ‘Bayesian
equilibria of axisymmetric plasmas’. In: *Nuclear Fusion*, (2020). In pre-
paration.
- [117] A. PAVONE, J. SVENSSON, S. KWAK, M. BRIX and R. C. WOLF. ‘Neural
network approximated Bayesian inference of edge electron density pro-
files at JET’. In: *Plasma Physics and Controlled Fusion*, Vol. 62.4 (Mar.
2020), page 045019. DOI: 10.1088/1361-6587/ab7732.
- [118] S. JOUNG et al. ‘Deep neural network Grad-Shafranov solver constrained
with measured magnetic signals’. In: *Nuclear Fusion*, Vol. 60.1 (Jan. 2020),
page 016034. DOI: 10.1088/1741-4326/ab555f.
- [119] S. KWAK, Y. JEON and Y.-C. GHIM. ‘Equilibrium reconstruction based
on the neural network algorithm in real time’. KSTAR Conference 2014.
Gangwon-do, Republic of Korea, 24th Feb. 2014.
- [120] S. KWAK, Y. JEON and Y.-C. GHIM. ‘Real-time EFIT data reconstruction
based on neural network in KSTAR’. 56th Annual Meeting of the APS
Division of Plasma Physics. New Orleans, Louisiana, USA, 27th Oct.
2014.
- [121] K.-R. PARK, K.-H. KIM, S. KWAK, J. SVENSSON, J. LEE and Y.-C. GHIM.
‘Feasibility study of direct spectra measurements for Thomson scattered
signals for KSTAR fusion-grade plasmas’. In: *Journal of Instrumentation*,
Vol. 12.11 (Nov. 2017), pages C11022–C11022. DOI: 10.1088/1748-022
1/12/11/C11022.

- [122] D. ZHANG et al. 'First Observation of a Stable Highly Dissipative Divertor Plasma Regime on the Wendelstein 7-X Stellarator'. In: *Physical Review Letters*, Vol. 123.2 (July 2019), page 025002. DOI: 10.1103/PhysRevLett.123.025002.
- [123] T. BARBUI et al. 'Radiative edge cooling experiments in Wendelstein 7-X start-up limiter campaign'. In: *Nuclear Fusion*, Vol. 59.7 (July 2019), page 076008. DOI: 10.1088/1741-4326/ab18c5.